Bruce George Pound

The Polarisation Behaviour of Silver in Potassium Hydroxide Solution at Elevated Temperatures

Submitted for the degree of

Doctor of Philosophy in Chemistry

at the Victoria University of Wellington.

November, 1977.

Abstract

The polarisation behaviour of silver in 1 mol kg^{-1} KOH solution over the temperature range 295-478 K was studied using cyclic voltammetry, potentiostatic, galvanostatic and a.c. impedance techniques.

Thermodynamic data for the silver/water system at temperatures up to 573 K is presented in the form of potential-pH diagrams which assist in the interpretation of results at elevated temperatures.

The cyclic voltammograms and galvanostatic charging curves indicate the principal changes to be the appearance of additional peaks and arrests, respectively, as the temperature is increased, followed by their disappearance at higher temperatures. The data obtained from cyclic voltammetry and also potentiostatic polarisation are analysed in terms of previously-derived relations for limiting rate control, in particular that due to diffusion.

The impedance data are examined using equivalent circuit models from which it is shown that surface roughness of the electrodes has a significant effect on the reaction kinetics over the temperature range studied. It is proposed that substantial changes in the electrochemistry of silver at 478 K are associated with extensive surface roughness evident from electron micrographs. The impedance data also indicates that a change in the kinetics of growth of the Ag_2O multilayer takes place at elevated temperatures with the rate of nucleation of Ag_2O growth centres becoming more important in relation to the rate of solid-state diffusion.

Contents

Figures

SECTION

I

INTRODUCTION

CHAPTER 1 INTRODUCTION

1.1 THE SIGNIFICANCE OF POLARISATION STUDIES IN AQUEOUS SYSTEMS AT ELEVATED TEMPERATURES

1.1.1 General Behaviour of Metals

The behaviour of metals in such an environment has attracted considerable interest over recent years (128). Alloys containing copper, nickel and iron as the major components are used industrially at elevated temperatures, often up to 573 K under which conditions most of these alloys are thermodynamically unstable.

The behaviour of various alloys and steels at temperatures greater than 373 K is of practical interest in electrical energy-producing industries since several types of nuclear and fossil-fueled power stations employ dilute hydroxide solutions as heat transport media. The nature of the electrolyte is a dominant factor in determining the behaviour of metals under such conditions. A pH of 7-9 at 473 K (neutral point = 5.7) in the case of nickel for example, corresponds to a minimum in the solubility of nickel oxides at this temperature (44).

The products formed by corrosion reactions can accumulate, thereby reducing the effectiveness of heat transfer processes and in the case of water-cooled nuclear reactors, they may cause a build-up of radioactivity. In practice, the use of alloys is clearly restricted by the reactions taking place at the surface, and their continued exposure to high temperature environments depends on the extent to which the rate of corrosion can be suppressed. This is normally achieved by maintaining conditions such that the metal or alloy spontaneously passivates. Hence, the effects of temperature on the formation of oxides or hydroxides are very important in these circumstances.

While some alloys, especially of the copper-nickel-iron type, have low corrosion rates, scale formation does occur particularly in the presence of oxygen (20,31,105). Studies of the structure and composition of these scales (105,143,199) in relation to properties such as temperature, pH, oxygen or hydrogen concentrations, give useful information which enables oxide formation to be minimised in practical systems. Often, however, the

electrochemical factors involved are not shown by such studies. Since the potential difference across the metal/solution interface strongly influences the kinetic and thermodynamic behaviour of corroding systems, the control and measurement of this parameter is very important.

Electrochemical studies have been undertaken for particular metals such as copper (127), nickel (44,134,157) and iron (18,133,158) but the amount of research at temperatures above 373 K is small compared with that at room temperature. In this work, the behaviour of silver is investigated using electrochemical techniques since they possess the advantage of either controlling the potential and thereby determining specific reactions to be examined, or controlling the rate of charge transferred across the metal/solution interface and hence the rate of the electrochemical reaction.

1.1.2 The Use of Silver

Considerable effort has been devoted to examining the anodic behaviour of silver at room temperature, stimulated largely by applications of the $Ag|Ag_2O$ electrode in batteries of high energy-to-mass ratio. The silver oxides possess high positive equilibrium potentials (see Table 5.2) and relatively high electrical conductivities (Ag_2O, 10^{-6} S m^{-1}; Ag_2O_2, 7 S m^{-1} (120)). Both factors offer significant advantages in lightweight alkaline storage batteries which are capable of producing high discharge rates.

Industrial and academic interest has grown also in applications of controlled electrosynthesis (195). Silver in the Ag(I) state has been used (54) for the oxidation of organic compounds, and higher valency states appear to be the cause of the catalytic effect of silver in persulphate oxidation (11).

The electrochemical formation and reduction of silver oxides have aroused interest as a result of the use of these substances as cathode materials in battery systems (61), and also because the various stages of surface oxidation of silver are well separated (34,177,182) which is not common amongst other metals, in particular Pt (178) and Pd (43). Numerous theories (for example 79, 88, 177, 182) have been advanced to explain various features of the oxidation and reduction kinetics of silver.

1.2 PAST WORK

1.2.1 Room Temperature

The oxidation of silver in 1 mol dm^{-3} KOH was first studied by Luther and Pokorney (126) using a galvanostatic technique, and Dirkse and De Vries (64) using a potential-sweep technique. Since this initial work, there have been extensive investigations of the polarisation behaviour of silver which are well reviewed (96,98,104). The following is a brief, essentially bibliographical summary of work included in and subsequent to these reviews in relation to the electrochemical reactions of silver. A critical discussion of past work is presented in later chapters as required.

Formation of Ag_2O. This will be considered in two stages:

(i) Formation of a monolayer. At potentials negative to the $Ag_2O|Ag$ potential*, that is, prior to the formation of solid phase Ag_2O at the electrode, Giles, Harrison and Thirsk (88) showed from a faradaic impedance study of single crystal electrodes that dissolution of silver occurs as the $Ag(OH)_2^-$ ion. The rate of this reaction is fast enough to maintain an equilibrium concentration at the electrode surface (exchange current density, i_o > 1 A cm^{-2}) so that the overall process is controlled by the rate of diffusion of AgO^- into the bulk solution as demonstrated by potentiodynamic and potentiostatic measurements (182). At -8 mV ($Ag_2O|Ag$), a monolayer of Ag_2O forms (87,88) which is the result of a dissolution-precipitation mechanism as indicated by a chromo-ellipsometric study (118). It was shown from a rotating ring-disc electrode study (141) that silver dissolution produces a super-saturated solution of AgO^- at the electrode surface which is followed by precipitation of a layer of Ag_2O.

---

* 0.342 V, SHE (95).

(ii) Formation of a multilayer. At more anodic potentials, the single layer of Ag_2O thickens producing an Ag_2O multilayer which was found from electron optical and electron and X-ray diffraction measurements (24) to consist of a dense primary layer formed initially, covered by a much thicker porous layer. Kabanov et al (111,121,189) using impedance techniques concluded that the multilayer formation involved the transport of silver ions through the dense primary layer to form the porous layer of Ag_2O. Subsequent studies involving potentiodynamic (182) and potentiostatic (79) methods demonstrated clearly that the rate of growth of the Ag_2O multilayer is controlled by solid state diffusion.

Formation of Ag_2O_2. Fleischmann et al (24,80) showed that oxidation of Ag_2O to Ag_2O_2 involves the progressive nucleation of Ag_2O_2 centres, initially at Ag_2O/electrolyte interface. The formation of Ag_2O_2 proceeds by three-dimensional growth on these centres, more of which are subsequently nucleated in the Ag_2O layer.

Reduction of Ag_2O_2. Miller (141) found in his rotating ring-disc electrode study that on reduction of Ag_2O_2, the surface is almost immediately covered with Ag_2O. The results showed a supersaturation of the solution indicating a mechanism of dissolution-precipitation.

Reduction of Ag_2O. Electron micrographs (24) indicate that the reduction of Ag_2O occurs by the progressive nucleation and growth of silver on two dimensional centres in the oxide layer. Subsequent potentiostatic measurements (79) were shown to be consistent with the electrochemical reaction at the surface of the centres as the rate determining step.

1.2.2 Elevated Temperatures

Little work has been done at elevated temperatures. The exchange current density and the charge transfer coefficient for Ag_2O formation have been obtained up to 333 K from galvanostatic measurements (34), while

the cyclic voltammogram and potentiostatic curve for silver at 333 K have been presented (42) for comparative purposes in a study of oxide formation on a nickel electrode.

1.3 PROPOSED RESEARCH

1.3.1 The Choice of Silver

The electrochemical behaviour of silver has been well studied and is well understood at 298 K and this forms a useful basis for an extension to elevated temperatures. In particular, silver is chosen since it has been shown at room temperature that

(i) the different stages of surface oxidation are quite distinct
(ii) it exhibits an active-to-passive transition which is typical of many corrosion-resistant industrial alloys.

The aim of this research then is to examine the temperature dependence of oxidation and reduction processes on silver, particularly anodic metal dissolution and the growth of oxide phases on the electrode surface. The study was performed using 1 mol kg^{-1} KOH solution over the temperature range 295-478 K.

1.3.2 Techniques

Four electrochemical techniques were employed. Cyclic voltammetry which is one of several methods enabling transient phenomena at electrodes to be examined, was used initially. This technique provides firstly, an indication of charge-transfer reactions which silver will undergo over a range of potentials at a given temperature and the chosen hydroxide concentration, and secondly, information on the kinetics of these processes particularly with regard to mass transport. Following cyclic voltammetry, application of a potentiostatic technique allows further information to be obtained where possible, with regard to the kinetics of oxide nucleation and growth, and permits the detection of active-to-passive transitions. A galvanostatic charging technique was also used which in this study was

intended to provide, specifically, further information on charge transfer processes over the range of temperatures.

The above techniques involve changes in current and potential with time. However, the use of the frequency domain enables the variation in impedance, with frequency, to be studied. The wide continuous frequency range which is available means that surface processes having substantially different relaxation times may be examined. The time-domain techniques then, were supplemented with an a.c. impedance method in which the frequency dispersion of the electrode impedance under potentiostatic conditions was investigated. In principle, the impedance method provides immediate experimental evidence of the state of the electrode surface, the concentration of dissolving species, double-layer capacity and the presence of an oxide film. The distinct form of the cyclic voltammogram of silver at room temperature suggests that it would be suitable to use in the application of an impedance technique at elevated temperatures. Consequently, a secondary purpose of this research was to demonstrate the usefulness of this technique in yielding information on the kinetics of film formation which is comparable, if not more detailed than that obtained jointly from cyclic voltammetry and potentiostatic polarisation.

While it is desirable in some experiments to control the hydrodynamic conditions in order to examine mass transfer processes, the extension of such studies to elevated temperatures presents significant technical problems. These problems may be overcome but this is achieved by the use of often complicated systems. In view of this fact, it was decided to apply the above techniques independent of hydrodynamic control. Consequently, experiments involving rotating disc or other controlled solution-stirring methods were not introduced into the present work.

The electrochemical techniques were complemented by studies of the electrode surface, after polarisation, using X-ray diffraction and electron microscopy.

In order to define better the electrochemistry of the oxidation products in alkaline solutions at elevated temperatures and thereby assist in the interpretation of experimental results, the effect of temperature on the equilibrium behaviour of the silver/water system was determined over the temperature range 298-573 K. The following chapter is devoted to a thermodynamic study of this system in a high temperature environment.

CHAPTER 2 THERMODYNAMICS OF THE SILVER/WATER SYSTEM

2.1 INTRODUCTION

The validity of the predicted thermodynamic behaviour of a metal in an aqueous high temperature environment depends on the accuracy with which free energy data for its reactions at a particular temperature are known. Potential-pH diagrams which present thermodynamic data for metal-water-oxide systems are generally used to represent corrosion equilibria. However, previously published potential-pH diagrams for the silver-water system (60,159) have been restricted to 298 K due to a lack of thermodynamic data at other temperatures.

Electrochemical determinations of free energy changes for reactions in aqueous systems at elevated temperatures have had little success, mainly because most reference electrodes no longer act reversibly above 423 K (109). An alternative approach is to evaluate free energies of formation for species at elevated temperatures using a knowledge of the free energies of formation and the entropies of these substances at 298 K (147,148), with empirical expressions for the variation of heat capacity with temperature (112,196). The equilibrium relationships between a metal and its oxidation products obtained from the free energy calculations, may then be summarised in potential-pH diagrams over the appropriate temperature range.

2.2 THEORY

2.2.1 Calculation of Free Energy Changes of Reactions from Isothermal Free Energies of Formation

The conventional method of evaluating the free energy change for a reaction at a temperature T (equation 2.1) involves determining the free energy of formation of each compound, $\Delta_f G_T^{\ominus}$ in that reaction at the appropriate temperature:

$$\Delta G_T^{\ominus} = \Sigma_P \nu_P \Delta_f G_T^{\ominus} - \Sigma_R \nu_R \Delta_f G_T^{\ominus} \qquad (2.1)$$

ν_P and ν_R are the stoichiometric coefficients for the products and reactants respectively.

The standard Gibbs free energy of a substance at temperature T, $G_T^{\ominus}$, can be expressed in terms of the standard entropy and standard free energy at T_1, the reference temperature (defined to be 298 K), and the heat capacity of the system over the temperature interval T_1 to T (equation 2.2).

$$G_T^{\ominus} = G_{298}^{\ominus} - S_{298}^{\ominus}(T-298) - T\int_{298}^{T} \frac{C_p^{\ominus}}{T}\,dT + \int_{298}^{T} C_p^{\ominus}\,dT \qquad (2.2)$$

By definition, the standard free energy of formation of a compound is equal to the change in the standard free energy for the hypothetical reaction in which the compound is formed from the component elements in their standard states at the temperature of interest. The standard free energy of formation at temperature T_2 can then be written as

$$\Delta_f G_T^{\ominus} = \Delta_f G_{298}^{\ominus} - (T-298)\Delta_f S_{298}^{\ominus} - T\int_{298}^{T} \frac{\Delta_f C_p^{\ominus}}{T}\,dT + \int_{298}^{T} \Delta_f C_p^{\ominus}\,dT \qquad (2.3)$$

It should be noted that if a phase transition occurs in the range 298-T K, a term allowing for the changes in entropy and enthalpy must be included. Also, the appropriate heat capacity for the temperature range following the transition should be used.

The free energy change for a particular reaction may then be calculated by substitution of values of $\Delta_f G_T^{\ominus}$ into equation 2.1.

The use of isobaric data to evaluate $\Delta G_T^{\ominus}$ for reactions in aqueous solutions over a range of temperatures is not strictly valid since the changing vapour pressure of the solvent in a closed system causes a pressure change. The chemical equilibrium is affected by the pressure in three ways:

(i) The activity of water will change and this introduces an additional free energy change given by

$$\Delta G = \int_1^P V\,dP \qquad (2.4)$$

where P is the vapour pressure of water at temperature T.

(ii) Changes of the partial molal volumes of the substances involved in the reaction cause a free energy change described by

$$\Delta G_i = \int_1^P \Delta V_i \, dP \qquad (2.5)$$

(iii) The pressure change will also affect the activity coefficients of dissolved species by

$$\frac{\partial \ln \gamma}{\partial P} = \frac{V_B - V_B^{\ominus}}{2RT} \qquad (2.6)$$

where V_B is the partial molal volume of some component B at a given concentration.

Cobble (36) has shown that although these effects are significant, they can be ignored up to 573 K since the magnitude of the errors introduced are within the limited accuracy of the data used in deriving the correspondence principle for ionic species (see section 2.2.3).

2.2.2 An Alternative Method to Evaluate Free Energy Changes of Reactions

In order to reduce the number of calculations required to evaluate the free energy change of a reaction, MacDonald et al (135) suggested that the equation

$$'G_T^{\ominus}' = \Delta_f G_{298}^{\ominus} - S_{298}^{\ominus}(T-298) - T\int_{298}^{T} \frac{C_P^{\ominus}}{T} dT + \int_{298}^{T} C_P^{\ominus} \, dT \qquad (2.7)$$

be used to evaluate quantities, $'G_T^{\ominus}'$, from which values of $\Delta G_T^{\ominus}$ may be obtained directly through

$$\Delta G_T^{\ominus} = \Sigma_P \nu_P \, 'G_T^{\ominus}' - \Sigma_R \nu_R \, 'G_T^{\ominus}' \qquad (2.8)$$

The use of the symbol, $G^{\ominus}_{T}$, in this context is however, ambiguous in the sense that it, by definition, refers to the free energy of a species obtained by integrating the fundamental differential equation 2.9 from 298 to T K, and not free energy changes as indicated by Macdonald.

$$dG = VdP - SdT \qquad (2.9)$$

Consequently, it is proposed here to represent the free energy changes so specified by Macdonald, by the notation, $\Delta^{T}_{298,f}\ G^{\ominus}$, which replaces $G^{\ominus}_{T}$ formerly used for these quantities.

It should be emphasised that the free energy changes proposed by Macdonald are not conventional free energies of formation, $\Delta_f G^{\ominus}_{T}$, that is, for an isothermal reaction of the component elements to form the product but represent free energies of formation of the compound at temperature T from its components at 298 K.

Equation 2.7 is now written

$$\Delta^{T}_{298,f}\ G^{\ominus} = \Delta_f G^{\ominus}_{298} - S^{\ominus}_{298}(T-298) - T\int_{298}^{T} \frac{C^{\ominus}_{p}}{T}\,dT + \int_{298}^{T} C^{\ominus}_{p}\,dT \qquad (2.10)$$

Substitution of $\Delta_f G^{\ominus}_{298}$ from equation 2.10 into equation 2.3 demonstrates that the free energy changes used by Macdonald are related to $\Delta_f G^{\ominus}_{T}$ by

$$\Delta_f G^{\ominus}_{T} = \Delta^{T}_{298,f}\ G^{\ominus} - \Sigma_R \nu_R G^{\ominus}_{T} \quad \text{(elements)} \qquad (2.11)$$

---

* This notation was chosen so as to have the same form as that commonly used for the change in a thermodynamic function which accompanies a change of phase of a pure substance, namely $\Delta^{\beta}_{\alpha}X$. In the present case, the notation indicates that the change of free energy is over the temperature interval, 298-T K and since the free energy change is associated with the formation of a compound from its elements, the operator is modified by the subscript, f.

The free energy change for the reaction is then given by

$$\Delta G_T^{\ominus} = \Sigma_P \nu_P \, \Delta^T_{298,f} G^{\ominus} - \Sigma_R \nu_R \, \Delta^T_{298,f} G^{\ominus} \qquad (2.12)$$

In summary, by the conventional definition, the free energy of formation of a substance MX is given by

$$\Delta_f G_T^{\ominus} = G_T^{\ominus}(MX) - [G_T^{\ominus}(M) + G_T^{\ominus}(X)] \qquad (2.13)$$

However, Macdonald proposed using '$G_T^{\ominus}(MX)$', now represented as $\Delta^T_{298,f} G^{\ominus}(MX)$, directly to evaluate the overall free energy change for a reaction involving MX. The advantage of Macdonald's technique is that it is a computational aid since it is not necessary to calculate values of $\Delta_f G_T^{\ominus}$ for every compound at each temperature. It has therefore been adopted for the following thermodynamic calculations.

2.2.3 Evaluation of $\Delta^T_{298,f} G^{\ominus}$

For non-dissolved substances, accurate heat capacity functions of the form

$$C_p^{\ominus} = A + BT + CT^{-2} \qquad (2.14)$$

are available, and $\Delta T_{298,f} G^{\ominus}$ can be calculated directly from equation 2.10.

Heat capacity data for ionic (dissolved) species are generally not available and consequently, free energy changes for each species must be estimated. The calculations are approached more easily by considering the integral containing the temperature-dependent $C_p^{\ominus}$ functions in terms of entropy. If the following approximation is used (135):

$$\int_{T_1}^{T} C_p^{\ominus} \, dT \approx C_p^{\ominus} (T - T_1) = \frac{T - T_1}{\ln(T/T_1)} \, (S_T^{\ominus} - S_{T_1}^{\ominus}) \qquad (2.15)$$

where $S_T^{\ominus}$ and $S_{T_1}^{\ominus}$ are absolute entropies of the ion at temperatures T and T_1, respectively, then equation 2.10 may be transformed into equation 2.16 for an ion with an error generally

less than one percent (132).

$$\Delta^{T}_{298,f}G^{\ominus} = \Delta_f G^{\ominus}_{298} - (T\,S^{\ominus}_{T} - 298\,S^{\ominus}_{298}) + \frac{T-298}{\ln(T/298)}\,(S^{\ominus}_{T} - S^{\ominus}_{298}) \qquad (2.16)$$

The absolute entropies of ions at elevated temperatures can be estimated using the correspondence principle of Criss and Cobble (45). They obtained an equation (2.17) relating the entropies of an ion at elevated temperatures to the corresponding entropy at 298 K:

$$S^{\ominus}_{T} = a + b\,S^{\ominus}_{T_1} \qquad (2.17)$$

where a and b are constants which are unique for a given temperature and class of ion. These constants were found to vary approximately linearly with temperature over the range 373-473 K. In many cases, further evidence allows the entropy parameters above 473 K to be estimated by extrapolation from the lower temperature range.

A reference state which was chosen by Criss and Cobble for each temperature such that only two terms were required to relate the respective entropies, corresponds to an ionic entropy of -20.9 J K^{-1} mol^{-1} for H^{+} at 298 K. This falls within the range of values (-8.8 to -26.4 J K^{-1} mol^{-1}) suggested by others (92,119) for the "absolute" ionic entropy of H^{+}. Consequently, for consistency the values of ionic entropy associated with the correspondence principle are assumed to be on the absolute scale. Entropies of ions, based on the conventional scale where the entropy of the hydrogen ion at 298 K is defined as zero, may be converted to the absolute scale using equation 2.18 (45):

$$S^{\ominus}_{(absolute)} = S^{\ominus}_{(conventional)} - 20.9\,z \qquad (2.18)$$

where z is the ionic charge.

2.2.4 Evaluation of Reduction Potentials

An electrochemical reaction occurring in aqueous solution can be represented in half-cell form

$$aA + xH^{+} + ne = bB + cH_2O \tag{2.19}$$

where A and B may be a solid or an ionic species. The half-cell reduction potential, E_T, for this reaction is given by

$$E_T = E_T^{\ominus} + \frac{RT}{nF} \ln [(a_B{}^b . a_{H_2O}{}^c)/(a_A{}^a . a_{H^+}{}^x)] \tag{2.20}$$

where a represents the activity of the particular species at the temperature T. By definition, $-\log a_{H^+} = pH$, and $\Delta G = -nFE$, and if a_{H_2O} is assigned unity, equation 2.20 can be written to permit substitution of $\Delta G_T^{\ominus}$

$$E_T = \frac{-\Delta G_T^{\ominus}}{nF} - \frac{2.303RT}{nF} [b\log a_B - a\log a_A] - \frac{2.303\ xRT}{nF}\ pH \tag{2.21}$$

In the present case, reduction potentials are referred to the standard hydrogen electrode (SHE, $P_{H_2} = 1$ atm) at the temperature of interest and therefore, $\Delta G_T^{\ominus}$ is the standard free energy change for the whole cell reaction 2.22.

$$aA + (x-n)H^{+} + \frac{n}{2}H_2 = bB + cH_2O \tag{2.22}$$

If reaction 2.19 does not involve electron transfer, n=0. In this case, equation 2.21 is expressed in the form, $nFE_T = -\Delta G_T$, which then yields equation 2.23 from which the effect of temperature and pH on solubility and hydrolysis reactions may be predicted.

$$pH = -\frac{1}{x} [\frac{\Delta G_T^{\ominus}}{2.303RT} + b\log a_B - a\log a_A] \tag{2.23}$$

In the general case where $n \neq 0$, the activity of a soluble species can be obtained from the free energy change for the whole cell reaction 2.22 in which the solid B dissolves to give the soluble species A. Hence

$$\log a_A = \frac{\Delta G_T^{\ominus}}{2.303bRT} + \frac{(x-n)}{b} pH - \frac{n}{2b} \log P_{H_2} \tag{2.24}$$

2.2.5 Potential-pH (Pourbaix) Diagrams

A full description of the general nature of potential-pH diagrams, in association with a discussion of the diagrams for a number of specific cases, is provided by Pourbaix (159). Essentially, the value of these diagrams lies in the fact that they may be used to indicate the thermodynamic limits of the stability of a metal in relation to its ions and to reaction products such as hydroxides and oxides as a function of solution pH and of the electrode potential. In effect, they display the equilibrium potentials of the electrochemical reactions and the relationship of these reactions to each other.

2.3 TEST CALCULATIONS

2.3.1 Electrode Potential

Macdonald has tested his method of evaluating free energy changes at elevated temperatures by calculating the standard electrode potentials of silver-silver halide cells over the range 298-573 K (132). These cells are particularly suitable for several reasons. They have been shown to be reversible at elevated temperatures, accurate standard electrode potentials are available in the literature (115,122,184), and no correction of the experimental electrode potentials for liquid junction potentials is required. The calculated and experimental standard free energy changes were shown (132) to agree to within ±1 kJ mol^{-1} at all temperatures where comparison was possible.

2.3.2 Solubility

This method of free energy calculation was further tested by determining the solubilities of AgCl and AgBr as a function of temperature using values of $\Delta^{T}_{298,f}G^{\ominus}$ calculated for Ag^{+}, and the corresponding data (132) for AgX and X^{-}.

$$AgX = Ag^{+} + X^{-} \qquad (2.25)$$

At equilibrium

$$\Delta G^{\ominus}_{T} = -RT \ln [a(Ag^{+})a(X^{-})] \qquad (2.26)$$

The solubility of AgX (mol kg^{-1}), $S_o = m(Ag^{+}) = m(X^{-})$

$$\therefore \log S_o = -\Delta G^{\ominus}_{T}/(4.606RT) - \log \gamma_{\pm} \qquad (2.27)$$

where $\gamma_{\pm}$ is the mean ionic activity coefficient of the ions, Ag^{+} and X^{-}. $\Delta G^{\ominus}_{T}$ is obtained from the individual values of $\Delta^{T}_{298,f}G^{\ominus}$:

$$\Delta G^{\ominus}_{T} = \Delta^{T}_{298,f}G^{\ominus}(Ag^{+}) + \Delta^{T}_{298,f}G^{\ominus}(X^{-}) - \Delta^{T}_{298,f}G^{\ominus}(AgX) \qquad (2.28)$$

It is important to note that for the silver halide species, as has been pointed out previously (45), it is difficult to account quantitatively for the hydrolysis of Ag^{+} at these temperatures under the experimental conditions.

The calculated and experimental (70) values of the solubilities of AgCl and AgBr are plotted in Figure 2.1.

For AgCl, the differences between experimental and calculated values of log S_o are less than 0.02 over the temperature range, except at 523 K, which is equivalent to a discrepancy of less than 1% in the values of $\Delta G^{\ominus}_{T}$ for the two sets of data at these temperatures. At 573 K, for example, the difference in log S_o corresponds to a difference of 0.02 kJ between the two values of $\Delta G^{\ominus}_{T}$.

The differences between the two sets of data for AgBr are considerably larger. Such differences at 473 K and above might have been expected since at these temperatures, it is necessary to use extrapolated Criss and Cobble parameters. Values of $\Delta G^{\ominus}_{T}$ for reaction 2.25 have an uncertainty of 8 kJ at 573 K which is equivalent to an uncertainty of 0.36 in log S_o.

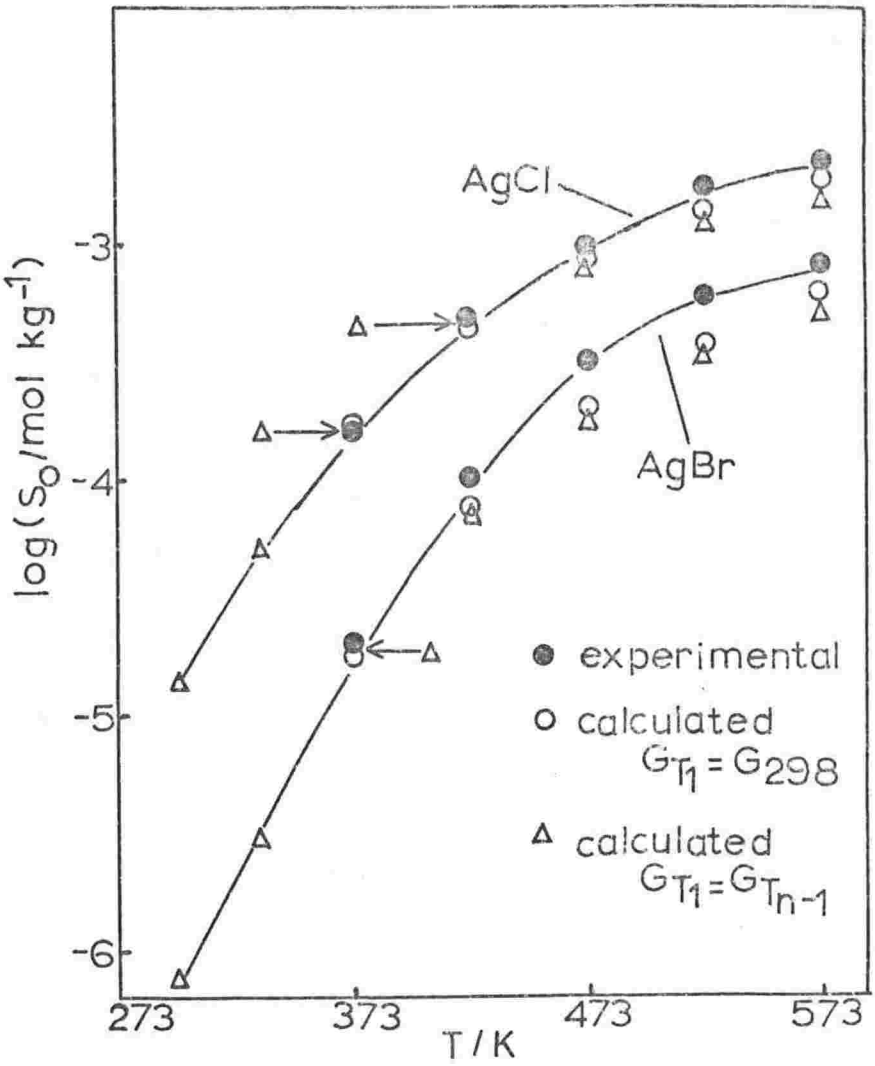

Figure 2.1 Solubility of AgX
(X = Br, Cl)

2.4 THERMODYNAMIC DATA FOR THE SILVER/WATER SYSTEM

2.4.1 Introduction

The equilibrium behaviour of silver under hydrothermal conditions is presented in the form of potential-pH diagrams over the temperature range 298-573 K. All thermodynamic calculations were performed by computer (Burroughs 6700). The program used is listed in appendix 1. It should be noted that the approximate quantity obtained for ionic species in equation 2.15 is an average value of the partial molar quantity (45) over the range 298-T K, and these averages are not the same over the temperature interval if the latter becomes too great (45). Values of $C_p^{\ominus}$ nevertheless, were calculated over the above temperature range using equation 2.15. The sizes of the temperature intervals were justified by the uncertainties in the

available data for the ionic species and the fact that only above 473 K, might discrepancies in the average values require consideration (45).

The program is also capable of calculating the half-cell reduction potential of a reaction and the solubilities of metals and metal oxides as a function of temperature and pH. A full calculation of the reduction potential of a selected half-cell reaction is given (appendix 2) in order to demonstrate the use of the required thermodynamic data.

The range of silver species available for which thermodynamic data at elevated temperatures could be determined, is restricted mainly due to a lack of initial data. However, it is possible to represent all essential experimental equilibria with regard to the present work. From this point of view, various electro-active silver species will be discussed in the following two sections.

2.4.2 Oxides of Silver

(i) Ag_2O. The existence of this oxide as an anodic oxidation product is well established (24,193).

(ii) Ag_2O_2. This oxide is relatively stable when dry and when in contact with alkaline solutions. The crystal structure is found to exhibit two distinct Ag-O distances (93,168) and in addition magnetic susceptibility measurements (155) show that Ag_2O_2 is diamagnetic. Hence this oxide, often represented as AgO, is considered to exist as $Ag(I)Ag(III)O_2$ and in this work will be described by the formula, Ag_2O_2. The relatively high electrical conductivity of Ag_2O_2 ($7\ S\ m^{-1}$ (110,120)) could also be accounted for by such a mixed oxidation state structure.

(iii) Ag_2O_3. This higher oxide of silver has been shown to exist when stabilised by oxyanions (138), although there is good evidence for its anodic formation at lower temperatures (182).

(iv) Ag_3O_4. This oxide is relatively unstable existing only in the presence of oxyanions (136) also, and will not be considered further.

(v) Ag_4O. There is conflicting evidence for such a suboxide (75,193) and it is now generally agreed that the evidence is better interpreted in terms of chemisorbed oxygen (153). This species also will not be considered further.

No data was available for the heat capacity of Ag_2O_3, and the only data for the heat capacity of Ag_2O_2 as a function of temperature referred to the gaseous state (112). However, the heat capacity of an inorganic compound, if it is a coordination lattice, may be estimated

by summing the heat capacities of all atoms in the molecule (117). Since the heat capacities of both Ag and Ag_2O as a function of temperature (112) are known, the heat capacity of an oxygen atom bound in an Ag_2O crystal lattice can be obtained. Hence, using the expressions for $C_p^{\ominus}$ as a function of temperature (in J K^{-1} mol^{-1}),

$$C_p^{\ominus}(Ag_2O): \quad 46.57 + 64.77\times10^{-3}\ T \tag{2.29}$$

$$2\times C_p^{\ominus}(Ag): \quad 42.60 + 17.08\times10^{-3}\ T + 3.02\times10^{5}\ T^{-2} \tag{2.30}$$

$$\therefore C_p^{\ominus}(O): \quad 3.97 + 47.69\times10^{-3}\ T - 3.02\times10^{5}\ T^{-2} \tag{2.31}$$

Assuming this value of $C_p^{\ominus}(O)$ remains approximately the same in the higher valence silver oxide lattices, then it may be used to obtain expressions for the heat capacities of Ag_2O_2 and Ag_2O_3 (equations 2.32 and 2.33).

$$C_p^{\ominus}(Ag_2O_2): \quad 50.54 + 112.46\times10^{-3}\ T - 3.02\times10^{5}\ T^{-2} \tag{2.32}$$

$$C_p^{\ominus}(Ag_2O_3): \quad 54.51 + 160.15\times10^{-3}\ T - 6.04\times10^{5}\ T^{-2} \tag{2.33}$$

$C_p^{\ominus}(Ag_2O_2)$ at 298 K is quoted in the NBS tables (148) as 87.9 J K^{-1} mol^{-1}* compared with 80.7 J K^{-1} mol^{-1} obtained from the above expression which implies an uncertainty in the value of $C_p^{\ominus}(Ag_2O_2)$ of at least 7.2 J K^{-1} mol^{-1}.

Similar calculations for Cu_2O and CuO using appropriate data (117) give $C_p^{\ominus}$(O,solid), respectively, as 20.42 and 20.25 J K^{-1} mol^{-1} compared with 17.07 J K^{-1} mol^{-1} from equation 2.31. The fact that the values for Cu_2O and CuO are similar tends to support the assumption of constancy in $C_p^{\ominus}(O)$ values in different oxides of the same metal. The difference between the values of $C_p^{\ominus}(O)$ obtained from Cu_2O and Ag_2O is significant but corresponding values from other metal oxides (NiO and FeO) lie between the range from the copper oxides to Ag_2O. Hence, the value of $C_p^{\ominus}$(O,solid) from Ag_2O is regarded as a satisfactory estimate from which to obtain expressions for the heat capacities of Ag_2O_2 and Ag_2O_3.

---

* Converted from the value in cal K^{-1} mol^{-1}.

2.4.3 Ionic Species of Silver

Three ionic species were considered for the silver/water system:

(i) Ag^+. It is recognised (108,159) that this ion exists under acid conditions.

(ii) $Ag(OH)_2^-$. The existence of this anion in alkaline solutions, in equilibrium with both Ag_2O and Ag_2O_2, is well established (3,66,78).

(iii) $Ag(OH)_3^-$. This species has been proposed (67) but MacMillan (136), by measurement of the magnetic properties of solutions resulting from Ag_2O_2 dissolution, showed that no silver(II) species was present.

(iv) $Ag(OH)_4^-$. The formation of a relatively soluble Ag(III) species by high current density (70 mA cm^{-2}) anodisation of a silver sheet has been reported (38). The ion was identified (38) as $Ag(OH)_4^-$. However, from ring-disc electrode experiments (141), it was concluded that there is no appreciable solubility of an Ag(III) species from a strongly oxidised silver disc. The experimental discrepancy would appear to be still unresolved.

Pourbaix (159) considered three other species, AgO^+, Ag^{++} and AgOH, for the potential-pH diagram of Ag at 298 K. There is a lack of thermodynamic data for the two ions but it appears from his diagram that Ag^{++} is likely to exist only in solutions of low pH*, and AgO^+ at highly anodic potentials. Hence, neither species is regarded as important for the present work in view of past studies of silver in alkaline solutions (see section 1.2). The third species, AgOH, was proposed to explain an anomalous observation in potentiodynamic experiments (see section 5.2.2) but its existence as a definite compound is doubtful and, therefore, it was not considered.

AgO^- and AgO_2^- are considered in these forms rather than $Ag(OH)_2^-$ and $Ag(OH)_4^-$ respectively, since firstly, the entropy equation (2.36) of Connick and Powell (39) applies only to oxyanions, XO_n^{-z} (see comments below on the use of this equation, particularly in regard to hydroxy-complexes) and secondly, difficulty arises in defining the class of ion with regard to the assignment of Criss and Cobble coefficients. Free energy changes for reactions involving AgO^- or AgO_2^- are not altered by using these forms.

$\Delta_f G^{\ominus}_{298}$ for AgO^- (-23.1 kJ mol^{-1}) was determined from the value

---

* Pleskov (155), in fact, has shown that divalent silver ions are unstable in alkaline solutions.

for $Ag(OH)_2^-$ (-260.2 kJ mol^{-1} (148)) by considering equation 2.34.

$$\Delta_f G^{\ominus}_{298}(AgO^-) = \Delta_f G^{\ominus}_{298}(Ag(OH)_2^-) - \Delta_f G^{\ominus}_{298}(H_2O) \qquad (2.34)$$

This value for AgO^- may be compared with that obtained by Pourbaix (-22.97 kJ mol^{-1}) from the dissociation constant of the species AgOH, ($K_a = 7.9 \times 10^{-13}$ (108)) for the reaction

$$AgOH = AgO^- + H^+ \qquad (2.35)$$

Although the existence of AgO_2^- is doubtful, thermodynamic data at elevated temperatures were calculated (but are not included in the potential-pH diagrams) using the value of $\Delta G^{\ominus}_{298}$ for $Ag(OH)_4^-$ estimated by MacMillan (136). This estimate was based on a value of $\Delta_f G^{\ominus}_{298}$ for $Ag(OH)_3^-$ and the corresponding value for $Ag(OH)_2^-$, and should therefore be regarded as tentative. Nevertheless, it was used to obtain $\Delta_f G^{\ominus}_{298}(AgO_2^-)$ from an equation analogous to 2.34.

No entropy data for AgO^- or AgO_2^- were available. However, Connick and Powell (39) proposed that the entropies of oxyanions, XO_n^{-z}, would be controlled by the ionic charge and charge distribution. From an analysis of experimental data, they obtained an empirical equation 2.36 relating the entropy of an aqueous oxyanion to the number of negative charges, z, per ion and the number of oxygen atoms, n_o, surrounding the central ion (excluding those in hydroxyl groups).

$$S^{\ominus} = 182.0 - 194.6(|Z| - 0.28\ n_o) \qquad (2.36)$$

The average discrepancy between experimental and estimated values was 15.5 J K^{-1} mol^{-1} (39). These workers observed that each hydroxyl group makes a negligible contribution to the entropy of ions and it was suggested that this would possibly be the case for other hydroxy-complex ions, $M(OH)_m^{2+}$. However, there are few entropy data to substantiate this suggestion, and the data that were available to Connick and Powell indicated that such calculated entropy values should be regarded as very approximate.

Values of $\Delta^{T}_{298,f}G^{\ominus}$ for H^+ at elevated temperatures were initially derived by Macdonald and Butler (132) using the technique described in section 2.2.2. These values were combined with the corresponding data for the hydroxyl ion to calculate the ionisation constant of water at elevated temperatures. However, discrepancies of up to 5% became apparent when experimental data (77,161) for K_W were compared with the calculated values. Macdonald and Butler assumed that inaccurate values of the free energy of the hydrogen ion were responsible for the differences although it was not possible to determine if these differences were due to the anomalous behaviour often exhibited by the hydrogen ion in aqueous solution. They preferred to use the experimental data for K_W which are now accurate to within ±0.2% (128), and values of $\Delta^{T}_{298,f}G^{\ominus}$ for the hydroxyl ion obtained from the correspondence principle to evaluate the corresponding data for H^+ (equation 2.37).

$$\Delta^{T}_{298,f}G^{\ominus}(H^+) = \Delta^{T}_{298,f}G^{\ominus}(H_2O) - \Delta^{T}_{298,f}G^{\ominus}(OH^-) - RT\ln K_{W,T} \qquad (2.37)$$

2.4.4 Standard States

The values of the thermodynamic properties of the pure substances given in Table 2.1 are for the substances in their standard states (indicated by the superscript $^{\ominus}$ on the thermodynamic symbol.) These standard states are defined as follows:

For a pure solid or liquid, the standard state is that of the substance in the condensed phase under a pressure of 1 atmosphere.*

For a gas, the standard state is the hypothetical ideal gas at unit fugacity in which state the enthalpy is that of the real gas at the same temperature and at zero pressure.

The standard state for an ion is specified by stipulating that, at any temperature and pressure, the activity coefficient of this species shall tend to unity as infinite dilution is approached. The standard state thus defined is a hypothetical solution in which the concentration and activity coefficient of this ion are unity and in which, by virtue of the above stipulation, there are no interactions between solute particles.

Each value of $\Delta_f G^{\ominus}_{298}$ given in Table 2.1 represents the change in free energy when one mole of the substance in its standard state is formed,

---

* 1 atmosphere pressure is maintained as the standard state, otherwise a numerical factor must be introduced into terms involving log P such as in equation 2.24.

isothermally, from the elements, each in its appropriate standard reference state. The standard reference state at 298 K for each element has been chosen to be the standard state that is thermodynamically stable at a pressure of 1 atmosphere.

Each value of $S^{\ominus}_{298}$ represents the absolute entropy of a substance in its standard state at 298 K.

The entropy and $\Delta_f G^{\ominus}_{298}$ values tabulated for the individual ions are based on the usual convention that the values of $\Delta_f G^{\ominus}_{298}$ and $S^{\ominus}$ for H^+ are zero.

2.4.5 Uncertainties

The majority of the data for $\Delta_f G^{\ominus}_{298}$ and $S^{\ominus}_{298}$ are drawn from the NBS tables (147,148). Values are tabulated in these tables "such that the overall uncertainty lies between 2 and 20 units of the last figure" (units of calories). However, these values are given so that the experimental data from which they are derived may be recovered with an accuracy equal to that of the original quantities. Hence,the number of significant figures does not necessarily represent the absolute accuracy of a particular value. The values of $S^{\ominus}$ with associated uncertainties for Ag and Ag^+ are taken from recently published CODATA tables (37).

Other specific cases such as $S^{\ominus}_{298}$ for AgO^- and AgO_2^- have already been mentioned with respect to the uncertainty (section 2.4.3).

In the case of heat capacity data, the precision for Ag and Ag_2O is taken as 0.3% and 0.2%,respectively (112). The errors in $C^{\ominus}_p$ functions for Ag_2O_2 and Ag_2O_3 were estimated from the discrepancy noted (9%) for Ag_2O_2 at 298 K (section 2.4.2). It is assumed a similar error would arise with Ag_2O_3 from the same origin, that is, the uncertainty in the heat capacity for "solid oxygen".

The remaining heat capacity data was taken from bulletins of the U.S. Bureau of Mines (112,196).

Table 2.1 Thermodynamic Data for the Silver/Water System

Substance	$\Delta_f G^{\ominus}_{298}$/kJ mol^{-1}	$S^{\ominus}_{298}$/J K^{-1}mol^{-1}	$C^{\ominus}_p$/J K^{-1}mol^{-1}
Ag	0	42.55±0.21	$21.30+8.54\times10^{-3}T+1.51\times10^{5}T^{-2}$
Ag_2O	-11.21	121.3	$46.57+64.77\times10^{-3}T$
Ag_2O_2	27.6	117	$51+112\times10^{-3}T-3\times10^{5}T^{-2}$
Ag_2O_3	121.3	100	$55+160\times10^{-3}T-6\times10^{5}T^{-2}$
Ag^+	77.124	73.38±0.40	
AgO^-	-23.1	41.9 ±15.5	
AgO_2^-	-1.4	96.4 ±15.5	
H^+	0	0	
H_2	0	130.574	$27.28+3.26\times10^{-3}T+0.50\times10^{5}T^{-2}$
O_2	0	204.999	$29.96+4.18\times10^{-3}T-1.67\times10^{5}T^{-2}$
H_2O	-237.183	69.92	75.291

2.4.6 Reactions in the Silver/Water System

The following set of reactions is used to derive the potential-pH diagrams for the silver/water system at elevated temperatures. These diagrams are based on the corresponding potential-pH equations given with the appropriate reaction. The values of $E^{\ominus}_T$ are given in Table 2.2.

Reaction Number	Reaction	Potential-pH Equation
Two soluble species (relative stability of dissolved substances)		
1	$AgO^- + 2H^+ = Ag^+ + H_2O$	$pH = \frac{\Delta G_T^\ominus}{4.6RT} + 0.5\log[a(AgO^-)/a(Ag^+)]$
2	$AgO_2^- + 2H^+ + 2e = AgO^- + H_2O$	$E_T = E_T^\ominus - \frac{2.3RT}{2F}\log[a(AgO^-)/a(AgO_2^-)] - \frac{2.3RT}{F}\,pH$
3	$AgO_2^- + 4H^+ + 2e = Ag^+ + 2H_2O$	$E_T = E_T^\ominus - \frac{2.3RT}{2F}\log[a(Ag^+)/a(AgO_2^-)] - \frac{4.6RT}{F}\,pH$
Two solid substances (relative stability of Ag and its oxides)		
4	$Ag_2O + 2H^+ + 2e = 2Ag + H_2O$	$E_T = E_T^\ominus - \frac{2.3RT}{F}\,pH$
5	$Ag_2O_2 + 2H^+ + 2e = Ag_2O + H_2O$	$E_T = E_T^\ominus - \frac{2.3RT}{F}\,pH$
6	$Ag_2O_3 + 2H^+ + 2e = Ag_2O_2 + H_2O$	$E_T = E_T^\ominus - \frac{2.3RT}{F}\,pH$
One solid and one soluble species (solubility of silver and its oxides)		
7	$Ag_2O + 2H^+ = 2Ag^+ + H_2O$	$pH = \frac{\Delta G_T^\ominus}{4.6RT} - \log[a(Ag^+)]$
8	$2AgO^- + 2H^+ = Ag_2O + H_2O$	$pH = \frac{\Delta G_T^\ominus}{4.6RT} + \log[a(AgO^-)]$
9	$2AgO_2^- + 2H^+ = Ag_2O_3 + H_2O$	$pH = \frac{\Delta G_T^\ominus}{4.6RT} + \log[a(AgO_2^-)]$
10	$Ag^+ + e = Ag$	$E_T = E_T^\ominus + \frac{2.3RT}{F}\log[a(Ag^+)]$
11	$AgO^- + 2H^+ + e = Ag + H_2O$	$E_T = E_T^\ominus + \frac{2.3RT}{F}\log[a(AgO^-)] - \frac{4.6RT}{F}\,pH$
12	$AgO_2^- + 4H^+ + 3e = Ag + 2H_2O$	$E_T = E_T^\ominus + \frac{2.3RT}{3F}\log[a(AgO_2^-)] - \frac{9.2RT}{3F}\,pH$
13	$Ag_2O_2 + 4H^+ + 2e = 2Ag^+ + 2H_2O$	$E_T = E_T^\ominus - \frac{2.3RT}{F}\log[a(Ag^+)] - \frac{4.6RT}{F}\,pH$
14	$Ag_2O_2 + 2e = 2AgO^-$	$E_T = E_T^\ominus - \frac{2.3RT}{F}\log[a(AgO^-)]$

Reaction Number	Reaction	Potential-pH Equation
15	$Ag_2O_3+6H^++4e = 2Ag^++3H_2O$	$E_T = E_T^\ominus - \frac{2.3RT}{2F}\log[a(Ag^+)] - \frac{6.9RT}{2F}$ pH
16	$Ag_2O_3+2H^++4e = 2AgO^-+H_2O$	$E_T = E_T^\ominus - \frac{2.3RT}{2F}\log[a(AgO^-)] - \frac{2.3RT}{2F}$ pH
17	$2AgO_2^-+4H^++2e = Ag_2O_2+2H_2O$	$E_T = E_T^\ominus + \frac{2.3RT}{F}\log[a(AgO_2^-)] - \frac{4.6RT}{F}$ pH
Oxygen evolution		
18	$O_2+4H^++4e = 2H_2O$	$E_T = E_T^\ominus + \frac{2.3RT}{4F}\log P_{O_2} - \frac{2.3RT}{F}$ pH
Hydrogen evolution		
19	$2H^++2e = H_2$	$E_T = O - \frac{2.3RT}{2F}\log P_{H_2} - \frac{2.3RT}{F}$ pH

Table 2.2 Calculated Values of $E_T^\ominus$

Reaction No.	$E_{298}^\ominus$	$E_{333}^\ominus$	$E_{373}^\ominus$	$E_{423}^\ominus$	$E_{473}^\ominus$	$E_{523}^\ominus$	$E_{573}^\ominus$
1	pH=12.01	pH=11.09	pH=10.40	pH=9.83	pH=9.58	pH=9.53	pH=9.68
2	1.342	1.32	1.29	1.26	1.22	1.18	1.13
3	2.05	2.05	2.06	2.08	2.12	2.17	2.23
4	1.171	1.154	1.135	1.112	1.090	1.068	1.047
5	1.430	1.42	1.41	1.40	1.38	1.37	1.36
6	1.715	1.71	1.70	1.69	1.68	1.67	1.67
7*	pH=12.29	pH=11.90	pH=11.58	pH=11.27	pH=11.05	pH=10.88	pH=10.82
8*	pH=11.73	pH=10.28	pH= 9.22	pH= 8.40	pH= 8.12	pH= 8.16	pH= 8.53
9*	pH= 3.91	pH= 2.90	pH= 2.18	pH= 1.64	pH= 1.46	pH= 1.53	pH= 1.81
10	0.799	0.76	0.72	0.67	0.62	0.56	0.50
11	2.219	2.23	2.26	2.32	2.41	2.54	2.70
12	1.63	1.62	1.62	1.61	1.62	1.63	1.65
13	1.802	1.81	1.82	1.84	1.86	1.88	1.91
14	0.382	0.35	0.28	0.19	0.06	-0.10	-0.29
15	1.758	1.76	1.76	1.76	1.77	1.78	1.79
16	1.049	1.03	0.99	0.94	0.87	0.79	0.69
17	2.30	2.30	2.30	2.33	2.38	2.45	2.55
18	1.229	1.200	1.167	1.127	1.088	1.050	1.013
19	0	0	0	0	0	0	0

* pH values for an ion molality = 10^{-6} mol kg^{-1}.

2.4.7 Uncertainties in Data at Elevated Temperatures

The uncertainty in the value of $\Delta G^{\ominus}_T$ and hence $E^{\ominus}_T$ (and solubility) for a particular reaction (substance) depends on the uncertainties in $\Delta^T_{298,f}G^{\ominus}$ for the various species involved in the reaction. The latter are in turn determined by the uncertainties of the initial data used for each species, and on the subsequent method used to evaluate the free energy changes.

At elevated temperatures, the free energies of formation of species for which precise heat capacity data are available, will also have a high precision. For species depending on the use of estimated entropy data, the accuracy of the $\Delta^T_{298,f}G^{\ominus}$ values is reduced compared with that of the values of $\Delta_f G^{\ominus}_{298}$. The accuracy of entropies obtained by the use of the correspondence principle is ± 2 J K^{-1} mol^{-1} for simple ions up to 423 K (45). This corresponds to an uncertainty in $\Delta^T_{298,f}G^{\ominus}$ of ± 1.5 kJ mol^{-1} for Ag^+ up to 423 K. Since less experimental data was available for oxyanions, the accuracy of the correspondence principle is expected to be less for AgO^- and AgO_2^- which also have a large uncertainty in $\Delta^T_{298,f}G^{o}$ from use of the Connick and Powell equation. For all classes of ions, the correspondence principle becomes less reliable above 473 K.

Values of $E^{\ominus}_T$ and solubility are tabulated such that the number of significant figures is dependent on the species appearing in the reaction which has the highest uncertainty in $\Delta^T_{298,f}G^{\ominus}$. However, as in Table 2.1, this number does not necessarily represent the absolute accuracy of that value. For most reactions, the hydrogen ion is involved and the error in $\Delta^T_{298,f}G^{\ominus}(H^+)$ (± 1.5 kJ mol^{-1} at 473 K) is an important contribution to the overall uncertainty in $\Delta G^{\ominus}_T$ for the reaction. If either Ag_2O_2 or Ag_2O_3 are present, the uncertainties in the values of $\Delta^T_{298,f}G^{\ominus}$ for these substances due to those in both the heat capacity and $S^{\ominus}_{298}$, also determine the overall uncertainty. The error in $\Delta^T_{298,f}G^{\ominus}$ for either oxide at 573 K is ± 3.8 kJ mol^{-1} compared with ± 0.2 kJ mol^{-1} for Ag and Ag_2O at this temperature. The uncertainty in $E^{\ominus}_T$ is further increased by the inclusion of ionic silver species in the reaction.

2.5 DISCUSSION

2.5.1 Potential-pH Diagrams

Potential-pH diagrams (Figure 2.2) for the silver/water system at temperatures up to 573 K have been constructed from the thermodynamic properties of the pure components. These diagrams are valid only when there are no substances present with which silver can form an insoluble salt or a soluble complex.

Where there is only one soluble species in a reaction, the activity of that species is defined to characterise the conditions of "practical existence" of this species, that is, the conditions of equilibrium in the presence of appreciable concentrations of that species. In these diagrams, the lines bounding regions of soluble species are defined to represent activities* of 10^{-3} mol kg^{-1} except for AgO^- at 298 K for which a = 10^{-6} mol kg^{-1}. The solid lines indicate the coexistence between the silver species while the vertical broken line distinguishes the regions of relative predominance of the dissolved species; at low values of pH, Ag^+ is the major ion present whereas AgO^- is the dominant species in solutions of high pH.

The diagonal broken lines in the diagrams represent the thermodynamic stability of water. The lower line represents the equilibrium potentials for the evolution of hydrogen (P_{H_2} = 1 atm) as a function of pH. Over the temperature range considered, the lower limit of stability of water lies well into the domain of thermodynamic stability of silver metal, while the upper limit of water stability, that is, the equilibrium between water and oxygen (P_{O_2} = 1 atm) moves into this region only at higher temperatures.

In agreement with the diagrams, silver will dissolve in acid oxidising solutions to give Ag^+. In neutral or moderately acidic media, strong oxidising action on solutions of Ag^+ produces Ag_2O_2 and Ag_2O_3. The positions of these oxides above the upper limit of water characterises them as substances which are expected to be very unstable in the presence

---

* Although in Table 2.2, a=10^{-6} mol kg^{-1}, for clarity in the diagrams, the minimum value of a for the appropriate lines was taken as 10^{-3} mol kg^{-1} with the one exception stated above.

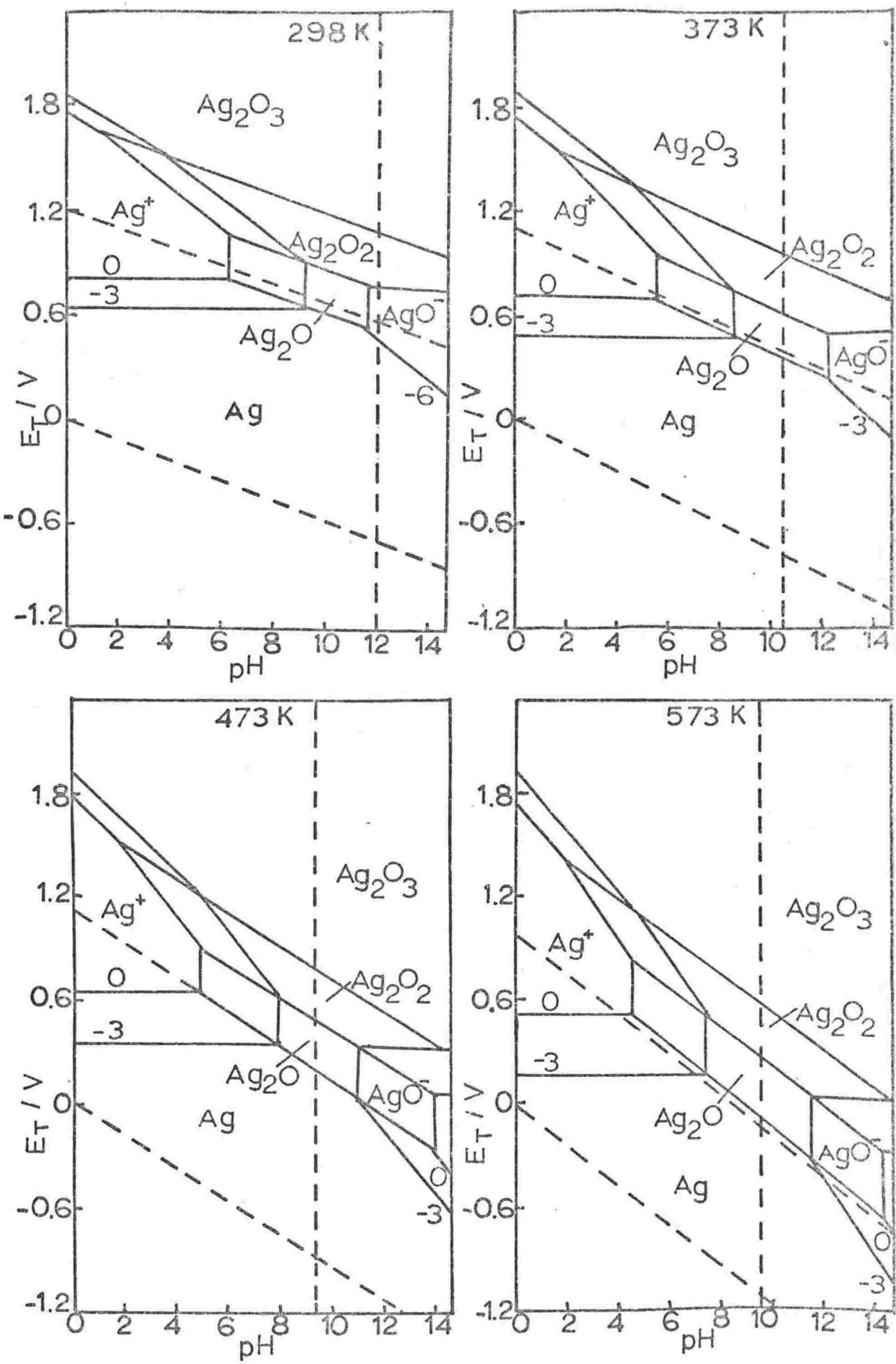

Figure 2.2 Potential-pH Diagrams for the Silver/H_2O System, 298-573 K

of water decomposing to release oxygen. For alkaline solutions, AgO^- and the oxide phases that silver can form, successively become the stable species as the potential becomes more positive. As the temperature increases, the diagrams show that the region of stability of AgO^- becomes greater, so that it is thermodynamically possible for higher concentrations of AgO^- to be present at a given pH.

The diagrams show two other significant changes which occur as a result of increasing temperature. Firstly, the region of stability of silver metal effectively decreases but, as mentioned above, the lower limit for the stability of water still lies in this domain. Secondly, the equilibrium line for the evolution of oxygen is lowered relative to the changes in the domains of stability of the oxide phases so that at 573 K, it appears at more negative potentials than the $Ag_2O|Ag$ equilibrium line. At these temperatures therefore, Ag_2O is unstable in the presence of water, and oxygen will be produced.

The theoretical conditions of corrosion, immunity and passivation of silver can be deduced from the potential-pH diagrams. Any strong oxidising action can cause silver to be corroded except at high potentials where the oxide Ag_2O_3 is stable. Ag_2O and Ag_2O_2 are too soluble to protect silver by passivation. According to Figure 2.2, the corrosion of silver by an oxidising action should be at a minimum (neither soluble species predominate) at a pH of 12 at 298 K decreasing to 9.6 at 573 K.

2.5.2 Further Comments on the Thermodynamic Data

The reliability of the correspondence principle at higher temperatures becomes dubious, as already indicated. Evidence that it may become less dependable was provided by a comparison of calculated data with standard partial molar entropies obtained from measurements of the vapour pressures of sodium chloride solutions at temperatures up to 573 K (124). Differences between experimental data and values calculated using equation 2.17 have been found (128) and these are ascribed to errors arising from the extrapolation of the Criss and Cobble coefficients above 473 K (see section 2.2.3).

An alternative expression (2.38) for estimating the standard free energy change for reactions in aqueous systems up to 473 K, particularly when complex ions are involved, has been suggested by Helgeson (100):

$$\Delta G^{\ominus}_T = \Delta H^{\ominus}_r - \Delta S^{\ominus}_r(T_r - \frac{\theta}{\omega}\{1-\exp[\exp(b+aT)-c+\frac{T-T_r}{\theta}]\}) \qquad (2.38)$$

where r designates the reference state (298 K) and θ, ω, a, b and c are temperature-independent constants characteristic of the dielectric properties of the solvent. This equation is useful for reactions involving those complex ions which are not easily classified in terms of the appropriate Criss and Cobble coefficients. Since high temperature thermodynamic data were available for the soluble silver species (equation 2.17) which became doubtful only above 473 K, the method of calculating $\Delta G^{\ominus}_T$ described in section 2.2 was preferred.

2.5.3 Half-Cell Potentials

Some reference to the measurement of the equilibrium potentials of silver oxide electrodes is worthwhile in view of the considerable industrial and scientific interest in them (see section 1.1.2).

Early determinations of E_{298} for the $Ag_2O|Ag$ electrode gave erratic and unstable values (83,126), possibly caused by adsorbed and/or absorbed oxygen. Hamer and Craig (95) prepared stable, reproducible $Ag_2O|Ag$ electrodes which were superior to those previously constructed. Their technique was to contain Ag_2O in a platinum gauze and then partially reduce the oxide with hydrogen to silver at 333 K. Using the cell

$$Ag|Ag_2O|OH^-|HgO|Hg$$

they obtained an equilibrium potential of 0.342 V (SHE) for the $Ag_2O|Ag$ electrode which is in accordance with the value calculated from free energy data at 298 K (0.343±.0001 V). A later determination (63) using the cell

$$Ag|Ag_2O|OH^-|H_2,Pt$$

yielded $E_{298} = 0.338$ V (SHE).

Dirkse (62) prepared $Ag_2O_2|Ag_2O$ electrodes by various methods and obtained a half-cell potential of 0.599±.001 V which fits the calculated value for the equilibrium potential (0.602 V, 298 K).

The equilibrium potential for the $Ag_2O_3|Ag_2O_2$ reaction was determined by Stehlik (176) to be 1.711 V which compares favourably with the value calculated in this work for 298 K, namely, 1.715 V.

Such similarity between the calculated and measured E_{298} values is not surprising since in many cases, tabulated free energy data are derived from experimental E_{298} data.

2.5.4 Solubility

Solubility data for Ag and Ag_2O are given in Table 2.3. Data for Ag_2O_2 are not presented for the reason that solid Ag_2O_2 is thermodynamically unstable in contact with alkaline solutions. Since its electrode potential is above the potential of the oxygen electrode, Ag_2O_2 decomposes to Ag_2O with evolution of oxygen. As a result of the decomposition reaction, solutions in contact with Ag_2O_2 will contain dissolution products of Ag_2O. However, polarographic measurements (2) have indicated that Ag_2O_2 is not dissolved in alkaline solutions in measurable quantities.* In spite of the thermodynamic instability, Ag_2O_2 has a reasonable degree of metastability in contact with alkaline solutions. This is probably the result of protection of the Ag_2O_2 by formation of an Ag_2O film which causes the decomposition to be relatively slow.

The solubilities of Ag and Ag_2O may each be represented in terms of two equilibria whose relative importance depends on the pH of the solution. In acid or neutral conditions, the reactions represented by

$$Ag + 2H^+ = 2Ag^+ + H_2 \qquad (2.39)$$

$$Ag_2O + 2H^+ = 2Ag^+ + H_2O \qquad (2.40)$$

will predominate. Hence the equilibrium constant for each reaction is expressed by

---

* While AgO^- is present, higher valent silver species are essentially absent (less than 10^{-6} mol dm^{-2}).

$$K = \left[\frac{a(Ag^+)}{a(H^+)}\right]^2 = \left[\frac{m(Ag^+)}{m(H^+)}\right]^2 \left[\frac{\gamma(Ag^+)}{\gamma(H^+)}\right]^2 \qquad (2.41)$$

P_{H_2} is arbitrarily defined as 1 atmosphere and $a(H_2O)$ is assigned unity. It appears reasonable to expect some resemblance between the activity coefficient curves of two univalent ions which have a similar structure (108) Using this assumption, the ratio of the activity coefficients may be regarded as approximately unity except perhaps at very low values of pH.* The solubilities of Ag and Ag_2O can then both be expressed in terms of the activities (described in section 2.2) of the soluble species, Ag^+, which is formed by dissolution of the solids. Hence, the solubility S_o, in each case may be expressed in the general form

$$S_o = \sum_B a_B/\nu_B \qquad (2.42)$$

In solutions of sufficient alkalinity, the solubility will chiefly be a result of the equilibria

$$2Ag + 2OH^- = 2AgO^- + H_2 \qquad (2.43)$$

$$Ag_2O + 2OH^- = 2AgO^- + H_2O \qquad (2.44)$$

where $$K = \left[\frac{a(AgO^-)}{a(OH^-)}\right]^2 = \left[\frac{m(AgO^-)}{m(OH^-)}\right]^2 \left[\frac{\gamma(AgO^-)}{\gamma(OH^-)}\right]^2 \qquad (2.45)$$

Biedermann and Sillen (17) found that the ratio of activity coefficients could be assumed to be 1 with a negligible error compared with the uncertainty in their experimental results. The activity coefficient curves of the two univalent ions each containing an oxygen atom might well be expected to be similar and therefore the solubility in each case may be expressed again by equation 2.42.

Calculated solubility data of Ag and Ag_2O at selected values of the pH are given below.

---

* In this region where the ratio might be expected to deviate appreciably from unity, $m(Ag^+)$ is extremely small for reaction 2.39. In the case of Ag_2O, the solubility is extremely large and any change in $\gamma(Ag^+)$ would be offset to some extent by the effect of pH on $\gamma(H^+)$ at these values.

Table 2.3 Solubility Data for Ag and Ag_2O

$S_o(Ag)$/mol kg^{-1} (from reactions 2.39 and 2.43, P_{H_2} = 1 atm)

pH	T/K						
3	1.5×10^{-17}	1.4×10^{-15}	8.8×10^{-14}	5.3×10^{-12}	1.4×10^{-10}	2.0×10^{-9}	2.1×10^{-8}
5	1.5×10^{-19}	1.4×10^{-17}	8.8×10^{-16}	5.3×10^{-14}	1.4×10^{-12}	2.0×10^{-11}	2.1×10^{-10}
7	1.5×10^{-21}	1.4×10^{-19}	8.8×10^{-18}	5.3×10^{-16}	1.4×10^{-14}	2.0×10^{-13}	2.1×10^{-12}
10	1.5×10^{-24}	1.4×10^{-22}	1.0×10^{-20}	1.7×10^{-18}	1.1×10^{-16}	2.0×10^{-15}	1.1×10^{-14}
12	0	9.3×10^{-23}	1.4×10^{-19}	1.1×10^{-16}	9.5×10^{-15}	1.8×10^{-13}	9.2×10^{-13}
14	0	9.2×10^{-21}	1.4×10^{-17}	1.2×10^{-14}	9.5×10^{-13}	1.8×10^{-11}	9.2×10^{-11}

$S_o(Ag_2O)$/mol kg^{-1} (from reactions 2.40 and 2.44)

3	9.6×10^{2}	3.9×10^{2}	1.9×10^{2}	92	56	38	33
5	9.6	3.9	1.9	0.92	0.56	0.38	0.33
7	9.6×10^{-2}	3.9×10^{-2}	1.9×10^{-2}	9.2×10^{-3}	5.6×10^{-3}	3.8×10^{-3}	3.3×10^{-3}
10	9.6×10^{-5}	3.9×10^{-5}	2.2×10^{-5}	2.9×10^{-5}	4.4×10^{-5}	3.8×10^{-5}	1.8×10^{-5}
12	1.9×10^{-6}	2.7×10^{-5}	3.0×10^{-4}	2.0×10^{-3}	3.9×10^{-3}	3.4×10^{-3}	1.5×10^{-3}
14	9.4×10^{-5}	2.7×10^{-3}	3.0×10^{-2}	0.20	0.39	0.34	0.15

From the values listed in Table 2.3, silver becomes progressively more soluble at elevated temperatures under acid or alkaline conditions.

The amphoteric behaviour of Ag_2O (reactions 2.40 and 2.44) was established experimentally by Johnston *et al* (108) who obtained evidence for the existence of the equilibrium (2.44) in alkaline solutions. This was achieved by measurement of the solubility of Ag_2O in pure water and over a range of concentrations of NaOH, KOH and $Ba(OH)_2$ using potentiometric titration methods.

On the basis of free energy data, the solubility of Ag_2O as a function of pH (Table 2.3) at a particular temperature is predicted to:

(a) fall off in solutions of low alkalinity, with increasing pH,

(b) go through a minimum and then

(c) increase in solutions of higher hydroxide concentration.

The experimental data, obtained at 298 K, is consistent with this behaviour, and exhibits a minimum at a pH of 12.2. The solubility was found to increase

from the minimum in a linear fashion up to a pH of 14.

Biedermann and Sillen (17) recalculated the data of Johnston et al using a more exact method than previously used. For the reaction

$$\tfrac{1}{2}Ag_2O + \tfrac{1}{2}H_2O + OH^- = Ag(OH)_2^- \qquad (2.46)$$

they determined

$$\log K = -3.72\pm0.03 \text{ at } 298 \text{ K where}$$
$$\log K = \log[a(Ag(OH)_2^-).a(OH^-).a(H_2O)^{-\frac{1}{2}}] \qquad (2.47)$$

From vapour pressure measurements (167), $\frac{1}{2}\log a(H_2O)$ was found to be -0.0075 at pH=14, which gives $m(Ag(OH)_2^-)$ as 1.87×10^{-4} mol kg^{-1}. This value is in accordance with the calculated value of the molality* of AgO^- at 298 K. If this value for the activity of AgO^- is substituted into the potential equation for reaction 11 (the dissolution of Ag to give AgO^-) the potential E_{298} has a value of 0.343 V. This potential defines the situation in which Ag_2O can precipitate out from a saturated solution** of AgO^- formed by the dissolution of Ag.

With an increase in temperature, two different effects on the solubility of Ag_2O are predicted to occur depending on the pH. At a pH less than 7, the solubility becomes less with a rise in temperature. At higher values of pH, the solubility as a function of temperature exhibits a maximum at about 473 K. The solubility minimum mentioned above, is exhibited at elevated temperatures also. However, the pH corresponding to the minimum moves to a lower value with increasing temperature, the transition occurring around 333 K.

---

* The molality of AgO^- is twice the solubility of Ag_2O since the latter dissolves to form two molecules of AgO^-.

**Precipitation of Ag_2O, in fact, occurs from a super-saturated solution of AgO^- (see section 1.2.1).

SECTION

II

EXPERIMENTAL

CHAPTER 3 ELECTROCHEMICAL CELL AND MATERIALS

3.1 INTRODUCTION

3.1.1 Requirements

In order to perform electrochemical polarisation studies in aqueous solutions at elevated temperatures, two problems must be overcome:

(i) corrosion of the internal sections of the autoclave by the high temperature solutions may result in contamination of the electrolyte and eventually the electrode surface. The choice of materials within the cell depends on the pH of the electrolyte, but the temperatures and pressures employed in the system must also be taken into account.

(ii) a suitable reference electrode arrangement is required which will give a half-cell potential that is thermodynamically meaningful.

These factors are discussed in detail in relation to the overall design of the cell in the following sections but in order to demonstrate the requirements for the reference electrode, the choice of such electrodes for use within the autoclave is first examined.

3.1.2 Internal Reference Electrodes

The use of internal reference electrodes which are maintained at the same temperature and pH as the working electrode is restricted firstly due to the frequent lack of thermodynamic reversibility and reproducibility at temperatures in excess of 423 K (29,123), and secondly, to the properties of the solution, in particular the pH.

Several electrodes have been examined for use in high temperature alkaline solutions. These are shown below with their approximate temperature limits.

Reference Electrode	pH range	Temperature Limit/K
Hg|HgO	alkaline	423
Ag|Ag_2O_2	alkaline	433
(α+β) Pd|H	acid and alkaline	523*

Discrepancies between calculated (128) and experimental (29) values for the e.m.f. of the cell

$$H_2\text{-Pt}|\text{NaOH}|\text{HgO}|\text{Hg}$$

at temperatures greater than 423 K have been demonstrated (128) which raises doubts as to the thermodynamic behaviour of the Hg|HgO electrode at such temperatures.

In the case of the Ag|Ag_2O_2 electrode (29), the Ag_2O_2 decomposes spontaneously to silver above 433 K and hence is unsatisfactory under these conditions.

Dobson et al (68) have found that the (α+β)Pd|H electrode behaves as a useful reference in NaOH, and HCl, solutions at elevated temperatures. The major obstacle to its use is an increasing rate of desorption of hydrogen from the palladium with temperature, resulting in a reduced lifetime. Nevertheless, this electrode appears to offer promise as an internal reference.

Since, in most cases, these reference electrodes operate over limited temperature ranges above 373 K, it was preferred to use an external reference electrode, maintained at room temperature, for this work which involved temperatures up to 473 K. Although such an arrangement must incorporate a suitable pressure/temperature junction (see section 3.5), temperature itself does not become a limiting factor in the choice of a reference electrode.

---

* Subject to further work.

3.2 ELECTROCHEMICAL CELL

3.2.1 Cell Design

An autoclave arrangement is required to provide a high strength vessel to withstand the pressures involved at elevated temperatures (1.6 MPa at 473 K (113)). The high temperature electrochemical cell used in this study (Figure 3.1) is similar to that used by Macdonald (133,134). However, it was found in initial work with such a cell that the sealing around the electrode mountings was not reliable and often resulted in solution creep, particularly around the working electrode. This problem became more severe on continued use at elevated temperatures and was no doubt caused by distortion of the teflon* as a result of the temperatures and pressures involved. Consequently, modifications to the original cell were made, these mainly involving redesign of the electrode fittings to prevent solution creep (section 3.2.3).

The autoclave itself is constructed of 316 stainless steel. Alumina, used previously (44) as an autoclave liner in the case of acidic solutions, is unsatisfactory for alkaline solutions due to contamination of the latter by aluminate ions. Instead, the autoclave in this work is fitted with a teflon liner.

The autoclave head was secured to the body by six equally-spaced hexagonal cap-head bolts. To ensure complete sealing, the head was fitted with a teflon "O" ring which was compressed on to a flanged section of the body as the bolts were tightened. The head was provided with six openings in which "Conax" fittings (Figure 3.1) were used to seal the electrode systems, gas inlet and outlet, and thermocouple, when necessary.

The gas inlet and outlet were stainless steel capillary tubes which protruded a short distance into the cell, with the inlet being extended into the solution by a teflon tube to allow thorough percolation by the gas. All other metal parts within the cell except the electrodes were protected by teflon covers to prevent possible contamination of the solution.

---

*Teflon - PTFE (polytetrafluoroethylene).

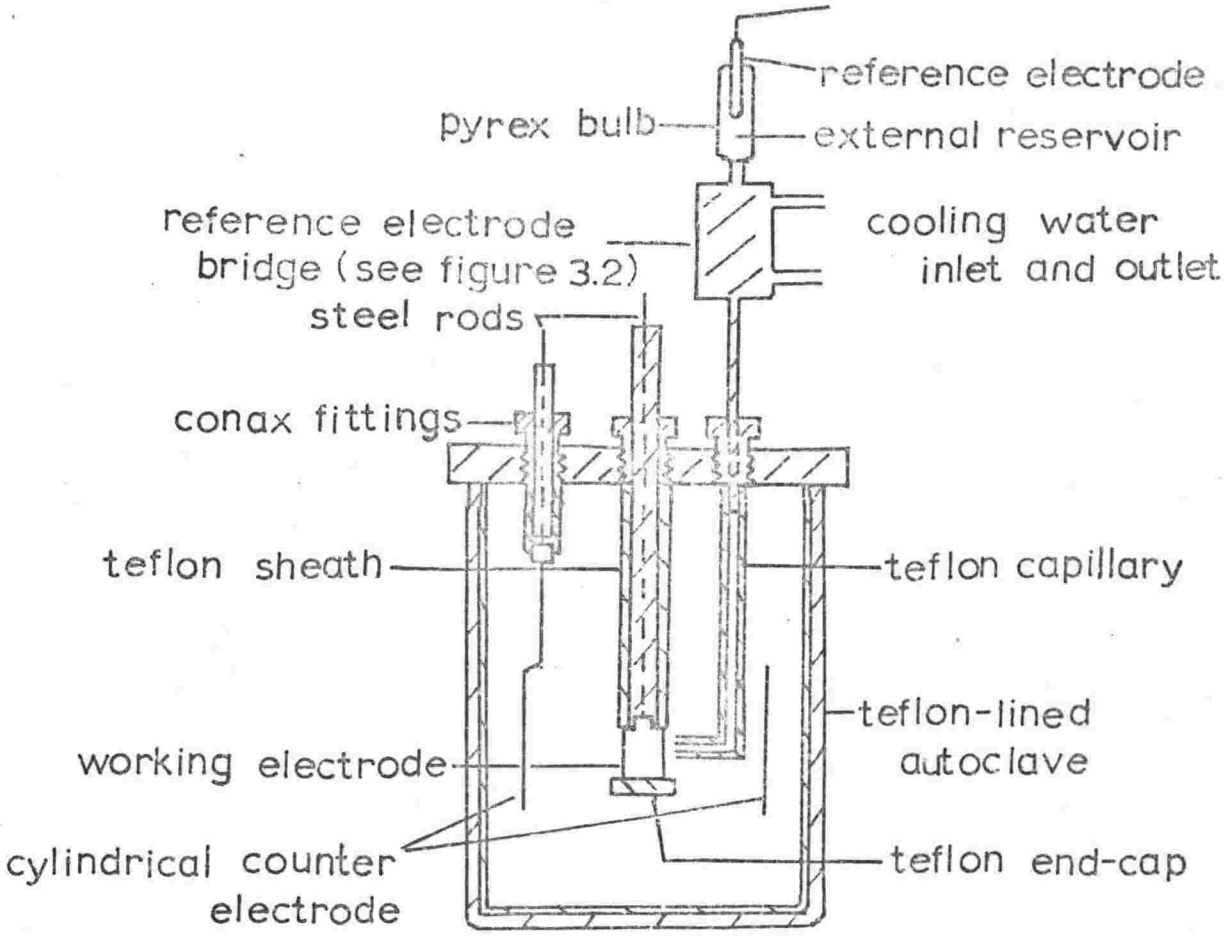

Figure 3.1 High-temperature electrochemical cell

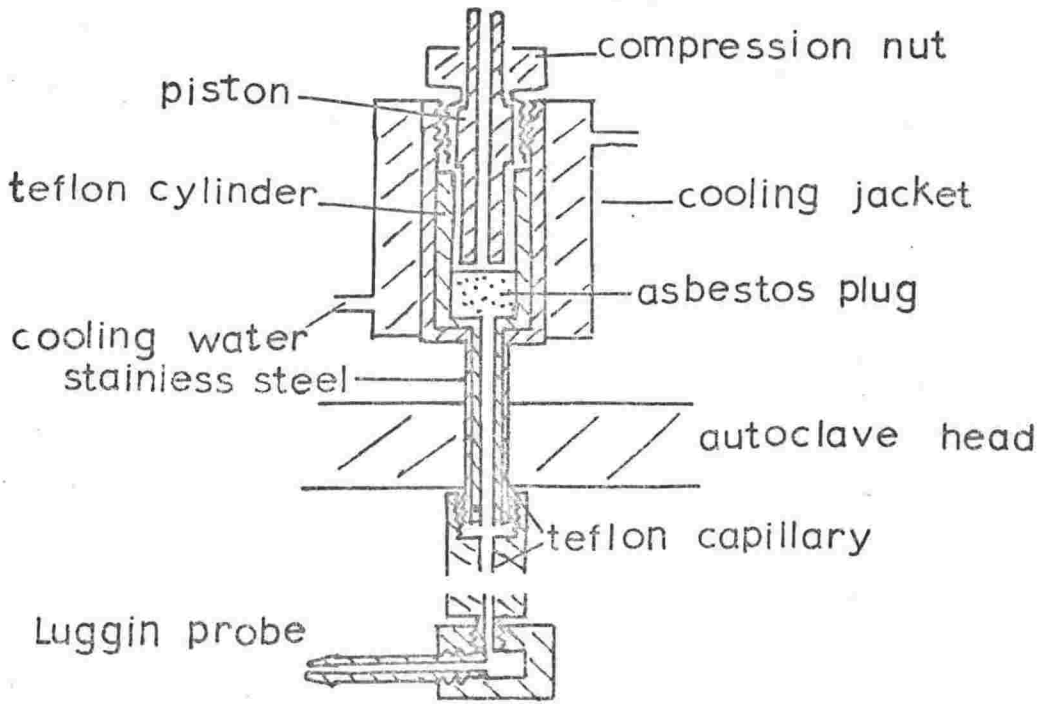

Figure 3.2 High-temperature reference electrode bridge

3.2.2 Temperature Control

The autoclave was heated by a non-inductively wound a.c. furnace coupled to an automatic Ether 'Mini' control unit. The controller was calibrated against the internal temperature of the autoclave using a chromel-alumel thermocouple, this being removed during experimentation with the alkaline solutions so as to avoid possible attack of the thermocouple.

The head of the autoclave which was exposed above the furnace was enclosed in "Fiberfrax"* to assist in stabilising the temperature of the cell. The temperature within the autoclave remained constant to ±1 K over the time required for an experiment. However, it was reproducible from one experiment to another only to ±3 K over the range 295-393 K and to ±5 K at higher temperatures.

In order to avoid ground loops and to reduce electrical noise caused by operation of the furnace and control unit, the autoclave, furnace and windings were insulated from ground using an isolating transformer.

3.2.3 Electrodes

The working electrode (WE) was insulated from the autoclave by a thin teflon tube within a stainless steel support (Figure 3.3). The electrode was fixed firmly into the teflon cover which was itself screwed up over the stainless steel tube. A steel connecting rod through this tube was then fitted into the electrode. The arrangement shown maintained electrical insulation from the autoclave and was also found to be the most effective means of preventing creep of solution into the tube containing the connecting rod. Teflon protective coverings in the cell, particularly on the electrode mountings, were designed with the intention of minimising the combined effect of temperature and pressure on them, thereby avoiding extrusion of the teflon and the inevitable pressure leaks. In order to maintain a pressure-tight system, it was generally

---

* A heat insulating material.

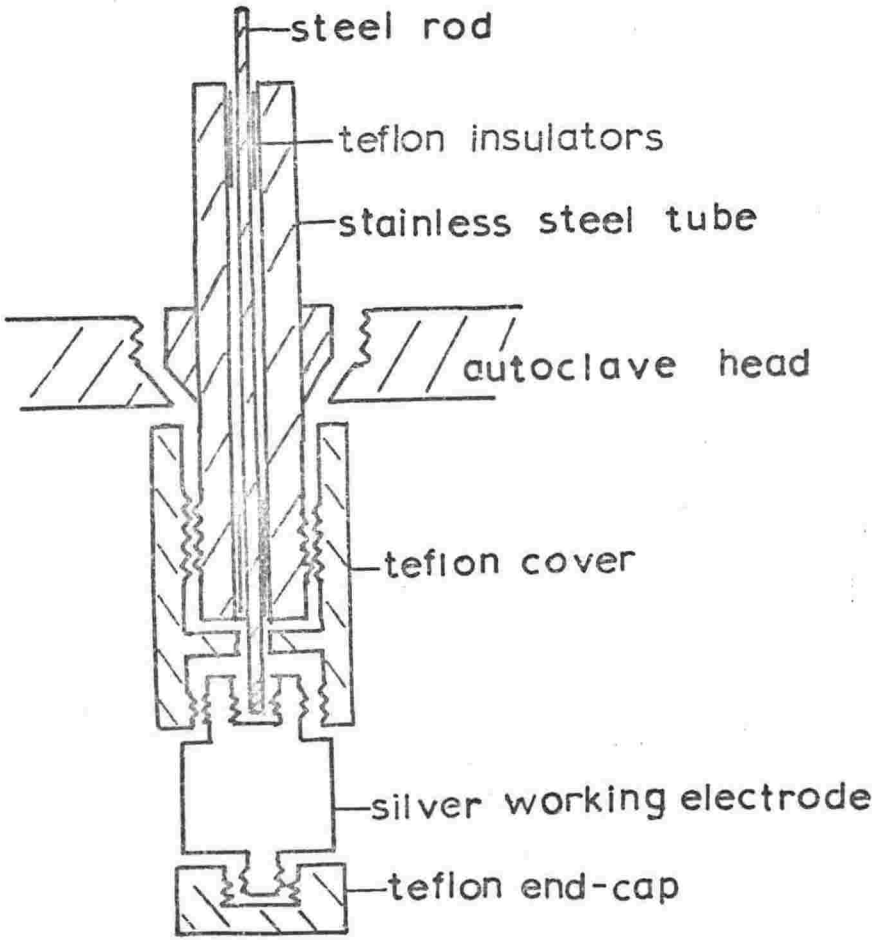

Figure 3.3 The Working Electrode

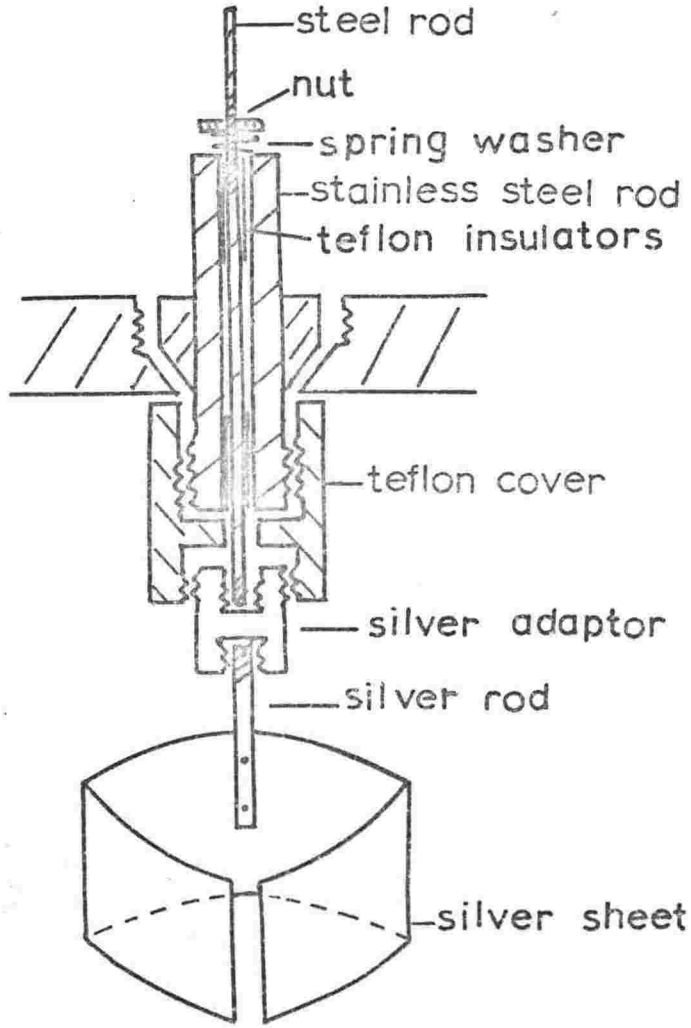

Figure 3.4 The Counter Electrode

necessary to use teflon tape between threaded sections of the metal and machined teflon parts. The working electrode arrangement was completed by fitting a teflon cap to the exposed end, insulating it from the solution, thus providing a symmetrical electric field in the solution around the electrode.

The counter electrode (CE) had a similar design to the WE (Figure 3.4) and consisted of a section of silver sheet, fixed into a slotted rod with screws, also of silver. In order to maintain a symmetrical field at the working electrode, the sheet was positioned coaxially around the working electrode. It was usually necessary to tighten the counter electrode assembly by drawing the electrode firmly against the teflon cover with the assistance of the nut and spring washer at the top of the stainless steel tube.

3.2.4 Reference Electrode System

The reference electrode (RE) system (Figure 3.2) used here is similar to arrangements employed by Cowan and Staehle (44), and Macdonald (133,134). A junction between the different pressures and temperatures of the reference and working electrode compartments is created across an asbestos plug which maintains electrolytic contact between the autoclave contents and the external reservoir containing the reference electrode. The compression nut on the junction is tightened until the rate of flow of solution through the asbestos is reduced to less than one cm^3/day.

The Luggin capillary (see Figure 3.2) consists of a teflon tube fitting into a threaded section at right angles which is positioned approximately one millimeter from the electrode surface. The tube is attached to the threaded stainless steel section (leading to the water-cooling jacket) which protrudes through the head. The use of the capillary is clearly required since the reference electrode is maintained external to the WE compartment but it also serves its usual purpose of minimising the IR potential drop between the WE and RE.

As found by the above workers, vapour bubble formation in the temperature/pressure bridge occurred occasionally, especially on the low temperature side, resulting in a loss of potentiostatic control. This was overcome by inserting asbestos string in the capillary to act as a wick and by enclosing the asbestos plug in a water-cooling jacket which also had the advantage of localising the temperature gradient about the junction.

Jones and Masterton (109) have modified the basic design of the reference electrode system to include a pressure-balancing arrangement, thereby removing the compressed plug junction and hence the streaming potential due to the pressure gradient across the plug (section 3.5.4). However, there are still significant contributions to the observed potential from thermal diffusion (section 3.5), so that it is doubtful if the complex arrangement required to eliminate the streaming potential is warranted, particularly in view of the relatively low pressures involved in this work.

3.3 EXPERIMENTAL PREPARATION

3.3.1 Influence of Surface Pretreatment of Silver Electrodes

The physical nature of a metal surface can strongly influence its behaviour, possibly affecting the adsorption of species from solution and subsequent surface film growth. It is essential, therefore, if meaningful and reproducible results are to be obtained that the working electrode should have well-defined, reproducible properties.

The effect of pretreatment on the surface activation of silver has been examined by Morley (144) using differential capacitance measurements. The pretreatment can be varied to yield a rough electrode, an active electrode or a deactivated electrode. The use of the differential capacitance of silver as an indication of the degree of activity of the electrode has been substantiated by a similar study of the effects of electrode pretreatment on the oxidation of silver (35).

3.3.2 Electrodes

In several previous studies at room temperature (24,88), electropolishing techniques have been used in the preparation of single crystal and polycrystalline silver electrodes. At high temperatures, roughening of the electrode surface takes place prior to polarisation probably due to corrosion processes. While the degree to which this surface roughening takes place before polarisation depends on the temperature, the extent to which it occurs is limited, even at the higher temperatures. However, extensive surface roughening following polarisation is clearly evident from an electron microscopic examination of the electrode (see Figure 5.6).

Since the condition of the surface for studies at elevated temperatures was determined by experiment rather than by pretreatment, mechanical polishing was considered an adequate method of preparing the electrodes. Although grinding and polishing techniques frequently produce a rough surface on a microscopic scale, it was found to be possible in this work to obtain a surface which was optically smooth, at least macroscopically. Chemical etching using nitric acid was examined as a means of preparing the electrodes but the measurements were less reproducible, particularly at high temperatures, than those obtained using a mechanical polishing pretreatment.

The working electrodes used (0.01 m long, 0.005 m diameter, 1.57×10^{-4} m^2 apparent surface area) were machined from spectroscopic grade silver rod and these were then polished successively with 320, 600 and 800 grit silicon carbide paper as they were rotated in a lathe. This method was found to produce a finer and more reproducible finish of the surface than grinding the electrodes manually against the silicon carbide. The electrodes were then washed in ammonia followed by double-distilled water, degreased in acetone, washed with water again and then dried. The working electrode was repolished after a run at each temperature.

The counter electrode was polished for each run using the various grades of silicon carbide paper, and then washed in the manner described for the working electrode.

3.3.3 Other Materials

The solutions were prepared using "Analar" grade potassium hydroxide and double distilled water. They were purged in situ with nitrogen before polarisation experiments began. The cell was then pressurised with nitrogen at 0.4 MPa which forced solution through the asbestos plug to provide electrolytic contact between the working electrode and external reference electrode.

All asbestos which was used in the cell was prepared by cleaning for thirty minutes in a boiling solution of potassium hydroxide at the same concentration as that used in the cell, washed liberally with double-distilled water and dried. It was assumed that this procedure would remove almost all the impurities susceptible to decomposition by high temperature alkaline solutions. Analyses of the autoclave contents (134) by atomic absorption spectroscopy provided no evidence of contamination of the solution by decomposition of the asbestos itself under such conditions. Asbestos string cleaned in the manner described, formed an adequate plug, particularly after the string had been well-divided, this apparently resulting in better electrolytic contact between the solutions at the two temperatures.

Before introducing the electrodes, the autoclave containing hydroxide solution, was heated initially to remove any surface-active impurities from the teflon tape which might be in contact with the solution. This treatment was expected to eliminate the possibility of slow adsorption of impurities at the electrode which might cause, for example, a time-dependence of the electrode impedance.*

After cooling from the higher temperatures, silver oxide was generally deposited on the teflon but was readily removed using nitric acid.

---

* Indeed, it was found that impedance measurements at potentials corresponding to silver dissolution did not exhibit a time dependence.

3.4 THE REFERENCE ELECTRODE

3.4.1 Choice of a Reference Electrode

By using an external reference electrode arrangement, any such electrode which functions at room temperature and is compatible with the test solution, can be employed. The use of the saturated calomel electrode (SCE) as an internal reference is limited by hydrolysis (123) and by the influence of the chloride ion on the behaviour of the working electrode (157). However, the calomel electrode may be used in hydroxide solutions at room temperature although an isothermal liquid junction potential is present between the saturated potassium chloride solution of the reference electrode and the alkaline solution. Nevertheless, the majority of measurements in this work were made with a SCE and all potentials have been referred to this scale.

Mercury|mercuric oxide reference electrodes, specially designed and prepared for use within the cell (see section 3.4.3), were used externally also to provide a reference for the calomel electrode. If the hydroxide ion concentrations of the Hg|HgO electrodes and the test solution are the same, then no correction for an isothermal liquid junction potential is required for such electrodes in alkaline solutions. While the Hg|HgO electrodes functioned adequately over short times (several days), over longer times they were not stable. Hence, despite the disadvantage of a liquid junction potential, the SCE was preferred since it was more convenient and reproducible over longer periods.

3.4.2 Isothermal Liquid Junction Potential

The use of the calomel electrode introduces a contribution as described above, to the observed potential, namely the liquid junction potential between the KCl and KOH solutions at the same temperature. The magnitude of this effect was estimated using the Henderson equation (101) in the form in which only univalent ions are involved (107).

$$E_{LJ} = \frac{RT}{F} \cdot \frac{(U_1-V_1)-(U_2-V_2)}{(U_1+V_1)-(U_2+V_2)} \ln \left(\frac{U_1+V_1}{U_2+V_2}\right) \qquad (3.1)$$

where the U and V terms are $\Sigma c_i u_i$ for cations and anions, respectively, appropriate to solutions indicated by subscripts, and the ionic mobilities*, u_i are taken as positive. In the derivation of the above equation, non-ideality is ignored and molar concentrations are used. It is also worth noting that, although the Henderson equation contains nothing characteristic of the "geometry" of the junction, it does require continuity of composition and assumes that ionic mobilities are independent of concentration.

As a first approximation, the liquid junction potential was initially estimated neglecting the effect of concentration on ionic conductivity, and using limiting molar conductivities, λ^o (174) for the ionic species at 298 K. Units are S m^2 mol^{-1}.

$$\lambda^o(K^+) = 7.45 \times 10^{-3}$$
$$\lambda^o(Cl^-) = 7.55 \times 10^{-3}$$
$$\lambda^o(OH^-) = 19.20 \times 10^{-3}$$

Substitution of these values into equation 3.1 gives a liquid junction potential of 6.9 mV.

Refinement of the above computation was attempted by using values of conductivity corresponding to the appropriate concentration. It is assumed that

$$\Lambda(KX) = \lambda(K^+) + \lambda(X^-) \qquad (3.2)$$

(X = Cl, OH) over the range of concentrations and since $u(K^+) \sim u(Cl^-)$ (107), then $\lambda(K^+)$ and $\lambda(Cl^-)$ may be evaluated at a particular concentration. From molar conductivity data reported in the literature for KCl (32) and KOH (48), values of Λ(KCl) and Λ(KOH)

---

* $u_i = \lambda_i/F$, where λ_i is the molar conductivity of the ion which is assumed to be univalent.

at $c = 1.05$ mol dm^{-3} * may be obtained. The value of $\lambda(K^+)$ is determined from Λ(KCl) which then enables $\lambda(OH^-)$ to be obtained from Λ(KOH) (see Table 3.1). The $\lambda(OH^-)$ may be compared with the value of 0.0149 S m^2 mol^{-1} for this quantity obtained from data for 1.05 mol dm^{-3} solutions of NaCl (32) and NaOH (48). A value of Λ(KCl) at $c = 4.2$ mol dm^{-3}, the concentration of a saturated solution of KCl (107), is also obtained from which $\lambda(K^+)$ and $\lambda(Cl^-)$ at this concentration are found. These values are shown in Table 3.1.

Table 3.1 Molar Conductivities of KX and X^- (X = Cl, OH)

Species	c/mol dm^{-3}	Molar Conductivity/S m^2 mol^{-1}
KCl	1.05	0.0112±0.03%
K^+	1.05	0.0056
KOH	1.05	0.0211±0.2%
OH^-	1.05	0.0155
KCl	4.2	0.0092±0.05%
K^+	4.2	0.0046
Cl^-	4.2	0.0046

By use of the Henderson equation, the liquid junction potential is evaluated as 8.7 mV.

Although the two values of E_{LJ} do not differ greatly, the second method is considered to be more reliable since the error involved in assuming limiting molar conductivities at the above concentrations might be expected to exceed the error due to deviations from ideality ($\gamma_\pm \neq 1$) arising from interactions between univalent relatively small ions.

3.4.3 Measurement of the Isothermal Liquid Junction Potential

The liquid junction potential was determined experimentally as the difference between the theoretical e.m.f., neglecting a liquid junction potential, and the measured e.m.f. of the cell:

---

* This concentration corresponds to the molality of KOH, 1 mol kg^{-1}, used in this work.

SCE|KOH|HgO|Hg

Small Hg|HgO electrodes which were to be used for thermal diffusion measurements, were also used for the present purpose. Two such electrodes were made specifically to be placed within the autoclave. Ives (107) recommends that "no very special precautions, except those needed to secure components of reasonable purity, seem to be needed in setting up mercury-mercuric oxide electrodes". Consequently, a slurry of Hg|HgO was prepared simply by grinding distilled mercury and 'Analar' mercuric oxide together. The two electrodes were then prepared and assembled following the design of commercially available calomel electrodes. On testing the constructed electrodes, a potential difference of 1.5 mV was found to exist between them. When measured against a SCE, the potential differences for the Hg|HgO electrodes were found to be 7 mV and 8.5 mV in excess of the theoretical e.m.f. at 295 K (E = 0.147 V*) for such a cell. These differences were found to be constant with time (several days) within 1 mV and are in agreement with the calculated liquid junction potential, which may therefore be used as a correction, where necessary, to observed potentials measured with respect to the SCE.

3.5 EFFECTS DUE TO THE THERMAL LIQUID JUNCTION

3.5.1 Introduction

In addition to the isothermal, isobaric liquid junction potential described above, the observed potentials contain two irreversible contributions due to the thermal liquid junction across the asbestos bridge. Since the working electrode is maintained at a different temperature and pressure from the reference electrode, both a pressure gradient and a temperature gradient exist over the junction giving rise, respectively, to a streaming potential and a thermal diffusion potential.

---

* E = 0.246 (107) - 0.099 (49) V.

Since these irreversible effects are present, the external reference electrode does not provide a direct thermodynamic standard although the potential of such an electrode appears to have been reproducible in studies by other workers (44) and was, in fact, found to be so in this research (see section 3.5.3).

Several methods have been developed to allow for such effects. Cowan and Staehle (44) used a procedure in which a calculated correction was applied to the hydrogen redox potential, measured through a solution bridge, of a floating hydrogen electrode within the cell. The measured potentials of the working electrode could then be referred to a thermodynamic (standard hydrogen) scale.

Alternatively, the contribution of thermal diffusion to the measured potential (the streaming potential contribution is discussed in section 3.5.4) may be estimated from available data on this effect in aqueous solutions. This method was applied to the present system and the estimated values were then compared with experimental data (see section 3.5.3).

The reference electrode arrangement under study involves the measurement of the potential of the WE at a temperature T with respect to an external SCE, E_{ext}. In order to relate the measured potentials to theoretical values, the potential difference, E_{ext}, is assumed to be a combination of three individual contributions (127) as represented in Figure 3.5 in which:

E_T' is the potential of the WE with respect to the SHE at the same temperature.

$E_{\Delta T}$ is the potential difference for the thermal cell containing a 1 mol kg^{-1} KOH bridge.

For the present analysis, the external SCE is considered to be at 298 K and its potential relative to the SHE will be taken as 0.244 V (107).

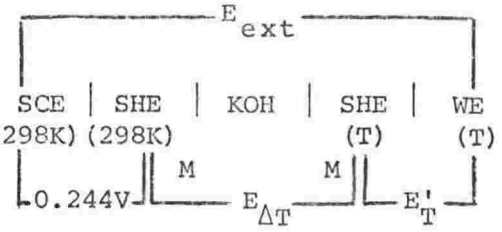

Figure 3.5 Contributions to the measured potential difference, E_{ext}.

3.5.2 Thermal Liquid Junction Potential

The e.m.f. of the thermal cell, $E_{\Delta T}$, that is, the observed thermal junction potential, before significant thermal diffusion occurs, may be formally split into contributions (1)* arising from:

(i) a thermocouple effect due to the temperature difference in the metallic conductor(s), M. This conductor is not necessarily the same metal as the electrode. Although this effect has been corrected for as in the work of Carr and Bonilla (27), it has a magnitude of the order of 1% of the sum of the two other contributions (49) and will be considered negligible.

(ii) an electrode temperature effect which is considered in terms of the thermal temperature coefficient $(\partial E/\partial T)_{Th,SHE}$ for the cell

SHE(298 K)/SHE (T)

De Bethune et al (49) have calculated $(\partial E/\partial T)_{Th,SHE}$ to be 0.871 ± 0.02 mV K^{-1} from which values of $E_{Th,SHE}$ for the above cell have been obtained by assuming that, as in the case of the thermal diffusion coefficient (see below), $(\partial E/\partial T)_{Th,SHE}$ is not strongly dependent on temperature. Macdonald (130)

---

* Isothermal liquid junction potentials due to the SHE in the hydroxide solution are not taken into account since Figure 3.5 is a hypothetical representation in that the measurements made in this study do not actually involve the use of hydrogen reference electrodes. However, a liquid junction potential does exist experimentally between the SCE and hydroxide solution which is taken into account (see equation 3.5).

has since evaluated $E_{Th,SHE}$ over the temperature range 298-573 K using free energy data for the reaction (3.3) corresponding to the thermal hydrogen cell.

$$H^+(T) + \tfrac{1}{2}H_2(298\ K) = H^+(298\ K) + \tfrac{1}{2}H_2(T) \qquad (3.3)$$

At low temperatures, the two sets of data (Table 3.2) agree but significant differences occur at higher temperatures which are presumably due to the assumption of temperature independence of the thermal coefficient over the temperature range shown and the fact that the previous workers obtained the value of 0.871 mV K^{-1} from data limited to temperatures less than 373 K. For these reasons, the values calculated by Macdonald are considered more reliable and are used to provide the necessary corrections in this work.

Table 3.2 Values of $E_{Th,SHE}$

T/K	298	333	373	423	473	523	573
$E_{Th,SHE}$/V							
Macdonald	0	0.030	0.058	0.085	0.098	0.100	0.096
De Bethune *et al*	0	0.030	0.065	0.109	0.152	0.196	0.240

(iii) Thermal diffusion: Available data (49) permit an estimate of this contribution and thereby allow a suitable correction to the measured potential to be made. Experimental evidence (171) indicates that the thermal diffusion potential coefficient $(\partial E/\partial T)_{TD}$ for a solution bridge, from the pressure vessel to the external reference electrode, is not strongly dependent on temperature. Hence E_{TD}* may be evaluated from equation 3.4.

---

* This quantity complies with the contribution referred to by Agar (1) as the "thermal diffusion potential" which in order to provide clarity will be adhered to in this work. This term replaces that used by some other workers (49,127), namely, the "thermal junction potential" which above describes the overall contribution, that is, the sum of the three effects.

Although $(\partial E/\partial T)_{TD}$ is estimated to be 0.5±0.1 mV K^{-1}* (49) for a strong alkali, this value should be regarded as only approximate, particularly since it was determined over a very limited range of temperature, as in the case of the thermal temperature coefficient.

$$E_{TD} = \int \left(\frac{\partial E}{\partial T}\right)_{TD} dT \approx 0.5\times10^{-3}(T-298) \text{ V} \qquad (3.4)$$

The potential of the WE with respect to the external reference electrode, E_{ext}, may be expressed in terms of the potential, E'_T, and the contributions to the thermal junction potential, $E_{\Delta T}$.

$$E_{ext} = E'_T + E_{Th,SHE} + 0.5\times10^{-3}(T-298) + E_{LJ} - 0.244 \text{ V} \qquad (3.5)$$

The values of $E_{\Delta T}$ over the temperature range 298-473 K are given in Table 3.3.

Table 3.3 Contributions to the observed Potential due to the Thermal Junction

T/K	E_{TD}/V	$E_{Th,SHE}$/V	$E_{\Delta T}$/V
298	0	0	0
333	0.018±.004	0.030	0.048
373	0.038±.008	0.058	0.096
423	0.063±.013	0.085	0.148
473	0.088±.018	0.098	0.186

The calculated $E_{\Delta T}$ corrections are large and should be considered as estimates only. For example, an uncertainty of ±0.1 mV K^{-1} in $(\partial E/\partial T)_{TD}$ will result in an error of ±8 mV in $E_{\Delta T}$ at 373 K. Furthermore, the value used for $(\partial E/\partial T)_{TD}$ is a general estimate for alkalis and does not apply specifically to a 1 mol kg^{-1} solution of KOH.

---

* Although no error is quoted, $(\partial E/\partial T)_{TD}$ is assumed to have the same magnitude of uncertainty as that for acids.

If the SCE is at room temperature which throughout this work will be taken as 295 2 K, then $E_{\Delta T}$ will contain an additional thermal diffusion potential arising from the SCE(295)|SHE(298) junction.

3.5.3 Measurement of the Thermal Diffusion Potential

Owing to the approximate nature of the value assigned to the thermal diffusion potential coefficient, experiments were performed to examine the accuracy of the calculated thermal diffusion potentials. A reference electrode was enclosed within the autoclave and another positioned externally in the reservoir.

The small Hg|HgO electrodes described in section 3.4.3 were used for these measurements. The potential difference between the electrode inside and that outside the autoclave was measured at 348 and 388 K, and was found to be reproducible. Measurements at higher temperatures were not attempted for two reasons. Firstly, the glass of the reference electrode is more subject to attack by the alkali and secondly, the Hg|HgO electrode may not be reliable as a reference electrode at temperatures greater than 423 K (see section 3.1.2). Despite the possible presence of these factors, on cooling the cell, the potential difference between the two reference electrodes was less than 1 mV and furthermore, remained stable within this range for their normal duration of several days.

The system used may be considered in the following form.

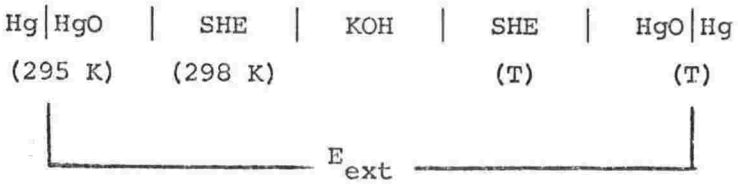

E_{ext} is given by equation 3.6.

$$E_{ext} = E_T + E_{\Delta T} - 0.099 \text{ V (Hg|HgO, 295 K)} \qquad (3.6)$$

It will be noted that since the external Hg|HgO electrode is at 295 K, an additional thermal diffusion potential is included in $E_{\Delta T}$. E_T is the equilibrium potential of the reference electrode (Hg|HgO) at temperature T with respect to the SHE at the same temperature. Assuming that the thermal temperature coefficient of the Hg|HgO electrode (49) is independent of temperature, E_T may be obtained from equation 3.8.

$$E_T = E_{Hg|HgO,298\ K} + \int_{298}^{T} \left(\frac{\partial E}{\partial T}\right)_{Th,Hg|HgO} dT - E_{Th,SHE} \qquad (3.7)$$

$$= 0.098 - 0.249\times10^{-3}(T-298) - E_{Th,SHE} \qquad (3.8)$$

Hence, substituting into equation 3.6 yields

$$E_{ext} = 0.098 - 0.249\times10^{-3}(T-298) + E_{TD} - 0.099\ V\ (Hg|HgO,295K) \qquad (3.9)$$

from which values of E_{TD} may be obtained using experimental data for E_{ext}. The results are summarised in Table 3.4.

Table 3.4 Measurement of the Thermal Diffusion Potential

T/K	E_{ext}/V	E_{TD}/V	$E_{TD(est)}$/V
348	0.0115± .001	0.0229	0.027
388	0.0255± .001	0.0469	0.047

It appears that there is sufficient agreement between the estimated (equation 3.4) and experimental values of the thermal diffusion potential to suggest that the value of 0.5 mV K^{-1} is a fair estimate for the temperature coefficient for these temperatures and may be considered reliable in the correction of the observed potential at least up to 388 K.

3.5.4 Effect of the Pressure Gradient

When a stream of electrolyte is forced through a porous material, a potential difference is created across it. Hence, the result of the pressure gradient across the junction is to produce an electrokinetic phenomenon known as the streaming potential, E_s, which is related to the electrokinetic (zeta) potential, ξ, by equation 3.10:

$$E_s = \frac{\xi \varepsilon P}{\eta \kappa} \qquad (3.10)$$

where the permittivity, ε (F m^{-1}), viscosity, η (kg m^{-1} s^{-1}), and conductivity κ (S m^{-1}), apply to the bulk solution. A lack of a value for ξ applicable to the present experimental conditions prevents an accurate evaluation of the streaming potential to be made using the above equation. The only data for the electrokinetic potential which appears to be available for consideration, applies to KOH solutions in glass capillaries up to concentrations of 2×10^{-4} mol dm^{-3} at which ξ = 136.5 mV (142). Using this value and the following data

$P = 0.8$ MPa
$\eta = 0.0890$ kg m^{-1} s^{-1} (201)*
$\varepsilon = 6.96 \times 10^{-8}$ F m^{-1} (174)*
$\kappa = 22.2$ S m^{-1} (1 mol kg^{-1} KOH, (48))

in equation 3.10 yields a streaming potential that is less than 5 mV at 0.8 MPa, the pressure used in experiments which will be described in the following section. Experimental data (142) show an 11% decrease in ξ as the concentration is increased from 2×10^{-5} to 2×10^{-4} mol dm^{-3}. Hence, it is reasonable to assume that the value of E_s for 1 mol kg^{-1} KOH solutions would be small enough to ignore, even though the glass capillary is replaced by a porous asbestos plug in this work. This

---

* Obtained from the values of η and the dielectric constant, D, for water at 298 K. $D = \varepsilon/\varepsilon_o$ where ε_o is the permittivity of a vacuum.

assumption could be expected to hold for temperatures up to 473 K since the pressures associated with aqueous systems under such conditions are less than 2 MPa for which the streaming potential should still be less than a few millivolts.

3.5.5 Measurement of the Streaming Potential

Attempts were made to establish experimentally the presence of a significant streaming potential in the system used in this study. These experiments were carried out in a similar manner to those performed to determine the thermal diffusion potential (section 3.5.3). The specially prepared Hg|HgO electrodes were again positioned with one in the cell and the other externally in the reservoir.

The first experiment performed was to pressurise the cell with nitrogen at 0.4 MPa which was the initial pressure applied at room temperature in the polarisation studies in order to provide electrolytic contact through the asbestos. No significant change in potential difference between the two Hg|HgO electrodes was observed. It was assumed that the potential pressure coefficient, $\partial E/\partial P$, (equation 3.11) was negligible

$$\frac{\partial E}{\partial P} = \frac{\Delta V}{nF} \qquad (3.11)$$

which is reasonable since the volume change, ΔV, for the half-cell reaction corresponding to a metal|metal oxide|OH^- electrode is expected to be small.

The second experiment was to increase the nitrogen pressure in steps to 0.8 MPa after obtaining a superimposable cyclic voltammogram at 0.4 MPa. Finally, a cyclic voltammogram was recorded using the reference electrode in the cell while passing a slow stream of nitrogen through the system. No appreciable shifts in the voltammograms were produced with the pressure increments, nor were the curves found to have moved relative to that at ambient pressure.

Hence, it may be assumed that to a first approximation at least, the streaming potential may be considered applicable.

CHAPTER 4 EXPERIMENTAL TECHNIQUES

4.1 ELECTROCHEMICAL EQUIPMENT

4.1.1 Potentiostat

The four electrochemical techniques involved in this work all made use of a potentiostat. The general principles of operation and applications of this instrument to corrosion studies have been described in detail previously by Von Fraunhofer and Banks (191). However, since a potentiostat is fundamental to the application of these techniques, the method by which it maintains the working electrode at a controlled potential will be briefly described.

Essentially, the potentiostat control loop compares the potential difference between the working and reference electrodes with an arbitrarily-adjustable external potential. If a difference exists between these two potentials, current is passed through a negative feedback current containing the counter electrode (Figure 4.1) in such a way as to reduce the difference to zero, thereby restoring the working electrode potential to the required value. In modern potentiostats, these operations are commonly performed by an operational amplifier, usually of the differential type, designed to remain stable with large amounts of negative feedback from output to input.

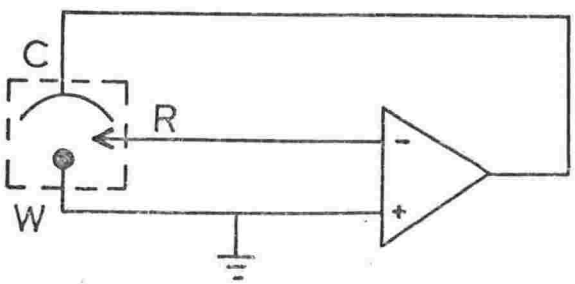

Figure 4.1 Generalized Basic Potentiostatic Control Circuit

Since one of the outputs is frequently the ground reference potential, it is omitted in the above figure. Provision must be made for inserting a resistor to measure the current flowing through the cell, and a signal generator to provide an arbitrarily-adjustable comparison potential for the control circuit.

A potentiostat having a fast rise-time is necessary for the transient techniques used in this work. This requirement was fulfilled by the model chosen, a Chemical Electronics Type 403A potentiostat for which the rise time is specified as approaching 0.3 μs (33).

4.1.2 Auxiliary Equipment

The electrochemical techniques required various auxiliary instruments:

(i) Function generator. The instrument used to provide a triangular voltage waveform to the potentiostat for cyclic voltammetry was a Philips PM 5168 function generator which has a frequency range of 0.5 mHz to 5 kHz.

(ii) Integrator. This device determines the charge passed over a defined period of time within a cyclic voltammetry potential scan. In effect, it measures the area under the current-potential (time) curves. The instrument used was a Chemical Electronics integrator.

(iii) X-Y recorder. The model chosen was a Houston 2000 X-Y recorder which has an input impedance of 1 MΩ(106) and has the facility for the X-input to be converted to a time base so that the recorder could function also as a single-input instrument.

(iv) Digital Multimeter. A Hewlett-Packard 3465 A, 4½ digit multimeter which had an input impedance of 10^{10} Ω (102), was calibrated against a standard cell using a Tinsley potentiometer, and was in turn used to calibrate the X-Y recorder and signal generator.

4.1.3 Additional Equipment for Impedance Measurements

The a.c. impedance technique utilised two other pieces of equipment:

(i) Signal source. The device chosen was a Brookdeal 9471 signal source which has a frequency range of 0.001 Hz to 11 MHz available for the generation of sine or square waves.

(ii) Phase-sensitive detector (P.S.D.). A Princeton Applied Research (P.A.R.) Model 129 A lock-in amplifier which can function either as a vector voltmeter or as a phase-sensitive detector was used. The output of the lock-in amplifier is a d.c.voltage, proportional to the input signal, which depends on the phase difference between the signal and reference. The P.A.R. model generates a reference signal at 90^{o} to the input reference, enabling simultaneous measurement of the in-phase and quadrature components of the input signal to be achieved. The frequency range of this instrument was specified as 0.5 Hz to 100 kHz (160) but it was found that accurate measurements may be made down to 0.3 Hz. A range of time constants, 1 ms to 100 s is available for a low pass filter through which the d.c. output signal is passed. For high frequencies, the time constant used was 0.3 s which was increased to 1 s at 30 Hz and 10 s at 5 Hz.

4.2 CYCLIC VOLTAMMETRY

4.2.1 Introduction

Cyclic voltammetry provides a means of obtaining an electrochemical spectrum of the charge transfer processes that a metal will undergo for the particular experimental conditions. It is capable of detecting very small amounts of charge consumed at the interface so that potential-sweep methods can be applied to the examination of surface phenomena of electrodes and used to determine quantitative surface coverages of adsorbed species (89,152,197). This technique has been employed also to establish the kinetics of electrode reactions by considering various diagnostic relationships (149,150,177).

The technique involves following the current response due to a linearly-varying potential difference controlled between the working electrode and reference electrode. Using this continuous voltage-sweep method, polarisation curves may be recorded automatically using an X-Y recorder or oscilloscope. The sweep rate is chosen to permit the recording of significant maxima or minima.

4.2.2 Principles

In order to show that this technique may be used to indicate the charge transfer processes possible at the surface of an electrode, the basic electrochemical principles under conditions of a varying potential imposed on the working electrode will be briefly discussed.

The total current passing consists of three components:

(i) A non-faradaic current due to double-layer charging

(ii) A pseudofaradaic current* associated with the discharge of ions to form adsorbed intermediates. The surface coverage changes with potential, thereby giving rise to a pseudo-capacitance.

(iii) A faradaic current associated with the rate of the overall electrode reaction.

Assuming that these processes are separable, then the total current density is given by (40)

$$i_T = C_{dl}\left(\frac{dE}{dt}\right) + C_{ps}\left(\frac{dE}{dt}\right) + i_o \exp\left[\frac{\eta}{b}\right] \qquad (4.1)$$

where C_{dl} is the double-layer capacitance, C_{ps} is the pseudocapacitance, i_o is the exchange current density, b is the Tafel slope and η is the overpotential.

The double-layer capacity** of a metal electrode in aqueous solution is usually less than 1 F m^{-2}. For the area of the working

---

* This term, as indicated by Conway (40), identifies the pseudo-capacitative origin of such a current and thereby distinguishes it from other components of the total current.

** Capacity = capacitance per unit area.

electrode in this work, 1.6×10^{-4} m^2, and a typical sweep rate of 40 mV s^{-1}, the charging current contribution should not exceed 6.4 μA, that is, several orders of magnitude less than the observed currents which therefore, are considered to arise almost entirely from charge transfer processes.

Under appropriate conditions, peaks representing current maxima or minima may be exhibited in a cyclic voltammogram (section 5.1). The increase in charge due to passage of the current over the interval t_1 to t_2 is given by equation 4.2

$$\Delta Q = \int_{t_1}^{t_2} i dt \qquad (4.2)$$

$$= [\int_{E_1}^{E_2} i \, dE]/(dE/dt) \qquad (4.3)$$

where E_1 and E_2 are the potentials corresponding to times t_1 and t_2. Since dE/dt is constant, the charge consumed at the electrode during this time interval is directly proportional to the area under the current/voltage curve between E_1 and E_2. Hence, the peaks observed in cyclic voltammograms indicate regions of potential in which charge transfer reactions occur at the electrode surface.

The interpretation of the peaks in terms of the corresponding reaction, and information deduced regarding the associated mechanisms are discussed in detail in chapter 5.

4.2.3 Circuit

The potential-scanning arrangement (Figure 4.2) consisted of the Philips function generator coupled to the potentiostat which provided potentiodynamic control. On applying the external voltage sweep, a varying current was produced as the potential of the working electrode, with respect to the reference electrode, was continuously adjusted by the potentiostat. The potential difference created across a fixed resistor due to the current response was applied to one input of the X-Y recorder, and that between the WE and RE fed to the

Figure 4.2 Block diagram of circuit for cyclic voltammetry

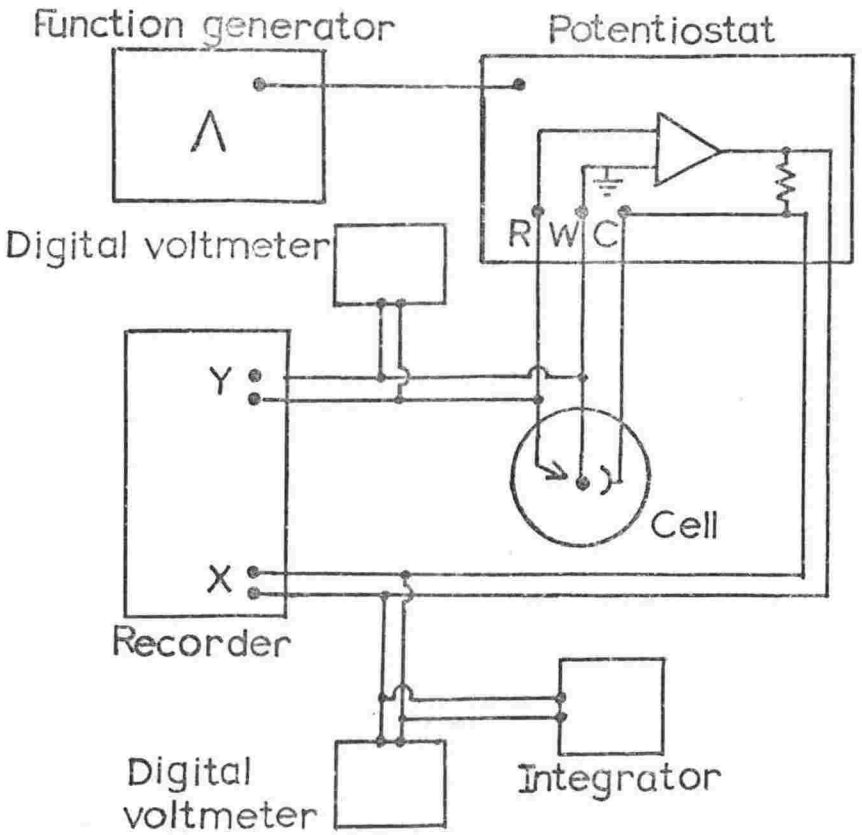

Figure 4.3 Block diagram of circuit for potentiostatic polarisation

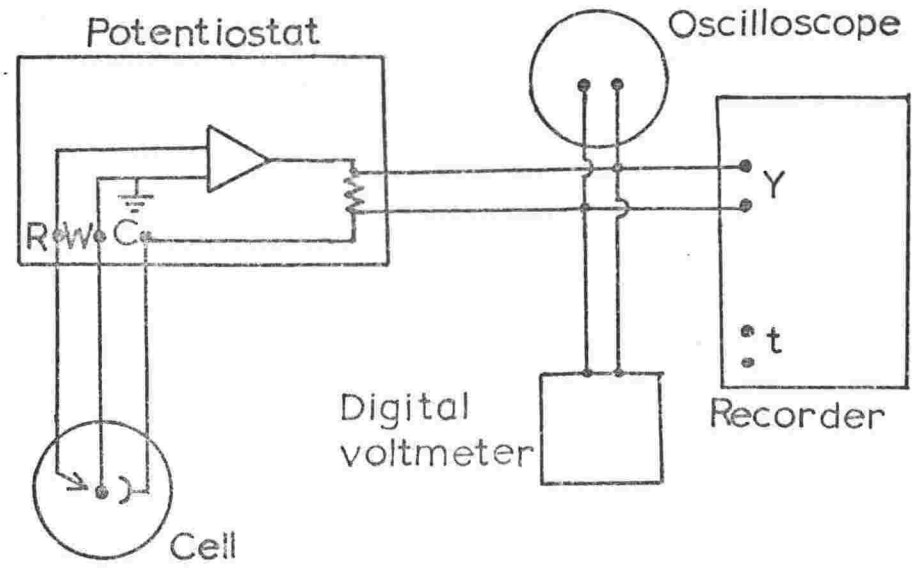

other input. Both input signals to the recorder were followed on digital voltmeters and in addition, the integrator was linked to the X-input in order to provide a measure of the voltage drop integrated with respect to time.

General precautions against electrical noise and ground loops were taken, including the use of coaxial cable in connections between instruments, and the isolation from ground of heating apparatus and all instruments except the potentiostat. Despite these precautions, a.c.pick-up* was a problem, generally resulting in instability of the X-Y recorder. Three additional precautions were required to reduce the noise level adequately:

(i) Shielding of the fixed resistor in the potentiostat circuit.

(ii) Grounding of the coaxial shielding of the leads from this resistor to the recorder guard.

(iii) A 1.5 nF capacitative shunt across the inputs of the reference and working electrodes.

4.2.4 Experimental Procedure

The procedure for each run was to sweep the potential initially in the anodic** direction. The anodic sweep was reversed at oxygen evolution and the potential swept in the cathodic direction. The potential sweeping was continued for a number of cycles until a steady state in which the current-voltage curves showed very little, if any change, was obtained. Such a state was achieved after four or five cycles at all temperatures except 478 K (discussed in section 5.2.4). Due to the behaviour exhibited at 478 K, this technique was extended to include an additional temperature, 458 K. Cyclic voltammetry was performed over a range of sweep rates from 9 to 40 mV s^{-1} at each temperature.

---

* The noise was largely 50 Hz a.c. mains pick-up on the electrodes but a significant level of high frequency noise was also present.

**Throughout this work, the following convention will be adopted in regard to potentials and currents: anodic potentials and currents are positive, cathodic potentials and currents are negative. Current-potential profiles will be plotted with anodic potentials as the positive abscissa and anodic currents as the positive ordinate.

4.3 POTENTIOSTATIC POLARISATION

4.3.1 Introduction

A polarisation curve can be obtained in two ways:

(i) galvanostatic charging - the potential/time transient at constant current is recorded and the resulting steady-state potential plotted against the appropriate current. Although it is reasonably easy to obtain polarisation measurements under constant current conditions, this approach is not capable of, for example, defining a current maximum in the current/potential curve in the case of an active-to-passive transition. In such cases potentiostatic polarisation is necessary.

(ii) potentiostatic polarisation - the potential of the working electrode is stepped to a new value which is then held constant for a given time interval and the current passing through the cell is followed as it changes with time until it approaches a near steady-state value. Each steady-state current may be plotted against the corresponding potential to provide a polarisation curve from which it is possible to determine the presence of an active-to-passive transition.

From an analysis of the current/time transient itself, it is often possible to determine the nucleation and growth characteristics of films on the electrode surface.

4.3.2 Circuit

The potentiostatic circuit is shown diagrammatically in Figure 4.3. The adjustment of the potential of the working electrode to some selected value by means of the potentiostat is associated with a current response which is monitored as a potential difference across a fixed resistor. This signal is fed into the Y input of the recorder, the X input being switched to the time base. Although the recorder had a fast response time, the current signal was recorded also on an oscilloscope to ensure that the observed response was not a consequence of the finite response time of the recorder. For

this technique also, all instruments except the potentiostat were isolated from ground.

Problems with electrical noise, similar to those encountered in the work with cyclic voltammetry, again arose. However, these were overcome by following the procedure employed previously (section 4.2.3).

4.3.3 Experimental Procedure

Potentiostatic polarisation curves for silver were obtained by increasing the potential from some initial value in steps of 10 mV up to 300 mV, followed by increments of 20 mV until oxygen evolution occurred. In most cases, the current changed very little after two minutes at each potential and the value of the current at this time was used to represent approximately steady-state conditions.

4.4 GALVANOSTATIC CHARGING

4.4.1 Introduction

This technique has often been used to determine the charge transfer characteristics of a reaction at an electrode surface. When a constant current is applied to the working electrode, its potential changes with time. Potential arrests occur as charge transfer processes become possible, with the potential rapidly shifting if the reactions become inhibited to the extent that they are unable to proceed sufficiently fast to carry the charge at the required rate.

4.4.2 Circuit

The apparatus used consisted of a constant current source capable of a fast response, and potential measuring and recording

Figure 4.4 Block diagram of circuit for the galvanostatic technique

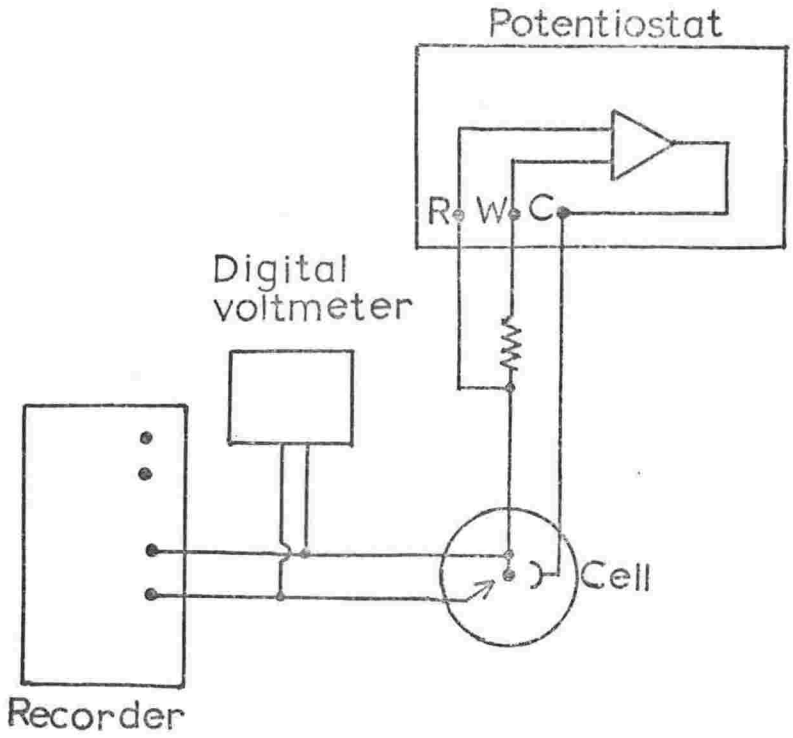

Figure 4.5 Block diagram of circuit for the a.c. impedance technique

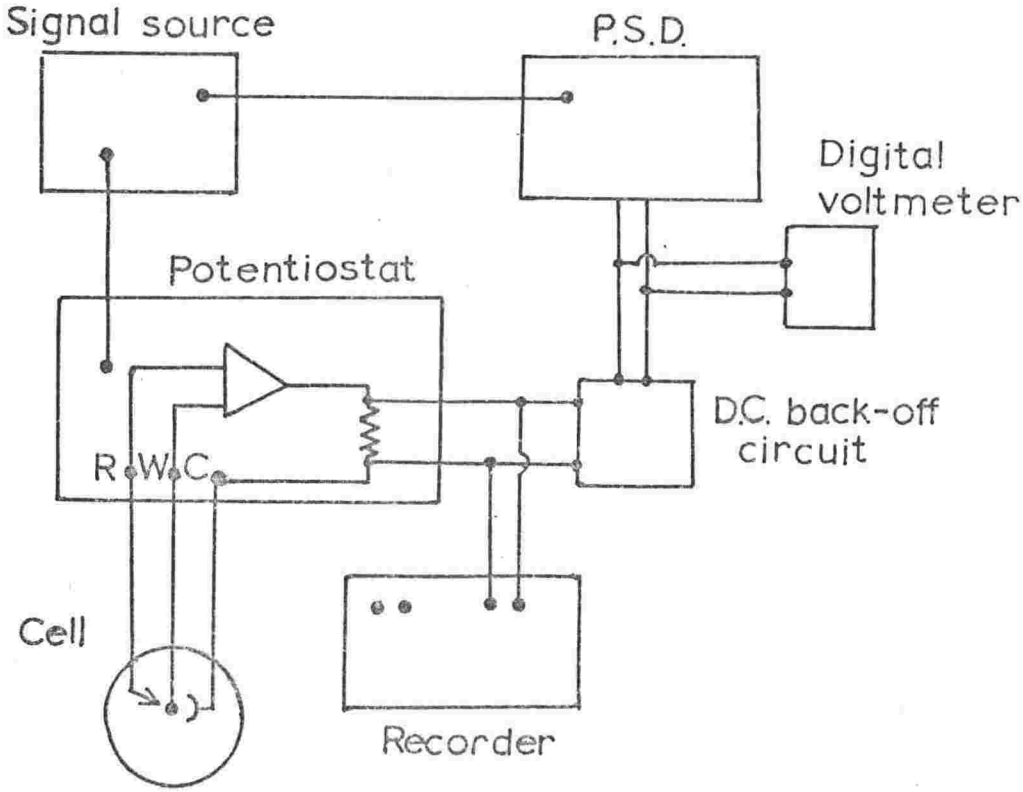

devices (Figure 4.4). In the present case, the galvanostat which is essentially a two terminal device capable of controlling the predetermined magnitude of the current in an external circuit, was provided by the potentiostat (isolated from ground) with a resistor across the inputs for the working and reference electrodes.

The basic operations performed by such a galvanostat are similar to those performed by a simple potentiostat. The voltage drop across the ohmic resistor placed in series with the cell (see Figure 4.4) must be compared with an arbitrarily-adjustable external potential. Then the instrument must be able to react to the difference between these two potentials through a negative feedback circuit containing the cell in such a way as to reduce the difference to zero. In addition, these operations must be performed without drawing significant current from the external circuit. Provided that the resistance of the control resistor and the reference potential are constant, the magnitude of the current flowing through the cell will also be constant. This means of galvanostating is more versatile than previous methods involving a series combination of a high voltage d.c. cell and a large resistance (59,139).

In the circuit shown in Figure 4.4, a constant current was applied between the working and counter electrodes and the potential response of the WE with respect to the RE followed using the digital voltmeter and X-Y recorder which is used in the single-input mode. Since the potentiostat is isolated from ground, the WE is grounded at the X-Y recorder.

4.4.3 Experimental Procedure

The anodic and cathodic charging curves for silver were recorded for temperatures up to 478 K. The electrode was polarised cathodically at a minimum current of 4 mA for 30 seconds. The current was then reversed to obtain the anodic charging curve. When the potential reached the point of oxygen evolution, the current was again reversed and the cathodic sweep recorded. This procedure of current reversal was repeated three to five times until the curves were superimposable

with respect to potential, although the duration of the potential arrests still showed very slight increases. The currents used varied from 4 to 25 mA (2.6-15.9 mA cm^{-2} apparent surface area).

4.5 A.C. IMPEDANCE

4.5.1 Introduction

The use of a.c. impedance methods is intended to provide a detailed knowledge of the behaviour of the electrical double layer, diffusional processes, adsorption at the electrode surface, and the kinetics of charge transfer.

The technique involves the determination of the real and imaginary components of the electrode impedance over a range of frequencies. From the experimentally-obtained impedance, it is possible in many cases to evaluate the components of an equivalent circuit (see section 8.1) for the electrode impedance, thereby enabling the various kinetic parameters to be determined.

4.5.2 Techniques of Measurement

The impedance components obtained in this work were derived from phase-sensitive current/voltage measurements. Two procedures are available to obtain such measurements:

(i) An a.c. signal having a small amplitude, is superimposed on the electrode potential as it is varied and the components are obtained as a function of potential at a particular frequency. This method was used by Tilak et al (182) in their examination of the electrolytic processes on silver. Potentiodynamic control of the a.c. signal superimposed on the linear voltage sweep was achieved by means of a potentiostat. The impedance components were proportional to the currents obtained from two phase-sensitive amplifiers operating in phase and at quadrature respectively, and could be recorded with the potentiodynamic current/potential profile.

(ii) The d.c. potential of the electrode is maintained constant and the a.c. signal superimposed on this bias potential. The components are then obtained for each frequency as the latter is varied. This method is employed in the present work using the arrangement described below.

4.5.3 Circuit

The Brookdeal signal source supplies the a.c. signal which has an amplitude of 3.2 mV r.m.s. and also feeds a reference signal (3.2 V r.m.s.) directly to the phase-sensitive detector (Figure 4.5). The potentiostat maintains a selected d.c. potential at the working electrode, and simultaneously modulates this potential with the external a.c. signal fed to the potentiostat from the signal source. Hence, the potential difference effectively applied between the WE and RE contains an a.c. component. If the impedance between the WE and RE includes a reactive component, then the a.c. signal of the output current will undergo a phase shift relative to the a.c. input voltage.

The potential drop measured across a shielded non-reactive resistor in the potentiostat circuit contains both the d.c. and a.c. components. The d.c. signal is removed by a back-off circuit (described in the following section), allowing the a.c. component to be fed to the phase-sensitive detector over the frequency range under examination (0.3 Hz to 5 kHz). The P.S.D. then compares the two sinusoidal signals - the reference taken directly from the signal source and the signal obtained as described above - and provides simultaneous output signals corresponding to the in-phase (real) and quadrature (imaginary) components of the input voltage.

A dummy cell consisting of known parallel R-C combinations was used initially to ensure that the entire system was operating reliably and that impedance components were obtained accurately from the P.S.D. in this arrangement.

4.5.4 Additional Circuitry

It was not possible to remove the d.c. component using only a capacitor between the resistor and P.S.D. since the a.c. signal extended down to frequencies of 0.3 Hz. In order to extract the a.c. component without any d.c. voltage, the active circuit shown in Figure 4.6 was employed. The two active components used were an operational amplifier (National LM308D) which in this circuit has a unity gain,and a voltage follower (National LM310D). The circuit is designed such that a d.c. voltage negates the incoming d.c. signal (nulled using a digital voltmeter).

Figure 4.6 D.C. Back-off circuit

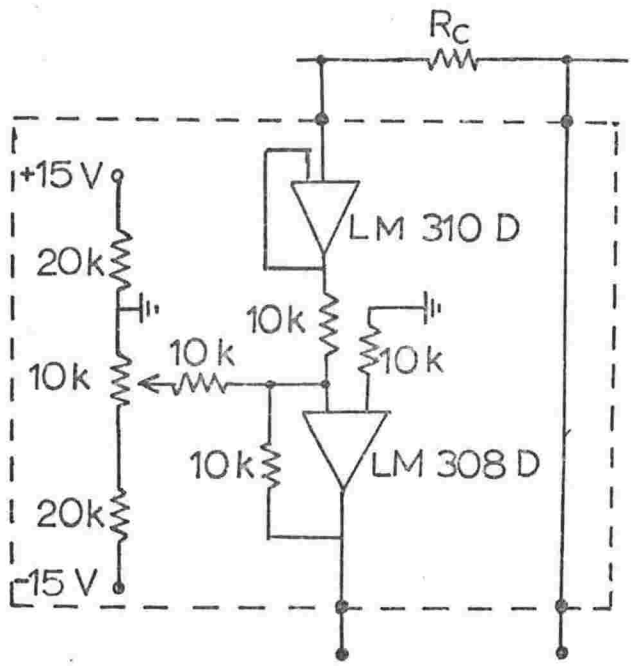

The circuit was tested in order to observe if any interference of the a.c. component occurred. The output from an a.c. signal fed directly to the active circuit from the signal source was compared with the reference signal by the lock-in amplifier operating as a vector voltmeter. The phase shift produced by the circuit was generally less than one degree over the frequency range and consequently could be ignored. At frequencies where a shift of one degree or more was observed, appropriate compensation to the phase angle could be made on the lock-in amplifier.

The overall system was particularly sensitive to electrical noise. As in the other techniques, most of the noise was 50 Hz pick-up from the mains but again a significant level of high frequency noise was present. Two further precautions were taken to reduce the noise:

(i) A floating differential input to the P.S.D. for the potential drop across the fixed resistor was used.

(ii) Coaxial leads, particularly to the reference electrode, were required.

The signal/noise ratio at the P.S.D. was improved by using a sufficient a.c. input voltage but this had to be balanced against the problem of significantly altering the steady-state conditions imposed by the d.c. bias potential.

4.5.5 Analysis

The voltage signals corresponding to the in-phase and quadrature current components were simultaneously obtained by nulling the respective meter on the P.S.D. and noting the offset-potentiometer readings.

The following complex algebraic analysis was performed in order to convert the in-phase and quadrature voltages into the corresponding impedance components. A simplified circuit which indicates only the a.c. voltages is shown in Figure 4.7.

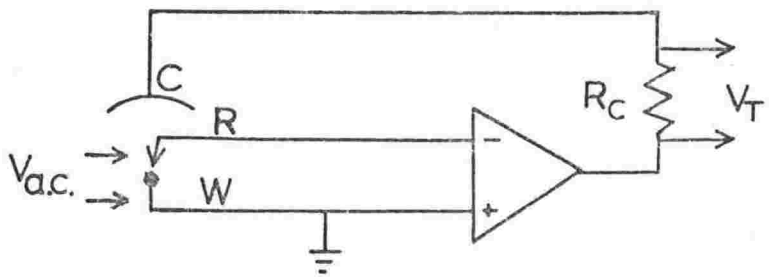

Figure 4.7 Simplified circuit showing only the a.c. voltages.

The total a.c. voltage drop, V_T, across the fixed resistance, R_c, consists of a real, V_R, and an imaginary, V_X, component:

$$V_T = V_R + jV_X = i_T R_c \qquad (4.4)$$

where $j = \sqrt{-1}$. The impedance of the working electrode and solution between the WE and RE, Z, is given by equation 4.5.

$$Z = \frac{V_{a.c.}}{i_T} = \frac{R_c V_{a.c.}}{V_T} = \frac{R_c V_{a.c.}}{V_R + jV_X} \tag{4.5}$$

where $V_{a.c.}$ is the modulating a.c. voltage. Rationalising the expression yields

$$Z = \frac{R_c V_{a.c.} V_R - jR_c V_{a.c.} V_X}{V_R^2 + V_X^2} \tag{4.6}$$

Since the impedance Z has the general form

$$Z = R - jX \tag{4.7}$$

then the components can be equated such that

$$R = cV_R \tag{4.8}$$

$$X = -cV_X \tag{4.9}$$

where $c = R_c V_{a.c.} / (V_R^2 + V_X^2)$. (4.10)

With the large amount of data to be processed, these calculations were carried out using a programmable calculator (Hewlett-Packard 25).

4.5.6 Experimental Procedure

The WE was potentiostated initially to 0.12 V and an a.c. signal at 5 kHz superimposed. Readings were then taken at decreasing frequencies down to 0.5 Hz, and in some instances to 0.3 Hz. Below this value, noise became a limiting factor although, in the majority of cases, it was not necessary to progress lower since the shape of the impedance plots in the complex plane (see Chapter 8) could be adequately inferred over the frequency range with a lower limit of 0.5 Hz.

Impedance measurements were made on the system over the temperature range 295-478 K for five potentials in the active and passive regions at each temperature. In addition, the impedance at a potential at which the higher silver oxide, Ag_2O_2, could be formed, was determined at all temperatures except 478 K (see section 8.6.3). In the passive region, measurements were commenced when the rate of film growth had reached a near steady-state, the d.c. steady-state current being followed on the X-Y recorder. Generally, 45 minutes were sufficient for the drift of the impedance components in this region to have reduced to a negligible level, although this time decreased with increasing temperature.

No attempt was made to apply this technique to reduction processes since the oxide film would not then be in a steady-state but continuously decreasing in thickness.

4.6 X-RAY DIFFRACTION

In an attempt to verify that the oxidation products on the electrode at elevated temperatures were the same as those produced at room temperature, X-ray diffraction was employed. Powder diffraction peaks were obtained with Cu Kα radiation using a Philips diffractometer and a Philips proportional counter. Following polarisation at 428 K, the electrodes were removed from the cell immediately the temperature had dropped sufficiently.

Although a dark shading of the electrode surface was apparent, the thickness of the film had apparently diminished in the hot alkaline solution to such an extent that it was not possible to observe any X.R.D. peaks other than those corresponding to silver metal.

Briggs et al (24) obtained X.R.D. patterns for silver electrodes under different stages of polarisation. They took the precaution of using a second working electrode in parallel to the main electrode so that the sample could be removed whilst still subject to polarisation, thereby minimising the possibility of self-discharge of the oxide before examination. However, this method would not have been useful in the present study since it was still necessary for the autoclave to cool before the electrodes could be extracted.

4.7 ELECTRON MICROSCOPY

Electrodes were examined with a scanning electron microscope (Cambridge Stereoscan 600) for surface roughening following polarisation at different temperatures. The two electrodes used were potentiostated to 0.30 V (SCE) at 295 K and 478 K respectively. In both cases, the electrodes were removed from the cell, washed in ammonia to remove

any oxide, followed by double-distilled water and then air-dried. The only preparation necessary for the specimens prior to examination under the microscope involved adhering the electrodes to the sample plate using silver paint.

SECTION III

RESULTS

CHAPTER 5 CYCLIC VOLTAMMETRY

5.1 THEORY

5.1.1 Introduction

The response of a simple, reversible charge transfer reaction involving soluble reactants and products, to a linearly varying potential was examined initially by Randles (162), and by Sevcik (170).

Although other types of reaction have since been examined (10, 149, 150), theoretical treatments of the kinetics of the anodic and cathodic reactions of silver, in most cases, have not yet been reported. The summary, therefore, is restricted to analyses which are considered to be the most appropriate to the present system.

5.1.2 Metal Dissolution

The case in which the anodic dissolution of a metal occurs reversibly in the presence of an inhibiting step due to an adsorption-redox process, has been examined by Casadio (28) for an infinite planar electrode surface.* He considered a simple metal dissolution reaction which is generally represented as

$$M = M^{n+} + ne \qquad (5.1)$$

by (i) neglecting the role played by the solvent molecules and the supporting electrolyte in the system.** This approximation is

---

* Although the electrode involved in this work was cylindrical in shape, this analysis may still be applied (see appendix 3).

**It will be assumed that

(i) this analysis may be applied to a metal dissolution reaction having the form

$$M + nOH^{-} = MO^{-} + \frac{n}{2}H_2O + (n-1)e$$

(ii) a similar dependence of peak current on sweep rate will hold in the case where inhibition is the result of a dissolution-precipitation mechanism (see section 1.2.1).

valid when the molecular and ionic species are at much larger concentrations or when they possess a higher diffusion coefficient than M^{n+}.

(ii) assuming that the concentration of the reduced species is invariant and unity.

In the absence of any interferring process, the current density (5.2) due to reversible anodic dissolution is entirely mass-transfer controlled.

$$i = nF \left(\frac{DnFv}{RT}\right)^{\frac{1}{2}} c_m \chi(j) \qquad (5.2)$$

where D = diffusion coefficient for M^{n+}

v = potential scan rate

c_m = surface metal, or "active site", concentration

$\chi(j)$ = adimensional flux for M^{n+} at x=0

j = adimensional potential-time triangular function.

However, it is assumed that inhibition of the dissolution reaction due to the redox adsorption process* 5.3 does take place.

$$M + A^- = MA + e \qquad (5.3)$$

A is an adsorbed radical produced by the anodic oxidation of the A^- species.

In the limiting case where the overall process is under control of reaction 5.1, the waveform is predicted to have an anodic peak current density and peak potential given by equations 5.4 and 5.5, respectively.

$$i_p = 0.446\ nF\left(\frac{nF}{RT}\ VD\right)^{\frac{1}{2}} (c_m)_o \exp\left[\left(\frac{nF}{RT}\right)(E'-E^o)\right] \qquad (5.4)$$

$$E_p = 1.11\left(\frac{RT}{nF}\right) + E' \qquad (5.5)$$

where E^o is the formal potential** for the metal ion system, E' is the formal potential for reaction 5.3 referred to half-coverage ($\theta = 0.5$) standard state, and $(c_m)_o$ is the value of c_m at $\theta = 0$.

---

* The theory for a redox-adsorption process under conditions of quasi-equilibrium was developed for linear potential scan voltammetry by Srinivasan and Gileadi (175).

** The term, formal potential is used instead of standard potential when the activity is replaced by any composition variable such as concentration.

The peak current density and peak potential relations under control of reaction 5.3 are given by equations 5.6 and 5.7, respectively:

$$i_p = \frac{qnFv}{4RT} \qquad (5.6)$$

$$E'_p = E' \qquad (5.7)$$

where q is the charge required to achieve a full "coverage" of the electrode surface, that is, complete inhibition of the active sites by the adsorbed species. While the current density due to reaction 5.1 depends on the square root of v, the pseudocapacitative term, i', is directly proportional to v. Hence, the scan rate may be used to provide evidence for the contribution of current from each of the two reactions. At lower v, the relative contribution of i to the total waveform is increased while at higher v, the current density, i', is more enhanced than i.

In the case of the metal dissolution reaction itself, a transition from reversible to irreversible behaviour at high sweep rates will occur if the rate of the electron exchange reaction does not occur sufficiently fast relative to mass transport processes to maintain Nerstian conditions at the electrode surface.

5.1.3 Film Growth

Film growth has been considered in terms of the electric field across the oxide for three cases (198). The current arising in each case is predicted to be a function of sweep rate as shown in the following table.

Table 5.1 The Current Due to Film Growth

	Conditions	Current
(i)	High field	$\log i = \log \bar{A} + (6FB/2.3\ V_m).\frac{v}{i}$
(ii)	Low field, in which ion migration through the film is rate limiting	$i = (12F\bar{A}B/V_m)^{\frac{1}{2}}.v^{\frac{1}{2}}$
(iii)	Low field, in which ion injection into the film is the rate limiting step	$i = (6F\alpha^{\frac{1}{2}}/V_m)(v/i^{\frac{1}{2}})$
(iv)	Place exchange	$i = \frac{B\beta\lambda}{1+c/[k.\exp(\beta Ea)]}$

V_m is the molar volume of the oxide and $\bar{A}$, B are film growth parameters.

Film growth has been described also in terms of a model involving a place exchange mechanism. According to Asakura and Nobe (10), the current due to formation of an oxide film by such a mechanism is given by the expression in the above table.

When the rate of film growth is controlled by diffusion in the film, the functional dependence of peak current and peak potential on sweep rate, as shown by Delahay (53), has been expressed (10) as

$$i_p = k(C_{red})_{ss}\, v^{\frac{1}{2}} \qquad (5.8)$$

$$E_p = E_p^{\,o} - \frac{RT}{nF} \ln(C_{red})_{ss} \qquad (5.9)$$

where k and $E_p^{\,o}$ are constants. These equations were derived for the case of iron in which

(i) the concentration of reduced species at the I/II interface*, $(C_{red})_o$ is related to the anodic potential by

$$E = E^o - \frac{RT}{nF} \ln(C_{red})_o \qquad (5.10)$$

---

* The iron oxide layer is assumed to have a duplex structure (10). The oxide adjacent to the Fe is Fe_3O_4(I), while the outer layer (II) is probably a non-stoichiometric solid solution composed of Fe(II) and Fe(III). It is assumed also that electron transfer for the Fe(II)/Fe(III) reaction occurs at the I/II interface.

(ii) $(C_{red})_{ss}$ is the steady state value of C_{red} corresponding to the anodic potential at t = 0.

Such a dependence for the peak current has been demonstrated for silver in previous studies at room temperature (182). However, the formation of silver oxides has been found (177) to be irreversible, and in this work, E_p is shown to be a function of v.

Analyses (51,150) of irreversible reactions taking place under diffusion control have indicated that in addition to the dependence of i_p on sweep rate, the peak potential should be proportional to ln v. Hence, where applicable this dependence of E_p on sweep rate will be examined.

5.2 CHARACTERISTICS OF THE CYCLIC VOLTAMMOGRAMS

5.2.1 General Shape

Cyclic voltammograms (-0.54 to 0.69 V SCE) for silver in 1 mol kg^{-1} KOH over the temperature range 295-478 K are shown in Figure 5.1. These curves were obtained at a sweep rate of 16.8 mV s^{-1} and were found to be superimposable after 4 to 5 cycles at all temperatures except 478 K (see section 5.2.4). The general shape of the current potential curve at 295 K is typical of those obtained by previous workers (177,182) at a similar temperature. At temperatures up to 458 K, the principal features of the voltammograms at 295 K are still evident. Three main peaks,* A1, A2 and A3 are observed on sweeping anodically until oxygen evolution occurs followed by two peaks, C3 and C2, on reversing the sweep. The current-potential curves at 478 K exhibit several major changes which will be discussed in section 5.2.4.

A fourth anodic peak has been observed below room temperature at 243 K by Tilak et al (182). As the temperature is raised, the oxygen evolution current becomes appreciable so that at room temperature this peak cannot be resolved. Evidence for the existence of this state at room

---

* These symbols which were used by Tilak et al (182) are chosen for this work since they indicate clearly the position of the peaks with respect to the direction of the potential sweep, and consequently, are associated with the corresponding anodic or cathodic reactions more readily.

Figure 5.1 Cyclic voltammograms for Ag in 1 mol kg^{-1} KOH

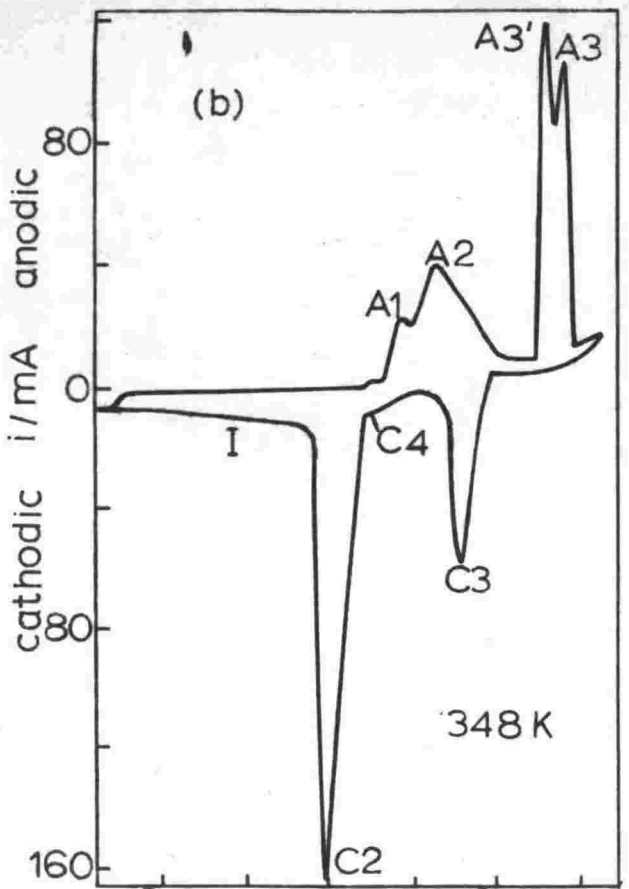

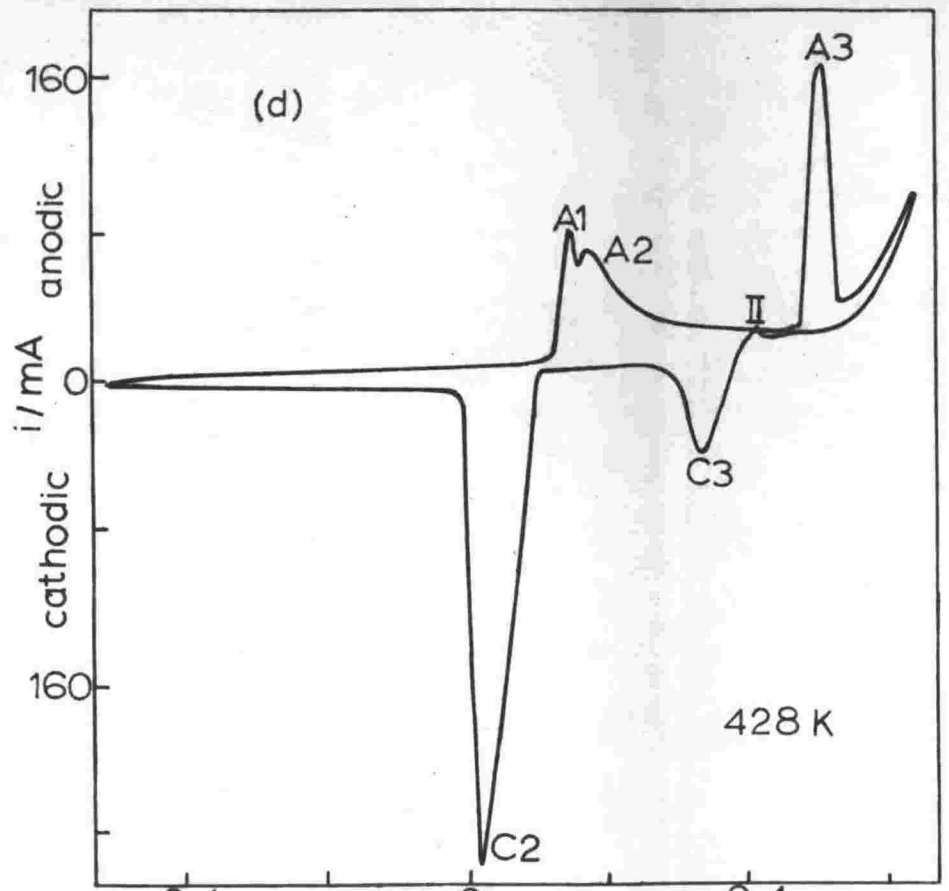

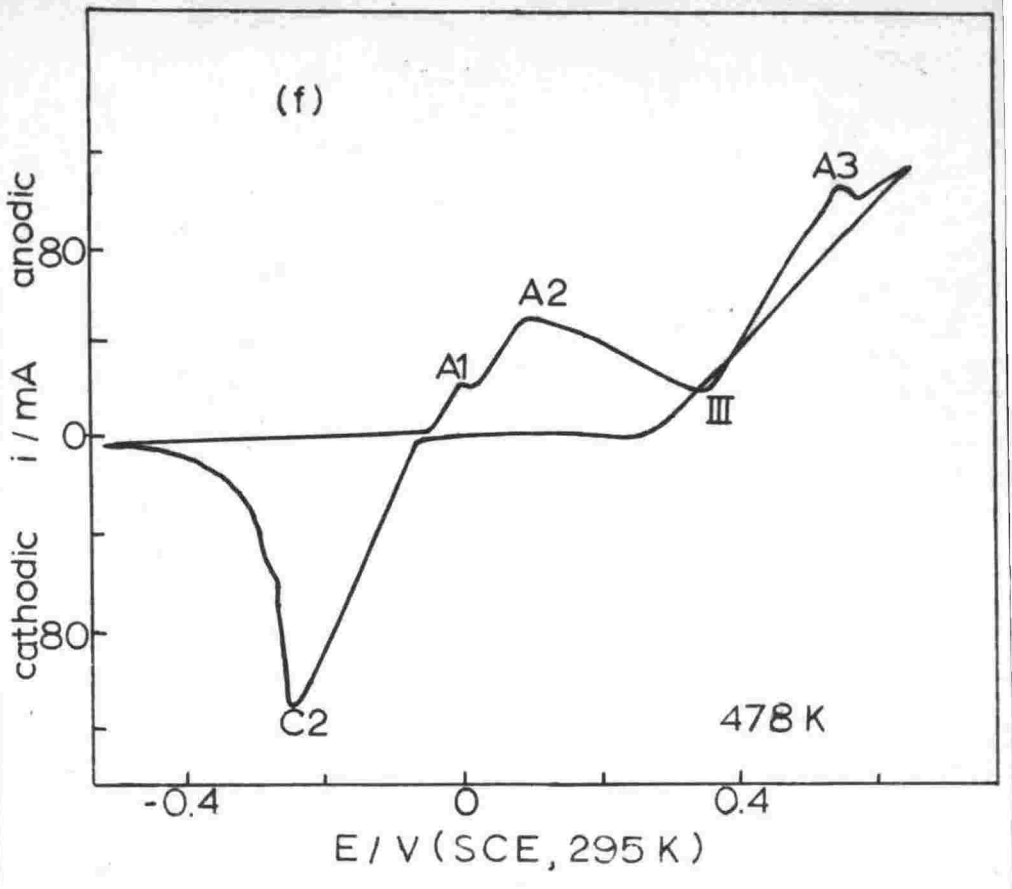

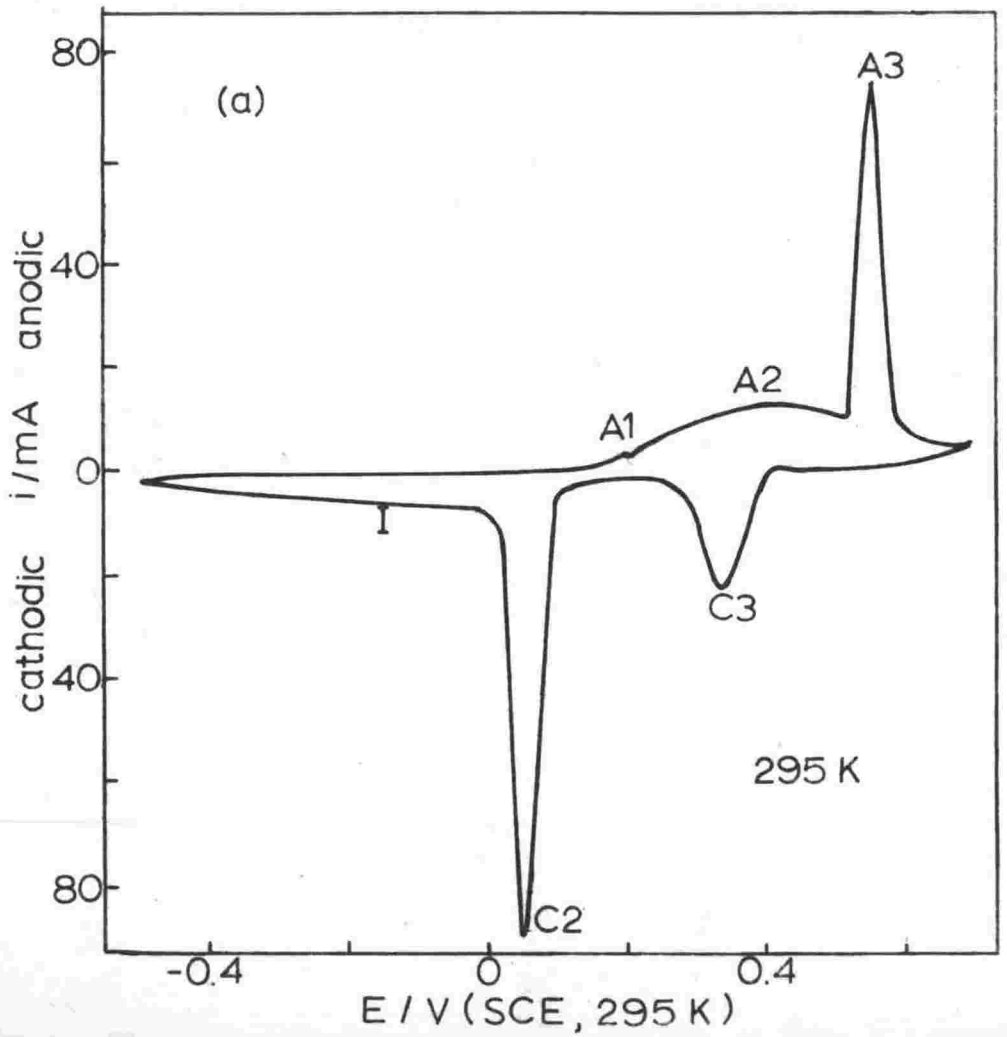

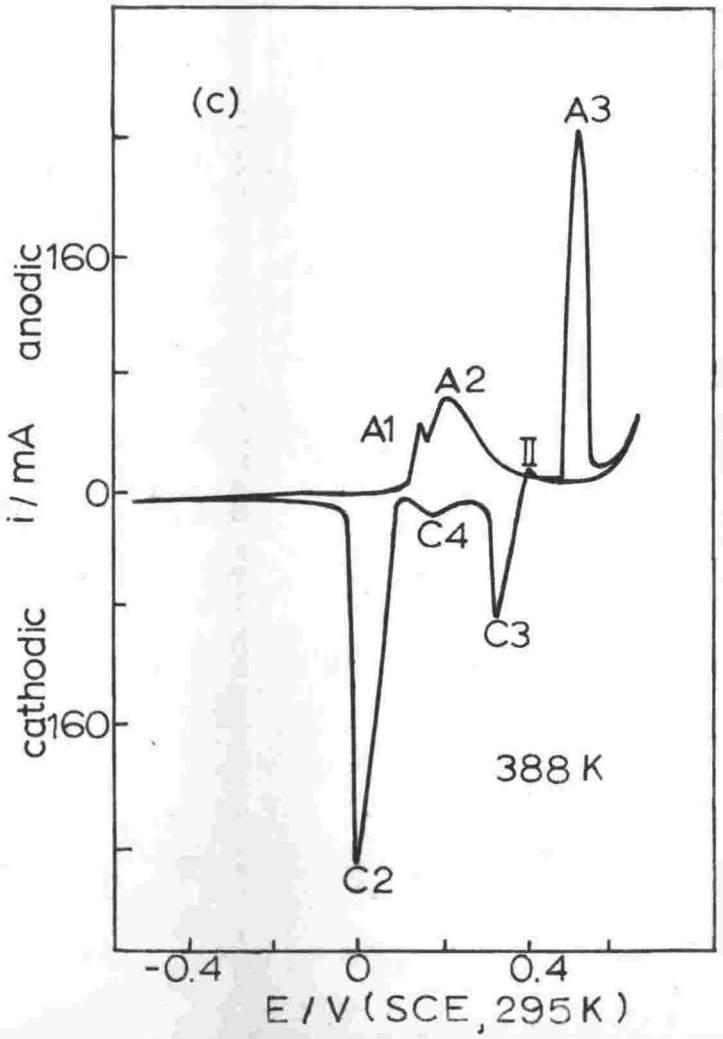

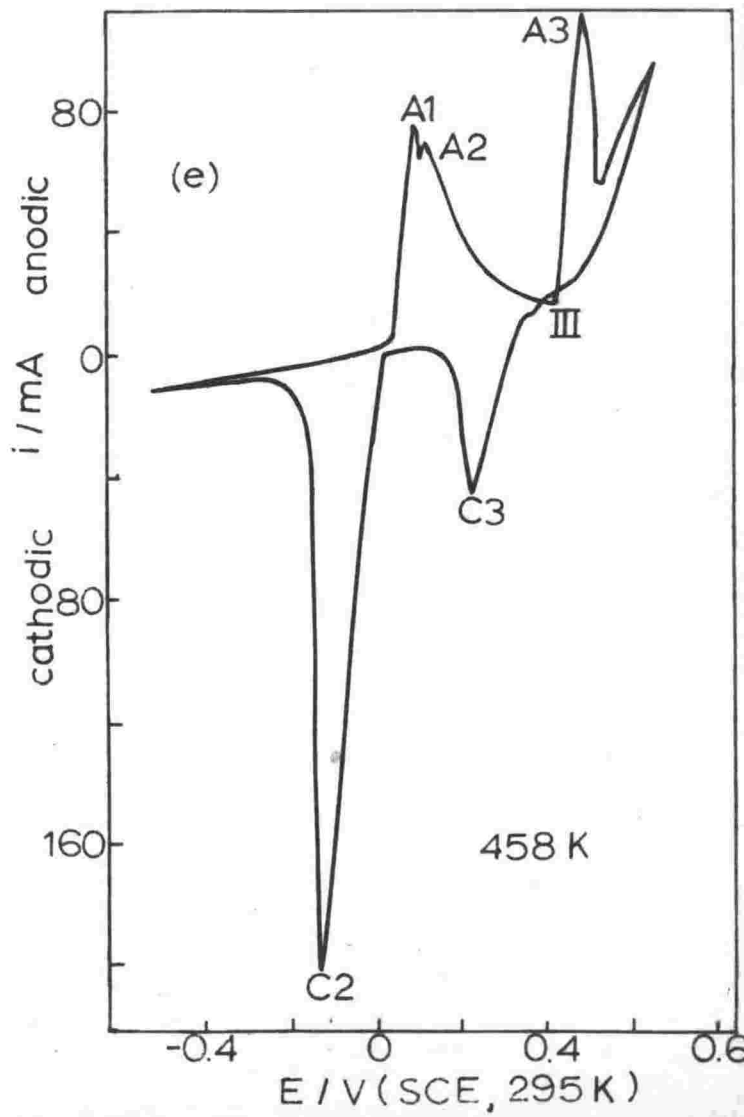

temperature was provided by these workers from impedance measurements.

At all temperatures, cyclic sweeping caused a general increase in peak heights corresponding to an increase in the charge transferred at each peak. The minor oxidation peak A1, in particular, was observed to become more prominent on cycling.

5.2.2 Assignment of Peaks

Previous studies (64,87,177) have established that the reactions given below correspond to the peaks at room temperature. In section 5.3.2, these assignments will be shown to be consistent with the thermodynamics of the reactions over the temperature range studied.

A1: This peak was attributed initially (64,177) to the formation of AgOH. However, it is now generally accepted that A1 corresponds to the dissolution of Ag as AgO^-

$$Ag + 2OH^- = AgO^- + H_2O + e \qquad (5.11)$$

The existence of this ion is supported by chemical stability studies (3,17). Furthermore, Giles and Harrison (87) found that an anodic current flows at potentials before the potential at which Ag_2O could begin to form, and showed by variation of the sweep rate that this current is faradaic with a steep potential dependence. These observations were in agreement with faradaic impedance results (88) which showed that dissolution of silver occurs as the soluble ion, AgO^-.

A2: This peak is generally attributed to the direct formation of Ag_2O by the reaction:

$$2Ag + 2OH^- \rightarrow Ag_2O + H_2O + 2e \qquad (5.12)$$

The presence of Ag_2O has been confirmed (64) by e.m.f. measurements.*

---

* The species formed at the corresponding arrest during constant current polarisation was identified as Ag_2O by X.R.D. measurements (24).

A3: It is recognised that this peak corresponds to the formation of Ag_2O_2 (64,179,182) according to the reaction:

$$Ag_2O + 2OH^- \rightarrow Ag_2O_2 + H_2O + 2e \qquad (5.13)$$

The presence of Ag_2O_2, as in the case of Ag_2O, was confirmed by e.m.f. measurements (64).

C3: Sweep reversal experiments (179) indicate that this peak corresponds to the reduction of Ag_2O_2.

C2: It is clear, also from sweep reversal experiments (177), that this peak is associated with the reduction of Ag_2O.

The fourth anodic peak which becomes resolvable when the temperature is lowered to 243 K (see section 5.2.1), is attributed to the formation of Ag_2O_3 from Ag_2O_2.

A tail, I, is often observed in the cyclic voltammograms following Ag_2O reduction. This tail probably arises from effects similar to those associated with anomalous impedance measurements obtained by previous workers (182) for this region. Since the oxide itself would normally be reduced, or not yet formed on the anodic sweep, these anomalous measurements were attributed to roughness or porosity of the electrode and possible occlusion of Ag^+ ions giving rise to a residual faradaic contribution in the pores at such potentials.

A small initial current peak also is observed occasionally prior to the A1 region. This peak has been noted in other studies (64,182) and is associated with carbonate impurities in the solution.

5.2.3 Current/Potential Profile over the range 295-458 K

All five peaks exhibited in the current/potential curve at room temperature appear at temperatures up to 458 K. However, the relationship between the shapes of peaks, A1 and A2, alters markedly with increasing temperature. Both peaks become sharper, with A1 developing into a well-defined spike at 388 K. At 428 and 458 K, A1 has grown to a height comparable with that of A2 and in fact, surpasses the latter at higher

sweep rates. It is worth noting here that this trend is completely reversed at 478 K. Notwithstanding these increases, A3 remains very much higher than A2 at all temperatures.

Other more specific changes in the current/potential profile occur with the rise in temperature, but at higher temperatures these changes disappear and the shape of the cyclic voltammograms becomes progressively simpler. Although these changes are quite abrupt in their appearance and subsequent disappearance over relatively small increases in temperature, they are quite reproducible over different runs at the same temperature. The following are the changes observed:

(i) The tail, I, while still evident at 348 K, ceases to be so at higher temperatures.

(ii) A fourth oxidation peak, A3', observed at 348 K, develops as a small peak at the base of A3 but it displays a greater sensitivity to sweep rate than the parent peak. After several cycles, particularly at high sweep rates, this region of the current/potential curve exhibits two clearly resolvable peaks which are of similar height and quite stable with respect to their position and height. A notable feature of this change is that Conway et al (42) did not observe a second peak at 333 K.

It is assumed in this chapter that the peak at 388 and 428 K is A3. However, it is possible that the peak at these temperatures is, in fact, A3' but this situation will not affect comments made in this chapter regarding the peaks, A3 and A3'. Such a possibility is discussed later (Chapter 9).

(iii) A third cathodic peak designated C4, appears between peaks, C2 and C3, at 388 K. This peak is smaller than either of the surrounding peaks but, as in the case of A3', it becomes more evident at high sweep rates. Although less distinct, a hump in this region of the current/potential curve at high sweep rates is also apparent at 348 K. C4 was not observed at 428 K but it may, in fact, have become evident at higher sweep rates than those used. The reactions which may be associated with peaks A3' and C4, are discussed in section 5.6.

(iv) A small anodic peak, II, occurs on the cathodic sweep immediately before C3 as the temperature is raised. Although this anomalous peak is not observed at the lower temperatures, it becomes quite distinct at 388 and 428 K. However, when the temperature is increased to 458 K, only a dip in the curve is evident while at 478 K, II has disappeared completely. In a room temperature study of thin films of silver, Stonehart and Portante (179) observed a similar peak which is associated with the completion of Ag_2O_2 formation. It would appear that this completion process can give rise to a peak for bulk silver electrodes with an increase in temperature.

5.2.4 Current/Potential Profile at 458 and 478 K

It is apparent in Figure 5.1 that the current/potential curve at 458 K possesses a similar form to the curve at 428 K. However, it also exhibits characteristics common to the curve at 478 K such as:

(i) A lowering of the overpotential for the oxygen-evolution reaction so that the current for this reaction occurs appreciably in the same potential region as A3, particularly at 478 K.

(ii) On reversal of the potential sweep from oxygen evolution, a current 'loop', III, is formed by the intersection of the anodic-sweep and cathodic-sweep currents.

(iii) Substantial shifts in the peak potential, particularly for A1, A2 and C2, in the direction of sweep, still occurred after four cycles - the number required to achieve superimposable traces at lower temperatures (section 4.2.4). Even after eight cycles, the peak potential continued to shift although the change on each cycle was reduced. These shifts were probably associated with a high degree of roughening of the electrode surface (see section 5.6.6). To reduce the effect on the peaks, the cyclic voltammograms were recorded after two cycles using only one sweep rate in each run. The shifts

reproducibility of these measurements over different runs is discussed further in section 5.3.3.

(iv) Similarly, the height of the peaks continued to increase on cycling so that it was not possible over eight cycles, at the least, to obtain stable measurements of the peak current.

All the above features observed at these temperatures were found to be present over different runs.

The polarisation behaviour of silver at 478 K exhibits further marked changes in relation to the behaviour over the temperature range 295-458 K. The peak, C3, has virtually disappeared at 478 K while C2 becomes distinctly asymmetric with the current decreasing sharply at potentials cathodic to the peak potential. Since C3 was still very evident at 458 K, the loss of this peak is clearly a relatively sudden effect taking place within a 20 K change in temperature. This feature is discussed further in section 5.6.6.

Electrodes which had been used at 478 K and were cleaned and repolished exhibited similar behaviour at room temperature with regard to the positions of the peaks. The peak potential for reduction of Ag_2O would initially lie between 20-40 mV more negative than that observed for a new electrode. On cycling, the peak potential would move to more cathodic values, but eventually a steady state was reached where E_{C2} could have a value from 0 to -0.1 V (SCE, 295 K). The anodic peaks obtained at room temperature, similarly were shifted to less positive potentials, generally over a range of 30 mV. Such effects were observed after using the electrode at 428 and 458 K also, but to a much lesser extent.

5.3 VARIATION OF PEAK POTENTIAL WITH TEMPERATURE

5.3.1 Introduction

In most cases the current peaks, or potential arrests in galvanostatic studies, represent irreversible processes. Although the associated overpotentials for such reactions are not included in the equilibrium potentials calculated from thermodynamic data, the possibility of a particular reaction corresponding to the peak of interest may be indicated (134) by showing that

$$E'_A > E_T > E'_C \qquad (5.14)$$

E'_A and E'_C are the corrected* anodic and cathodic peak potentials for the conjugate oxidation/reduction peaks, respectively, and E_T is the equilibrium potential for the process responsible for the peaks with respect to the SHE at the same temperature. The difference between peak potentials, E'_p and the calculated equilibrium potentials is due to the presence of often significant overpotentials, $(E'_p - E_T)$, which are positive and negative for anodic and cathodic processes, respectively.

Inequality 5.14 is usually sufficiently restrictive to identify the charge processes occurring at the electrode. However, for simple, symmetrical processes occurring at constant current, the overpotentials in both directions are equal and the equilibrium potential is given by

$$E_T = \tfrac{1}{2}(E'_A + E'_C) \qquad (5.15)$$

For complex, unsymmetrical reactions, the anodic and cathodic overpotentials are almost certain to differ but the average value of E'_A and E'_C, although not equal to E_T, will lie within the limits defined by inequality 5.14.

For a dissolution process (127)

$$E'_{diss} > E_{T,diss} \qquad \text{anodic} \qquad (5.16a)$$

$$E'_{diss} < E_{T,diss} \qquad \text{cathodic} \qquad (5.16b)$$

where E'_{diss} is the corrected potential at which this process with equilibrium potential, $E_{T,diss}$ achieves maximum current. At moderate sweep rates, the soluble species formed have sufficient time to diffuse from the electrode surface. Hence, the conjugate reduction process is not expected to be significant.

5.3.2 Changes in Peak Potential

Although specific effects of the increase in temperature on the peak potential as a function of sweep rate will be discussed later (see

---

* The experimentally observed peak potentials, E_p, are corrected for reference to the SHE at the temperature of interest using equation 3.5. In this case, rearrangement of the equation yields

$$E'_p = E_p - E_{\Delta T} - E_{LJ} + 0.246 \text{ V}$$

section 5.4), the general changes in peak potential with temperature will be briefly examined in this section.

The corrected peak potentials, E_p' at a sweep rate of 16.8 mV s^{-1}, and the equilibrium potentials* for the reactions associated with the cyclic voltammograms at room temperature are given in Table 5.2. While the values of E_p' apply to a specific sweep rate, they do provide a general guide to the changes in peak potential with temperature over the range of sweep rates studied.

Table 5.2 Comparison of Peak Potentials with Equilibrium Potentials over the range 295-478 K

	Potential V (SHE, T)					
T/K	295	348	388	428	458	478
E'_{A1}	0.41	0.33	0.28	0.23	0.14	0.03
$E_{AgO^-\|Ag}$	0.22	0.07	-0.03	-0.15	-0.23	-0.28
E'_{A2}	0.60	0.42	0.35	0.26	0.17	0.14
$E_{Ag_2O\|Ag}$	0.35	0.27	0.21	0.13	0.07	0.02
E'_{C2}	0.27	0.18	0.14	0.11	-0.08	-0.21
E'_{A3}	0.76	0.74	0.66	0.59	0.53	0.59
$E_{Ag_2O_2\|Ag_2O}$	0.61	0.54	0.48	0.42	0.36	0.31
E'_{C3}	0.56	0.48	0.46	0.42	0.28	-

From the above table, it is clear that both the anodic and cathodic peaks move to less positive potentials at higher temperatures.

---

* These data were obtained by interpolation from plots of E_T against temperature for which values of E_T were calculated from the equations listed in section 2.4.6, in most cases for 50 K intervals. The molality, $m(AgO^-)$, is arbitrarily set at 10^{-6} mol kg^{-1} and $m(OH^-)$ = 1 mol kg^{-1}. No activity coefficient corrections were applied but these coefficients would appear in log terms including pOH and therefore in effect pH, and should not change E_T too much. The value of pH is adjusted for the change in temperature using literature data for pK_W^o (77).

It will be noted from Table 5.2 that the peaks in the current/potential curves in the anodic direction generally exhibit large over-potentials and consequently, in most cases are clearly irreversible.

The peak potentials and equilibrium potentials are in accordance with inequalities 5.14 and 5.16a which shows that the reactions assigned at room temperature (section 5.2.2) are also applicable at elevated temperatures.

5.3.3 Reproducibility

The cyclic voltammograms obtained after four cycles over the temperature range 295-428 K were sufficiently reproducible* over different runs to allow

(i) measurements of the potential within ±15 mV.

(ii) measurements of the current within ±10 mA.

(iii) an examination of the sweep rate dependence of the peak-current and peak potential.

The reproducibility of these measurements varied within the above limits depending on the particular peak and the temperature. Generally, the reproducibility was better for the peaks, A1 and A2. The lack of reproducibility is quite large compared with the experimental uncertainty in the potential and current measurements, ±3 mV and ±4 mA respectively, in a particular run.

In addition to the relatively large uncertainty in the values of E_p and i_p at 458 and 478 K, measurements of E_p and i_p were reproducible only to within ±60 mV and ±40 mA, respectively. These figures apply to cyclic voltammograms obtained after two cycles where the potential was swept at only one rate in that run.

The large variation in peak currents over different runs at these two temperatures meant that these values could be used only for qualitative purposes.

The reproducibility at all temperatures is influenced by three factors which have already been indicated:

(i) The temperature control although constant to ±1 K for each run is reproducible to only ±5 K at the higher temperatures, 428-478 K.

---

* Many 'hard' metals behave differently (129,134). The lack of reproducibility in such cases is ascribed to difficulty in obtaining reproducible surfaces by cold-working techniques.

(ii) Use of a repolished electrode following a run at 478 K. The behaviour of such electrodes was unpredictable and generally prevented their further use.

(iii) Polishing by grinding techniques often makes it difficult to prepare a highly reproducible surface. While the state of the surface often influences the values of the potential and particularly the current, it was concluded in section 3.3.2 that the initial surface roughness has little effect in the present work.

5.4 SWEEP RATE DEPENDENCE

5.4.1 Introduction

Cyclic voltammograms were obtained at a number of sweep rates over the range 9 to 40 mV s^{-1} at each temperature. The peak currents, and in many cases the peak potentials, were found to be sensitive to sweep rate at all temperatures as has been observed for other metals in alkaline solutions at elevated temperatures (127,133). The peak currents increase with sweep rate for all peaks over the temperature range, whereas the effect of sweep rate on the peak potential varied with the particular peak and the temperature.

On the anodic sweep, the peak potential for A1 was found to be independent of sweep rate at all temperatures. By contrast A3, and also A3', shift to more positive potentials with increasing sweep rate at each temperature. A2 was intermediate in behaviour exhibiting a transition from a dependence on sweep rate up to 348 K to a non-dependence at 388 K and above.

On the cathodic sweep, C2, and also C4, shift to more cathodic potentials with increasing sweep rate. However, C3 exhibits no apparent dependence on sweep rate except at 388 K. Small shifts which are sweep rate dependent may take place for C3, and at higher temperatures for A2, but these shifts could not be distinguished from the scatter of data. For this work, the peak potentials in these cases will be considered independent of sweep rate.

Figure 5.2 Dependence of E_p on ln v

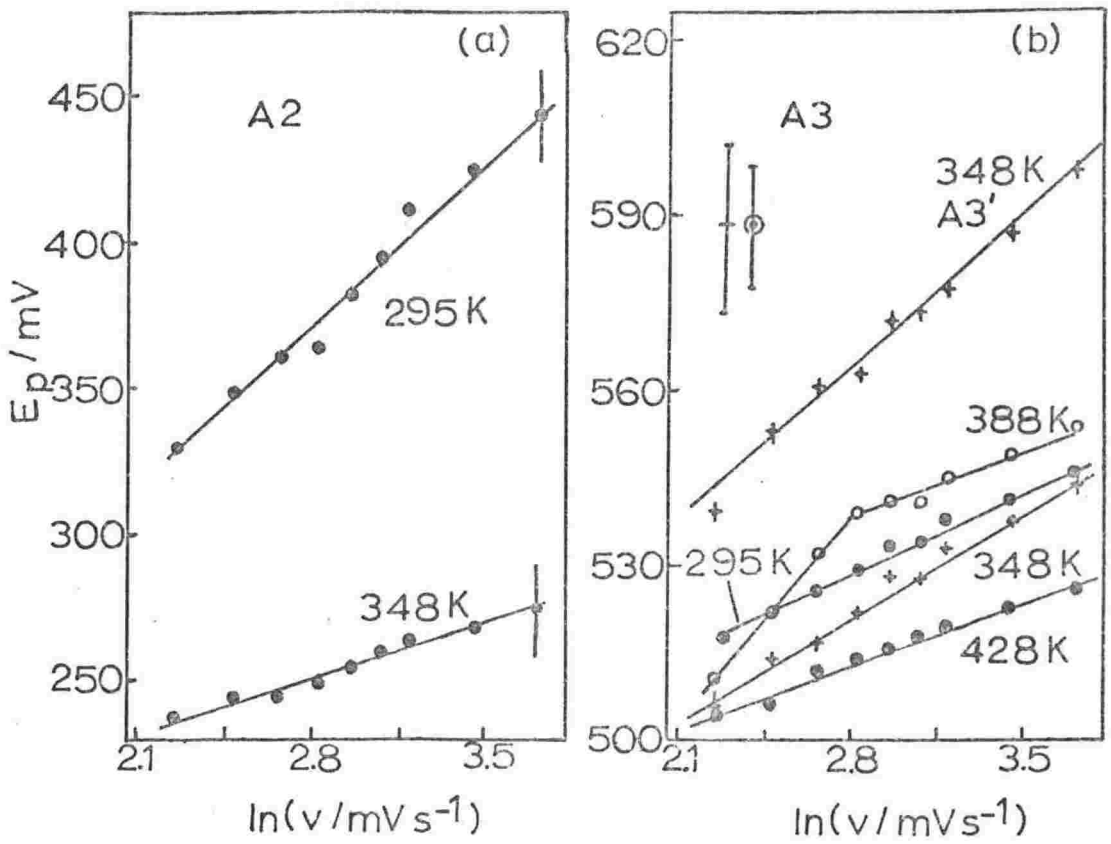

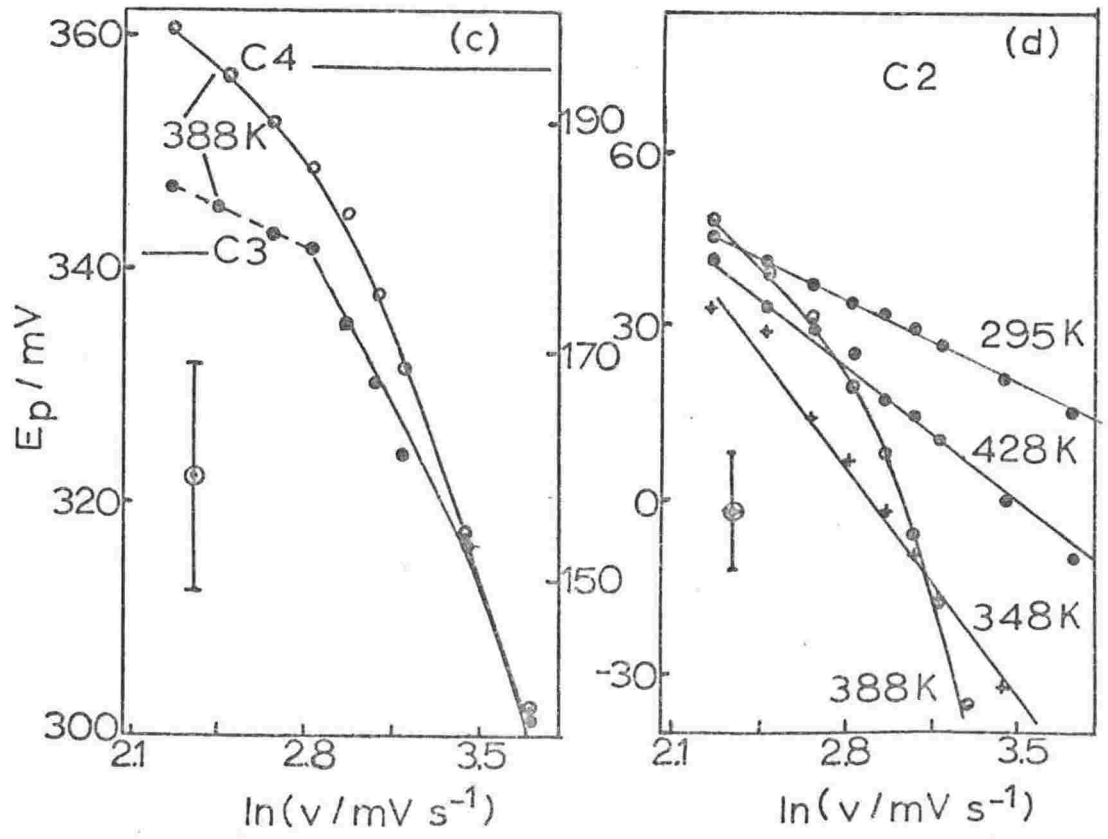

5.4.2 Peak Potential as a Function of Sweep Rate

In section 5.1.3, it was proposed to examine the dependence of E_p on ln v for irreversible film formation when diffusional processes are present. In those cases where E_p was found to vary with sweep rate the E_p/ln v relations are plotted in Figure 5.2.

Linear E_p/ln v plots are observed for the following peaks:

(i) A2 at 295 and 348 K. The lower slope of 348 K probably reflects a tendency of the reaction towards reversibility as observed at the higher temperatures.

(ii) A3 at all temperatures, although at 388 K, two linear regions are observed. In this case the lower slope at higher sweep rates suggests that the associated reaction is becoming more reversible in character.

(iii) C2 at all temperatures except 388 K.

The non-linear plots for C2, C3 and also C4 at 388 K are probably associated with the appearance of C4. As this peak becomes more prominent with increasing sweep rate, the deviation from the initial linear regions for C3 and C2 becomes greater. This behaviour is discussed further in section 5.6.4.

5.4.3 Peak Current as a Function of Sweep Rate

The dependence of peak current on sweep rate was investigated to determine the presence of diffusional processes in the dissolution reaction and in the formation and reduction of the silver oxides. The general characteristic of reactions under diffusion control is a linear relation between the peak current and the square root of the sweep rate.

The $i_p/v^{\frac{1}{2}}$ relations shown in Figure 5.3 exhibit certain features which are common to all peaks:

(i) Linearity. This behaviour is observed for all plots except that for A3 at 295 and 348 K, and at low sweep rates, C4 (388 K). In the case of A3 at 295 K, the plot curves at intermediate sweep rates. At 348 K, a limiting value of i_p for A3 appears to be attained at higher sweep rates whereas linear relations are displayed for A3'.

Figure 5.3 Dependence of i_p on $v^{1/2}$

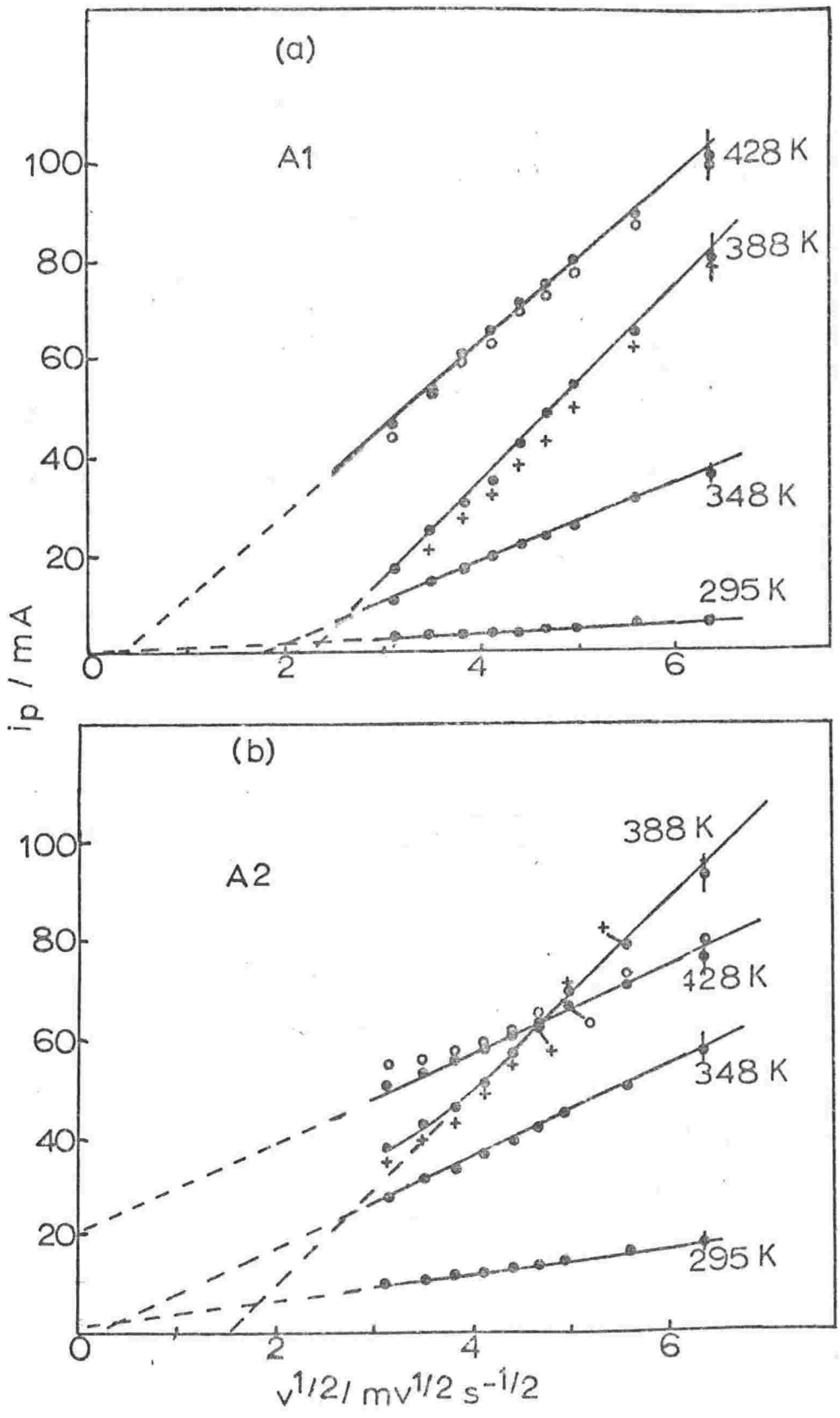

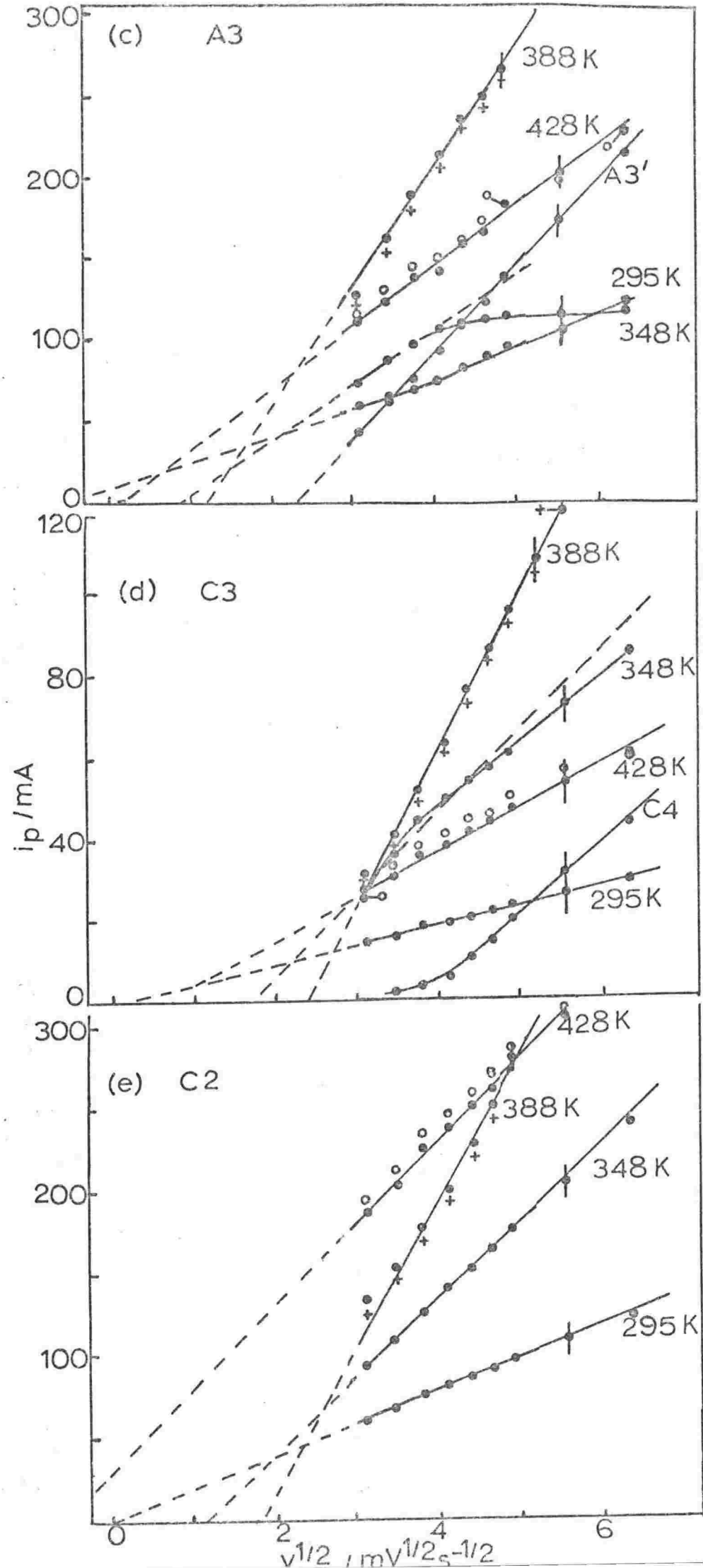
(c) A3
388 K
428 K
A3'
295 K
348 K
(d) C3
388 K
348 K
428 K
C4
295 K
(e) C2
428 K
388 K
348 K
295 K
i_p / mA
$v^{1/2}$ / $mV^{1/2}s^{-1/2}$

(ii) Slope. For each of the main peaks, the slopes of the lines increase up to 388 K and then become less at 428 K. This behaviour was reproducible over separate runs which is illustrated by the data shown for two such runs at both 388 and 428 K, the temperatures between which the reversal of slope occurs. The data at 458 K (not shown for the reason stated in section 5.3.3) appears to follow the trend evident at 428 K. For example, from Figure 5.1, the peak currents at the sweep rate of 16.8 mV s^{-1} ($v^{\frac{1}{2}}$ = 4.1 $mV^{\frac{1}{2}}$ $s^{-\frac{1}{2}}$) are either similar (A1, A2, C3) or are already much less (A3, C2) than those at 428 K.

(iii) Intercepts. At 295 K, all lines except that for A3 which exhibits a small i_p intercept, extrapolate approximately to the origin. At 348 and 388 K, a significant, non-zero $v^{\frac{1}{2}}$ intercept observed at zero i_p, increases with the change in temperature. At 428 K, the lines for A2 and C2 give a non-zero i_p intercept at zero $v^{\frac{1}{2}}$.

The behaviour of the $i_p/v^{\frac{1}{2}}$ relations at 295 K is in agreement with that observed in previous work (182) at room temperature for the same range of sweep rates.

5.5 CHARGE RATIO

5.5.1 Introduction

An examination of the charge transferred at the electrode can provide evidence of dissolution processes at the surface of the metal and/or oxide film during the potential sweep.

The change in anodic charge, ΔQ_A, over a particular potential range consists of two components, ΔQ_D and ΔQ_F, associated with dissolution and film formation processes, respectively.

$$\Delta Q_A = \Delta Q_D + \Delta Q_F \qquad (5.17)$$

At sufficiently low sweep rates, dissolution causes ΔQ_A to be generally greater than the change in cathodic charge, ΔQ_C, for the same

potential range.

$$\frac{\Delta Q_A}{\Delta Q_C} \approx 1 + \frac{\Delta Q_D}{\Delta Q_F} \qquad (5.18)$$

At high sweep rates, the dissolving species may diffuse into the solution at an inadequate rate, and ΔQ_C tends to become equal to ΔQ_A.

5.5.2 Data at 295 K

In this work, the charge ratio*, Q_A/Q_C , was determined over a cycle in which the anodic sweep was reversed at the end of A3. Over the range of sweep rates used, the anodic charge passed was found to be approximately equal to the total cathodic charge. This behaviour implies that virtually all the charge transferred in the anodic sweep is recovered on the reverse sweep which is consistent with previous work (182) for sweeps up to potentials beyond the A2 region.

5.5.3 Effect of Temperature

The charge ratio was found to vary only slightly with temperature over the range 295-388 K; the charge involved in the dissolution of silver remaining small relative to the total charge passed in the anodic sweep.

At 428 K, Q_A/Q_C increased to $1.14 \pm .06$ over the range of sweep rates studied. This value is relatively high in view of the fact that the charge components, Q_A and Q_C, were obtained over a cycle as described above. The charge transferred on the anodic sweep is clearly greater than that recovered on the cathodic sweep indicating significant dissolution of the metal and/or oxide film.

---

* From equation 4.3 , ΔQ_A may be expressed by

$$\Delta Q_A = \int_{E_1}^{E_2} i dE/(dE/dt)$$

If $Q(E_1) = 0$, $\Delta Q_A = Q(E_2) = Q_A$.

Although the results at 458 and 478 K were not sufficiently reproducible to justify inclusion, values of the charge ratio may be estimated at these temperatures. At 458 K, Q_A/Q_C is similar to that at 428 K. However, a substantial increase in Q_A/Q_C is evident at 478 K such that Q_A is approximately twice Q_C. This change is to be expected from the form of the cyclic voltammogram at this temperature; charge transfer clearly continues to take place in the A3 region but evidently is recovered to a negligible extent on the cathodic sweep.

The increased values of the charge ratio for the higher temperatures might be expected from the substantial increases, with temperature, in the solubilities of Ag and Ag_2O calculated from thermodynamic data (see section 2.5.4). The temperature dependence of the solubility of Ag_2O in a 1 mol kg^{-1} hydroxide solution* is shown in Figure 5.4. The solubility increases by a factor of ten over the range 295-428 K, and in fact, continues to show a significant increase up to 478 K.

Although the dissolution of silver is a function of potential, the thermodynamic calculations (chapter 2) show its solubility increases considerably with temperature.

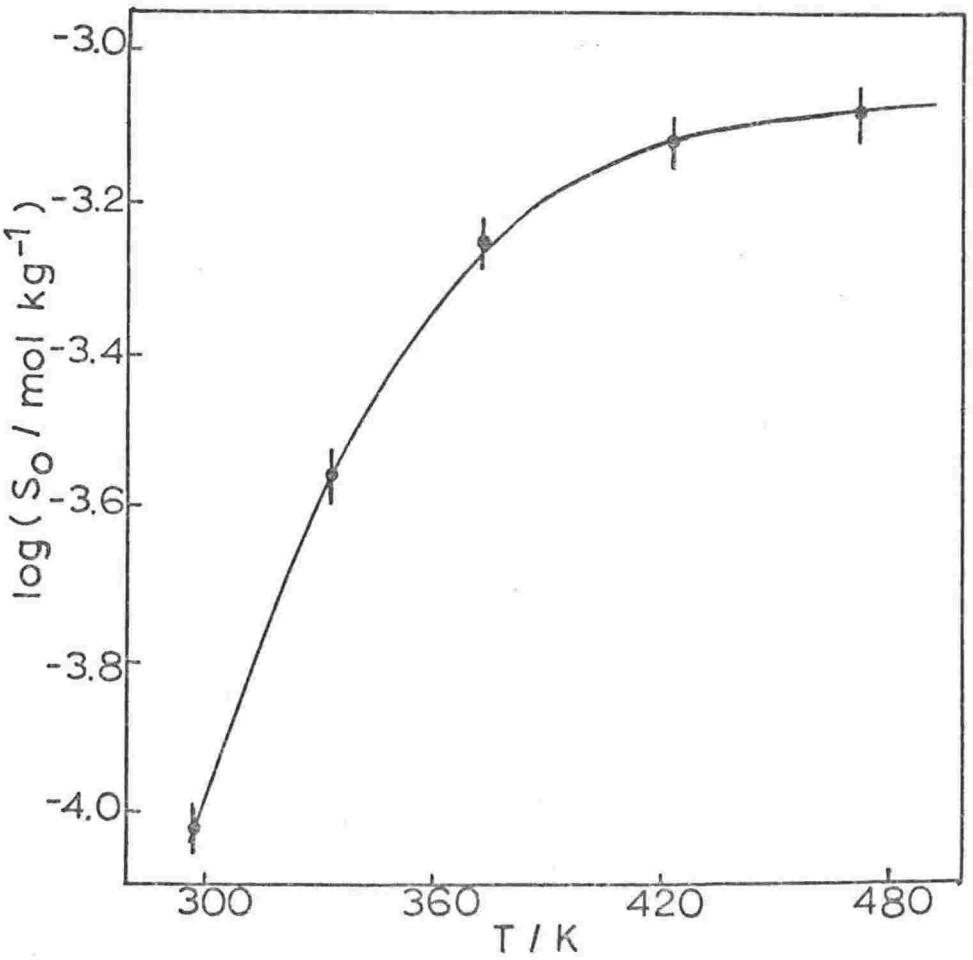

Figure 5.4 Solubility of Ag_2O over the temperature range 298-473 K.

* The solubility data refer to the pH appropriate to each temperature.

5.6 DISCUSSION

5.6.1 Peak A1

General Behaviour over the range 295-428 K:

In the A1 region, dissolution of silver occurs directly from the metal surface as AgO^-. The lack of dependence of peak potential on sweep rate indicates that this reaction is reversible; the formation of AgO^- occurs at a sufficient rate to maintain the equilibrium concentration of the soluble species at the electrode surface. The linear dependence of i_p on $v^{\frac{1}{2}}$, in agreement with previous work at room temperature (182), shows that the limiting step in the dissolution process is diffusion of AgO^- into the bulk solution.

It is not possible to determine either the concentration of soluble species at the electrode surface or even the term $(c_m)_o D^{\frac{1}{2}}$ using equation 5.4

$$i_p = 0.446\ nF\left(\frac{nF}{RT}\ VD^{\frac{1}{2}}\right)\ (c_m)_o\ \exp\ \left[\left(\frac{nF}{RT}\right)(E'-E^o)\right]$$

unless perhaps, gross assumptions are made. In the case of silver, inhibition is the result of a dissolution-precipitation process in which the dissolution eventually produces a supersaturated solution of AgO^- causing precipitation of Ag_2O (see section 1.2.1). Furthermore, it has already been assumed (section 5.1.2) that this equation may be applied to a dissolution reaction involving the formation of an oxyanion.

Effect of Temperature:

348 and 388 K. Notwithstanding the above comments regarding equation 5.4, it is possible to interpret qualitatively changes in the slopes of the plots if it is assumed that an applicable $i_p/v^{\frac{1}{2}}$ relation has similar temperature terms. For diffusion-controlled processes generally (53), under potential-sweep conditions, the slopes of the $i_p/v^{\frac{1}{2}}$ plots are proportional to the concentration of the diffusing species, c, and to the square root of its diffusion coefficient. Both c and D (165) increase

with temperature as shown in Figures 5.4* and 5.5**, respectively. It is clear then, that in order to account for the change in slope over the temperature range 295-388 K, the quantity $cD^{\frac{1}{2}}$, and any term analogous to $E'-E^{o}$ in equation 5.4 must show a sufficient increase to compensate for the change in the temperature terms.

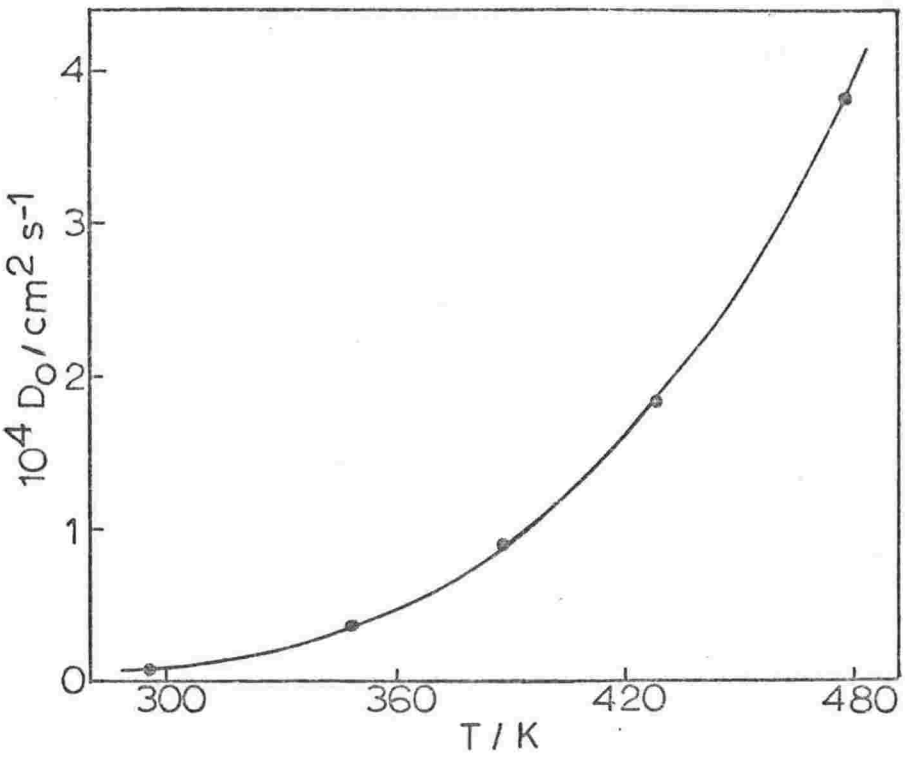

Figure 5.5 Dependence of $D_O(AgO^-)$ on temperature

---

* For the peak current, the concentration of AgO^- is taken as that in equilibrium with Ag_2O. In fact, the actual concentration will be somewhat higher since the Ag_2O precipitates from a supersaturated solution of AgO^-. Nevertheless, the effect of temperature on the AgO^- concentration is still evident from Figure 5.4.

** The data plotted in Figure 5.5 are taken from Table 8.2.

The non-zero $v^{\frac{1}{2}}$ intercept at zero i_p at 348 and 388 K might be interpreted in terms of a minimum sweep rate necessary to achieve the diffusion conditions associated with the $i_p/v^{\frac{1}{2}}$ relations shown in Figure 5.3a. This effect may be explained by a faster rate of redeposition of silver ions at the electrode surface compared with that at 295 K. Experimental evidence obtained by Tilak et al (182) at room temperature indicated that such behaviour was responsible for Q_A/Q_C approaching unity at low sweep rates. Under such circumstances, the tendency for ions to be transferred from the electrode surface into the bulk solution is decreased. Hence, the relative influence of diffusion in limiting the overall rate of the dissolution process is reduced.

At high sweep rates, the higher rate of accumulation overcomes the effect of redeposition, thereby allowing the diffusion-controlled current to become significant.

428 K. The lower slope of the $i_p/v^{\frac{1}{2}}$ plot relative to that at 388 K suggests that some change in the diffusion conditions occurs. At low sweep rates, the increased solubilities of Ag and Ag_2O (see section 5.5.3) give rise to a sufficiently high value of the activity of AgO^- at each potential of the sweep so that redeposition is relatively ineffective. At high sweep rates, the rate of accumulation becomes great enough to increase the precipitation of Ag_2O, so that the more extensive surface blocking which results, suppresses the dissolution process.

5.6.2 Peak A2

General behaviour over the range 295-428 K:

The linear $i_p/v^{\frac{1}{2}}$ plots indicate that the rate-determining step for Ag_2O formation is diffusion. This is consistent with previous room temperature work by Tilak et al (182) who also found that

(i) the charge values for the regions corresponding to solid-phase formation are much greater than the value for a monolayer.

(ii) solution-stirring effects on the A2, and A3, peaks are absent.

These workers concluded that the linear $i_p/v^{\frac{1}{2}}$ plots for the formation of the Ag_2O multilayer correspond to diffusion in the solid state.

It was pointed out in the previous section that for diffusional processes under potential-sweep control

$$i_p \propto cD^{\frac{1}{2}} v^{\frac{1}{2}}$$

For anodic films, the diffusion coefficient of the mobile ionic species (185) has the same temperature dependence as that for soluble ions. Hence, it seems likely that, as for Al, increased values of D and c, in this case the metal/oxide interfacial concentration of diffusing species, contribute to the higher peak currents, at low sweep rates, associated with Ag_2O formation at elevated temperatures. However, the diffusion conditions within the multilayer are complicated by the effect that an increasing solubility of the oxide with temperature, particularly at 428 K, has on the film thickness.

Effect of Temperature:

295 and 348 K. The dependence of E_p on ln v, indicating that Ag_2O formation is irreversible, is probably associated at least in part, with a non-equilibrium distribution of diffusing ions at the metal/oxide interface for each potential of the sweep.

388 K. The transition from irreversible behaviour at 295 and 348 K to reversible behaviour at 388, and 428 K, may be explained by

(i) a higher rate of electrochemical oxidation, that is, an increase in the rate of the Ag^+ formation at the metal/oxide interface which may assist in,

(ii) an enhancement of the rate of nucleation of Ag_2O growth centres* on the primary oxide layer formed by precipitation (see section 1.2.1).

The significant non-zero $v^{\frac{1}{2}}$ intercept for A2 at 388 K, also may be interpreted in terms of a minimum sweep rate necessary to achieve the diffusion conditions associated with the $i_p/v^{\frac{1}{2}}$ plots (Figure 5.3b). At

---

* Ag_2O grows on these centres to produce a multilayer but the rate-determining step for this growth is in the primary layer and not at the expanding interfaces of the centres (79).

low sweep rates the film formed may not be sufficiently thick for diffusion to limit the overall rate. This condition may be the result of

(i) a higher solubility of Ag_2O, coupled with an increased diffusion coefficient of AgO^- formed by dissolution of the film

(ii) higher rates of diffusion of Ag^+ and/or O^{2-} involved in film growth.

428 K. The substantial increase in the solubility of Ag_2O would compete to a very significant extent with a higher rate of film growth which might be expected with the increase in temperature. This solubility effect is probably associated with the i_p intercept at zero $v^{\frac{1}{2}}$ which is indicative of a process taking place independent of a change in potential with time.

5.6.3 Peaks A3 and A3'

A3:

The irreversibility indicated by the $E_p/\ln v$ plots is no doubt associated with the difficulty involved in nucleating Ag_2O_2 growth centres which were indicated from previous work (24) at room temperature to form in the oxidation of Ag_2O (see section 1.2.1). Such nucleation and growth processes complicate the interpretation of the behaviour of A3. Nevertheless, the presence of a non-zero peak current at zero sweep rate (Figure 5.3c) at 295 K may be considered as evidence, in accordance with previous work (182), of the nucleation process taking place independent of potential sweeping.

The interpretation of the behaviour of the $i_p/v^{\frac{1}{2}}$ relations for A3 over a temperature range is complex since changes in both the rates of nucleation and diffusion may contribute to changes in the reaction mechanism at elevated temperatures. Nevertheless, the linear dependence of i_p on $v^{\frac{1}{2}}$ exhibited at 388 K and 428 K implies the presence of a diffusion-controlled step at these temperatures. This behaviour is discussed further in Chapter 9.

Table 5.3 Comparison of E'_{C3} with $E_{Ag_2O_2|Ag_2O}$

Potential/V (SHE,T)

T/K	295	348	388	428	458	478
$E_{Ag_2O_2\|Ag_2O}$	0.73	0.74	0.71	0.70	0.65	0.61
E'_{C3}	0.56	0.48	0.46	0.42	0.28	-

Since $E_{Ag_2O_2|Ag_2O}$ and E'_{C3} satisfy inequality 5.16b over the temperature range studied, the assignment of the overall process 5.19 to C3 at room temperature is also applicable at elevated temperatures.

With the exception of 388 K, the C3 process is reversible at each temperature as indicated by the lack of dependence of E_p on sweep rate. On the basis of the above mechanism, this reversibility is consistent with a fast dissolution step which provides an equilibrium concentration of soluble species at the electrode surface for each potential of the sweep. The presence of reaction 5.19a suggests that the linear $i_p/v^{\frac{1}{2}}$ relations shown in Figure 5.3d may be associated with diffusion of AgO^- away from the oxide layer.

The increasing values of i_p over the temperature range, 295-388 K are presumed to be consistent with increases in both the concentration of AgO^- and the diffusion coefficient of this species.

At 428 K, a greater extent of Ag_2O precipitation caused by an increased rate of accumulation of AgO^- at high sweep rates may, as in the case of Al, be responsible for the reduced slope relative to those at lower temperatures.

While the C3 peak does not exhibit linear $E_p/\ln v$ plots at 388 K, the reaction corresponding to this peak clearly tends towards irreversibility. However, it is at this temperature that C3 is followed by C4.

C4:

To assist an examination of the effect of temperature on the C3 reaction, it is desirable to determine the nature of the process corresponding to C4.

The following information concerning C4 was obtained from this work:

(i) Its position in the potential range is less than 0.32 V (SHE, 388 K).

A3':

At 348 K, A3' appears in a potential region close to that for A3 but the nature of the charge transfer process giving rise to A3' is by no means certain. This peak is unlikely to be associated with the formation of a soluble species since the magnitude of such a peak would cause an appreciable difference between Q_A and Q_C. Such a difference was not observed. Alternatively, A3' might correspond to formation of Ag_2O_3 but this is unlikely at this temperature (see section 5.2.1).

A3' may, in fact, be indicative of an increasing participation by a diffusion-controlled step in the formation of Ag_2O_2, particularly at high sweep rates; whereas the peak current for A3 apparently tends towards a limiting value, the $i_p/v^{\frac{1}{2}}$ relation for A3' remains linear at high sweep rates. Comparison of $E'_{A3'}$ (0.70 V) and $E_{Ag_2O_2|Ag_2O}$ (0.54 V) demonstrates that inequality 5.14 is obeyed which shows that the reaction proposed for A3' is thermodynamically consistent.

5.6.4 Peaks C3 and C4

C3:

The constant current study, at room temperature, by Miller (see section 1.2.1) indicated that reduction of Ag_2O_2 occurs by a dissolution-precipitation mechanism to deposit Ag_2O. Such a mechanism implies that the Ag_2O is formed as follows:

$$Ag_2O_2 + 2e \longrightarrow 2AgO^- \qquad (5.19a)$$

$$2AgO^- + H_2O \rightleftharpoons Ag_2O + 2OH^- \qquad (5.19b)$$

The peak potentials for C3 and the equilibrium potentials for reaction 5.19a* are given in Table 5.3 for the range 295-478 K.

---

* $m(AgO^-)$ is arbitrarily set at 10^{-6} mol kg^{-1}. $E_{Ag_2O_2|Ag_2O}$ given in Table 5.2, may be considered as the value of $E_{Ag_2O_2|AgO^-}$ for reaction 5.19a using the molality of AgO^- which is in equilibrium with Ag_2O.

(ii) An additional anodic peak is not observed.

(iii) The dependence of i_p on $v^{\frac{1}{2}}$ is linear.

(iv) E_{C4} is a function of sweep rate indicating a lack of reversibility.

The lack of an additional anodic peak, and its position anodic to the equilibrium potential for Ag_2O reduction (0.21 V) suggests that C4 is likely to correspond to reduction of Ag_2O_2. Since this peak becomes significant at higher sweep rates, its appearance could be attributed to further, and possibly completion of, Ag_2O_2 reduction. It is assumed that at these rates of potential sweeping, sufficient Ag_2O_2 remains unreduced following C3 to permit additional conversion at a significant rate of reduction. On this basis, the charge transfer process giving rise to the C4 peak is the same as that for C3, namely reaction 5.19a. Clearly, since C4 is cathodic to C3, the peak potential for C4 also will satisfy inequality 5.16b.

5.6.5 Peak C2

The irreversibility indicated by the $E_p/\ln v$ plots is probably associated, at least in part, with the nucleation of two-dimensional centres of silver formed in the reduction process (see section 1.2.1). The $i_p/v^{\frac{1}{2}}$ plots are then probably attributable to diffusion of Ag^+ ions in the film to these growth centres.

The nucleation and growth process described above, as with A3, complicate an explanation of the effect of temperature on the $i_p/v^{\frac{1}{2}}$ dependence. Nevertheless, the slope of the lines follow the trend by the other peaks; the increasing slope up to 388 K is consistent with higher diffusion coefficients while at 428 K, solubility effects again probably influence the conditions for diffusion.

5.6.6 Behaviour at 458 and 478 K

The behaviour exhibited by the cyclic voltammograms at 458 and 478 K show progressive trends. However, the changes at 478 K were more pronounced with the virtual disappearance of the C3 peak and the asymmetric

form of C2. Two factors may contribute to the loss of C3:

(i) A lowered overpotential for oxygen-evolution which occurs possibly at the expense of complete formation of Ag_2O_2.

(ii) A high solubility of the Ag_2O which allows dissolution of the Ag_2O layer that is considered to protect the Ag_2O_2 in solution (section 2.5.4). Removal of this layer would allow decomposition of more Ag_2O_2 so that by the time the potential region for the reduction of Ag_2O is reached on the cathodic sweep, only an insignificant amount of Ag_2O_2 remains. This hypothesis assumes that not all the Ag_2O is oxidised on the anodic sweep.* Hence, the oxide multilayer is considered to have the form $Ag|Ag_2O|Ag_2O_2|Ag_2O$.

A porous silver surface, obtained after potentiostating the electrode to 0.3 V at 478 K, is evident from the electron micrographs shown in Figure 5.6. Comparison of the micrographs for 295 and 478 K illustrates the severe pitting which takes place generally in alkaline solutions at higher temperatures, particularly 478 K. This surface roughening is probably caused by the following:

(i) A greatly increased dissolution of the silver.

(ii) A greater transfer of Ag^+ into the oxide layer formed, due to the high solubility of Ag_2O at this temperature (see section 5.5.3).

Local concentrations of AgO^- formed in the pores would exceed supersaturation of the solution at lower potentials than is possible for sites on the electrode surface exposed to the bulk solution, thereby facilitating precipitation of Ag_2O in the pores. Such a structure would probably produce a highly porous, thin oxide which in some way, may be responsible for the asymmetric form of the C2 peak.

---

* This is a reasonable assumption since it has been found in a potentiostatic study by Fleischmann et al (80), that in the formation of Ag_2O_2 at high overpotentials, only a part of the Ag_2O was oxidised to Ag_2O_2.

Figure 5.6 Electron Micrographs

(a) 0.3 V, 295 K Magnification = 1500

(b) 0.3 V, 478 K Magnification = 1500

(c) 0.3 V, 478 K Magnification = 3000

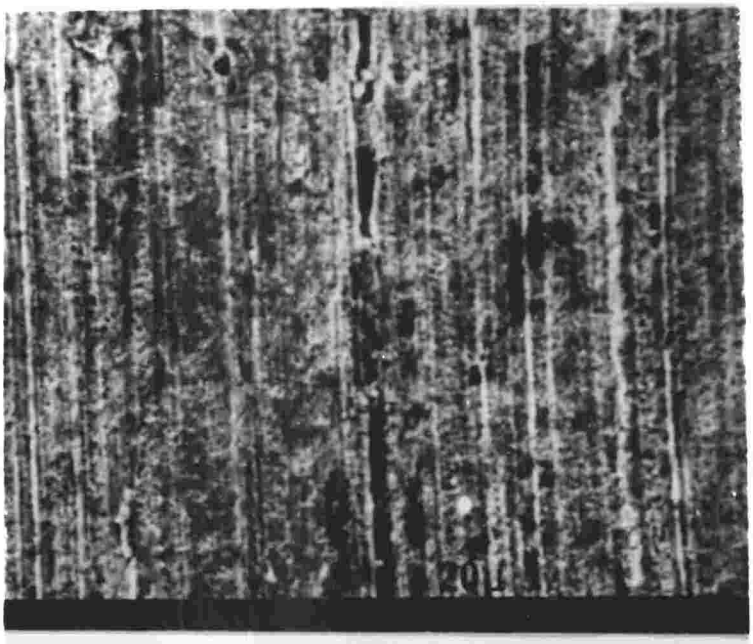

(a)

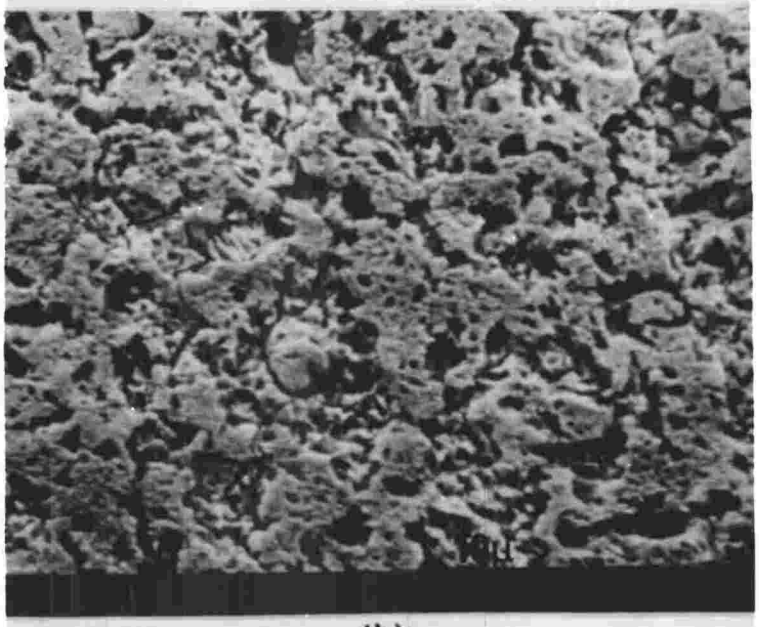

(b)

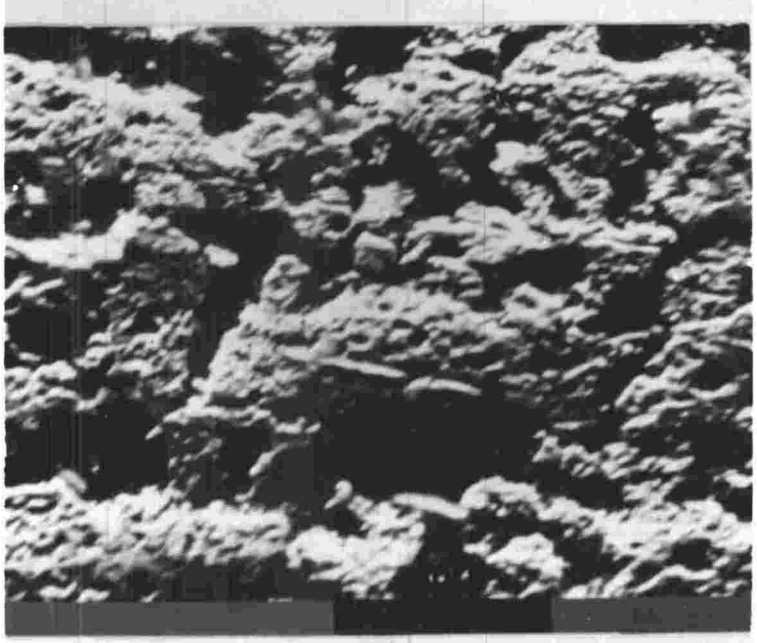

(c)

CHAPTER 6 POTENTIOSTATIC POLARISATION

6.1 THEORY

6.1.1 Introduction

Theoretical treatments of electrode reactions under potentiostatic conditions are simplified as a result of the nature of the perturbation since, at constant potential, the electrochemical rate constant does not change with time. Although the kinetics of various processes under such conditions have been analysed, the following summary includes only the equations derived for those processes which may be examined in the present work.

6.1.2 Metal Dissolution (12,91,131)

In the simplest case of metal dissolution (reaction 5.1),

$$M = M^{n+} + ne$$

it is assumed that the discharge of ions into solution is completely reversible. For a planar electrode surface (see appendix 3), the potential stepped from the equilibrium value produces a current

$$i = nFA_e D^{\frac{1}{2}} c_b [\exp(\frac{\alpha n F \eta}{RT}) - 1]/\pi^{\frac{1}{2}} t^{\frac{1}{2}} \qquad (6.1)$$

where A_e is the electrode area and c_b is the concentration of M^{n+} at t=0. Hence, the current-time transient depends on the size of the potential step, η, and as in the case of other diffusion-controlled reactions, it is predicted that the current varies with the inverse of the square root of time.

6.1.3 Growth of Films

Various models (10,200) have been proposed to describe the growth of films on electrodes but the following is restricted to those involving mass transport. If the rate-limiting step in the oxide growth is transport of ions through the oxide already formed on the electrode, the current

density is given by (46)

$$i = F(\eta)\ t^{-\frac{1}{2}} \tag{6.2}$$

where $F(\eta)$ is some function of the overpotential.

The dominant driving force may be a gradient in

(i) electrostatic potential for which

$$F(\eta) = \left(\frac{\kappa\eta}{2\Omega}\right)^{\frac{1}{2}} \tag{6.3}$$

where κ is the ionic conductivity and Ω is the volume of oxide formed per coulomb of electricity.

(ii) ion concentration in which case

$$F(\eta) = \left(\frac{kT}{e} \cdot \frac{\kappa}{2\Omega}\right)^{\frac{1}{2}} \left[1-\exp-\left(\frac{e\eta}{kT}\right)\right]^{\frac{1}{2}} \tag{6.4}$$

where k and e are the Boltzmann constant and the charge on the electron, respectively.

6.2 CURRENT-TIME TRANSIENTS

6.2.1 Introduction

The potentiostatic experiments were performed with the aim of obtaining a steady-state polarisation curve in order to determine the existence of active-to-passive transitions for silver over a range of temperatures. At the same time, an examination of various current-time transients observed in establishing the steady-state currents, provided kinetic data which can be correlated with the data obtained from the cyclic voltammetry study for the anodic processes.

6.2.2 Shape of the Transients

Current-time transients for silver in 1 mol kg^{-1} KOH over the range 295-478 K are shown in Figure 6.1. With the exception of 478 K, the same two basic shapes which are similar to those found previously (79,80) at room temperature, are observed at each temperature:

Figure 6.1 Current-time transients for Ag oxidation

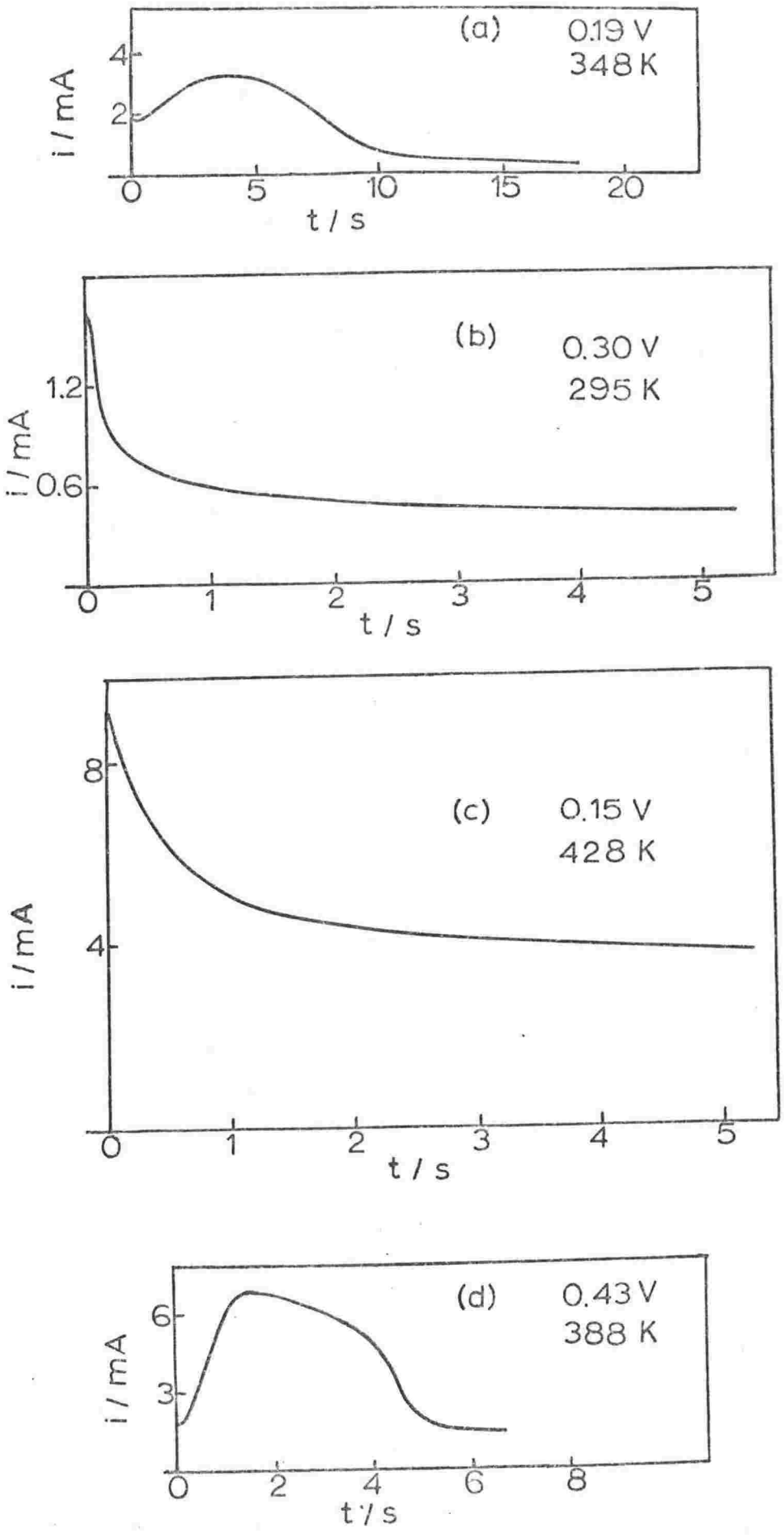

(i) Falling current-time curves as shown in Figures 6.1b and 6.1c are exhibited over the potential regions corresponding to silver dissolution and Ag_2O formation. In each case, an immediate fall in the rate of reaction occurs after the potential is imposed.

In the dissolution region, stepwise increases in the positive potential yield increasing values of the steady-state current.* However, at a particular potential which is dependent on the temperature, the transient initially exhibits a falling current but this is followed by a maximum in the curve (Figure 6.1a) at longer times.

The falling current-time curves observed at potentials corresponding to Ag_2O formation, continue to be exhibited at potentials well above the $Ag_2O_2|Ag_2O$ equilibrium potential at the temperature of interest. Fleischmann et al (79) noted such behaviour at 298 K and found that when silver electrodes were charged to 0.308 V ($Ag_2O|Ag$)**, powder diffraction patterns of the deposit on the electrode exhibited only the lines characteristic of Ag_2O. Hence, the nucleation of Ag_2O_2 must be markedly inhibited.

Comparison of the curves in Figures 6.1b and 6.1c shows that although the characteristic shape is observed for the Ag_2O formation region over the temperature range studied, the magnitude of the current at any instant is considerably higher at elevated temperatures.

(ii) A low initial current, increasing to a maximum and subsequently decaying non-linearly to a final low value (Figure 6.1d) is exhibited for the formation of Ag_2O_2 from Ag_2O at all temperatures except 478 K (see section 6.2.4). The time taken to reach the maximum current decreases with increase of overpotential.

At higher potentials, oxygen is evolved and this additional reaction is reflected in the shape of the transients by an increase in the value of the final current.

6.2.3 Analysis of the Transients

The role of mass transport in the electrode processes was examined in terms of the functional dependence of current on time. If the rate-determining step is mass transport, the current is proportional to $t^{-\frac{1}{2}}$

---

* As stated in section 4.3.3, this is taken as the value of the current after two minutes. Subsequently, the current changes only slowly with time.

**0.308 V ($Ag_2O|Ag$) ≡ 0.650 V (SHE). For the $Ag_2O_2|Ag_2O$ electrode (62), E_{298} = 0.599 V (SHE).

Figure 6.2 Dependence of i on $t^{-1/2}$

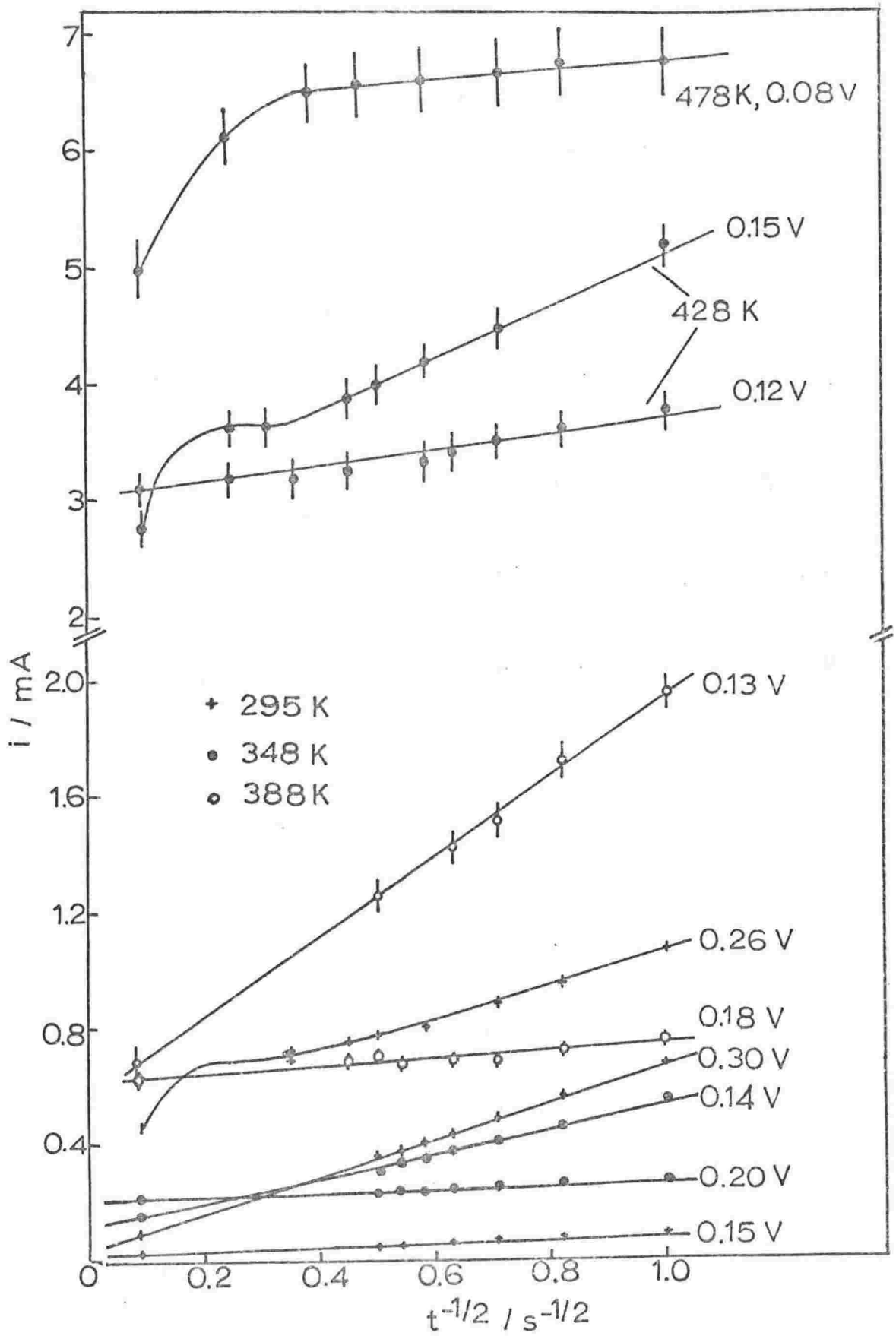

for both dissolution* (equation 6.1) and solid-state processes (equation 6.2).

The $i/t^{-\frac{1}{2}}$ plots, some of which are shown in Figure 6.2, were found to exhibit the following behaviour:

(i) In the dissolution region, i is linearly dependent on $t^{-\frac{1}{2}}$. At sufficiently low potentials, the linear relations extrapolate approximately to the origin but when the potential is raised to a certain value, a peak is observed in the $i/t^{-\frac{1}{2}}$ plot at long times.

(ii) At potentials corresponding to the formation of Ag_2O, the current is proportional to $t^{-\frac{1}{2}}$ at sufficiently long times.

This behaviour is similar to that observed in previous work (79,182) at room temperature.

An analysis of the current/time dependence for Ag_2O_2 formation was not performed in the present study due to the difficulty of determining the kinetics of nucleation in the initial stages. This difficulty arose from:

(i) The procedure by which the polarisation curve was obtained, namely, increasing the potential by increments of 10 or 20 mV.

(ii) The increased rate of reaction at elevated temperatures (see section 6.2.4).

6.2.4 Effect of Temperature on the Transients

Since similar current-time transients are exhibited over the whole temperature range 295-478 K (Figures 6.1b and 6.1c), for the regions of potential in which dissolution and solid-phase formation occur, it may be assumed that the mechanisms of these processes remain unchanged. This assumption is consistent with the observation that the $i/t^{-\frac{1}{2}}$ relations (Figure 6.2) remain linear at elevated temperatures. However, the fall in the rate of Ag_2O formation following a potential step becomes less marked as the temperature is increased which is reflected in the extrapolation of the $i/t^{-\frac{1}{2}}$ relations to yield relatively large currents at long times.

---

* At short enough times that the system is not disturbed by natural convection.

In the case of the transients corresponding to the formation of Ag_2O_2, the time taken to reach the maximum decreases with increasing temperature. Consequently, at elevated temperatures, the current had passed through a maximum and decayed to a low value over the selected two-minute interval. The situation is further complicated at 428 K in that it is difficult to distinguish this peak in the transient due to the additional contribution to the current from the oxygen-evolution reaction. As might be expected from this trend, such a peak is not observed in the current-time curve at 478 K.

6.3 STEADY-STATE POLARISATION CURVES

6.3.1 Shape and Interpretation

Plots of log i_{ss} (steady-state current) against potential for the temperature range 295-478 K are shown in Figure 6.3 and can be accounted for as follows. The initial region of increasing current as the applied potential is made more positive represents the active state of silver in which dissolution takes place to form the AgO^- species. A peak is reached where further increase in the rate of dissolution ceases and the onset of passivation occurs. This point is characterised by two coordinates, the primary passive potential, E_{pp}, and the critical current density, i_c. Moving beyond E_{pp}, the current decreases rapidly due to the formation of a passivating film of Ag_2O on the electrode surface. As the potential is increased further, there is relatively little change in the current until oxygen is evolved at higher potentials which is reflected by the increased value of the overall current.

6.3.2 Effect of Temperature

All the polarisation curves obtained over the temperature range studied, exhibit typical active-to-passive transitions at anodic potentials. However, the effect of temperature was quite evident in these curves:

(i) Over the range 295-388 K, the slope of the curve in the active region does not change appreciably but at 428 K, it appears

Figure 6.3 Steady-state polarisation curves

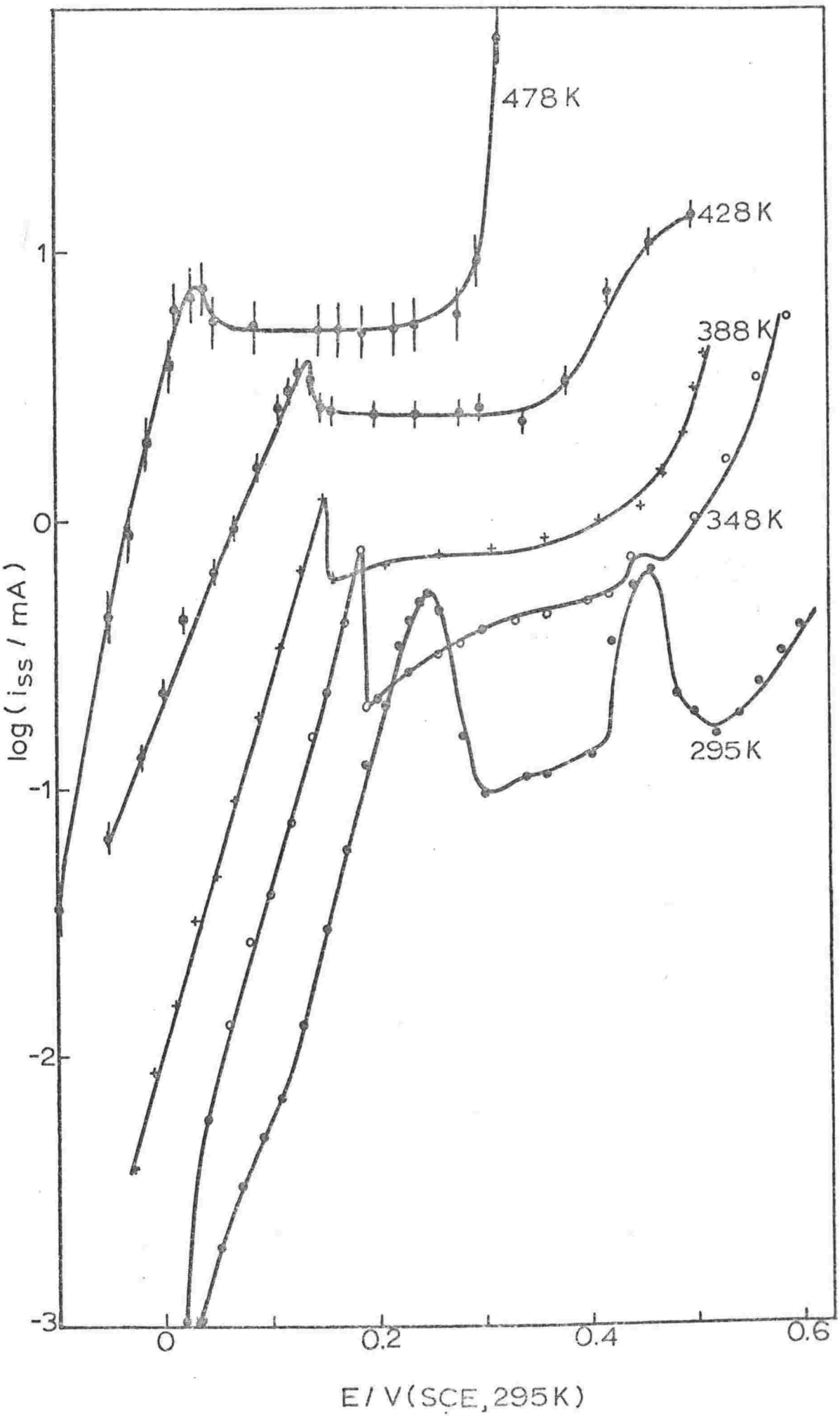

to decrease. Measurements of the current in this region at 478 K were not reliable and made interpretation of the slope uncertain. The surface roughening occurring at this temperature (see section 5.6.6) further complicates a comparison of the slope with those at lower temperatures.

(ii) The magnitude of the decrease from the critical current density to the current density in the passive region is substantially reduced at elevated temperatures, particularly 478 K. Nevertheless, the fact that the ∼-shaped curves are obtained over the temperature range indicates that passivation of the electrode surface continues to be effective but with apparently decreasing success at the higher temperatures.

(iii) The passive potential, E'_{pp}, shifts to less positive values with increasing temperature. Values of the passive potential corrected using equation 3.5 are shown in Table 6.1 from which it is evident that the shift in E'_{pp} from 428 to 478 K is greater than might be expected from the tendency at lower temperatures.

Table 6.1 Values of E'_{pp}

T/K	E'_{pp}/V (SHE,T K)
295	0.50
348	0.37
388	0.28
428	0.23
478	0.10

(iv) The secondary peak disappears at elevated temperatures which may be accounted for by the shorter time taken to achieve the maximum in the current-time curves for Ag_2O_2 formation.

(v) The oxygen-evolution overpotential is lowered, particularly at 428 and 478 K.

6.3.3 Reproducibility

The reproducibility of the measurements depends on several factors (see section 5.3.3) including temperature control and surface preparation. The potentiostatic experiments were performed on the freshly polished

electrode surface, that is, the potential was not cycled until superimposable curves were obtained as in the potential-sweep method. It is likely then, that the potentiostatic measurements would be more sensitive to the initial surface than those from cyclic voltammetry. In general, the pretreatment of the electrode is known (24,79) to have an influence on the anodic products of silver at constant potential (24). For example, the orientation and degree of coverage of Ag_2O growth centres is so dependent, although the current-time transients were shown to be insensitive to these factors (79). However, the method of preparation described in section 3.3.2 was considered sufficient since the relative influence of the pretreatment on the reproducibility is reduced due to roughening of the surface .

Measurements became less reproducible with increasing temperature. However, provided that the time allowed to achieve the steady-state was adequately controlled, the measurements were sufficiently reproducible, 2-5% over the range 295-428 K, to permit an examination of the $i/t^{-\frac{1}{2}}$ relations.

At 478 K, the steady-state currents were not very stable with respect to time and were less reproducible. Although, the reproducibility was sufficient to allow the results at this temperature to be analysed for the presence of diffusional processes, the instability in the steady-state current gave rise to large uncertainties in the low values of i_{ss} at negative potentials (see Figure 6.3).

6.4 DISCUSSION

6.4.1 Active Region

The linear $i/t^{-\frac{1}{2}}$ relations provide evidence that diffusion is the rate-limiting step in the dissolution of silver. Diffusion of the ions from the electrode reduces the initial concentration gradient at the surface and the current decreases, as shown by the shape of the current-time transients at these potentials.

At more positive potentials, initial formation of Ag_2O begins by a dissolution-precipitation mechanism (see section 1.2.1) which provides a sink for AgO^- ions. The peak observed at long times in the transients

corresponds to extensive blocking of the surface caused by substantial precipitation of Ag_2O.

From equation 6.1, it will be seen that the slopes of $i/t^{-\frac{1}{2}}$ plots are proportional to the concentration of the diffusing species* c_o, and to the square root of the diffusion coefficient. It is not possible to evaluate c_o or $c_o D^{\frac{1}{2}}$ over the temperature range studied, since α, the charge-transfer coefficient for the dissolution reaction, is usually a function of temperature (40). However, both c_o and D are temperature dependent (see section 5.6.1) and must increase sufficiently to compensate for the change in the temperature term if the slope is to increase with temperature for a particular potential. Since an interpretation of such behaviour is likely to be complicated by the effect of temperature on the precipitation of Ag_2O, it is useful to consider first, changes in the polarisation curves at elevated temperatures.

The decreased slope of the polarisation curve at 428 K relative to that at the lower temperatures might be explained as follows. As the potential is increased anodically, the AgO^- accumulates so that the precipitation of Ag_2O causes a greater extent of surface blocking. This increased surface blocking is opposed by the high solubility of the oxide which therefore gives rise to a more gradual approach to the active-to-passive transition than observed at lower temperatures.

Such behaviour should give rise to a situation similar to that at room temperature where precipitation of Ag_2O provides a sink for AgO^-. This hypothesis is supported by the appreciable intercepts which develop on the current axis in the $i/t^{-\frac{1}{2}}$ plots as the temperature is increased. It is assumed that precipitation does not occur at a sufficiently fast rate to provide complete blocking of the surface over the time interval under investigation. Nevertheless, the more extensive precipitation accounts for the lowering in the passive potential at elevated temperatures.

It is desirable to isolate the contribution of dissolution from that of precipitation. This would allow changes in the slope of the $i/t^{-\frac{1}{2}}$ plots with temperature to be related to changes in c_o and D. It is proposed that a hypothetical line in these plots taken from currents measured at short times, to the origin, corresponds approximately to unblocked dissolution. It is evident in Figure 6.4 that the slopes of such lines increase with temperature which is consistent with higher

---

* $c_o = c_b \exp\left(\frac{\alpha n F \eta}{RT}\right)$.

values of the concentration and the diffusion coefficient.

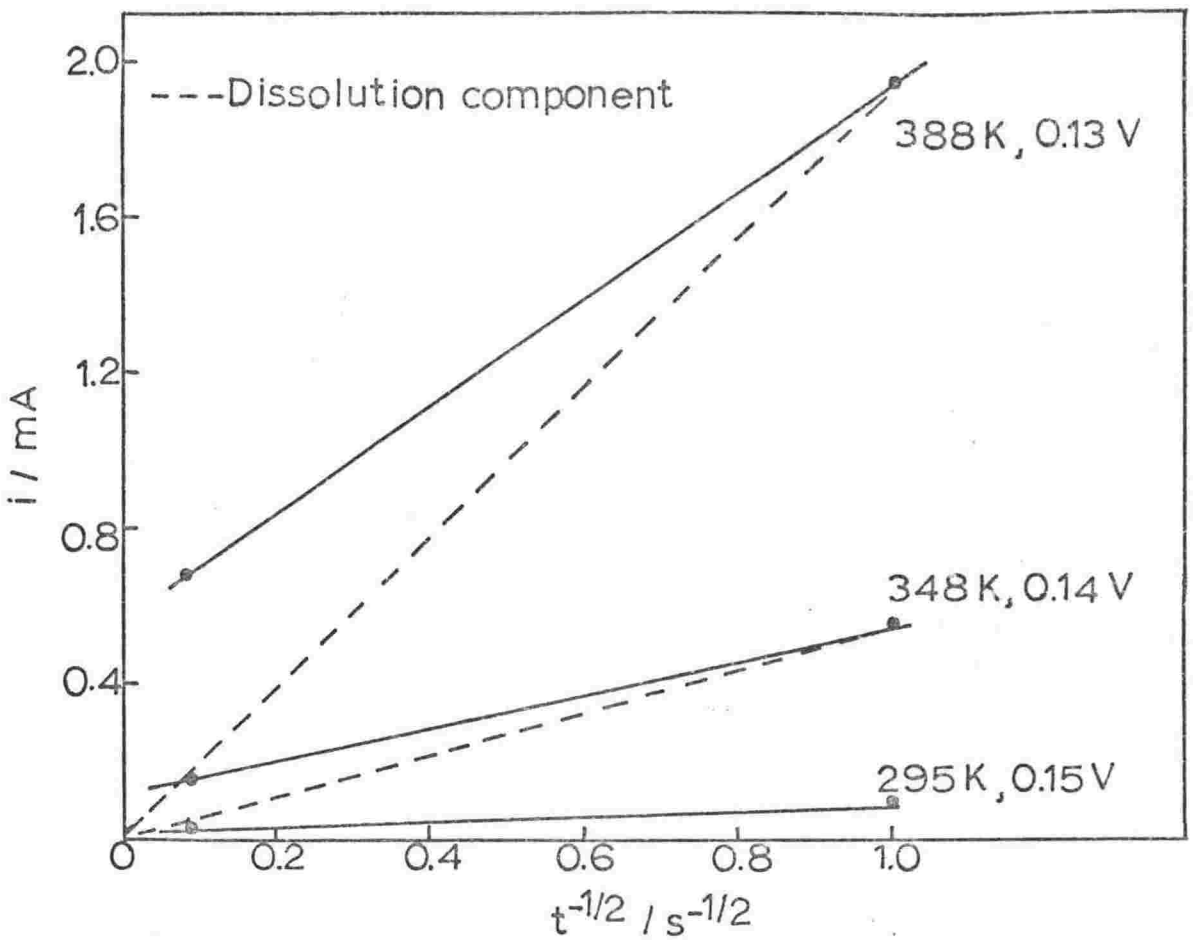

Figure 6.4 Separation of dissolution from precipitation contribution to the $i/t^{-1/2}$ dependence

6.4.2 Passive Region

The linear $i/t^{-\frac{1}{2}}$ dependence is consistent with mass transport as the rate-determining step which is in agreement with the results of Fleischmann et al (79). These workers concluded that diffusion through the solution is not relevant since the slope of such plots at room temperature were at least two orders of magnitude higher than would arise from the solubility of Ag_2O. This conclusion is supported by

the absence of solution-stirring effects in this region as noted by Tilak et al (see section 5.6.2), thereby indicating that the above dependence is associated with film thickening by transport of ions through the oxide.

The oxide film formed at constant potential becomes less protective with increasing temperature as shown by the temperature dependence of the passive current in Figure 6.3. It is apparent, particularly at 428 and 478 K, that the currents in the passive region approach the magnitude of the peak dissolution current. In this region of potential, the increased solubility of the Ag_2O multilayer (see section 5.5.3) would give rise to a large dissolution component in the overall current. The decreasing effectiveness of the oxide layer as a passivating agent, presumably due to the increase in the solubility of Ag_2O, is evident from the $i/t^{-\frac{1}{2}}$ plots themselves by the magnitude of the intercepts on the current axis at higher temperatures.

6.4.3 $Ag_2O|Ag_2O_2$ Phase Change

The effect of temperature on the current-time transients for the formation of Ag_2O_2 is analogous to the effect of overpotential. In both cases, the time taken to reach the maximum current decreases. The rise in temperature presumably facilitates the overall process of nucleation and three-dimensional growth of Ag_2O_2 centres (see section 1.2.1). Consequently, impingement of the growth centres on each other, thereby reducing the area for the interfaces to expand, may occur at shorter times.

CHAPTER 7 GALVANOSTATIC CHARGING

7.1 INTRODUCTION

The galvanostatic charging method involves an analysis of overpotential-time transients as a function of the applied current which may be expressed as

$$i = C_{dl}\left(\frac{d\eta}{dt}\right) + i_F \qquad (7.1)$$

where i_F is the faradaic component of the current and C_{dl} is the double-layer capacitance. However, the analytical solution is normally difficult because rate constants of the form

$$k = k_o \exp(aE) \qquad (7.2)$$

will be time-dependent under galvanostatic conditions. The problem is further complicated by the potential and hence time-dependence of the double layer capacitance. Consequently, the galvanostatic charging technique has not been widely used for the quantitative analysis of the kinetics of surface processes. Nevertheless, as in studies of other metals (133,134), this method enables a qualitative examination of passivation and film growth processes of silver to be made.

7.2 SHAPE OF POTENTIAL-TIME CURVES

7.2.1 General Features

The galvanostatic charging curves for silver in 1 mol kg^{-1} KOH solution over the temperature range 295-478 K are shown in Figure 7.1. These curves were obtained at a current of 9 mA (5.7 mA cm^{-2} apparent surface area) and were found to be superimposable after 3 to 5 cycles at all temperatures except 478 K (see section 7.3.3). The form of the curve at 295 K is typical of those observed in past studies of silver at a similar temperature, with the potentials of the arrest generally in good agreement with previously measured values (103).

Figure 7.1 Galvanostatic charging curves for Ag in 1 mol kg^{-1} KOH

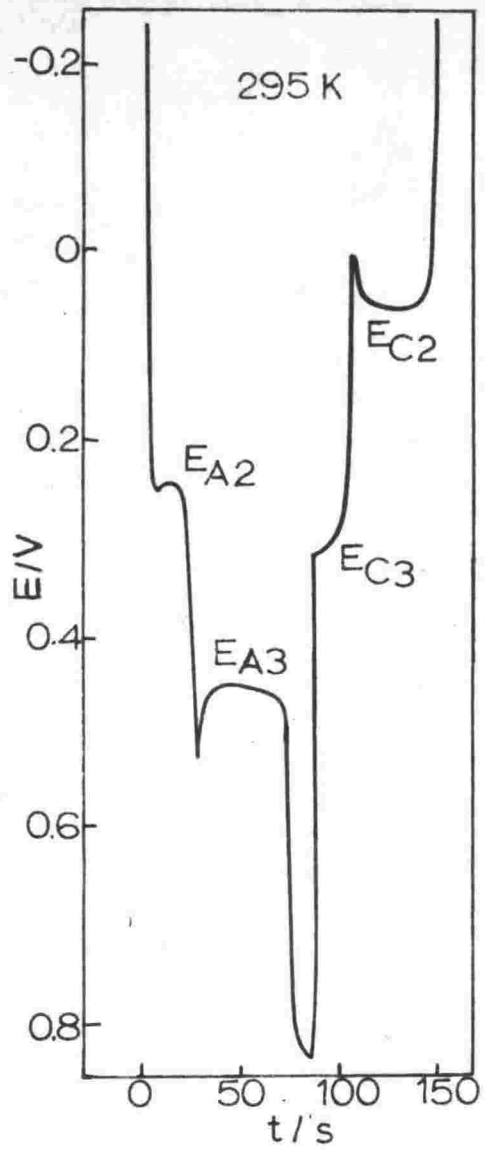

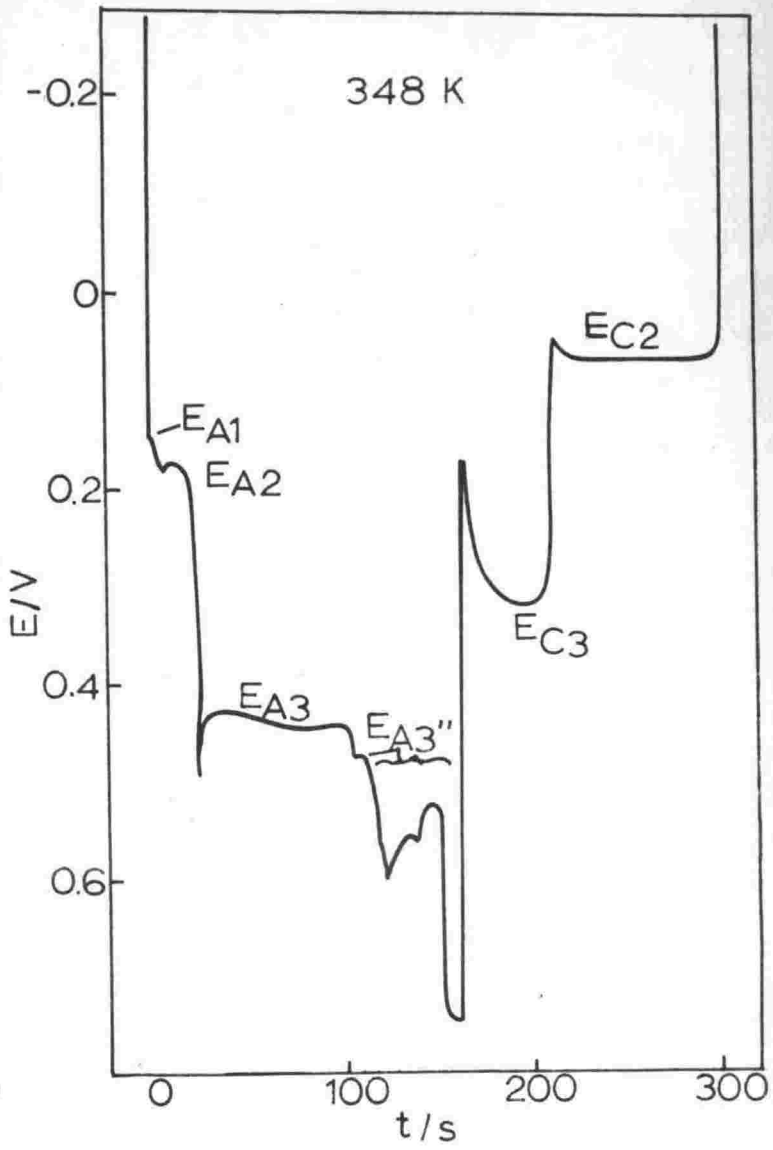

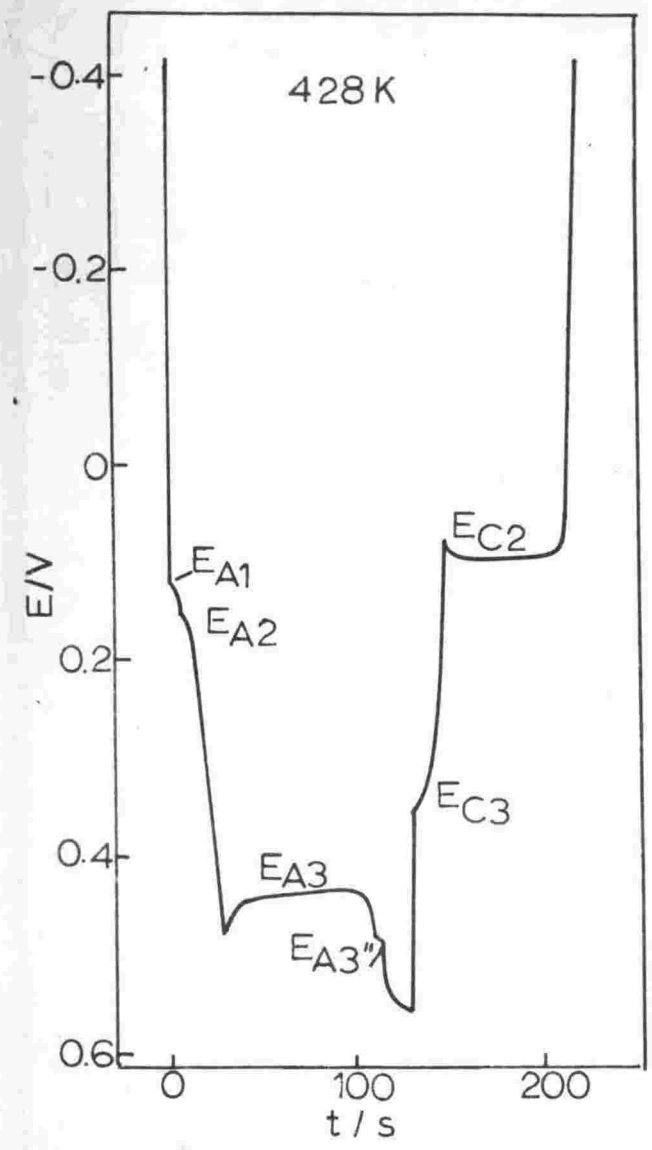

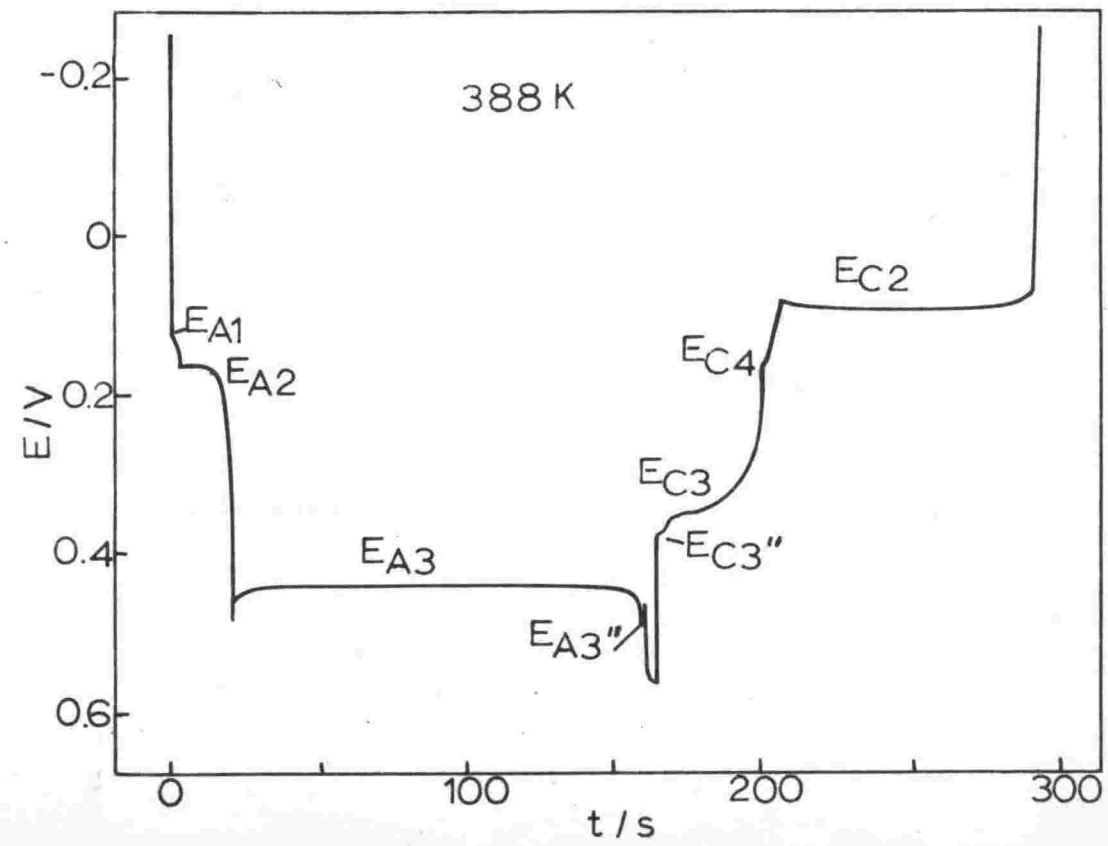

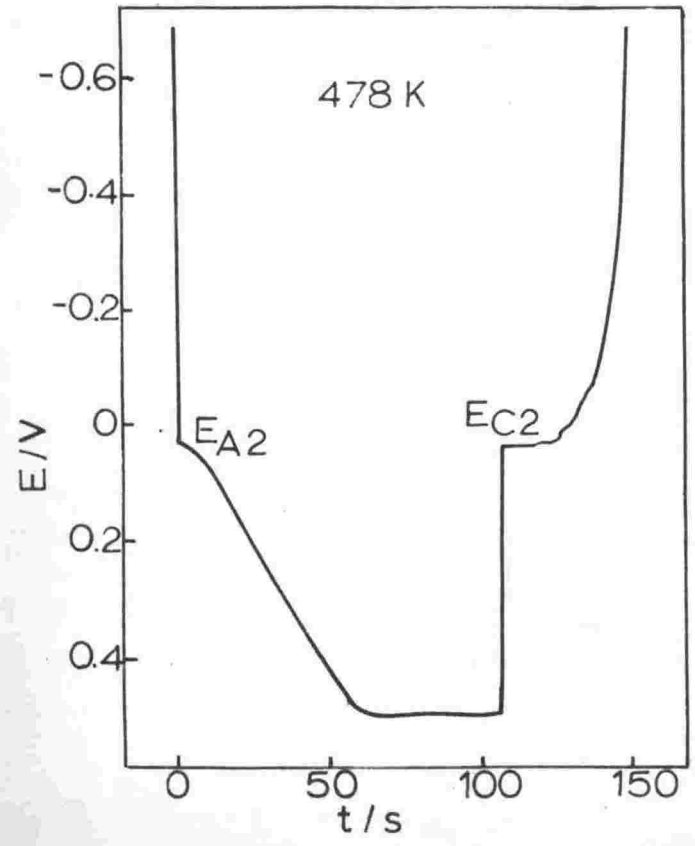

The initial rapid change in potential in the positive direction due principally to charging of the double layer, is followed by two regions of relatively constant potential, E_{A2} and E_{A3} with a rapid transition between them. The duration of the arrest, E_{A3} is very much longer than the initial arrest, E_{A2} and is immediately preceded by a peak (discussed in section 7.3.2). Subsequently, inhibition of the process corresponding to E_{A3} causes the potential to shift to a value at which oxygen evolution will consume charge at the required rate. If the current is then reversed, the potential moves rapidly to the first of two arrests on the cathodic sweep, E_{C3} followed by a shift to the second, longer arrest E_{C2} which occurs at a practically steady potential and, similarly to E_{A3} is accompanied by a small initial peak (discussed in section 7.3.2). Termination of the reaction associated with E_{C2} causes a rapid change in potential to the hydrogen evolution region.

The characteristics of the potential variation with time were found to be dependent on current density over the range 2.6-15.9 mA cm^{-2}:

(i) The time interval of the arrests decrease with increasing current density. In particular, E_{A2} is reduced from a distinct arrest at low current densities to an inflexion in the potential/time curve at high current densities.

(ii) The potentials of the anodic and cathodic arrests move to more positive and negative values, respectively, with increasing current density.

7.2.2 Effect of Temperature

Changes in the potential/time curves with increasing temperature are notable by their appearance over the range 295-388 K and subsequent disappearance at higher temperatures so that the shape of the curves becomes simplified. The following are the changes observed at elevated temperatures:

348 K: (i) A distinct inflexion designated E_{A1} appears prior to E_{A2} and probably represents an enhancement of an initial process which can proceed for a longer time at the higher temperature before inhibition takes place. In addition, the potential minimum at E_{A2}

evident at 295 K is not so apparent at elevated temperatures.

(ii) A series of arrests appear after E_{A3}. These consist of one main arrest and several secondary ones.

(iii) E_{C3} is preceded by a large peak whereas the peak accompanying E_{C2} is reduced.

388 K: (i) The region following the initial arrest*, E_{A3} is reduced to a small peak.

(ii) The peak preceding E_{C3} disappears but a brief arrest now occurs in this region of potential.

(iii) An inflexion, E_{C4} appears after E_{C3}. This feature is, in fact, present at 348 K but only for low current densities.

428 K: Although no further arrests appear, the effect of temperature is apparent:

(i) The potential-time curve exhibits a relatively slow rate of shift of potential between E_{A2} and E_{A3} compared with the lower temperatures.

(ii) The brief arrest and inflexion before and after E_{C3}, respectively, which appeared at 388 K on the cathodic sweep, now disappear.

478 K: As was the case in the previous techniques, appreciable changes in the polarisation behaviour of silver occur at this temperature.

(i) The most significant feature is the simple form of the potential/time curve. Only one anodic and one

---

* In this chapter, it will be assumed that the initial arrest is E_{A3} at all temperatures. However, as the temperature is increased, one of the arrests in the $E_{A3''}$ group at 348 K may develop to become the main arrest at 388 and 428 K. A similar possibility was suggested for the peaks, A3 and A3', in the cyclic voltammograms (section 5.2.3) and this will be discussed further in section 9.2.4. However, the situation regarding E_{A3} and $E_{A3''}$ will not affect the comments made in this chapter.

cathodic arrest can be distinguished and the potentials of these arrests are approximately the same.

(ii) Particularly emphasised at this temperature is the slow rate of change, noted at 428 K, following the initial arrest.

(iii) The potential adjusts to a final steady-state region which appears to correspond to oxygen evolution since on reversal of the current, the potential moves directly to an arrest in the region associated with E_{C2}.

(iv) Cycling of the current caused larger shifts in the arrest potentials than at lower temperatures. The potential arrests continued to shift after five cycles - the maximum number required to achieve superimposable arrests with respect to potential, at lower temperatures. However, this effect, as at lower temperatures, was less marked compared with the cyclic voltammetry.

7.3 ARREST POTENTIALS

7.3.1 Introduction

As discussed in section 5.3.1, the potential at which a transition is observed experimentally will contain not only an activation overpotential contribution but very likely also significant contributions due to, for example, mass transport, film resistance. Nevertheless, the possibility of a reaction may be demonstrated with respect to inequalities 5.14 and 5.16:

$$E'_A > E_T > E'_C$$

$$E'_{diss} > E_{T,diss} \qquad \text{anodic}$$

$$E'_{diss} < E_{T,diss} \qquad \text{cathodic}$$

where E'_A and E'_C are the corrected potentials* for conjugate oxidation/reduction arrests, respectively, E_T is the equilibrium potential for the corresponding reaction, and E'_{diss} is the corrected arrest potential for a dissolution process with equilibrium potential $E_{T,diss}$. By this means, the charge transfer processes occurring at the predetermined rate (current) can, in many cases, be identified.

7.3.2 Assignment of Arrests

Previous workers (24,25,59) have established the electrode processes in relation to the galvanostatic oxidation and reduction curves at room temperature. The two arrests, E_{A2} and E_{C2}, are attributed to the formation and reduction of Ag_2O, respectively. It is generally accepted that the second arrest following termination of Ag_2O formation corresponds to conversion of the Ag_2O to Ag_2O_2, and that reduction of the Ag_2O_2 occurs at the arrest E_{C3}. The presence of Ag_2O and Ag_2O_2 at E_{A2} and E_{A3} respectively, has been confirmed by X-ray diffraction measurements (24).

The potential peak preceding E_{A3} indicates commencement of Ag_2O_2 formation which takes place by an electrocrystallisation process (see section 1.2.1). The appearance of this peak is consistent with the relatively large nucleation overpotential exhibited in potentiostatic polarisation studies for the formation of Ag_2O_2. Similarly, the peak prior to E_{C2} is probably associated with the nucleation of Ag centres (section 1.2.1).

---

* The observed arrest potentials E(arrest) are corrected using equation 3.5 in the form

$$E'(\text{arrest}) = E(\text{arrest}) - E_{\Delta T} - E_{LJ} + 0.246 \text{ V}.$$

7.3.3 Effect of Temperature

In Table 7.1, the corrected potentials of each main arrest in the potential/time curves shown in Figure 7.1 (current density = 5.7 mA cm^{-2} apparent surface area) are given with corresponding equilibrium potentials for the temperature range studied.

Table 7.1 Comparison of Arrest Potentials with Equilibrium Potentials

	Potential V (SHE,T)				
T/K	295	348	388	428	478
E'_{A1}	-	0.31	0.25	0.19	0.05 ? *
$E_{AgO^-\|Ag}$	0.22	0.07	-0.03	-0.15	-0.28
E'_{A2}	0.51	0.34	0.28	0.20	0.05 ?
$E_{Ag_2O\|Ag}$	0.35	0.27	0.21	0.13	0.02
E'_{C2}	0.30	0.25	0.21	0.15	0.06
E'_{A3}	0.69	0.60	0.55	0.50	-
$E_{Ag_2O_2\|Ag_2O}$	0.61	0.54	0.48	0.42	0.31
E'_{C3}	0.56	0.49	0.48	0.43	-

From the above table, the following changes are evident with increasing temperature:

(i) The arrest potentials move to less positive values. It will be observed in Figure 7.1 that the shift in the arrest for oxygen-evolution decreases the range of potential over which the charging behaviour of the electrode can be studied, particularly at 478 K.

(ii) The potential differences, $(E_{A2}-E_{C2})$ and $(E_{A3}-E_{C3})$, both decrease.

---

* Since separate arrests corresponding to E_{A1} and E_{A2} could not be distinguished, the assignment of the arrest potential is uncertain.

The arrest potentials and equilibrium potentials satisfy inequalities 5.14 and 5.16 within the limits of experimental uncertainty (section 7.3.3) and the precision estimated for the corrections due to the thermal junction potential (section 3.5.2). This consistency shows that the reactions proposed to account for the galvanostatic behaviour at room temperature are also applicable at elevated temperatures.

The potentials at which arrests occur in the galvanostatic curves generally lie in similar regions to the potentials at which peaks occur in the cyclic voltammograms. The responses of the arrests and peaks to varying temperature suggest that the two experimental techniques respond to the same electrochemical processes at the metal surface. In particular, it was found in the charging studies at 348 K that the change in the E_{A3} region (see section 7.2.2) is consistent with the change in behaviour exhibited by the cyclic voltammograms in the potential region corresponding to the formation of Ag_2O_2 at this temperature.

7.3.4 Reproducibility and Uncertainties

The uncertainty in the arrest potentials in any particular run was ±5 mV at temperatures up to 428 K. At 478 K, the potential continued to shift to some extent on cycling so that the potential could only be estimated to within ±20 mV. Such shifts were observed in cyclic voltammetry and were thought to be associated with roughening of the electrode surface (section 5.6.6). For this reason, the potential sweep under galvanostatic conditions was also cycled only twice at this temperature.

As in the previous techniques, the measurements were less reproducible at higher temperatures. Over the range 295-388 K, the potential was reproducible to within ±10 mV which increased to ±15 and ±25 mV at 428 and 478 K, respectively. However, the lack of reproducibility of the arrest potentials at 478 K after two cycles was noticeably less than that for the cyclic voltammetry study (see section 5.3.3).

7.4 CHARGE CONSIDERATIONS

At all temperatures, it was observed that the charge consumed during the arrests increased on cycling which is in accordance with the behaviour of the peaks in cyclic voltammetry.

The total charge consumed on anodic polarisation during the transition from E_{A1} to the termination of E_{A3} relative to that involved in reduction is similar at 295 and 348 K but increases substantially at higher temperatures particularly at 478 K (see Figure 7.2). These changes are generally consistent with the cyclic voltammetry measurements. The difference in charge is attributed to greater dissolution of both the metal and the oxide film at higher temperatures (see section 5.5.1); the dissolved species diffuse away from the electrode surface and are therefore largely unavailable for reduction.

It is noticeable that the time of the arrest, E_{A1} and therefore the charge passed, is greater at elevated temperatures. This is in contrast to the situation at 295 K when it was not possible to distinguish this arrest, implying that relatively little charge was transferred during the reaction at this temperature. However, in a room temperature study, Dignam et al (59) were able to show that for particular pretreated electrodes, the current efficiency for the formation of Ag_2O films at low current densities is less than 100% which was attributed to the simultaneous dissolution of silver.

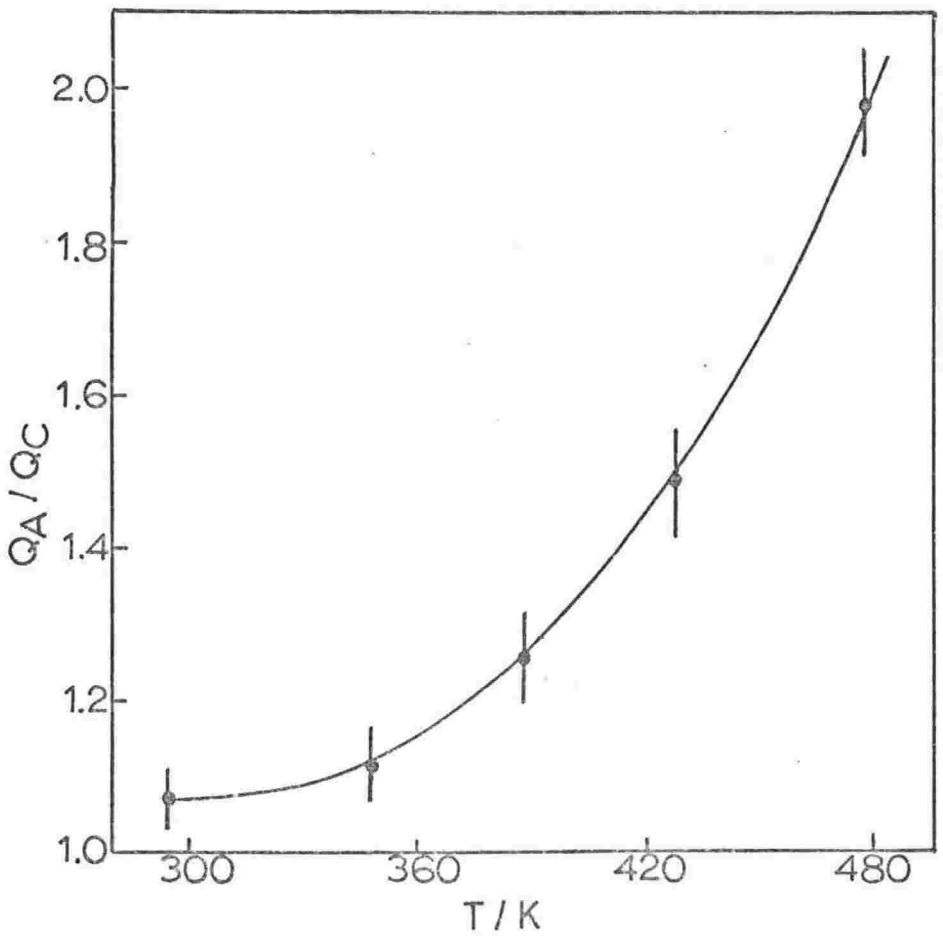

Figure 7.2 Dependence of Q_A / Q_C on temperature

7.5 DISCUSSION

7.5.1 General Behaviour at Elevated Temperatures

The dissolution of silver is shown to become appreciable by the distinct arrest for this process which appears at elevated temperatures. It is evident that this process can take place for a longer time at higher temperatures before inhibition due to precipitation of Ag_2O occurs. The lack of hindrance in the early stages of silver dissolution is no doubt a result of an increased rate of diffusion of AgO^- and the higher solubility of Ag_2O. The charge difference between anodic and cathodic charging confirms the formation of a soluble species during oxidation. On inhibition, the potential shifts to more positive values due to the increasing current density as the surface area for dissolution decreases.

7.5.2 Specific Behaviour at Elevated Temperatures

348 K: The series of arrests in the E_{A3} region is the most significant change at this temperature. By comparison with the charging curves at 295 K, the initial plateau is assumed to correspond to formation of Ag_2O_2 by an electrocrystallisation process (see section 7.3.2). The remaining arrests are probably associated with the conversion to (secondary) Ag_2O_2 also, but possibly under different kinetic control which is effective at a different overpotential.

Although it is unlikely that the large peak prior to E_{C3} corresponds to a large nucleation overpotential because

(i) Ag_2O_2 is considered to be a mixed oxide $Ag(I)Ag(III)O_2$ and hence already contains Ag(I) centres,

(ii) at elevated temperatures, the nucleation overpotentials for the formation of Ag_2O_2 and the reduction of Ag_2O_2 are both lowered,

this possibility should not be entirely discounted. Indeed, this peak may correspond to reduction of the secondary Ag_2O_2 which might have different resistive characteristics so that when it is reduced, the primary Ag_2O_2 layer then becomes available for reduction at the higher potential. Tilak *et al* (182) showed that a similar situation exists for the more

ohmically-resistive Ag_2O formed in potentiodynamic experiments at room temperature. Impedance measurements obtained in this region by these workers indicated a "more nearly stoichiometric, less conducting, surface region in the Ag_2O film which, when reduced, reveals a material of different capacitative and ohmic properties."

388 K: The charging curve is consistent with the cyclic voltammograms at this temperature in that the double peak observed in the latter at 348 K has now disappeared. The small peak, $E_{A3"}$, remaining at the end of E_{A3} is unlikely to represent conversion of Ag_2O_2 to Ag_2O_3 since this process is obscured at room temperature by oxygen evolution and only becomes resolvable at low temperatures. Presumably $E_{A3"}$ represents some additional formation of the Ag_2O_2 and the brief arrest, $E_{C3"}$, might then be attributed to the corresponding reduction reaction.

The arrest, E_{C4} following E_{C3} probably corresponds to the small peak observed between C3 and C2 in the cyclic voltammograms, and similarly is associated with the reductive dissolution of Ag_2O_2, not yet reduced at E_{C3} ,to AgO^- (section 5.6.4).

428 K: Although the arrest, $E_{C3"}$, is not evident at 428 K, its disappearance may be explained possibly by the

(i) smaller amount of charge passed during oxidation at $E_{A3"}$,

(ii) increased solubility of the oxides which allows the removal of the additional layer before reduction can occur to any extent.

The high solubility of the oxides probably accounts for the more gradual transition from Ag_2O formation to Ag_2O_2 formation since an increased rate of dissolution would cause the limiting film thickness to be achieved more slowly and hence, the potential adjusts itself accordingly to the lower rate of inhibition.

478 K: The simple form of the potential/time curve at this temperature is probably associated with two factors:

(i) The rate of film thickening is reduced to such an extent that the current can be maintained by Ag_2O formation and dissolution over a now decreased potential range following the initial arrest. The decreased range is the result of

(ii) the lowered overpotential for oxygen evolution, thereby preventing the formation of Ag_2O_2. It would be expected that any Ag_2O_2 formed on anodic oxidation would be subsequently reduced causing an inflexion, even if brief, on the cathodic sweep. However, it is clear that no such inflexion occurs.

CHAPTER 8 A.C. IMPEDANCE

8.1 INTRODUCTION

8.1.1 Electrode Impedance

The overall reaction at an electrode is generally composed of a series of partial reactions at least one of which must involve charge transfer across the electrical double layer. Others may include transport of reactants or products by diffusion, and crystallisation at the electrode surface. A chemical reaction, the rate constant of which is, by definition, independent of potential, may also be involved. Any step in the overall reaction may be hindered or impeded, and hence exhibit a slow response to an applied potential. This hindrance gives rise to an overpotential for a particular rate (current), the magnitude and type of which is governed by the slowest partial reaction.

A.C. impedance methods, in many cases, permit the determination of kinetic parameters in electrochemical processes. In order to evaluate these parameters, it is common to examine them in terms of the components of a circuit (94) which is equivalent to the impedance of the electrode/electrolyte system obtained experimentally. Hence,a model of an equivalent-circuit type must be advanced.

8.1.2 Equivalent Circuits

The overall electrode impedance (94,188) is commonly represented by an equivalent circuit of the form shown in Figure 8.1.

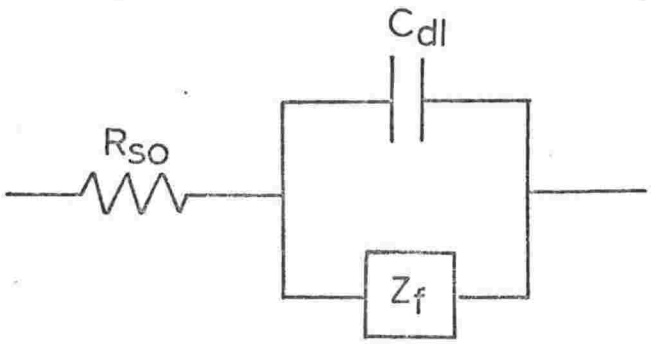

Figure 8.1 Generalized Equivalent Circuit for Electrode Impedance

The impedance of the basic equivalent circuit consists of R_{so}, the solution resistance, and C_{dl}, the double layer capacitance, in parallel with the faradaic impedance, Z_f. It is usual to regard the electrolyte resistance as ohmic since the frequency dispersion of this impedance is significant only for frequencies above 1 MHz* - much greater than the frequencies employed in charge transfer studies in aqueous systems. The other component, C_{dl} is associated with the electrical double layer of charge at the electrode/electrolyte interface and appears as a result of a change in the excess charge of the double layer caused by a voltage change.

8.2 AN EQUIVALENT CIRCUIT FOR METAL DISSOLUTION

8.2.1 Introduction

Generally, in an impedance analysis an equivalent circuit which has the same form of impedance locus in the complex plane as that obtained experimentally, is proposed. Known equivalent circuits and the corresponding loci generated in the complex plane, in many cases, by computer simulation (4,6), are derived from the theoretical expression for the impedance of an electrode under particular conditions. Comparison of the experimental locus with the theoretical shape often (8) enables the impedance data to be fitted to the equivalent circuit. However, a subsequent analysis of the frequency-dependent data is required to test whether the proposed equivalent circuit is adequate.

8.2.2 Impedance Components for the Randles Equivalent Circuit

The impedance of an electrode undergoing dissolution is generally considered to be equivalent (for example, 7) to the simple Randles circuit shown in Figure 8.2.

---

* Debye-Falkenhagen Effect (50,76): The increase in conductance of an electrolytic solution produced by alternating currents of sufficiently high frequencies over that observed with low frequencies or with direct current.

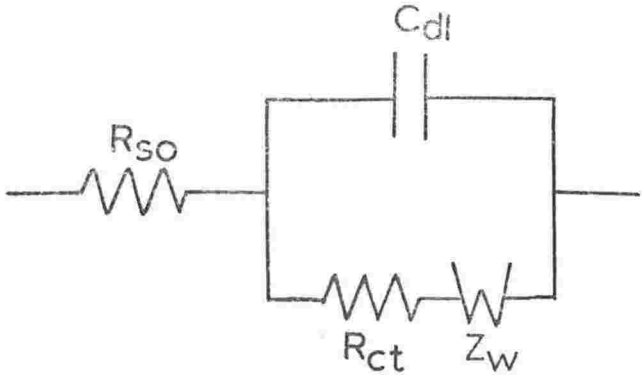

Figure 8.2 Randles Equivalent Circuit

The faradaic impedance for this equivalent circuit is expressed by

$$Z_f = \left(\frac{RT}{nF}\right)\left[\frac{1}{i_o} + \frac{1}{nF(2\omega)^{\frac{1}{2}}}\left[\frac{1}{c_o D_o^{\frac{1}{2}}} + \frac{1}{c_R D_R^{\frac{1}{2}}}\right]\right]$$

$$- j\left(\frac{RT}{nF}\right)\left[\frac{1}{nF(2\omega)^{\frac{1}{2}}}\left[\frac{1}{c_o D_o^{\frac{1}{2}}} + \frac{1}{c_R D_R^{\frac{1}{2}}}\right]\right] \qquad (8.1)$$

R_{ct} is the charge transfer resistance representing the hindrance to the passage of charge across the electrode/electrolyte interface and is related to the exchange current density i_o, by

$$R_{ct} = \frac{RT}{nFi_o} \qquad (8.2)$$

Z_W, the Warburg impedance (194), corresponds to pure diffusion control and is frequency-dependent according to equation 8.3.

$$Z_W = \sigma\omega^{-\frac{1}{2}} - j\sigma\omega^{-\frac{1}{2}} \qquad (8.3)$$

If, at the interface, c_o, the concentration of the oxidised species is much greater than c_R, the concentration of the reduced species, then the Warburg coefficient, σ, is given by

$$\sigma = \frac{RT}{n^2F^2(2D)^{\frac{1}{2}}c_o} \qquad (8.4)$$

The impedance locus for this equivalent circuit (116) has the form shown in Figure 8.3 and involves the following combination:

(i) a semi-circle at high frequencies arising from charge transfer. This semi-circle, centred on the real axis, has a radius $R_{ct}/2$ and a high frequency intercept R_{so}.

(ii) a line of slope 45^{o} at low frequencies due to the Warburg impedance.

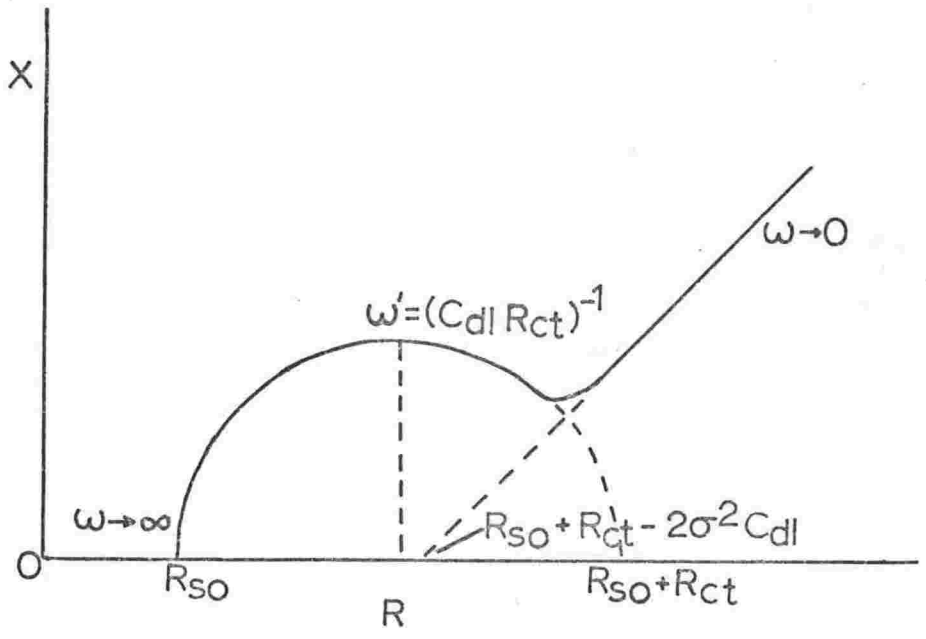

Figure 8.3 Dependence of X on R upon variation of frequency for a quasi-reversible reaction.

8.2.3 Analysis by Admittance Components

The concept of interaction between the faradaic and non-faradaic components of the electrode impedance was developed clearly in work by Llopis et al (125). The determination of the double layer capacity*, C''_{dl}

---

* $C''_{dl} = C_{dl}/A_e$.

by extrapolation to infinite frequency was shown by these workers to be unreliable,* and it was found that the Randles circuit did not adequately represent their data even if all the parameters of the circuit were adjustable. This method, therefore, is not used in the present work.

Since the impedance components of the Randles equivalent circuit for the electrode itself are in parallel, it is more convenient to consider the admittance** and data obtained in this study are treated by the method proposed by Sluyters et al (172,183). Such a technique has the advantage that C''_{dl} may be conveniently obtained as the slope of an appropriate admittance plot (see section 8.3.4). The solution resistance is obtained as the high frequency intercept of the impedance spectrum plotted in the complex plane.† The electrode impedance Z', is determined as

$$Z' = Z - R_{so} = R' - jX' \tag{8.5}$$

The real and imaginary components of the admittance are calculated using the following expressions:

$$A' = R'/(R'^2 + X'^2) \tag{8.6}$$

$$B' = X'/(R'^2 + X'^2) \tag{8.7}$$

and the frequency dependence of the components, A' and B', is then investigated. If the Randles equivalent circuit is adequate to represent the electrode impedance, then the real component, A", is given by (172)

$$A'' = A'/A_e = \frac{\omega^{\frac{1}{2}}}{\sigma}\left[\frac{p+1}{p^2+2p+2}\right] \tag{8.8}$$

where A_e is the area of the electrode and p is the irreversibility coefficient defined by

---

* This method has the disadvantage that the result depends very much on the measurements at high frequencies where the error due to the inaccuracy of R_{so} is large.

** The admittance is defined as $Y = \frac{1}{Z}$.

† Alternatively, R_{so} could be obtained directly from measurements at other potentials where the electrode impedance is purely capacitative.

$$p = R_{ct}/\sigma\omega^{-\frac{1}{2}} \tag{8.9}$$

If $A''/\omega^{\frac{1}{2}}$ is independent of frequency, then it may be assumed that the system behaves reversibly (p=0) with $A''/\omega^{\frac{1}{2}} = 1/2\sigma$.

The imaginary component, B", is given by (172)

$$B'' = B'/A_e = \frac{\omega^{\frac{1}{2}}}{\sigma}\left[\frac{1}{p^2+2p+2}\right] + \omega C_{ap} \tag{8.10}$$

Hence, the apparent double layer capacity can be calculated from

$$C_{ap} = [B'' - A''/(1+p)]/\omega \tag{8.11}$$

If C_{ap} is found to be frequency independent but at some potentials differs from the value of C''_{dl} for the supporting electrolyte, it can be inferred that weak reactant adsorption is present (183). On the other hand, if $A''/\omega^{\frac{1}{2}}$ increases with frequency, then it is probable that strong reactant adsorption is present.

8.3 DETERMINATION OF AN EQUIVALENT CIRCUIT FOR SILVER DISSOLUTION AT 295 K

8.3.1 Comparison with Data

The impedance components, R and X, at a potential of 0.12 V (SCE) are plotted in the complex plane in Figure 8.4a.* At 295 K, this potential lies in the active region of the steady-state polarisation curve (Figure 6.3). At high frequencies, X tends to zero, the limiting value of R being equal to R_{so}. However, no definite semicircle is evident and the low frequency line has a slope of 54^{o}. The lack of a distinct semicircle can be explained if R_{ct} is very small (see Figure 8.3) but

---

* The numbers shown at various points are the corresponding frequencies, f, in Hz.

Figure 8.4 Impedance and admittance data at 0.12 V, 295 K

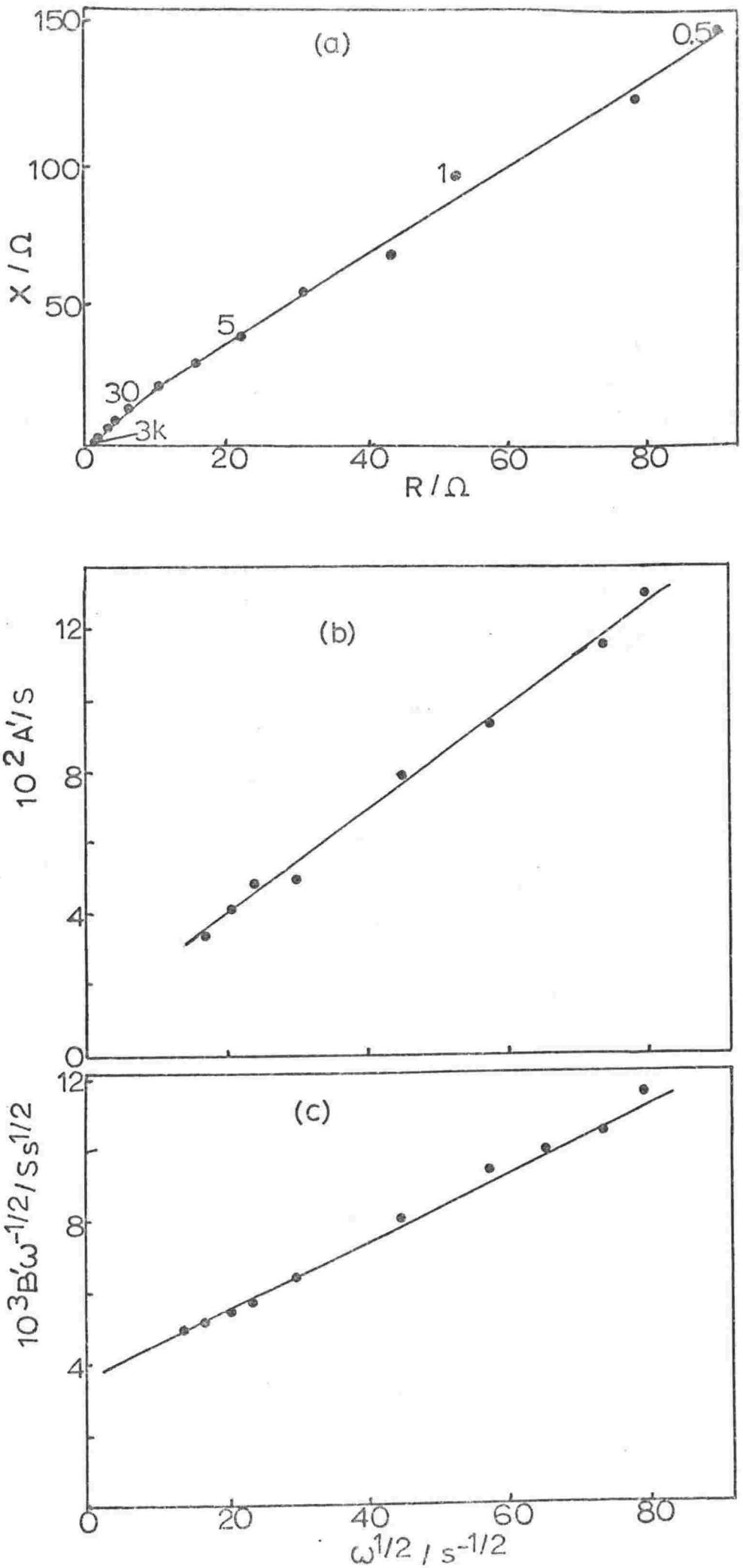

the angle of 54^{o} is clearly much greater than the expected value of 45^{o}.

Following removal of R_{so} from the impedance, the real and imaginary components of the admittance were calculated. If the system is reversible, $A'/\omega^{\frac{1}{2}}$ should be independent of frequency* and equal to $A_e/2\sigma$. It was found that plots of A' vs $\omega^{\frac{1}{2}}$ were linear over the frequency range shown in Figure 8.4a from which it can be inferred that over this range at least, p=0, and the reaction is therefore reversible. However, at high frequencies, the slope of the $A'/\omega^{\frac{1}{2}}$ plot was observed to increase, and furthermore, C_{ap} was found to be frequency dependent. Hence, it must be concluded that the simple Randles circuit does not adequately represent the electrode impedance.

8.3.2 Origin of the Observed Behaviour

The frequency dependence of C_{ap} has been observed by previous workers (88,182) and was attributed to roughness and/or porosity of the electrode surface. Indeed, high real/apparent area factors, r, have been determined (182) from double layer capacitance measurements derived from currents passing in the double layer region in potential sweep studies. For example, in a 1 N KOH solution, r was found to be 26 assuming a true double-layer capacity of 40 $\mu F\ cm^{-2}$ for positive surface charge.

Surface roughness is not the only cause of frequency dependence of electrode impedance. Certain adsorption phenomena (140), even in the absence of reducible and oxidizable species may cause such effects. Whereas weak reactant adsorption does not give rise to a frequency dependent C_{ap}, strong reactant adsorption for which also $A''/\omega^{\frac{1}{2}}$ increases, does give rise to a frequency-dependent C_{ap}.

It is more likely that surface roughness is responsible for the observed behaviour since, in the present work, it is shown that there is

(i) an increase in $A'/\omega^{\frac{1}{2}}$ only at high frequencies

(ii) agreement between the experimental and predicted frequency dependence for the apparent electrode impedance assuming surface roughness.

---

* It was more convenient to use A' rather than $A''(= \frac{A'}{A_e})$.

8.3.3 Impedance due to Surface Roughness

Hence, the apparent impedance due to surface roughness must be taken into account in the parallel equivalent circuit. De Levie (55) has treated the effects of surface roughness on the double layer capacitance using a model of grooves as a representation of a surface which had been mechanically polished and is left with a large number of fine, nearly parallel scratches.

Two simplifying assumptions were made in the theoretical treatment

(i) the grooves have virtually infinite length

(ii) each half-groove may be described as a tapered transmission line, that is, a transmission line with longitudinal and transversal impedance, per unit length, which varies with x.

Using this model, he derived the components of the apparent electrode admittance, and impedance, arising only from the geometry of the surface, that is, in the absence of charge transfer processes.

The frequency dependence of these components is determined by a parameter, z, which is given by

$$z = 2\sqrt{\left(\frac{\omega\kappa\rho b}{\sin\beta \tan\beta}\right)} \qquad (8.12)$$

where ω is the angular frequency, κ is the double-layer capacitance per unit true area and 2β is the groove angle. If the only variable is ω, then for $z >> 2$ (high ω)*, the apparent parallel capacity, C_{ap}, due to surface roughness is found to be proportional to $\omega^{-\frac{1}{2}}$. Experimental evidence (57) confirms the frequency dependence of C_{ap} predicted by de Levie. In the same frequency region, it was also predicted that R_{ap} would vary linearly with $\omega^{-\frac{1}{2}}$ (N.B. Giles et al (88) apparently (incorrectly) quote the dependence as ω^{-2}). However, experimentally R_{ap} is found to be proportional to ω^{-1}. It was proposed (88) that R_{ap} is proportional to ω^{-n} where $1 < n < 2$ and in fact, log log plots of R_p and ω for 1 N and 7 N KOH solutions were found (182) to be linear with n between 0.9 and 1.4 depending on the history of the electrode.

---

* For $z << 2$ (that is, at lower frequencies), C_{ap} tends to a constant value. Hence as apparently considered by other workers (88), although it is not stated, the behaviour of C_{ap} is accounted for by the frequency dependence for $z >> 2$.

8.3.4 Proposed Equivalent Circuit

Giles et al (88) separated out the frequency dependent component of the apparent capacity from C''_{dl}, the true double layer capacity, which is assumed initially to be potential independent at the potentials of dissolution, according to

$$C_{ap} = C''_{dl} + g''\omega^{-\frac{1}{2}} \qquad (8.13)$$

Hence

$$Y_a = \frac{1}{R_{ap}} + j\omega C_{ap}$$

$$= b''\omega^n + jg''\omega^{\frac{1}{2}} \qquad (8.14)$$

where b" and g" are surface roughness coefficients. The capacity components are considered in parallel since the remainder of the equivalent circuit is parallel to C_{ap}.

The treatment proposed by Giles et al is equivalent to the circuit shown in Figure 8.5 and this circuit will be used in the present work to represent the impedance of a silver electrode undergoing dissolution.

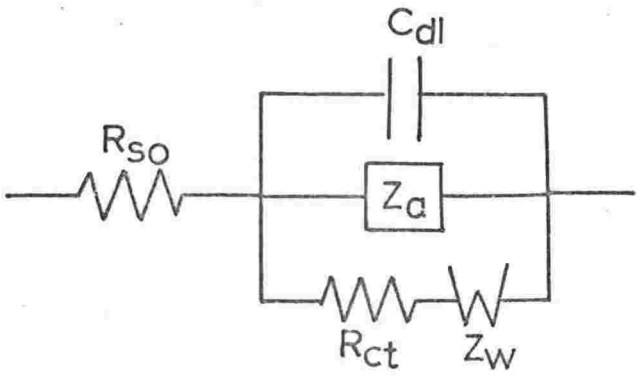

Figure 8.5 Equivalent circuit representing the impedance of the silver electrode in the active region.

Z_a is the apparent impedance due to roughness effects and the admittance components given by equation 8.8 and 8.10 can be conveniently extended to allow for such effects. The overall expression for the

admittance is simplified if R_{et} can be neglected. This approximation is justified by:

(i) An estimate of 0.06 Ω cm^2 for R_{ct} by previous workers (88). This value corresponds to a very high exchange current density (greater than 1 A cm^{-2}) for the dissolution process implying that this reaction is reversible.

(ii) The close agreement of the potential-dependence of c_o $(\frac{2.3RT}{nF})$ with 60 mV which has been demonstrated in previous work (88).

(iii) The constant slope of the $A'/\omega^{\frac{1}{2}}$ plot over the frequency range (see section 8.3.1).

The overall admittance is then given by

$$Y'' = (1+j)\omega^{\frac{1}{2}}/2\sigma + b''\omega^{n} + jg''\omega^{\frac{1}{2}} + j\omega C''_{dl} \qquad (8.15)$$

for which the real and imaginary components of the admittance, A" and B", respectively, are

$$A'' = \omega^{\frac{1}{2}}/2\sigma + b''\omega^{n} \qquad (8.16)$$

$$B'' = \omega^{\frac{1}{2}}/2\sigma + \omega C''_{dl} + g''\omega^{\frac{1}{2}} \qquad (8.17)$$

There are two limiting cases for A"; at high frequencies, the slope will be proportional to ω^{n} and at lower frequencies, to $\omega^{\frac{1}{2}}$. Such a plot of A" against $\omega^{\frac{1}{2}}$ exhibits a linear region at low frequencies with slope $1/2\sigma$. It is evident from equation 8.16 that the effect of surface roughness is to increase the real component of the diffusion admittance at high frequencies causing the deviation from Warburg behaviour.

Division of equation 8.17 by $\omega^{\frac{1}{2}}$ yields

$$\frac{B''}{\omega^{\frac{1}{2}}} = \frac{1}{2\sigma} + g'' + \omega^{\frac{1}{2}} C''_{dl} \qquad (8.18)$$

Hence, a plot of $B''\omega^{-\frac{1}{2}}$ vs $\omega^{\frac{1}{2}}$ will be a line of slope C''_{dl} and intercept $(\frac{1}{2\sigma} + g'')$.

Table 8.1 Data from Impedance and Admittance Plots

	Potential /V	C''_{dl} /μF cm^{-2}	σ_T /Ω $cm^2 s^{-½}$	σ_s /Ω $cm^2 s^{-½}$	c_o /mol dm^{-3}	σ_F /Ω $cm^2 s^{-½}$	X_F	$\frac{\varepsilon k}{2\sigma_T^2}$ /$\Omega^{-1} cm^{-2}$	$\frac{\varepsilon k}{2\sigma_F^2}$ /$\Omega^{-1} cm^{-2}$	$\bar{c}(Ag_2O)$ /mol cm^{-2}	$\bar{c}(Ag_2O_2)$ /mol cm^{-2}
295K	0.12	59.7	479	479	1.4×10^{-4}	a	a	a	a	a	a
	0.15	49.4	752	752	8.9×10^{-5}	a	a	a	a	a	a
	0.18	6.1	3927	b	b	b	b	a	a	a	a
	0.20	3.6	5685	b	b	b	b	a	a	a	a
	0.30	0.4	36791	6037	1.1×10^{-5}	30754	1.6×10^{-5}	a	a	a	a
	0.50	61	722	722	9.2×10^{-5}	a	a	2.2×10^{-4}	a	a	6.9×10^{-10}
348 K	0.13	828	65	65	5.8×10^{-4}	a	a	a	a	a	a
	0.15	876	50	50	7.5×10^{-4}	a	a	a	a	a	a
	0.18	1.5	4030	b	b	b	b	9.0×10^{-5}	b	b	a
	0.20	1.3	3085	b	b	b	b	1.1×10^{-4}	b	b	a
	0.30	0.1	1376	6731	5.4×10^{-6}	7034	6.0×10^{-5}	8.3×10^{-5}	1.3×10^{-4}	1.2×10^{-11}	a
	0.50	c	99	50	7.5×10^{-4}	49	8.5×10^{-3}	4.8×10^{-4}	a	a	8.3×10^{-8}
388 K	0.12	2756	49	49	5.3×10^{-4}	a	a	a	a	a	a
	0.15	c	562	b	b	b	b	5.0×10^{-3}	b	b	a
	0.18	c	3281	b	b	b	b	7.0×10^{-4}	b	b	a
	0.20	c	7806	2316	1.2×10^{-4}	5490	7.4×10^{-5}	5.1×10^{-4}	1.3×10^{-3}	2.8×10^{-12}	a
	0.30	0.05	26378	12186	2.1×10^{-4}	1419	1.1×10^{-4}	2.6×10^{-3}	3.7×10^{-4}	1.4×10^{-12}	a
	0.50	c	462	161	1.9×10^{-4}	301	1.2×10^{-3}	2.2×10^{-3}	a	a	5.5×10^{-10}
428 K	0.12	3121	16	16	1.3×10^{-3}	a	a	a	a	a	a
	0.15	c	429	b	b	b	b	2.1×10^{-3}	6.2×10^{-3}	b	a
	0.18	3.7	788	b	b	b	b	1.3×10^{-3}	1.9×10^{-3}	b	a
	0.20	3.2	1201	b	b	b	b	1.2×10^{-3}	1.7×10^{-3}	b	a
	0.30	2.5	2529	b	b	b	b	2.9×10^{-4}	8.9×10^{-4}	b	a
	0.50	c	846	742	2.6×10^{-5}	103	3.4×10^{-3}	2.0×10^{-2}	a	a	8.3×10^{-12}

Table 8.1 continued.

	Potential /V	C''_{dl} /μF cm^{-2}	σ_T /Ω cm^2 s$^{-½}$	σ_s /Ω cm^2 s$^{-½}$	c_o /mol dm^{-3}	σ_F /Ω cm^2 s$^{-½}$	X_F	$\frac{\varepsilon k}{2\sigma_T^2}$ /Ω^{-1}cm^{-2}	$\frac{\varepsilon k}{2\sigma_F^2}$ /Ω^{-1}cm^{-2}	$\bar{c}(Ag_2O)$ /mol cm^{-2}	$\bar{c}(Ag_2O_2)$ /mol cm^{-2}
478 K	0.12	c	2005	b	b	b	b	1.5×10^{-3}	2.4×10^{-3}	b	a
	0.15	c	3062	b	b	b	b	1.5×10^{-3}	2.5×10^{-3}	b	a
	0.18	0.6	3198	b	b	b	b	1.2×10^{-3}	2.5×10^{-3}	b	a
	0.20	c	1367	c	c	c	c	1.2×10^{-3}	2.0×10^{-3}	b	a
	0.30	c	342	b	b	b	b	7.6×10^{-3}	b	b	a

a = not present, b = data not available, c = uncertain interpretation

8.3.5 Testing of Model

The impedance data at 0.12 V was re-examined in terms of the model represented by the equivalent circuit shown in Figure 8.5. In order to demonstrate that the proposed equivalent circuit is adequate, the frequency dependence of A' and $B'\omega^{-\frac{1}{2}}$ is investigated. If the model holds, A' is still expected to be proportional to $\omega^{-\frac{1}{2}}$ but C_{dl} may now be determined from the slope of a linear $B'\omega^{-\frac{1}{2}}$ vs $\omega^{\frac{1}{2}}$ plot, while the intercept gives the roughness coefficient*, g, after subtraction of $A_e/2\sigma$. Plots of the experimental data (Figures 8.4b and 8.4c) are found to be consistent with the relations predicted on the basis of the proposed equivalent circuit model. Hence, use of the equivalent circuit in Figure 8.5 is justified and the impedance data may be converted into the parameters, σ and C''_{dl}, given in Table 8.1. From the value of σ, c_o, the equilibrium concentration of AgO^-, may be obtained using equation 8.4 with the diffusion coefficient** of AgO^-, $D_o = 8\times10^{-6}$ cm^2 s^{-1} (295 K).

The value of c_o at 0.12 V and 295 K, $1.4\pm0.2\times10^{-4}$ mol dm^{-3}, is in reasonable agreement with other values at room temperature obtained from previous impedance measurements (6.3×10^{-5} mol dm^{-3} (88)†) and from solubility data for Ag_2O††(1.87×10^{-4} mol dm^{-3}, see section 2.5.4). The double-layer capacity at 0.12 V and 295 K, 59±8 μF cm^{-2} is consistent with the value of 27±3 μF cm^{-2} obtained by Giles et al (88) from impedance measurements using electropolished, single-crystal electrodes. The present value is less than those obtained from overpotential-time transients (85±20 μF cm^{-2} (34)) and differential capacitance measurements (70±20 μF cm^{-2} (97)). Since the electrodes used by Giles et al were shown to have very smooth surfaces, the higher values of C''_{dl} in these studies and the present work are probably associated with a greater degree of surface roughness.

It is worth noting that for the equivalent circuit shown in Figure 8.5, that is, in a situation where surface roughening is present,

---

* $g = g''A_e$.

** The diffusion coefficient obtained at 298 K by Miller (141), 8.6×10^{-6} cm^2 s^{-1} was used to determine values of D_o over the temperature range 295-478 K which will be discussed in section 8.7.2.

† Read from c_o/E plots for which the c_o values were calculated using $D_o = 1\times10^{-5}$ cm^2 s^{-1}.

†† The value of c_o may be compared with Ag_2O solubility data since it has been shown (see section 1.2.1) that a monolayer of Ag_2O is formed at .090 V (SCE) and the AgO^- ions should be in equilibrium with Ag_2O at $E_{Ag_2O|Ag}$ (=.098 V).

the phase angle, ϕ, is not 45° as expected for a Warburg impedance. From equations 8.16 and 8.17, at low frequencies where Warburg behaviour is expected

$$\text{Tan } \phi = \frac{B''}{A''} = \frac{\omega^{\frac{1}{2}}(\omega^{\frac{1}{2}}+g'')}{(\omega^{\frac{1}{2}}/2\sigma)} \qquad (8.19)$$

$$= 1 + 2\sigma g'' \qquad (8.20)$$

At 295 K, the roughness coefficient, g", is of the order of 10^3 $\mu F\ cm^{-2}\ s^{-\frac{1}{2}}$, and σ is of the order of 10^2 $\Omega\ cm^2\ s^{-\frac{1}{2}}$. Using these values, the phase angle is found to be typically $50\pm5^{\circ}$ which agrees with the experimental value of ϕ within the uncertainty stated.

8.4 DETERMINATION OF THE EQUIVALENT CIRCUIT FOR FILM FORMATION AT 295 K

8.4.1 Proposed Equivalent Circuit

The frequency dispersion of the impedance of the silver electrode was examined over a range of potentials extending from the region of dissolution through film formation to regions where phase changes in the oxide film occur. Hence, it is only to be expected that modifications to the initial equivalent circuit (Figure 8.5) must be made.

The locus shown in Figure 8.6 for 0.3 V is typical of the changes which take place as the potential is increased anodically from 0.12 V; the locus is observed to bend off at lower frequencies and at 0.2 V particularly, decreases towards low values of X.

This form of locus might be regarded as typical of that derived (4) for an active-to-passive transition in which the model considered involves the progressive inhibition of the dissolution reaction by adsorbed species at the metal surface. This model would be expected to fit those cases of passivation of metals for which the steady-state current/voltage curve is bell-shaped. This is in contrast to the shape of the curve shown in Figure 6.3. Furthermore, the impedance loci for the film formation region of silver exhibit the following features:

Figure 8.6 Impedance and admittance data at 0.30 V, 295 K

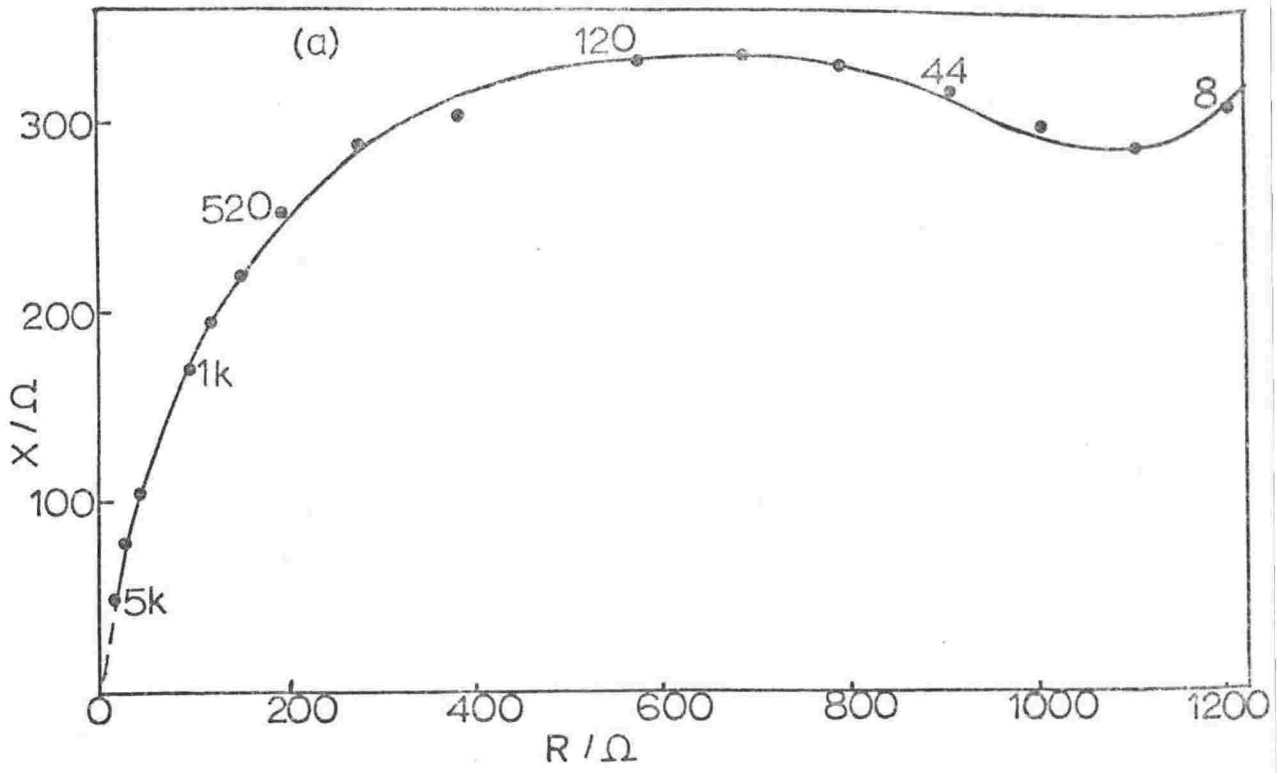

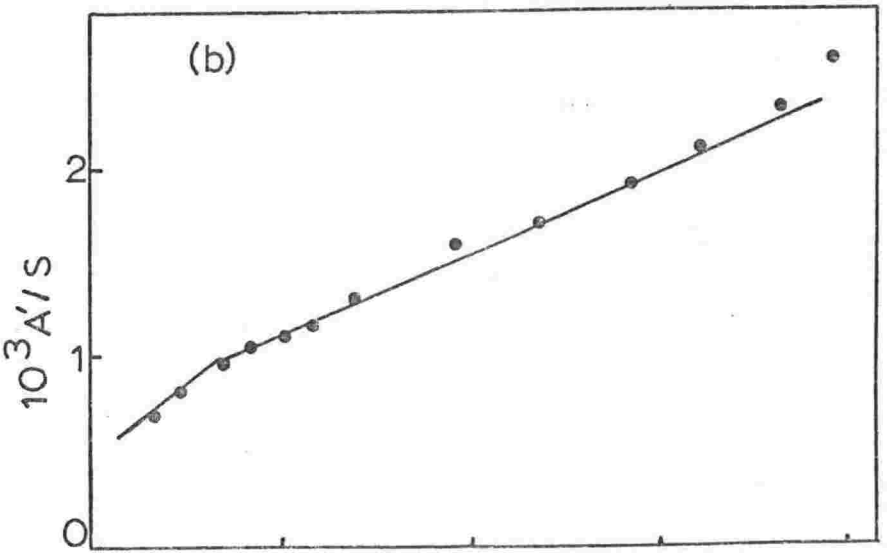

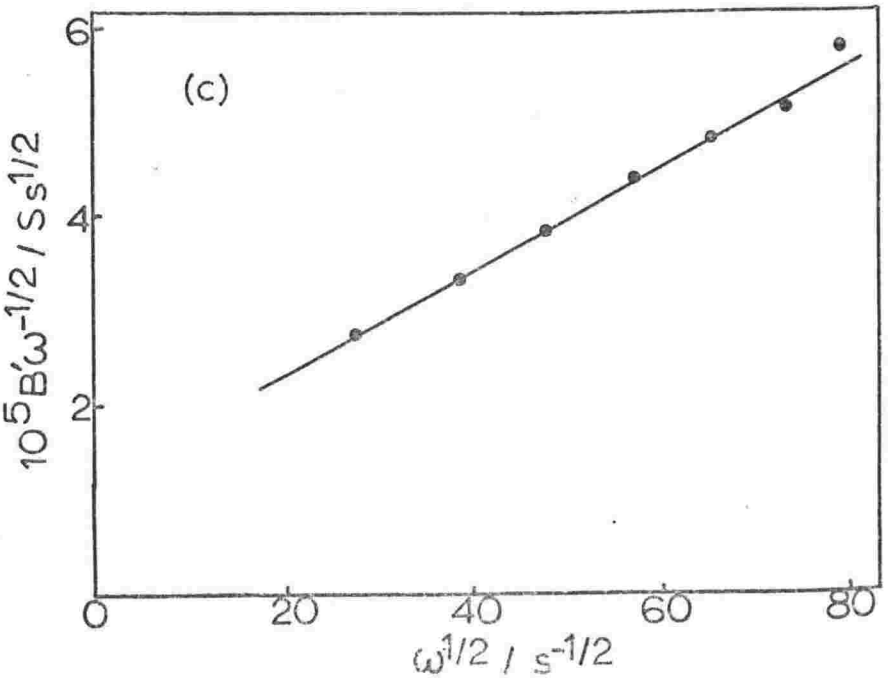

(i) a high frequency Warburg region similar to that at 0.12 V.

(ii) a linear low-frequency region at higher temperatures.

It will be shown that such behaviour may be interpreted in terms of a modified Randles circuit as proposed by Armstrong and Edmondson (7). Essentially, provision is made for the interaction of the a.c. diffusion layer with the Nernstian layer and if necessary, the inclusion of an additional Warburg impedance to account for diffusion of species in the film present on the electrode surface.

The total diffusion impedance (Warburg coefficient, σ_T) is considered to consist of diffusion in solution (Warburg coefficient, σ_s) and diffusion in the film (Warburg coefficient, σ_F) such that

$$\sigma_T = \sigma_s \, f(\omega) + \sigma_F \qquad (8.21)$$

The function, $f(\omega)$, allows for interaction between the a.c. diffusion layer and the Nernst diffusion layer as they become comparable at lower frequencies and consequently cause a deviation from the normal behaviour of the Warburg impedance.

$$f(\omega) = \tanh \left[\delta (j\omega/D_o)^{\frac{1}{2}} \right] \qquad (8.22)$$

where δ is the Nernstian diffusion layer thickness and D_o is the diffusion coefficient of the AgO^- ion. The faradaic impedance is therefore given by

$$Z_f = R_{ct} + (1-j)(\sigma_s/\omega^{\frac{1}{2}}) f(\omega) + (1-j)\sigma_F/\omega^{\frac{1}{2}} \qquad (8.23)$$

Two limiting cases may be considered for equation 8.21

(1) when ω is large, $f(\omega) \rightarrow 1$, and hence $\sigma_T = \sigma_s + \sigma_F$

(2) when ω is small $f(\omega) \rightarrow$ real part only, $\sigma_T = \sigma_F$.

This form of analysis was tested by these workers for the active and passive regions. Using experimentally-obtained values of the components in the Randles equivalent circuit for the Cd/KOH system and the theoretical expressions for σ_T and Z_d*, the impedance spectra in the

---

* Z_d is given by the second term in equation 8.23.

complex plane were generated by computer simulation. Comparison of simulated and experimental spectra showed qualitative agreement, thus justifying the analysis used.

It will be assumed here that R_{ct} is negligible. The exchange current density for the formation of Ag_2O is given as 2.8 mA cm^{-2} (34), so that R_{ct} = 4.6 Ω cm^2. This value of R_{ct} is small compared with the real component of the Warburg impedance over most of the frequency range shown and hence, the assumption is reasonable. The equivalent circuit used in the dissolution region can then be used as a model, with a modified Z_W, for the electrode impedance for film formation at these potentials.

8.4.2 Comparison with Data

If the equivalent circuit proposed by Armstrong and Edmondson is adequate, a subsequent analysis of the frequency dependence of the components of the admittance should demonstrate that two regions of linearity are present. Two such regions are in fact found to be quite distinct in the $A'/\omega^{\frac{1}{2}}$ plot at 295 K and 0.3 V* (Figure 8.6b) and particularly at 348 and 388 K (see Figure 8.9b). From these plots, σ_T was determined from the Warburg slope at high frequencies and σ_F from the Warburg slope at low frequencies. Hence, where possible, σ_s can be obtained using $\sigma_s = \sigma_T - \sigma_F$. Having found σ_s, the equilibrium concentration, c_o, of dissolving silver species may be calculated from equation 8.4 (see Table 8.1).

Assuming that the Warburg coefficient for diffusion in the film is given by an equation of the form (7);

$$\sigma_F = RT/2^{\frac{1}{2}}n^2F^2D_F^{\frac{1}{2}}C_F \qquad (8.24)$$

---

* At 295 K, the duration of the steady-state d.c. current at 0.3 V was limited. Over different runs, the lowest frequency which could be attained was 8 Hz before the d.c. current exhibited severe fluctuations. The most likely explanation for this behaviour which was evident only at the temperature and this potential, is a cracking of the thick oxide multilayer. As a result, the low frequency Warburg region is rather uncertain and hence, this value of σ_F is subject to a large error.

it is possible to obtain a value of $c_F D_F^{\frac{1}{2}}$ relating to the mobile species in the film. The difficulty now is that the diffusion coefficient, D_F, is not known and therefore, c_F cannot be determined by this method alone. However, the steady-state current in the film under potentiostatic control is given by (7),

$$i_{ss} = nF\, D_F\, \Delta c_F / x \qquad (8.25)$$

where x is the film thickness and Δc_F is the difference in concentration of the mobile species between the metal-film interface, c_1, and the film-solution interface, c_2. If it is assumed firstly that silver ions and not oxide ions are the mobile ionic species and secondly, that the following approximation is valid:

$$\Delta c_F = c_1 - c_2 \approx c_1 \qquad (8.26)$$

then the impedance and steady-state terms involving c_F and D_F can be compared. The thickness, x, was estimated from the constant current measurements of Dignam et al (59) for the steady-state current at 0.3 V. The value of x, 3×10^{-5} cm, was consistent with the observations of Briggs et al (24) which indicate "deposits reaching a thickness of several thousand 1000 A." Substitution of x and i_{ss} enabled $D_F c_F$ to be evaluated, and using the value of $c_F D_F^{\frac{1}{2}}$ obtained from the impedance measurements, c_F and D_F could be determined. At 0.3 V, the fraction of sites*, X_F, occupied by mobile species is 1.6×10^{-5} and D_F is 2.3×10^{-12} cm^2 s^{-1}. This value of D_F is reasonably consistent with that (4×10^{-14} cm^2 s^{-1}) obtained from the Nernst-Einstein equation (see appendix 4) for which it was assumed that Ag^+ are the charge carriers. However, it should be noted that Ag_2O is commonly described as an n-type semiconductor (187) and Ag_2O films evidently exhibit such behaviour (59) which is difficult to reconcile with the above consistency.

---

* c_F, and therefore X_F, relate to the mobile Ag^+ ions at the $Ag|Ag_2O$ interface.

Fraction of sites = $c_F \times V_m/2$, where V_m is the molar volume of Ag_2O, 32.7 cm^3 mol^{-1}. V_m = molecular weight/density. It is assumed that

(i) the bulk density of Ag_2O, 7.1 g cm^{-3} (203), may be applied to the oxide film,

(ii) in the estimation of X_F at elevated temperatures, the density of Ag_2O does not change greatly over the range 295-478 K. Since the coefficient of volume expansion $\approx 3 \times$ coefficient of linear expansion ($\sim10^{-4}$ K^{-1}), then for a 200 K interval, the change in density $\approx$ 6%.

In order that the diffusion layer thickness for diffusion in the film should be less than the film thickness, the following inequality must hold (7):

$$(D_F/2\omega)^{\frac{1}{2}} < x \qquad (8.27)$$

The lower frequency limit of the range studied, 0.5 Hz (ω=3.1 s^{-1}) would clearly lie in the low frequency Warburg region, that is, where diffusion in the film is rate controlling. Then for ω=3.1 s^{-1}, the above inequality requires that $D_F < 5.6 \times 10^{-9}$ which is consistent with the value obtained experimentally. This consistency implies that use of the model invoked to represent the diffusional processes in the solution and in the film is justified.

8.5 DETERMINATION OF EQUIVALENT CIRCUIT FOR Ag_2O_2 FORMATION AT 295 K

8.5.1 Proposed Equivalent Circuit

The impedance spectrum in the complex plane at 0.5 V (Figure 8.7a) exhibits a line at low frequencies having a slope very close to 45°. However, while the plot of A' vs $\omega^{\frac{1}{2}}$ (Figure 8.7b) is linear, the corresponding plot of $B'\omega^{-\frac{1}{2}}$ vs $\omega^{\frac{1}{2}}$ (Figure 8.7c) is clearly not so. This potential lies in the region for formation of Ag_2O_2 which has been shown to occur by an electro-crystallisation process (see section 1.2.1). This process must be considered as part of the overall faradaic electrode reaction and therefore corresponds to an additional faradaic impedance in series with the Warburg impedance associated with Ag_2O formation.

A mechanism for the lattice formation of Ag_2O_2 proposed by Fleischmann et al (79), involved slow formation of the lattice by the reaction of Ag^+ ions with adsorbed OH radicals, these radicals being formed from OH^- by an electrochemical reaction;

$$OH^- = OH_{ads} + e \qquad (8.28)$$

$$Ag^+ + OH_{ads} \xrightarrow{\text{slow}} AgO + H^+ \qquad (8.29)$$

On the basis of this mechanism, it may again be assumed that the charge transfer resistance may be neglected, since the charge transfer reaction presumably occurs at a sufficiently fast rate to maintain a

Figure 8.7 Impedance and admittance data at 0.50 V, 295 K

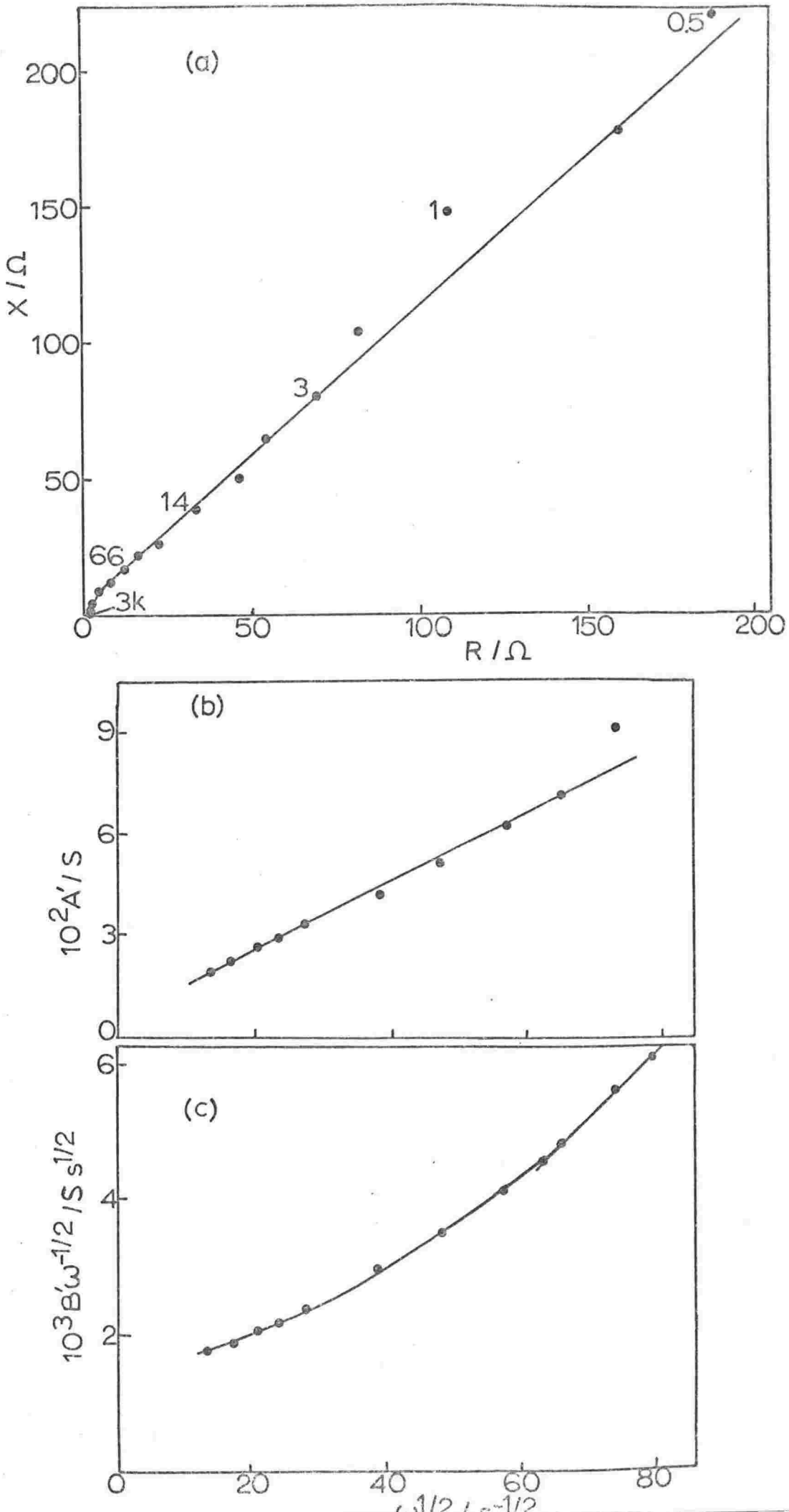

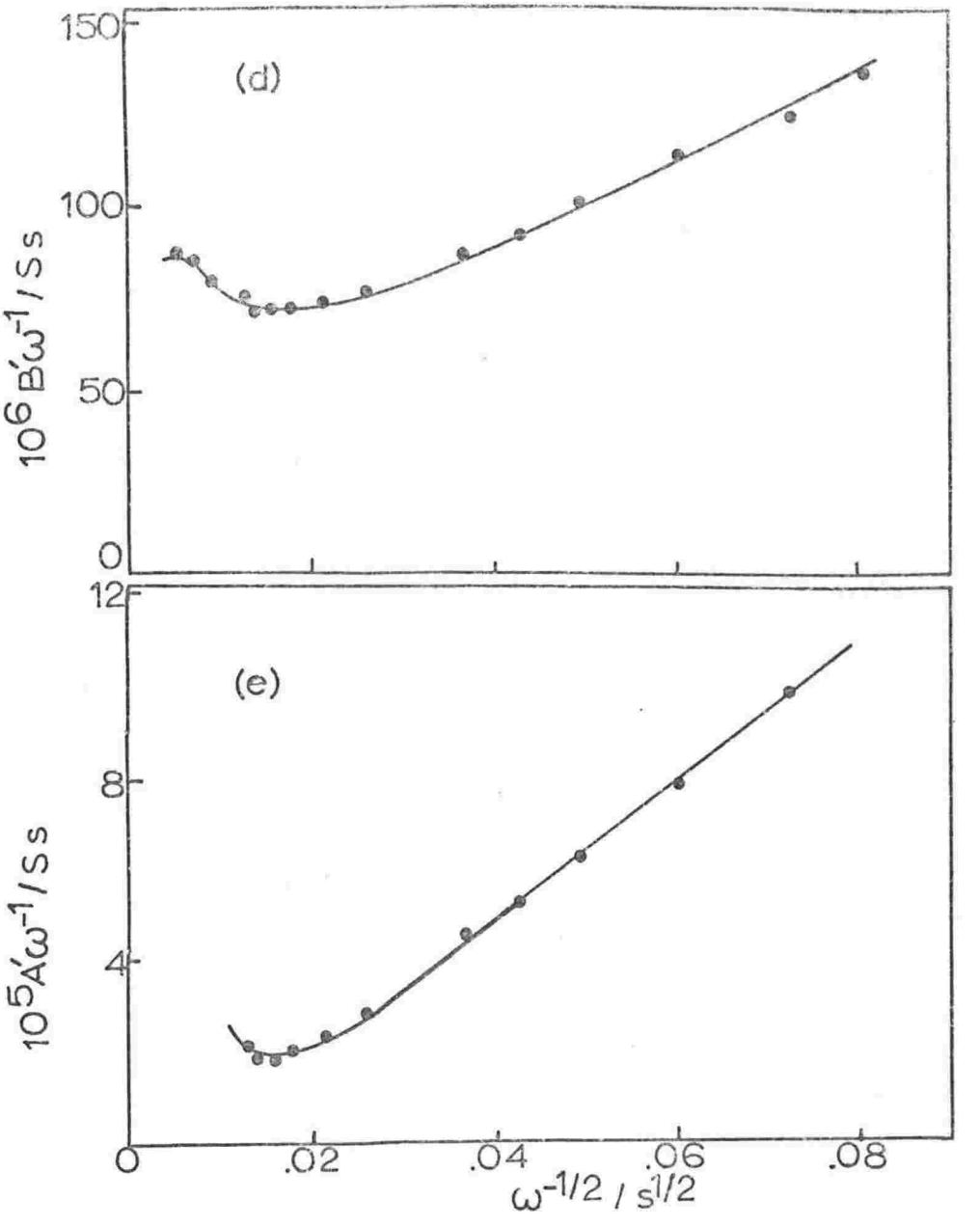
(d)
150
100
50
0
$10^6 B'\omega^{-1}$ / S s
(e)
12
8
4
0
.02
.04
.06
.08
$\omega^{-1/2}$ / $s^{1/2}$
$10^5 A'\omega^{-1}$ / S s

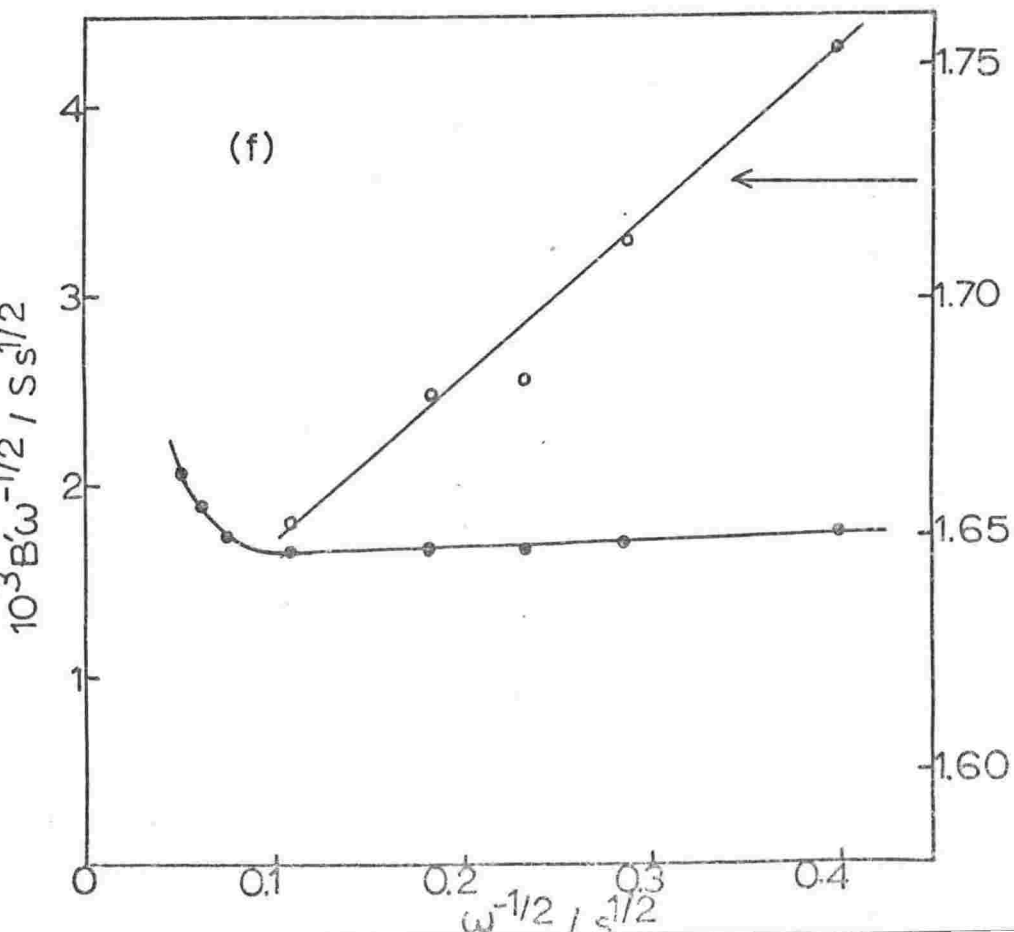
(f)
4
3
2
1
0
0.1
0.2
0.3
0.4
$\omega^{-1/2}$ / $s^{1/2}$
$10^3 B'\omega^{-1/2}$ / S $s^{1/2}$
1.75
1.70
1.65
1.60

pre-equilibrium. From an examination of Tafel plots, Clarke et al (34) had previously estimated i_c for Ag_2O_2 formation as 0.02 mA cm^{-2}. However, steady-state measurements of Tafel lines cannot be applied to this type of electro-crystallisation process and furthermore, it is likely that for a significant potential range of these plots, further formation of Ag_2O is the main faradaic process.

It is proposed therefore, that the following equivalent circuit may be used to represent the electrode impedance for rate control by diffusion and crystallisation:

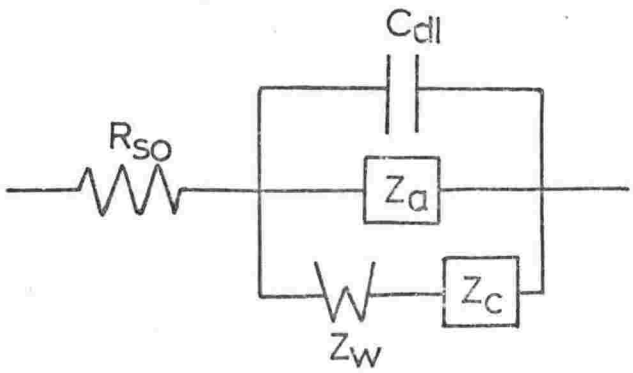

Figure 8.8 Equivalent circuit representing the impedance of the silver electrode during formation of Ag_2O_2.

where Z_c is the electro-crystallisation impedance. The faradaic impedance of the series components, Z_W and Z_c* is given by (84,188)

$$Z_f = Z_W + Z_c$$

---

* The expression for the impedance, Z_c, was considered for the case of crystallisation on a metallic lattice, that is, metal deposition. It is possible that an analogous expression for electro-crystallisation on an oxide film would apply and involve a similar frequency dependence. The results of Takehara et al (180) in fact, appear to indicate this to be the case.

$$= (1-j)\sigma/\omega^{\frac{1}{2}} + (\varepsilon k_c^{\,2} - j\varepsilon k_c\omega)/(k_c^{\,2} + \omega^2) \qquad (8.30)$$

where $\varepsilon = RT/n^2F^2\bar{c}k_c$, k_c being the rate constant for crystallisation and $\bar{c}$, the concentration of adsorbed species. Rate control in the crystallisation process is assumed to be due to incorporation of the adsorbed species formed in the charge transfer step, OH_{ads}, into an oxide structure.

Crystallisation rate control may be present (188) when the values of R_f and $1/\omega C_f$ in the plots versus $\omega^{-\frac{1}{2}}$ do not show a linear relationship for very high frequencies where the components of the diffusion impedance become relatively small and assuming roughness effects are absent. Hence, the case $\omega >> k_c$ will be considered, since it is then that the presence of a crystallisation impedance may be indicated and possibly identified.

Equation 8.30 then simplifies to

$$Z_f = (1-j)\sigma/\omega^{\frac{1}{2}} + (\varepsilon k_c^{\,2} - j\varepsilon\omega k_c)/\omega^2$$

$$= \left(\frac{\sigma}{\omega^{\frac{1}{2}}} + \frac{\varepsilon k_c^{\,2}}{\omega^2}\right) - j\left(\frac{\sigma}{\omega^{\frac{1}{2}}} + \frac{\varepsilon k_c}{\omega}\right) \qquad (8.31)$$

$$Y_f = \frac{1}{Z_f} = \frac{\omega^{\frac{1}{2}}\omega^2\,(\sigma\omega^2 + \varepsilon k_c^{\,2}\omega^{\frac{1}{2}}) - j(\sigma\omega^2 - \varepsilon k_c\omega^{3/2})}{(\sigma\omega^2 + \varepsilon k_c^{\,2}\omega^{\frac{1}{2}})^2 + (\sigma\omega^2 + \varepsilon k_c\omega^{3/2})^2} \qquad (8.32)$$

For $\omega >> k_c$ (high frequencies), only terms containing ω^4 are retained in the denominator. Hence the real component, A_f, is given by

$$A_f = \frac{\sigma\omega^{9/2} + \varepsilon k_c^{\,2}\omega^{6/2}}{2\sigma^2\omega^4} \qquad (8.33)$$

and the overall real component of the admittance of the equivalent circuit (Figure 8.8)

$$A'' = \frac{\omega^{\frac{1}{2}}}{2\sigma} + \frac{\varepsilon k_c^{\,2}}{2\sigma^2\omega} + b''\omega^n \qquad (8.34)$$

which can be rewritten

$$\frac{A''}{\omega} = \frac{1}{2\sigma\omega^{\frac{1}{2}}} + \frac{\varepsilon k_c^2}{2\sigma^2\omega^2} + b''\omega^{n-1} \qquad (8.35)$$

Similarly, the imaginary component, B_f, is given by

$$B_f = \frac{\sigma\omega^{9/2} + \varepsilon k_c \omega^4}{2\sigma^2\omega^4} \qquad (8.36)$$

and the overall imaginary component is

$$B'' = \frac{\omega^{\frac{1}{2}}}{2\sigma} + \frac{\varepsilon k_c}{2\sigma^2} + g''\omega^{\frac{1}{2}} + \omega C''_{dl} \qquad (8.37)$$

which can be rewritten

$$\frac{B''}{\omega^{\frac{1}{2}}} = \frac{1}{2\sigma} + g'' + \omega^{\frac{1}{2}} C''_{dl} + \frac{\varepsilon k_c}{2\sigma^2\omega^{\frac{1}{2}}} \qquad (8.38)$$

or as

$$\frac{B''}{\omega} = (\frac{1}{2\sigma} + g'')/\omega^{\frac{1}{2}} + \frac{\varepsilon k_c}{2\sigma^2\omega} + C''_{dl} \qquad (8.39)$$

8.5.2 Comparison with Data at 0.5 V

Equations 8.35 and 8.39 exhibit the same form of frequency dependence as the faradaic series components of the impedance (equation 8.31) in the absence of surface roughness effects. Since the dependence of $A''\omega^{-1}$ (for n=1) and R_f, and $B''\omega^{-1}$ and $(\omega C_f)^{-1}$ on frequency are similar, it is expected that the admittance components as a function of $\omega^{-\frac{1}{2}}$ will exhibit similar behaviour.

The superposition of diffusion and crystallisation reaction rate control results in characteristic behaviour of the impedance components which have been represented diagrammatically by Vetter (188). In this work, the high frequency region of $A\,\omega^{-1}$ (= $A''\,A_e\omega^{-1}$) vs $\omega^{-\frac{1}{2}}$ plots is expected to be influenced by the roughness term ω^{n-1}. This is indeed the case (Figure 8.7c) and therefore, a comparison of the form of this plot with that predicted by Vetter is not likely to be useful.

Notwithstanding the effect of surface roughness, the curve of the capacitative component $(\omega C_f)^{-1}$, as represented by Vetter, is similar in shape to the $B'\omega^{-1}/\omega^{-\frac{1}{2}}$ plot in Figure 8.7d. The similarity in the curves provides justification for applying the expression for the crystallisation impedance to the present case.

The real component, A', is linearly dependent on $\omega^{\frac{1}{2}}$ (Figure 8.7b), the slope of the plot being $A_e/2\sigma$. Since it is more desirable to obtain C_{dl} as a slope rather than by extrapolation to high frequencies (see section 8.2.3), it is determined from plots of $B'\omega^{-\frac{1}{2}}$ vs $\omega^{\frac{1}{2}}$ (Figure 8.7c) which as might be expected, are linear only at high frequencies. At low frequencies, the crystallisation component becomes effective and $B'\omega^{-\frac{1}{2}}$ as predicted, is proportional to $\omega^{-\frac{1}{2}}$ (Figure 8.7f) and hence $\varepsilon k_c/2\omega^2$ can be determined. The parameters, C''_{dl}, σ and $\varepsilon k_c/2\omega^2$ with subsequent values of c_o and $\bar{c}$ (in this case, $\bar{c}$ is the surface concentration of adsorbed OH_{ads} species in the equilibrium state) are given in Table 8.1. These values are discussed in section 8.7.

8.6 EFFECT OF TEMPERATURE

8.6.1 General Changes

The impedance spectrum in the complex plane is modified as the temperature increases. The two basic changes which take place may be summarised as:

(i) The appearance, at lower potentials, of a locus in which the imaginary component decreases at low frequencies.

(ii) The appearance of the low frequency Warburg region, as shown in the $A'/\omega^{\frac{1}{2}}$ plots, in the complex plane at potentials in the passive region. These changes in the loci are obviously dependent on the position of the particular potential in the active-passive regions of the current/potential (i_{ss}/E) curve at that temperature.

8.6.2. Basis for the Proposed Equivalent Circuit for 0.30 V

The basic equivalent circuits used to represent the electrode impedance at 295 K are applicable at elevated temperatures. However, at potentials in the passive region, modifications to the equivalent circuit as suggested by the form of the plots of the admittance components, in particular $B'\omega^{-\frac{1}{2}}$ against $\omega^{\frac{1}{2}}$ (see Figure 8.9d), are necessary. Although some plots of $B'\omega^{-\frac{1}{2}}/\omega^{\frac{1}{2}}$ in the passive region are linear at higher frequencies, generally this is not the case. It is more common for approximately constant values of $B'\omega^{-\frac{1}{2}}$ to be exhibited at high frequencies probably reflecting very low values of the double layer capacity at these potentials. However, the scatter of data does not permit an estimation of C_{dl} in most cases. Deviations from the predicted behaviour imply that the equivalent circuit proposed at room temperature is no longer adequate.

The observed behaviour may be associated with changes in the kinetics of oxide growth with an increase in temperature. Studies at room temperature by Briggs et al (24) showed the three-dimensional growth of Ag_2O on centres formed on a primary layer of the oxide (see section 1.2.1). The form of the current-time transients at constant potential indicated that the rate-determining process did not occur at the expanding interfaces of the growth centres but rather in the primary layer. However, an increasing rate of diffusion of species through the film with increasing temperature might cause the relative rate of formation of the growth centres to become more significant. Nevertheless, it should be pointed out that diffusion would probably remain the dominant influence in the overall rate control.

8.6.3 Equivalent Circuit and Data for 0.30 V

It is proposed that the impedance data at elevated temperatures be analysed in terms of an equivalent circuit which makes provision for an impedance component associated with the establishment of the 3-D growth centres. Initially, it is assumed that, as for the formation of Ag_2O_2 at room temperature, the nucleation impedance may be represented as having the frequency dependence shown in equation 8.30. Hence, an equivalent circuit of the form shown in Figure 8.8 is used as the model to represent the electrode impedance under these conditions although Z_c will now refer

Figure 8.9 Impedance and admittance data at 0.30V, 388K

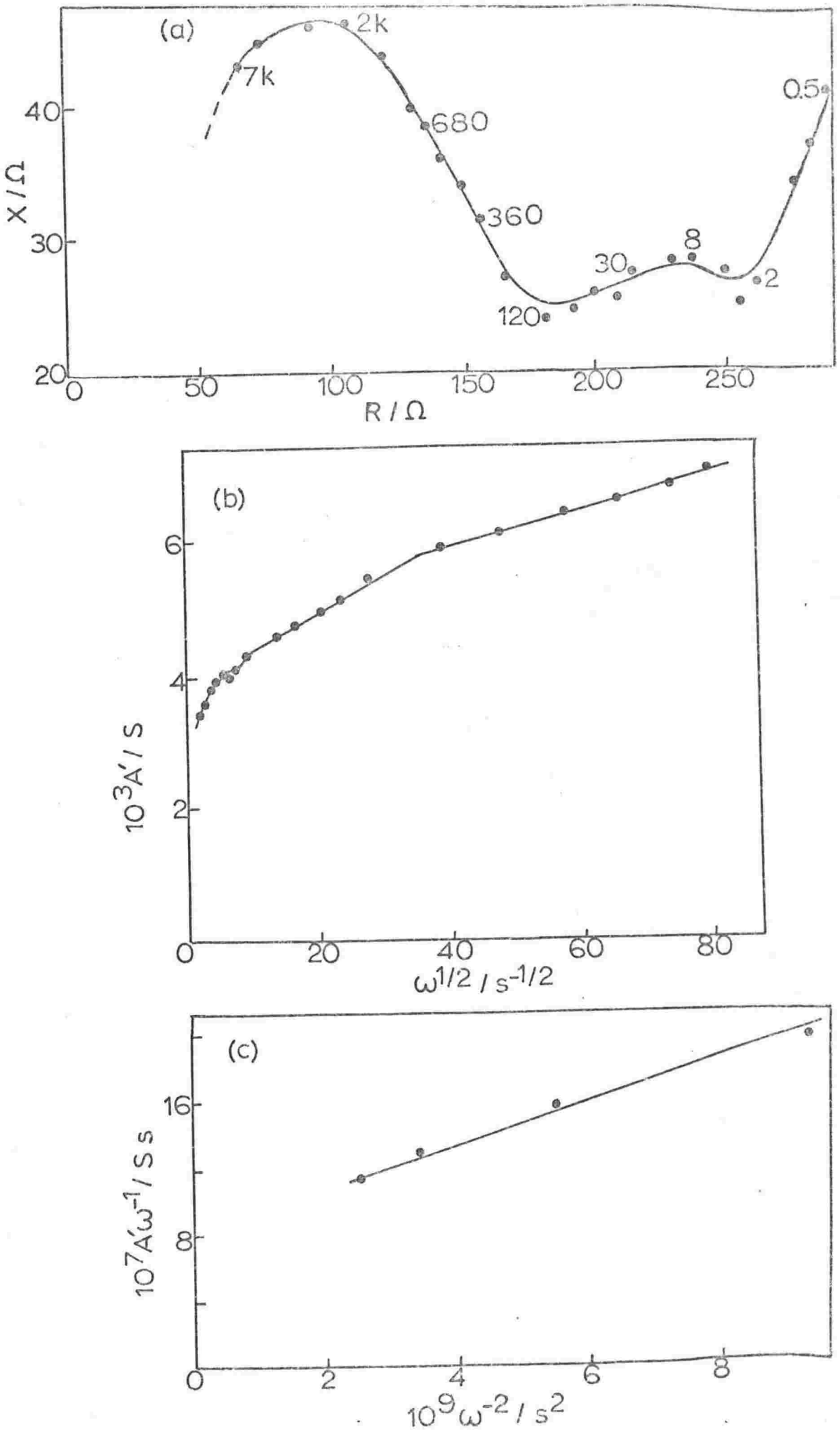

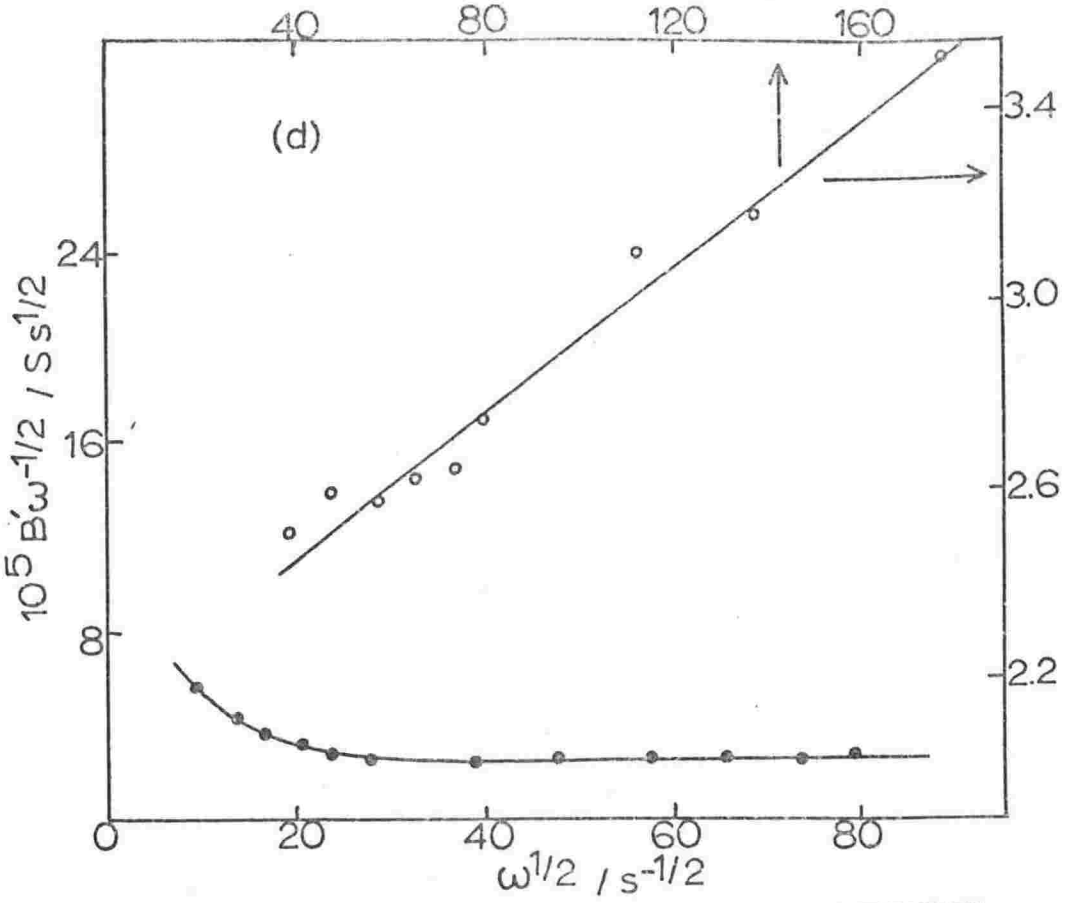
(d)
40
80
120
160
3.4
3.0
2.6
2.2
24
16
8
0
20
40
60
80
$10^5 B'\omega^{-1/2}$ / S $s^{1/2}$
$\omega^{1/2}$ / $s^{-1/2}$

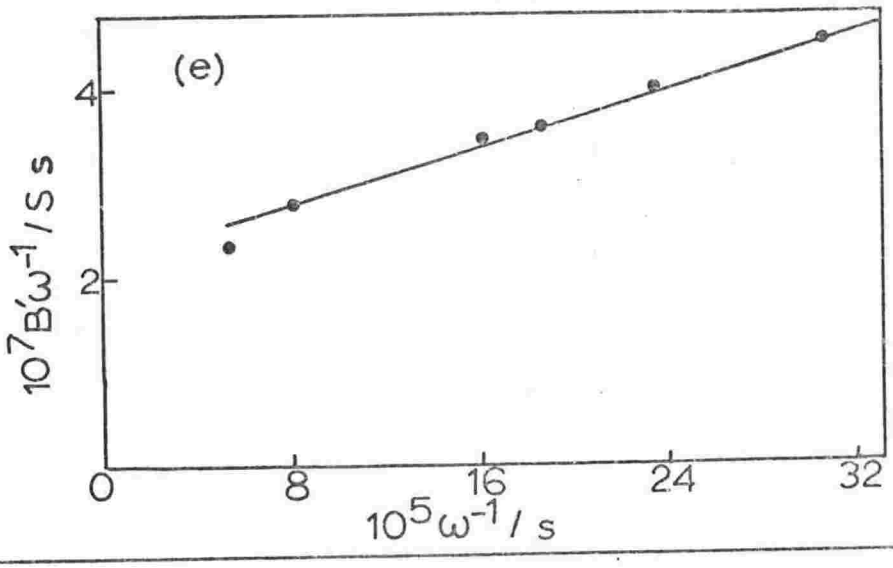
(e)
4
2
0
8
16
24
32
$10^7 B'\omega^{-1}$ / S s
$10^5 \omega^{-1}$ / s

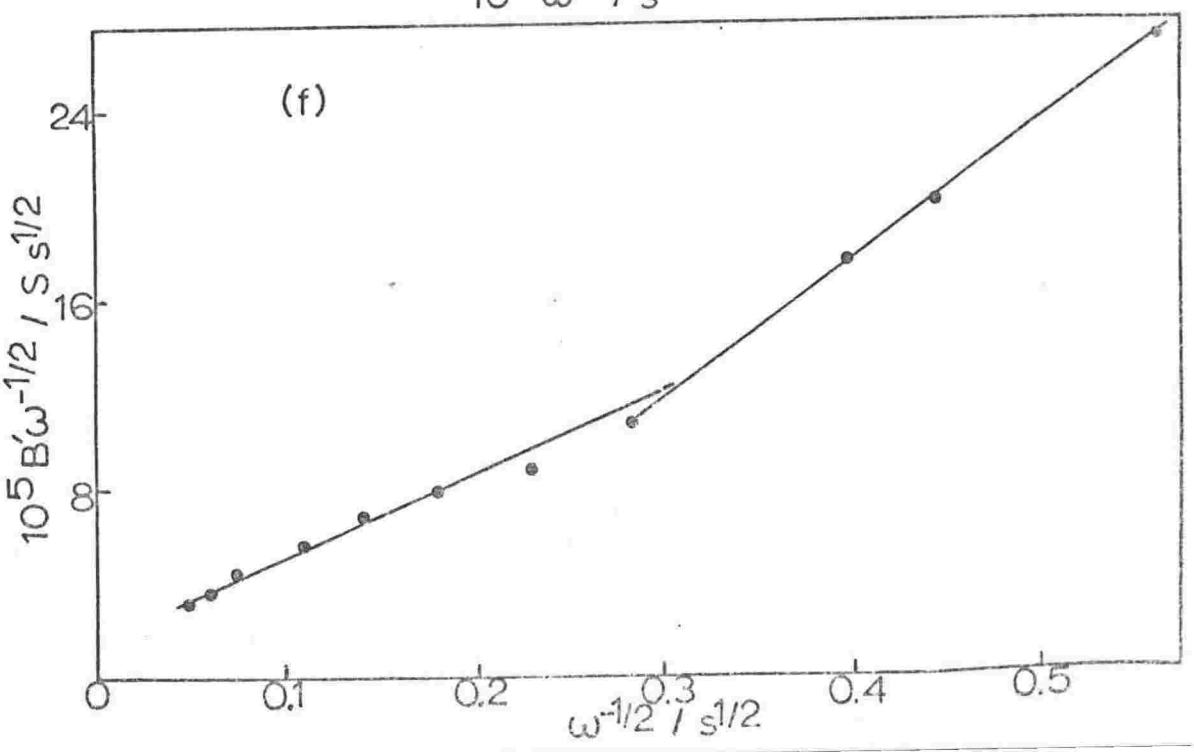
(f)
24
16
8
0
0.1
0.2
0.3
0.4
0.5
$10^5 B'\omega^{-1/2}$ / S $s^{1/2}$
$\omega^{-1/2}$ / $s^{1/2}$

to the formation of Ag_2O nuclei.

The frequency dependence of the admittance components was given earlier in a form similar to that presented by Vetter, that is, at high frequencies ($\omega >> k_c$) $A''\omega^{-1}$ and $B''\omega^{-1}$ should vary according to ω^{-2} and ω^{-1}, respectively. Plots of $A''\omega^{-1}/\omega^{-2}$ (Figure 8.9c) and $B\omega^{-1}/\omega^{-1}$ (Figure 8.9e) are found to be linear at high frequencies justifying the application of the equations for a crystallisation impedance to the present situation involving formation of oxide growth centres.

$A''/\omega^{\frac{1}{2}}$ relations are linear over the potential range exhibiting two such regions very clearly at 0.3 V (Figure 8.9b). This is simply due to the appearance of the low frequency Warburg region associated with diffusion of ionic species through the oxide layer. According to equation 8.34, it is expected that A' would be proportional to $1/\omega$ at low frequencies. In some cases, a temporary increase of A' with a decrease in frequency is observed (see low frequency region of Figure 8.9b), but generally such a change is brief and more detailed examination of the data is not possible.

At low frequencies, plots of $B'\omega^{-\frac{1}{2}}$ vs $\omega^{-\frac{1}{2}}$ (Figure 8.9f) also show two linear regions since the slope is given by $\varepsilon k_c A_e/2\sigma^2$, and equation 8.21 which expresses the total Warburg coefficient as a combination of σ_s and σ_F, then applies.

8.6.4 Equivalent Circuit and Data at 0.50 V, 348-428 K

At 0.5 V, it is likely that the Ag_2O growth centres will have overlapped to such an extent that the overall electrode impedance for oxide formation for this potential at elevated temperatures may still be considered in terms of the equivalent circuit in Figure 8.8, that is, a Warburg impedance in series with a crystallisation impedance associated with the conversion of Ag_2O to Ag_2O_2. Some modification is required, however, to the equivalent circuit for this potential at elevated temperatures since examination of the steady-state current/potential curves over the range 348-478 K (Figure 6.3) shows that 0.5 V now lies in the region at which oxygen evolution can take place at a significant rate. Accordingly, provision in the equivalent circuit must be made for components representing the controlling factor in this process.

The evolution of oxygen may be represented by the discharge of hydroxide ions according to the reaction (64)

$$2OH^- = \tfrac{1}{2}O_2 + H_2O + 2e \qquad (8.40)$$

Hoare (104) has suggested that the mechanism of oxygen evolution in alkaline solutions could involve

$$OH^- \longrightarrow (OH)_{ads} + e \qquad (8.41a)$$

$$(OH)_{ads} OH^- = (O)_{ads} + H_2O + e \qquad (b)$$

$$(O)_{ads} + (O)_{ads} = (O_2)_{ads} \qquad (c)$$

$$(O_2)_{ads} = O_2 \qquad (d)$$

although he did not indicate whether such reactions occur on metal oxide surfaces.

The impedance, Z_o, corresponding to the mechanism proposed by Hoare, might be represented by a simple equivalent circuit as shown in Figure 8.10.

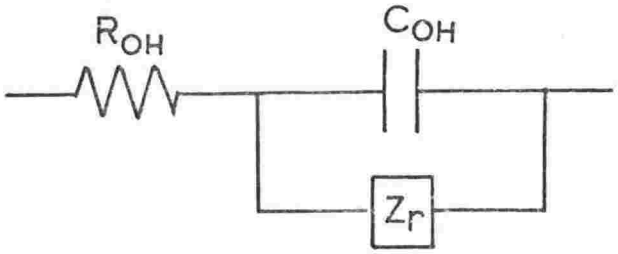

Figure 8.10 Equivalent circuit representing the faradaic impedance Z_o of the silver electrode associated with oxygen evolution.*

* As indicated by the steady-state current/potential curve at 478 K, 0.5 V lies well into the region of oxygen evolution. Since the large d.c. current due to this process hinders any useful examination of the faradaic impedance associated with oxide formation, this potential was not studied at 478 K.

R_{OH^-} is the charge transfer resistance associated with the discharge of the OH^- ions, C_{OH} is the pseudocapacity due to adsorption of OH (also O and O_2) species and Z_r is the reaction impedance corresponding to removal of the adsorbed species. Since oxide formation occurs simultaneously, oxygen evolution is assumed to take place in parallel as indicated in the following equivalent circuit.

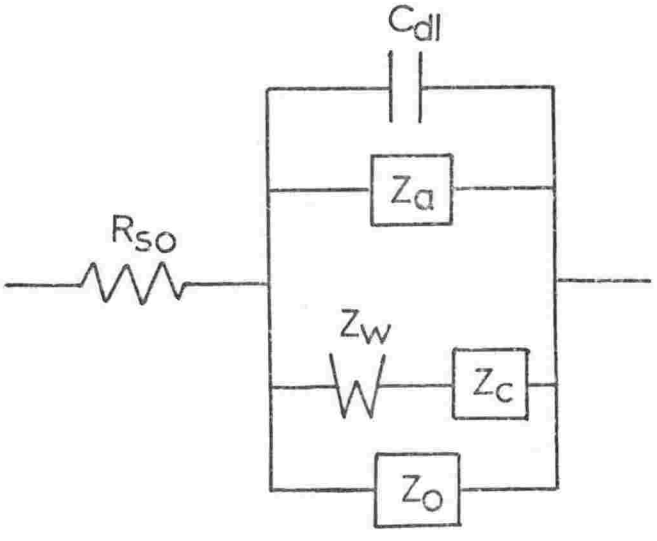

Figure 8.11 Equivalent circuit representing the overall impedance of the silver electrode at 0.5 V over the temperature range 348-428 K.

However, inclusion of Z_o into the equivalent circuit in Figure 8.11 yields a complicated expression for the overall faradaic admittance. For simplification, it will be assumed that the initial charge transfer step 8.41a is sufficiently slow so that it is predominant in determining the overall rate of oxygen evolution. It is worth noting that conduction of electrons through the oxide multilayer on silver is possible since both Ag_2O and Ag_2C_2 are n-type semiconductors (59). For the purpose of this analysis then, the electrode impedance associated with reaction 8.40 is represented by a simple charge transfer resistance in the equivalent circuit. Hence, the real component of the admittance is given by

Figure 8.12 Impedance and admittance data at 0.50 V, 388 K

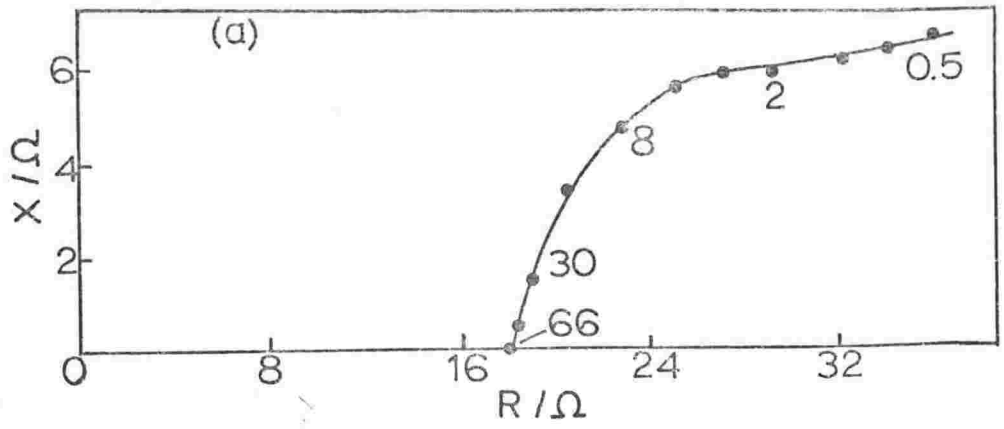

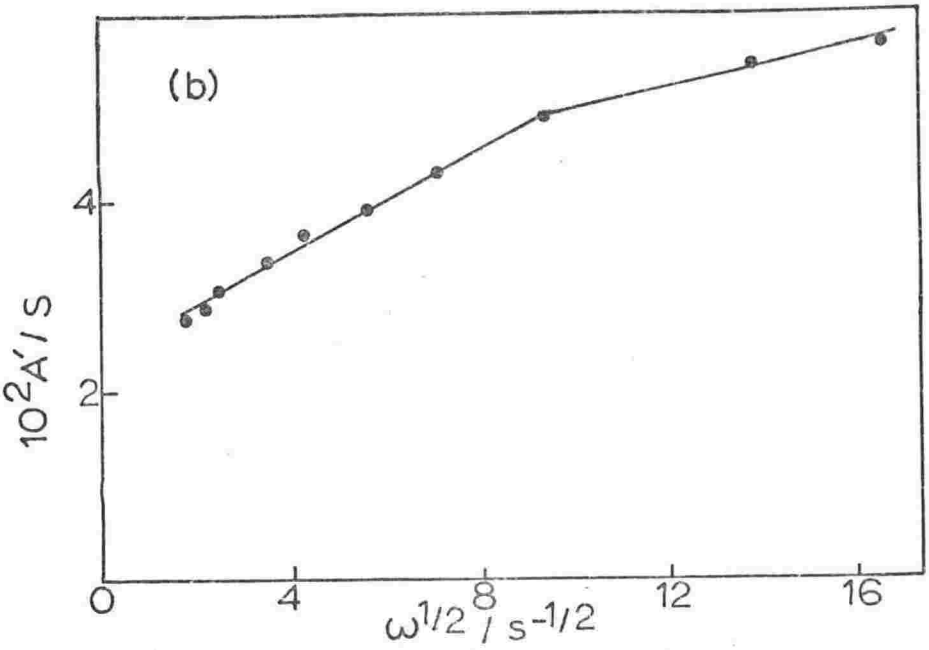

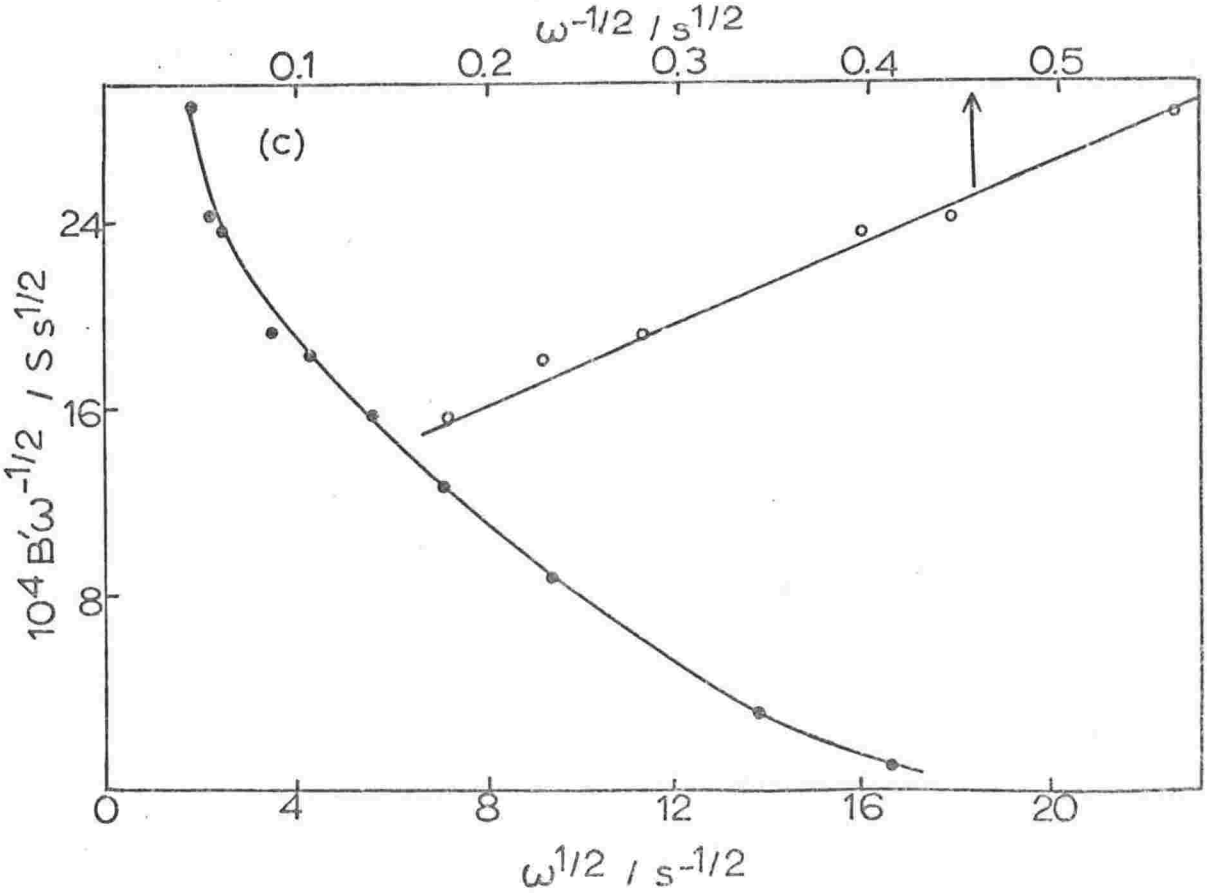

$$A'' = \frac{\omega^{\frac{1}{2}}}{2\sigma} + \frac{\epsilon k_c^2}{2\sigma^2 \omega} + a\omega^n + \frac{1}{R_{OH}} \qquad (8.42)$$

which clearly does not alter the frequency dependence of A". The expression for the imaginary component as given by equation 8.37 remains unchanged.

As predicted, plots of $B'\omega^{-\frac{1}{2}}$ vs $\omega^{\frac{1}{2}}$ are linear at low frequencies (Figure 8.12c) but it should be noted that, in contrast to the potential of 0.3 V at these temperatures, only one linear region appears in such plots. However, two regions are now exhibited by the $A'/\omega^{\frac{1}{2}}$ relations (Figure 8.12b) for the temperature range, thereby demonstrating that diffusion in the solid state must give rise to a component in the overall faradaic impedance.

8.7 DISCUSSION

8.7.1 Effect of Potential on the Impedance Parameters

The following changes are observed as the potential becomes more anodic:

(i) c_o decreases which is attributable to an inadequacy of the Randles circuit with $R_{ct}=0$ since the concentration of AgO^- should remain constant at anodic potentials greater than that corresponding to the formation of bulk Ag_2O.

(ii) C''_{dl} achieves quite low values (0.4 μF cm^{-2} at 0.3 V and 295 K). This trend is consistent with the potential-dependence of the double-layer capacity at room temperature observed by Giles et al, following the formation of a monolayer of Ag_2O, particularly at potentials greater than 0.13 V (SCE).

(iii) $\bar{c}$ is observed to decrease in the cases where comparison of data is possible. The low values of $\bar{c}$ are no doubt indicative of the extent to which overlap of the growth centres has taken place.

(iv) X_F increases, again where comparison of data is possible.

8.7.2 Effect of Temperature on the Impedance Parameters

Several temperature-dependent quantities, namely T, D and c are contained in σ. In order to evaluate c_o and c_F, the associated diffusion coefficients must be determined at each temperature. D_o (165) and D_F (185) are both a function of temperature as expressed by equation 8.43

$$D = Z_o \exp(-\frac{E_D}{RT}) \qquad (8.43)$$

where E_D is the activation energy for diffusion. For aqueous solutions, $Z_o \approx 0.2$ (165) and for the AgO^- ion in 1 mol dm^{-3} KOH, D_o has been evaluated as 8.6×10^{-6} cm^2 s^{-1} (141). Assuming that E_D is independent of temperature, D_o can be evaluated over the range 295-478 K (Table 8.2)

In section 8.4.2, D_F was estimated to be 2.3×10^{-12} cm^2 s^{-1} at 295 K. The most applicable value for the activation energy of diffusion of Ag^+ in Ag_2O which appears to be available is for Ag^+ in Ag_2S and this was found by Okazaki (145) to be 11 kJ mol^{-1}. Using this value, D_F for Ag^+ may then be determined over the temperature range studied (Table 8.2).

Table 8.2 Diffusion Coefficients, D_o and D_F over the temperature range 295-478 K

T/K	10^5 D_o/cm^2 s^{-1}	10^{12} D_F/cm^2 s^{-1}
295	0.8	2.3
348	3.6	4.6
388	8.9	6.7
428	18.2	9.3
478	37.9	12.8

The following features are evident in Table 8.1 as the temperature increases:

(i) At a particular potential, the value of c_o increases except at potentials where a shift into the passive region occurs with the temperature change.

(ii) X_F, in general, increases. The lack of a distinct σ_F in the $A'/\omega^{\frac{1}{2}}$ plots at 428 K could be attributed to a thickness of the oxide film such that a higher rate of diffusion at this temperature reduces the significance of the solid-state diffusion impedance. Nevertheless, two distinct slopes are evident in the $B'\omega^{-\frac{1}{2}}/\omega^{-\frac{1}{2}}$ plots and the high slope at low frequencies could be attributed to a small σ_F.

(iii) The surface density of Ag_2O growth centres appears to decrease.

(iv) $\bar{c}(Ag_2O_2)$ passes through a maximum in the region of 348 K and decreases at 388 and 428 K. This decrease probably reflects a higher degree of overlap of Ag_2O_2 nuclei at a particular potential due to the increase in temperature.

(v) The double-layer capacity is found to increase. Since C''_{dl} is associated with the double-layer of charge at the electrode/electrolyte interface, the high values of this parameter for elevated temperatures, at least for the active region in which the dissolution reaction is highly reversible, may be attributed firstly to an increase in the accumulation of ionic species at the electrode surface with temperature, and secondly, to more extensive roughening of the surface by dissolution. The second factor is reflected in the increased values of the surface roughness coefficient, g" (Table 8.3) which were determined from the plots of $B'\omega^{-\frac{1}{2}}$ vs $\omega^{\frac{1}{2}}$ over the temperature range 295-428 K by the method described in section 8.3.5.

Table 8.3 The surface roughness coefficient, g", over the temperature range 295-428 K

T/K	E/V	g"/μF cm^{-2} $s^{-\frac{1}{2}}$
295	0.12	1.3×10^{3}
348	0.13	1.9×10^{3}
388	0.12	1.3×10^{2}
428	0.12	1.7×10^{2}

8.7.3 Reproducibility

It is evident from the trends exhibited by the impedance parameters, particularly C''_{dl} and c_o, that since surface roughening becomes more severe at higher temperatures these parameters will depend strongly on the reproducibility of the electrode surface. Surface roughness of the electrode is reflected in an increase in C''_{dl} but it also affects the faradaic component. It was assumed throughout the analysis that the roughness has no effect on the faradaic component, for example, with regard to the diffusional area. This assumption is not strictly valid since the diffusion impedance (admittance) at high frequencies is lowered (increased) by surface roughness (see section 8.3.4), in other words diffusion is facilitated by a rough surface. However, as in previous work (88), these are treated as second-order effects.

The methods used to prepare the electrode surface were considered adequate (see section 3.3.2) and are justified by a reasonable degree of reproducibility, particularly in view of the temperature range examined. The average reproducibility for the values shown in Table 8.1 ranges from ±10-12% at room temperature, to ±15% at higher temperatures up to 428 K, and approximately ±20% at 478 K.

SECTION IV

DISCUSSION

CHAPTER 9 DISCUSSION

9.1 INTRODUCTION

The effect of temperature on the oxidation and reduction reactions corresponding to the peaks and arrests of the cyclic voltammograms and galvanostatic charging curves, respectively, are interpreted in terms of the mechanism accepted for each electrode reaction at room temperature. The data available from each technique over the temperature range 295-478 K are combined in order to provide a description of the effect of temperature on the overall mechanism. Finally, the contribution of data from each technique is taken into account and the advantages of the impedance technique compared with the other electrochemical techniques are considered in relation to its application at elevated temperatures.

9.2 ELECTRODE REACTIONS OF SILVER AT ELEVATED TEMPERATURES

9.2.1 General Features

These studies show that temperature has a marked effect on the electrochemical behaviour of silver in potassium hydroxide solution. The most notable feature with an increase in temperature is the trend towards more complex forms of the cyclic voltammograms and galvanostatic charging curves over the range 295-388 K, followed by a change to progressively simpler forms at higher temperatures.

The principal changes in the polarisation behaviour include:

(i) the appearance of additional charge transfer peaks in cyclic voltammetry (Figure 5.1) and associated arrests in galvanostatic charging (Figure 7.1),

(ii) a shift in rate control of the growth of the Ag_2O multilayer,

(iii) a marked decrease in the oxygen-evolution overpotential.

Comparison of the charge consumed on the anodic sweep to that on the cathodic sweep (sections 5.5.3 and 7.4) indicates that solubility effects appear to have significant implications in the electrochemical behaviour of silver. Under controlled potential-sweep conditions in cyclic

voltammetry over the temperature range 295-388 K, dissolution of the metal and the oxide layer are limited in relation to film formation processes, in terms of the overall charge involved. However, for constant current charging in which film growth is generally not so extensive, dissolution processes are shown to become significant at 388 K. In both techniques, a considerable increase in the charge ratio is observed at 428 K, and a further marked increase is evident at 478 K. These relatively high values of the charge ratio indicate that extensive dissolution takes place at these temperatures.

For the complete potential range between hydrogen evolution and oxygen evolution, the following reactions were proposed to account for the polarisation behaviour of silver in 1 mol kg^{-1} KOH over the temperature range 295-478 K. In the following sections, the behaviour of the associated peaks shown below are discussed in relation to these reactions.

	Reaction	Peak	Arrest
(i)	$Ag + 2OH^- \rightarrow AgO^- + H_2O + e$	A1	E_{A1}
(ii)	$2Ag + 2OH^- \rightarrow Ag_2O + H_2O + 2e$	A2	E_{A2}
(iii)	$Ag_2O + 2OH^- \rightarrow Ag_2O_2 + H_2O + 2e$	A3,A3'	E_{A3}
(iv)	$Ag_2O_2 + 2e \rightarrow 2AgO^-$ $2AgO^- + H_2O = Ag_2O + 2OH^-$	C3,C4	E_{C3}
(v)	$Ag_2O + H_2O + 2e \rightarrow 2Ag + 2OH^-$	C2	E_{C2}

9.2.2 Peak A1

General Behaviour:

Potentiostatic polarisation curves for silver at elevated temperatures (Figure 6.3) exhibit an active region which no doubt is associated with the formation of the AgO^- ion as recognised for alkaline solutions at room temperature. Thermodynamic calculations show that the argentite ion should become increasingly stable with respect to silver metal for a given hydroxide concentration as the temperature is increased (see Figure 2.2). Although it is not valid to interpret rate phenomenon in terms of equilibrium thermodynamics directly, the increased equilibrium

concentration of AgO^- at higher temperatures is no doubt a contributing factor in the dependence of peak current on temperature. Such a tendency is consistent with the increases in the following parameters with temperature:

(i) Diffusional currents for Al (Figure 5.3a).

(ii) Steady-state currents in the active region (Figure 6.3).

(iii) Arrests for E_{Al} with time as observed in the galvanostatic curves (Figure 7.1).

(iv) Values of c_o (Table 8.1) obtained from impedance data.

All the techniques indicate clearly the substantial changes which are observed upon oxidation at 428 K relative to the lower temperatures. A higher rate of dissolution of the metal probably contributes to the increased charge ratio Q_A/Q_C and is reflected in the greatly increased currents in the steady-state curves, and potential-sweep experiments, particularly at low sweep rates.

Specific behaviour:

Features such as non-zero sweep-rate intercepts in the $i_p/v^{\frac{1}{2}}$ plots (Figure 5.3a) have been discussed in section 5.6.1. However, it is worthwhile to refer briefly to some of the changes in these plots with temperature in order to make comparisons with the steady-state current/potential curves. It was proposed that an increased tendency towards redeposition at 348 and 388 K lowers the diffusional current of ionic species from the electrode surface. At 428 K, a higher rate of accumulation of dissolved species possibly compensates for such a redeposition process thereby enabling a high diffusional current to be maintained at low sweep rates. Both the concentration of AgO^-, c_o, at a particular potential and the rate of diffusion, which is indicated by the steady-state polarisation curves in Figure 6.3, also increase with temperature. However, at high sweep rates, the rate of accumulation of dissolved species at 428 K apparently predominates, so that a greater extent of surface blocking by precipitated Ag_2O increases the hindrance to the dissolution process. This tendency is opposed by the relatively high solubility of the oxide which becomes evident in the more gradual approach to an active-to-passive transition at 428 K.

Part of the increased current at 428 K may also be due to surface roughening of the electrode since this factor will cause the currents in the potential-step technique for example, to be larger than predicted from the equations for diffusion at short times (57). However, if diffusion is the current-limiting factor, and also, diffusion very close to the electrode is faster than that at some distance from the electrode, then roughness will have a negligible influence (57) on the steady-state diffusion current. This current is determined essentially by diffusion towards and away from the apparent (projected) macroscopic surface of the electrode (57).

9.2.3 Peak A2

General behaviour:

At elevated temperatures, the Ag_2O oxide layer clearly becomes less protective as shown by the temperature dependence of the steady-state currents in the passive regions (Figure 6.3). It is evident that the increasing solubility of the oxide is effective in causing more charge to be required for film formation in order to maintain a steady-state thickness i.e. the current in the passive region contains a large dissolution component.

At 428 K, the increased effect of the solubility is evident in the finite intercept of i_p at zero v (Figure 5.3b) which is consistent with the high steady-state current in the passive region (Figure 6.3) and the slow transition following the initial arrest associated with Ag_2O formation in the galvanostatic curves (Figure 7.1d). Presumably, since the slow transition in the latter is even more enhanced at 478 K, it is probable that such tendencies may be present at this temperature also but any interpretation is complicated by the highly porous nature of the electrode surface now evidently existing (see the electron-micrographs, Figure 5.6). Possible consequences of this type of surface on the charge transfer processes at 478 K, particularly those corresponding to A_1 and A_2 are discussed in section 5.6.6.

Specific behaviour:

The kinetics of the oxide growth exhibits modifications at elevated temperatures. The change to reversible behaviour at 388 K (section 5.4.2)

is possibly attributable to the Ag^+ ions which now exist in equilibrium concentrations at each potential, transferred into the Ag_2O layer. Since the concentration of Ag^+, c_F, at the metal/oxide interface at a particular potential is increased as shown in Table 8.1, the rate of diffusion is likely to be greater. At 348 and 388 K, the impedance data (section 8.6.3) indicate that a deposition step in the formation of the growth centres on the primary oxide layer becomes more significant in controlling the overall rate of oxide growth. Although the higher rate of solid-state diffusion no doubt enhances the rate of formation of growth centres, it would also account for the increasing role played by surface reactions in growth-centre formation.

At 348 and 388 K, it was concluded (section 5.6.2) that a minimum sweep rate must be achieved before diffusion controls the rate of film growth. This behaviour may be explained as follows. At low sweep rates, the rate of accumulation of Ag^+ in the oxide layer at the $Ag|Ag_2O$ interface, and hence the rate of diffusion, is insufficient to maintain the rate of film thickening above the rate of dissolution due to the higher solubility of Ag_2O. As the sweep rate is increased, the rate of accumulation allows a rate of diffusion which enables the film to thicken. Eventually the rate of diffusion is determined by the film thickness and so limits the overall rate of film growth. The admittance plots shown in Figure 8.9 for these temperatures clearly demonstrate the presence of diffusional processes both through the film and in solution.

Assuming that the above hypothesis holds, then it is possible that at 428 K for a particular potential, a higher concentration of Ag^+ at the metal/oxide interface gives rise to an increased rate of film thickening which is adequate, even at low sweep rates, to permit limiting control by solid-state diffusion. Nevertheless, the lack of a σ_F in the $A'/\omega^{\frac{1}{2}}$ plots (see section 8.7.2) indicates that the rate of diffusion through the oxide has increased sufficiently at this temperature to be exerting a much reduced influence on the reaction rate.

9.2.4 Peaks A3 and A3'

General behaviour:

In discussing the cyclic voltammograms, changes in mechanism with temperature may be accounted for in terms of the activation energies for nucleation and diffusion. The polarisation behaviour at 348 K provides

some insight into the mechanism at higher temperature. Changes which take place in the A3 region of potential as the temperature is increased from 295 K to 348 K were common to both the cyclic voltammograms (Figure 5.1) and galvanostatic charging curves (Figure 7.1). However, the latter were considerably more complex and correspondingly more difficult to interpret. Consequently, the following discussion is centred around the results obtained from the cyclic voltammograms.

It was concluded that the additional peak A3' was most likely associated with the formation of Ag_2O_2 (see section 5.6.3) but under different kinetic control from the conversion occurring in the A3 region. The question then remains as to the differences in mechanism which would permit the formation of Ag_2O_2 to take place at a different potential, that is, under a clearly separated peak.

Specific behaviour:

The same shape of current-time transient (Figure 6.1d) at constant potential is observed over the temperature range which implies that the overall mechanism for Ag_2O_2 formation remains unchanged. However, the complex-plane impedance plots at a potential of 0.5 V (Figures 8.7 and 8.12) do show some changes which is supported by equivalent-circuit analyses of the data. At 295 K, such an analysis (section 8.5) showed the presence of a crystallisation process in which deposition of species at appropriate sites was assumed to be rate-controlling, but at elevated temperatures (section 8.6), it was evident that in addition to a crystallisation process, diffusion within the solid also contributed to rate control.

At 295 and 348 K, it appears that a deposition step may be responsible for rate-limiting control of the reaction corresponding to A3. However, A3' is observed at 348 K, and it was found in the $i_p/v^{\frac{1}{2}}$ plots (Figure 5.3c) that the limiting step in the associated reaction is a mass transport process. Since this peak occurs at lower potentials than A3, the A3' reaction is apparently more favoured by the increase in temperature. When the conversion at A3' which takes place under diffusion control is eventually inhibited, further formation of Ag_2O_2 can evidently occur at A3 but the rate of this conversion stage is limited by a deposition step.

Since A3' appears with the increase in temperature from 295 to 348 K, it is possible that the peaks observed in this region at higher temperatures may, in fact, be A3'. This hypothesis is supported by the diffusional

behaviour exhibited for the observed peak at 388 and 428 K (Figure 5.3c). Further evidence is provided by the trend in the surface density of nuclei, $\bar{c}$, (Table 8.1) with temperature, this parameter passing through a maximum at 348 K and decreasing at higher temperatures. In other words, the decrease in density of nuclei with temperature occurs in conjunction with the increasing significance of diffusion in controlling the rate of the conversion process. Nevertheless, the admittance data at these temperatures, shown in Figure 8.12, are still consistent with a crystallisation process involving a slow deposition step. Hence, it appears that at elevated temperatures, both diffusion in the oxide and a deposition process are involved in controlling the formation of Ag_2O_2.

The potential-sweep curves (Figures 5.1f and 7.1e) indicated that the conversion of Ag_2O is not significant at 478 K. Apparently Ag_2O_2 may be formed to a small extent as inferred from the cyclic voltammograms but it is evident from the latter and the galvanostatic charging curves that no reduction process takes place, implying that any Ag_2O_2 formed is immediately decomposed or dissolved at this temperature. This behaviour was discussed in section 5.6.6.

9.2.5 Peaks C3 and C4

The reduction processes were investigated using only two of the techniques, namely cyclic voltammetry and galvanostatic charging. Consequently, the information regarding the kinetics of these reactions is more restricted.

One feature emphasised by the current/potential (Figure 5.1), and potential/time (Figure 7.1) curves at elevated temperatures is the apparently incomplete reduction of Ag_2O at C3 (section 5.6.4). As the temperature is increased from 295 K, the C4 peak began to appear at 348 K and became clearly resolvable at 388 K. In a constant current study at room temperature, Miller (141) demonstrated the presence of a dissolution-precipitation mechanism in the reduction of Ag_2O_2 (see section 5.6.4). The thickness of the Ag_2O layer formed in this process increases to some limiting value at which the reduction is effectively terminated. At higher temperatures, dissolution of the Ag_2O in the region following C3 may enable reduction to be completed, or at least almost so, at C4. It was concluded in section 5.6.4 that the reduction process at C4 is the same as that taking place at C3, namely reaction v shown in section 9.2.1.

Since the dissolution of Ag_2O at C3 would be expected to be more extensive at high temperatures, it is likely that some other factor such as the formation of a thicker film also contributes to the appearance of C4. Although some dissolution of such a film occurs, it might be expected then that a greater extent of incomplete reduction is present following termination of the reaction in the C3 region. Hence, a thicker film may assist in C4 becoming more significant with increasing temperature. The lack of reversibility apparent from the E_p/ln v plots for C3 and C4 at 388 K is then possibly associated with the thicker film at this temperature. If it is assumed that the oxide multilayer has the form $Ag|Ag_2O|Ag_2O_2$ (see section 5.6.6) then a thicker layer of the more ohmically resistive Ag_2O could give rise to IR effects.

The disappearance of the C4 peak at 428 K is probably attributable to the increased oxide solubility so that:

(i) the Ag_2O_2 layer is decreased sufficiently for complete reduction to occur at C3.

(ii) the Ag_2O layer formed by precipitation does not limit continued reduction at C3.

9.2.6 Peak C2

From the cyclic voltammetry data, the $i_p/v^{\frac{1}{2}}$ relations for the reduction of Ag_2O (Figure 5.3c) are consistent with diffusion of Ag^+ ions probably to the two-dimensional centres of silver formed in the oxide layer by a nucleation and growth mechanism (79). Although current-time curves (at constant potential) characteristic of such a mechanism are exhibited in this potential region (79), diffusion is clearly a significant factor. It was pointed out that a detailed interpretation of these plots was complicated by the occurrence of the nucleation and growth process (see section 5.6.5). However, solubility effects are no doubt significant as for the other electrode reactions. Indeed, the lowered slope of the $i_p/v^{\frac{1}{2}}$ plot at 428 K is probably associated with a decreased film thickness available for reduction relative to that formed on the anodic sweep.

The distinct asymmetric shape of this peak at 478 K has been commented on previously (section 5.6.6) in relation to the extensive surface roughening found to have occurred at this temperature.

9.3 EVALUATION OF THE IMPEDANCE TECHNIQUE

It is desirable initially to determine a spectrum of the charge transfer processes as obtained from cyclic voltammetry. From such a spectrum, it is possible to select desired potentials at which to obtain impedance measurements which may be compared with the results from other techniques. In the dissolution region for example, the information obtained from impedance measurements was found to be quite consistent with that indicated by potentiostatic and potential-sweep methods, namely, evidence was provided for the presence of diffusional processes. However, the impedance technique clearly demonstrated a number of advantages:

(i) A feature only inferred from the other methods and furthermore only at 478 K, was the effect of surface roughness of the silver electrodes. Using the impedance method, it was possible not only to detect, but also obtain a measure of, the roughness by estimation of a roughness coefficient g.

(ii) c_o is evaluated more readily from this technique since its determination relies only on D, whereas a lack of data for additional parameters hinders the evaluation using the other techniques.

(iii) The double-layer capacity may be readily obtained, in principle throughout the regions where charge transfer is taking place, in contrast to the other techniques in which it is usually determinable only from currents in the double-layer region of potential-sweep curves or from the initial section of over-potential-time transients at constant current. In particular, the double layer capacity may be measured, in many cases, throughout the passive region where in the case of silver, lower values are coincident with the growth of the oxide layer.

(iv) In the passive region, the separate diffusion processes within the solid and solution are demonstrated simultaneously and in addition, the presence of nucleation processes may also be evident. Although potentiostatic studies would normally indicate nucleation by a current-time curve exhibiting a maximum (see Figure 6.1d), exceptions occur as in the case of silver; falling current-time transients continue to be observed at elevated temperatures, yet the impedance data show that nucleation (crystallisation) processes become more prominent.

Perhaps one of the most significant advantages of the impedance technique is that it requires an equivalent circuit for an analysis. Such a circuit is strictly only equivalent, in terms of its properties, to the system studied. Nevertheless, it is possible to rationalise the electrode polarisation behaviour, for example with temperature, in relation to the parameters of the equivalent circuit.

The obvious disadvantage with this technique as used potentiostatically, is that an examination of reduction processes is not possible, although the cathodic sweep has been investigated by potentiodynamic impedance methods (182).

9.4 FUTURE RESEARCH

It should be emphasised that the explanations suggested for the polarisation behaviour observed for silver at elevated temperatures are often probably not the only ones possible and the interpretation of this behaviour, in such cases, is provisional depending upon further information. In particular, the reactions giving rise to the additional peaks and arrests in the cyclic voltammograms and galvanostatic charging curves, respectively, require more evidence as to the nature of the overall processes. Notwithstanding the difficulties in using rotating-disc methods at elevated temperatures, such studies may well provide the necessary data.

Although studies have been conducted on other metals such as copper (127), nickel (44,134,157) and iron (18,133,158) in aqueous solutions at elevated temperatures, various features of their reaction mechanism remain unclear. These studies have usually employed one or more of either cyclic voltammetry, galvanostatic or potentiostatic techniques. The application of the impedance technique as demonstrated in this research, indicates that its use can be extended to the investigation of other metals which exhibit more complex polarisation behaviour than silver. Such an extension would be particularly advantageous for those metals and alloys having corrosion problems that are important because of their industrial significance.

Appendix 1

Computer (Fortran) Program To Perform Thermodynamic Calculations

```
C FREE ENERGY OF CHEMICAL SYSTEMS
C
C A ------ACTIVITY OF SPECIES
C ADD ----SOLUBILITY FROM INDIVIDUAL REACTION
C AP -----LOG OF ACTIVITY/SOLUBILITY CALCULATED
C ARN ----REACTION ACTIVITY CALCULATION INDICATOR
C C ------COEFFICIENTS OF EQTN E(T) = C(1) + C(2)*LOG(PRODUCT) +
C                C(3)*LOG(REACTANT) + C(4)*PH
C              OR OF NH*PH=C(1) + NR*LOG(REACTANT) - NP*LOG(PRODUC
C CC -----CRISS AND COBBLE ENTROPY PARAMETERS
C CP -----COEFFICIENTS OF SPECIFIC HEAT EQUATION
C          SP.HT.=CP(1) + CP(2)*1.E-3*T + CP(3)*1.E5*T**(-2)
C DG -----FREE ENERGY OF REACTION
C EL -----ELEMENT OF CONCERN
C F ------FARADAY CONSTANT (CAL/VOLT)
C G(IT,IS)GIBBS FREE ENERGY
C ILM ----NUMBER OF LINES OF ACTIVITY/SOLUBILITY OUTPUT REQUIRED TO
C                COVER PH RANGE
C IPS ----PRODUCT SPECIES CODE
C IR -----REACTION INDEX
C IRS ----REACTANT  SPECIES CODE
C IS -----SPECIES INDEX
C ISC ----SOLUBILITY CODE
C              10 --IONIC WITH CP COEFFICIENTS
C              11 --CATION
C              12 --SIMPLE ANION + OH-
C              13 --OXYANION
C              14 -- ACID OXYANION
C              20 --SOLID
C              30 --GAS
C ISR(NS,I) REACTION NUMBERS REQUIRED FOR SOLUBILITY DETERMINATION
C                OF SPECIES NS
C ISS(NS) SPECIES NUMBER FOR WHICH SOLUBILITY IS TO BE DETERMINED
C IT -----TEMPERATURE INDEX
C LXDX ---NUMBER OF UNITS INCLUDED IN PH RANGE
C M ------DENOMINATOR OF LOG OF ACTIVITY CALCULATED FROM PH EQUATIO
C NH -----NUMBER OF MOLES H+
C NH2 ----NUMBER OF MOLES H2
C NH2O ---NUMBER OF MOLES H2O
C              NEGATIVE NUMBER OF MOLES EFFECTIVELY CHANGES THE
C      NORMAL  REACTANT-PRODUCT RULE OF THAT SPECIES IN THE EQTN:
C              REACTANT + H+ + H2 ---> PRODUCT + H2O
C NP -----NUMBER OF MOLES PRODUCT
C NR -----NUMBER OF MOLES REACTANT
C NRS ----NUMBER OF REACTIONS USED TO CALCULATE SOLUBILITY OF
C NS -----SOLUBILITY SPECIES INDEX                          SPECIES
C NSS ----NUMBER OF SPECIES REQUIRING SOLUBILITY DETERMINATION
C PH -----NEG LOG ACTIVITY H+
C PH2 ----HYDROGEN GAS PRESSURE
C R ------IDEAL GAS CONSTANT (J/G MOLE DEG K)
C RM -----DENOMINATOR OF LOG OF SOLUBILITY CALCULATED FROM POTENTIA
C                EQUATION
C S ------ENTROPY AT 25 DEG C
```

```
C SPEC ---SPECIES NAME
C SPEC(1)=H+
C SPEC(2)=H2
C SPEC(3)=H2O
C SPEC(4)=O2
C SS -----ENTROPY OF SPECIES AT TEMPERATURE
C T ------TEMPERATURE,(DEG K)
C XMIN ---MINIMUM FOR PH AXIS
C Z ------FORMULA UNITS OF ELECTRONS TRANSFERED IN REACTION
C
      LOGICAL ARN(50)
      DOUBLE PRECISION TYPE(3)
      DIMENSION CC(4,14),ISC(30),CP(3),A(30),T(7),SS(7),IRS(50),NR(5
     1 NH(50),NH2(50),IPS(50),NP(50),NH2O(50),DG(7,50),
     2 C(50,4),PHA(5),AA(5),G(7,20),TT(7),ISR(15,20),
     3 ISS(20),NRS(15),PH2(50),SPEC(30),TY(3)
      REAL LXDX,XMIN
      DATA TYPE/'SOLUBLE      SOLID        GASEOUS      '/
      DATA T/298.,333.,373.,423.,473.,523.,573./,F/23060.9/,R/1.9869
      DATA TT/'298','333','373','423','473','523','573'/
      DO 5 I=1,50
    5 ARN(I)=.FALSE.
      READ (5,1000)EL

 1000 FORMAT(A6)
      READ(5,1001)LXDX,XMIN
 1001 FORMAT(2F10.0)
      ILM=INT((2*LXDX + 1)/5 + 0.99)
      READ(5,1002)((CC(I,J),J=1,14),I=1,4)
 1002 FORMAT(14F5.3)
      WRITE(6,2000)

 2000 FORMAT('1')
 2001 FORMAT(/////)
      WRITE(6,2002)
 2002 FORMAT(2X,'SPECIES',3X,'TYPE',5X,'FREE ENERGY 25C',4X,
     1 'ENTROPY 25C',7X,'CP( ,1)',8X,'CP( ,2)',8X,'CP( ,3)',6X,
     2 'ACTIVITY'/)

C READ DIRECT G VS. T VALUES
C
      IS=1
   70 READ(5,1004)SPEC(IS),ISC(IS),(G(IT,IS),IT=1,7),A(IS)
 1004 FORMAT(A6,4X,I2,3X,4E15.0/3E15.0,23X,E12.0)
      IF(ISC(IS).EQ.0)GO TO 10
      WRITE(6,2005)SPEC(IS),TYPE(ISC(IS)/10),G(1,IS),A(IS)
 2005 FORMAT(1X,A6,4X,A10,E15.6,60X,E15.6)
      IS=IS+1
      GO TO 70
C
C OBTAIN DATA FOR EACH SPECIES
C
   10 READ(5,1003)SPEC(IS),ISC(IS),S,G(1,IS),(CP(I),I=1,3),A(IS)
 1003 FORMAT(A6,4X,I2,F8.0,5E12.0)
      IF(A(IS).EQ.0)A(IS)=1
      IF(ISC(IS))20,65,20
   20 IF(CP(1).NE.0.0)GO TO 50
C
C CALC FREE ENERGY FOR IONIC SPECIES
C
```

```
      WRITE(6,2003)SPEC(IS),TYPE(ISC(IS)/10),G(1,IS),S,A(IS)
 2003 FORMAT(1X,A6,4X,A10,2E15.6,45X,E15.6)
      DO 30 IT=1,7
   30 SS(IT)=CC(ISC(IS)-10,IT) + S*CC(ISC(IS)-10,IT+7)
      DO 40 IT=2,7
   40 G(IT,IS)=G(1,IS) + SS(1)*T(1) - SS(IT)*T(IT) +
     1 (SS(IT) - SS(1))*(T(IT) - T(1))/ALOG(T(IT)/T(1))
      IS=IS+1
      GO TO 10
C
C CALC FREE ENERGY FOR NON-IONIC SPECIES
C
   50 CP(2)=CP(2)*1.E-3
      CP(3)=CP(3)*1.E5
      WRITE(6,2004)SPEC(IS),TYPE(ISC(IS)/10),G(1,IS),S,(CP(I),I=1,
     1 ,A(IS)
 2004 FORMAT(1X,A6,4X,A10,6E15.6)
      DO 60 IT=2,7
      DT=T(IT)-T(1)
   60 G(IT,IS)=G(1,IS) - S*DT + CP(1)*(DT-T(1)*ALOG(T(IT)/T(1)))
     1 CP(2)*DT**2/2. + CP(3)*(2./T(1)-T(IT)/T(1)**2-1./T(IT))/2
      IS=IS+1
      GO TO 10
C
C OUTPUT G VS. T TABLE
C
   65 IS=IS-1
      WRITE(6,2001)
      WRITE(6,2006)TT
 2006 FORMAT(1X,'FREE ENERGY VS. TEMPERATURE'/70X,'DEG KELVIN'/13X
     1 7(13X,A3)/)
      WRITE(6,2007)(I,SPEC(I),(G(J,I),J=1,7),I=1,IS)
 2007 FORMAT(1X,I2,5X,A6,4X,7E16.6)
C
C READ AND WRITE REACTIONS
C
      WRITE(6,2001)
      WRITE(6,2008)
 2008 FORMAT(1X,'REACTIONS'/)
      IR=1
   90 READ(5,1005)IRS(IR),NR(IR),NH(IR),NH2(IR),IPS(IR),NP(IR),
     1 NH20(IR),PH2(IR)
 1005 FORMAT(7I5,30X,E10.0)
      IF(IRS(IR).EQ.0)GO TO 300
      IF(PH2(IR).EQ.0.)PH2(IR)=1.0
      WRITE(6,2009)IR
 2009 FORMAT(/1X,I2,';')
      IPP=-1
      IF(NR(IR))110,110,100
  100 CALL RITE(IPP,NR(IR),SPEC(IRS(IR)))
  110 IF(NH(IR))130,130,120
  120 CALL RITE(IPP,NH(IR),SPEC(1))
  130 IF(NH2(IR))150,150,140
  140 CALL RITE(IPP,NH2(IR),SPEC(2))
  150 IF(NP(IR))160,170,170
  160 CALL RITE(IPP,-NP(IR),SPEC(IPS(IR)))
  170 IF(NH20(IR))180,190,190
  180 CALL RITE(IPP,-NH20(IR),SPEC(3))
  190 CALL ARROW(IPP)
      IPP=-IPP-1
      IF(NR(IR))200,210,210
```

```
  200 CALL RITE(IPP,-NR(IR),SPEC(IRS(IR)))
  210 IF(NH(IR))220,230,230
  220 CALL RITE(IPP,-NH(IR),SPEC(1))
  230 IF(NH2(IR))240,250,250
  240 CALL RITE(IPP,-NH2(IR),SPEC(2))
  250 IF(NP(IR))270,270,260
  260 CALL RITE(IPP,NP(IR),SPEC(IPS(IR)))
  270 IF(NH2O(IR))290,290,280
  280 CALL RITE(IPP,NH2O(IR),SPEC(3))
  290 IR=IR+1
      GO TO 90
C
C CALC FREE ENERGY OF REACTION
C
  300 IR=IR-1
      IF(IR .LE. 0) GO TO 650
      WRITE(6,2001)
      WRITE(6,2010)TT
 2010 FORMAT(1X,'FREE ENERGY OF REACTION VS. TEMPERATURE'/
     1 68X,'DEG KELVIN'//7X,'REACTION',8X,A3,6(13X,A3)/)
      DO 320 JR=1,IR
      DO 310 IT=1,7
  310 DG(IT,JR)=NP(JR)*G(IT,IPS(JR)) + NH2O(JR)*G(IT,3) -
     1 NR(JR)*G(IT,IRS(JR)) - NH(JR)*G(IT,1) - NH2(JR)*G(IT,2)
  320 WRITE(6,2011)JR,(DG(I,JR),I=1,7)
 2011 FORMAT(10X,I2,3X,7E16.6)
C
C READ SOLUBILITY INFORMATION
C
      DO 325 I=1,20
  325 READ(5,1006,END=326)ISS(I),NRS(I),(ISR(II,I),II=1,NRS(I))
 1006 FORMAT(16I5)
  326 NSS=I-1
      IF(NSS.LE.0)GO TO 328
      DO 327 I=1,NSS
      DO 327 II=1,NRS(I)
  327 ARN(ISR(II,I))=.TRUE.
  328 DO 640 IT=1,7
C
C CALC PH OR POTENTIAL EQUATION COEFFICIENTS
C
      WRITE(6,2000)
      WRITE(6,2012)EL,TT(IT)
 2012 FORMAT(1X,'POTENTIAL-PH EQUATIONS FOR REACTIONS OF ',A10,' AT
     1 A3,' DEG K'//1X,'REACTION'/)
      DO 350 JR=1,IR
      Z=2.*NH2(JR)
      IF(Z)330,340,330
  330 C(JR,1)=-DG(IT,JR)/(Z*F)
      C(JR,2)=-2.303*R*T(IT)*NP(JR)/(Z*F)
      C(JR,3)=2.303*R*T(IT)*NR(JR)/(Z*F)
      IF(IRS(JR) - 1)336,335,336
  335 C(JR,4)=-C(JR,3)
      C(JR,3)=0.0
      GO TO 337
  336 C(JR,4)=-2.303*R*T(IT)*(NH(JR)+Z)/(Z*F)
  337 WRITE(6,2013)JR,TT(IT),C(JR,1),C(JR,2),SPEC(IPS(JR)),C(JR,3),
     1 SPEC(IRS(JR)),C(JR,4)
 2013 FORMAT(4X,I2,4X,'E(',A3,') =',E12.5,' + ',E12.5,'(LOG(',A10,
     1 ')) + ',E12.5,'(LOG(',A10,')) + ',E12.5,'(PH)')
      GO TO 350
  340 C(JR,1)=-DG(IT,JR)/(2.303*R*T(IT))
```

```
      WRITE(6,2014)JR,NH(JR),L(JR,1),NR(JR),SPEC(IRS(JR)),NP(JR),
     1 SPEC(IPS(JR))
```

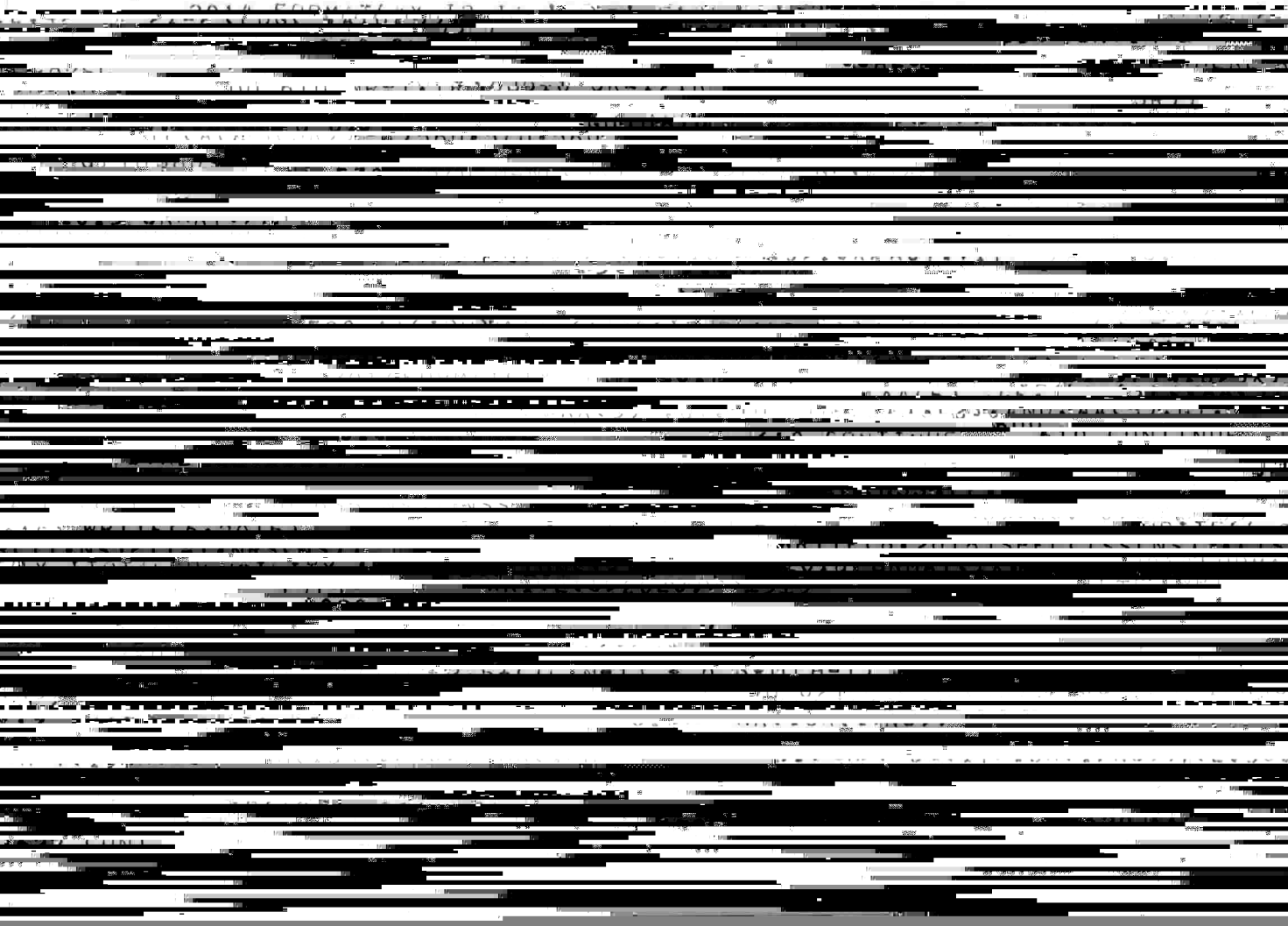

```
      WRITE(6,2017)(PHA(J),AA(J),J=1,5)
      IF(AA(5) .LE. 1.E-25 .OR. AA(5) .GE. 1.E25)GO TO 635
  630 CONTINUE
  635 CONTINUE
  640 CONTINUE
  650 WRITE(6,2000)
      CALL EXIT
      END


      SUBROUTINE RITE(I,N,NAM)
C
      SIGN='+'
      IF(I .LE. 0)SIGN=' '
      I=IABS(I) + 1
      J=I-1
      GO TO (10,20,30,40,50,60),J
   10 WRITE(6,1000)SIGN,N,NAM
 1000 FORMAT('+',3X,A1,I3,'(',A6,') ')
      RETURN
   20 WRITE(6,1001)SIGN,N,NAM
 1001 FORMAT('+',20X,A1,I3,'(',A6,') ')
      RETURN
   30 WRITE(6,1002)SIGN,N,NAM
 1002 FORMAT('+',37X,A1,I3,'(',A6,') ')
      RETURN
   40 WRITE(6,1003)SIGN,N,NAM
 1003 FORMAT('+',54X,A1,I3,'(',A6,') ')
      RETURN
   50 WRITE(6,1004)SIGN,N,NAM
 1004 FORMAT('+',71X,A1,I3,'(',A6,') ')
      RETURN
   60 WRITE(6,1005)SIGN,N,NAM
 1005 FORMAT('+',86X,A1,I3,'(',A6,') ')
      RETURN
      END


      SUBROUTINE ARROW(I)
C
      GO TO (20,30,40,50),I-1
   20 WRITE(6,1000)
 1000 FORMAT('+',20X,'  ------------> ')
      RETURN
   30 WRITE(6,1001)
 1001 FORMAT('+',37X,'  ------------> ')
      RETURN
   40 WRITE(6,1002)
 1002 FORMAT('+',54X,'  ------------> ')
      RETURN
   50 WRITE(6,1003)
 1003 FORMAT('+',71X,'  ------------> ')
      RETURN
      END
```

Appendix 2

Calculation of a Reduction Potential

Consider the half-cell reaction

$$AgO^- + 2H^+ + e = Ag + H_2O \qquad (1)$$

If the reduction potential is measured with respect to the SHE, the cell reaction is

$$2AgO^- + 2H^+ + H_2 = 2Ag + 2H_2O \qquad (2)$$

A calculation of $E^{\ominus}_{473}$ for this reaction will be performed using the method proposed by Macdonald (see section 2.2.2). The first step is to evaluate $\Delta^{T}_{298,f}G^{\ominus}$ for each species. The following data is available for Ag:

$$C^{\ominus}_p = 21.30+8.54\times10^{-3}T + 1.51\times10^{5}T^{-2} \text{ J K}^{-1} \text{ mol}^{-1}$$

$$S^{\ominus}_{298} = 42.55 \text{ J K}^{-1} \text{ mol}^{-1}$$

$$\Delta_f G^{\ominus}_{298} = 0 \text{ kJ mol}^{-1}$$

Since $C^{\ominus}_p$ is known, equation 3 may be used:

$$\Delta^{T}_{298,f}G^{\ominus} = \Delta_f G^{\ominus}_{298} - S^{\ominus}_{298}\,(T-298) - T\int_{298}^{T} \frac{C^{\ominus}_p}{T}\,dT + \int_{298}^{T} C^{\ominus}_p\,dT \qquad (3)$$

Substituting the appropriate values yields

$$\Delta^{473}_{298,f}G^{\ominus} = 0 - 42.55(473-298) - 473\int_{298}^{473} \frac{(21.30+8.54\times10^{-3}T+1.51\times10^{5}T^{-2})}{T}\,dT + \int_{298}^{473} (21.30+8.54\times10^{-3}T+1.51\times10^{5}T^{-2})\,dT$$

$$= -8.56 \text{ kJ mol}^{-1}$$

A heat capacity function for AgO^- is not available and $\Delta^T_{298,f}G^\ominus$ for this species must be evaluated from equation 4:

$$\Delta^T_{298,f}G^\ominus = \Delta_f G^\ominus_{298} - (TS^\ominus_T - 298S^\ominus_{298}) + \frac{T-298}{\ln(T/298)}(S^\ominus_T - S^\ominus_{298}) \qquad (4)$$

A value of $S^\ominus_{298}(AgO^-)$ has not been reported but it may be determined from the equation of Connick and Powell:

$$S^\ominus = 182.0-194.6(|Z| - 0.28\ n_o) \qquad (5)$$

For AgO^-, the number of oxygen atoms, n_o=1 and the charge, Z= -1 and therefore $S^\ominus = 41.9\ J\ K^{-1}\ mol^{-1}$. To use this value in the Criss and Cobble equation (7), $S^\ominus$ must be converted to the absolute scale.

$$S^\ominus(\text{absolute}) = S^\ominus(\text{conventional}) - 20.9\ Z \qquad (6)$$
$$= 62.8\ J\ K^{-1}\ mol^{-1}$$

The constants, a and b, in the Criss and Cobble equation

$$S^\ominus_T = a + bS^\ominus_{298} \qquad (7)$$

for oxyanions at 473 K are $-280.5\ J\ K^{-1}\ mol^{-1}$ and 2.020 (dimensionless), respectively.

Therefore $$S^\ominus_{473} = -280.5+2.020\times62.8$$
$$= -153.7\ J\ K^{-1}\ mol^{-1}$$

Substitution of this value and $\Delta_f G^\ominus_{298}$ (= $-23.1\ kJ\ mol^{-1}$) into equation 4 yields

$$\Delta^{473}_{298,f}G^\ominus(AgO^-) = -23100 - [473(-153.7) - 298(62.8)]$$
$$+ \frac{473 - 298}{\ln(473/298)}(-153.7-62.8)$$
$$= -13.7\ kJ\ mol^{-1}.$$

A value of $\Delta^{473}_{298,f}G^{\ominus}$ for H^+ has been evaluated previously by Macdonald (see section 2.4.3), while the corresponding values for H_2 and H_2O may be determined using equation 3.

$$\Delta^{473}_{298}G^{\ominus}(H_2) = 0 + 130.574(473-298) - 473\int_{298}^{473}\frac{(27.28+3.26\times10^{-3}T+0.50\times10^{5}T^{-2})}{T}\,dT + \int_{298}^{473}(27.28+3.26\times10^{-3}T+0.50\times10^{5}T^{-2})\,dT$$

$$= -24.12 \text{ kJ mol}^{-1}$$

$$\Delta^{473}_{298}G^{\ominus}(H_2O) = -237183 + 69.92(473-298) - 473\int_{298}^{473}\frac{75.291}{T}\,dT + \int_{298}^{473}(75.291)\,dT$$

$$= -252.69 \text{ kJ mol}^{-1}$$

The free energy change for reaction 2 may now be evaluated.

$$\Delta G^{\ominus} = 2\times\Delta^{473}_{298,f}G^{\ominus}(Ag) + 2\times\Delta^{473}_{298,f}G^{\ominus}(H_2O) - 2\times\Delta^{473}_{298,f}G^{\ominus}(AgO^-) - 2\times\Delta^{473}_{298,f}G^{\ominus}(H^+) - \Delta^{473}_{298,f}G^{O}(H_2) \qquad (8)$$

$$= -465.8 \text{ kJ}.$$

To obtain the reduction potential at 473 K as a function of pH, equation 9 is considered.

$$E_T = \frac{-\Delta G^{\ominus}_T}{nF} - \frac{2.303RT}{nF}[\text{blog } a_B - \text{alog } a_A] - \frac{2.303\times RT}{nF}\,pH \qquad (9)$$

Since $a(H_2O)$ and $a(Ag)$ are both assigned as unity, and for reaction 1, the number of hydrogen ions, x=2 and the charge transferred, n=1, then

$$E_{473} = 2.41 + 0.094\log[a(AgO^-)] - 0.188\,pH.$$

Appendix 3

Diffusion from a Cylindrical Surface

The problems of cylindrical diffusion can be treated in terms of linear diffusion under certain conditions (166). Provided that the following condition holds

$$\frac{D\tau}{r^2} \leq 3\times10^{-3}$$

where D is the diffusion coefficient, τ is the time elapsed since the beginning of electrolysis and r is the radius of the electrode, the error in calculating the current in the initial stage of an electrolysis at constant potential from the equation for linear diffusion is less than 5%. Taking $D = 10^{-5}$ cm^2 s^{-1} and r = 0.25 cm, the error does not exceed 5% if τ is less than 19 seconds. The time corresponding to the ascending branch of a peak in cyclic voltammetry is generally less than 10 s for this work and consequently the treatment for linear diffusion can be regarded as a good approximation for cylindrical diffusion.

Appendix 4

Calculation of D_F using the Nernst-Einstein Equation

The diffusion coefficient, D, of an ion may be obtained from the Nernst-Einstein equation (167,204)

$$D = \frac{RT\lambda}{zF^2} \qquad (1)$$

where λ is the molar conductivity of the ion and z is its charge. If Ag^+ ions are assumed to be the charge carriers, then a component of ionic conductivity corresponding to migration of Ag^+ ions may be estimated from the conductivity of Ag_2O, 10^{-6} S m^{-1} (120).

From equation 2

$$\lambda(Ag^+) = \kappa \times \frac{V_m}{2} \qquad (2)$$

where κ is the ionic conductivity, 10^{-6} S m^{-1}, and V_m is the molar volume of Ag_2O, 32.7 cm^3 mol^{-1} (see section 8.4.2), $\lambda(Ag^+) = 1.64\times10^{-11}$ S m^2 mol^{-1}. Using this value of $\lambda(Ag^+)$, D_F for Ag^+ at 295 K may be calculated from equation 1:

$$D_F = \frac{8.314\times295\times1.64\times10^{-11}}{1\times(9.65\times10^4)^2}$$

$$= 4\times10^{-18} \text{ m}^2 \text{ s}^{-1}.$$

Bibliography

1. Agar J. N., Rev. Pure and App. Chem., 8, 1 (1958).
2. Amlie R. F. and Ruetschi P., J. Electrochem. Soc. 108, 813 (1961).
3. Antikainen P. J., Hietanen S., and Sillen L. G., Acta Chem. Scand., 14, 95 (1960).
4. Armstrong R. D., J. Electroanal. Chem. 34, 387 (1972).
5. Armstrong R. D., Corros. Sci. 11, 693 (1971).
6. Armstrong R. D. and Edmondson K., Electrochim. Acta 18, 937 (1972).
7. Armstrong R. D. and Edmondson K., J. Electroanal. Chem. 53, 371 (1974).
8. Armstrong R. D., Firman R. E. and Thirsk H. R., Disc. Faraday Soc., 56, 244 (1973).
9. Armstrong R. D. and Henderson M., J. Electroanal. Chem. 39, 81 (1972).
10. Asakura S. and Nobe K., J. Electrochem. Soc. 118, 536 (1971).
11. Bacon R. G. and Stewart D., J. Chem. Soc. C, 1384 (1966).
12. Bachmann K. J. and Bertocci U., Electrochim. Acta 15, 1877 (1970).
13. Barker G. C. and Jenkins I. L., Analyst 77, 685 (1952).
14. Barradas R. G. and Fraser G. H., Can. J. Chem. 42, 2488 (1964).
15. Baticle A. M., Rudelle R., Vennereau P., and Vernieres J., J. Electroanal. Chem. 45, 439 (1973).
16. Berzins T. and Delahay P., J. Am. Chem. Soc. 75, 555 (1953).
17. Biedermann G. and Sillen L. G., Acta Chem. Scand. 14, 717 (1960).
18. Bignold G. J., Corrosion Sci. 12, 145 (1972).
19. Bignold G. J., Garnsey R., Mann G.M.W., Corrosion Sci. 12, 325 (1972).
20. Boden P. J., Corrosion Sci. 11, 363 (1971).
21. Bottger W., Z. Physik. Chem. 46, 521 (1903).
22. Brainina Kh.Z. and Yarunina G. V., Electrokhimiya 2, 781 (1966).
23. Breiter M., J. Electrochem. Soc. 112, 845 (1965).
24. Briggs G.W.D., Fleischmann M., Lax D. J., and Thirsk H. R., Trans. Faraday Soc. 64, 3120 (1968).
25. Cahan B. D., Ockerman J. B., Amlie R. F. and Ruetschi P., J. Electrochem. Soc. 107, 725 (1960).
26. Calandra A. J., de Tacconi N. R., Pereiro R., and Arvia A. J. Electrochim. Acta 19, 901 (1974).
27. Carr D. S. and Bonilla C. F., J. Electrochem. Soc. 99, 475 (1952).
28. Casadio S., J. Electroanal. Chem. 67, 123 (1976).
29. Case B. and Bignold C. J., J. Appl. Electrochem. 1, 141 (1973).

30. Casey E. J. and Moroz W. J., Can. J. Chem. 43, 1199 (1965).

31. Castle J. E., Harrison J. T. and Masterton H. G., Proc. 2nd Int. Conf. Met. Corr. 822 (1963).

32. Chambers J. F., Stokes J. M. and Stokes R. H., J. Phys. Chem. 60, 985 (1956).

33. Chemical Electronics, Instruction Manual for the Potentiostat Type 403A.

34. Clarke T. G., Hampson N. A., Lee J. B., Morley J. R., and Scanlon B., Can. J. Chem. 46, 3437 (1968).

35. Clarke T. G., Hampson N. A., Lee J. B., Morley J. R., and Scanlon B., Ber. Bunsenges Phys. Chem. 73. 279 (1969).

36. Cobble J. W., J. Am. Chem. Soc. 86, 5394 (1964).

37. CODATA Recommended Key Values for Thermodynamics, 1975, J. Chem. Thermodynamics 8, 603 (1976).

38. Cohen G. L. and Atkinson G., J. Electrochem. Soc. 115, 1236 (1968).

39. Connick R. E. and Powell R. W., J. Chem. Phys. 21, 2206 (1953).

40. Conway B. E., The Theory and Principles of Electrode Processes, Ronald Press, New York (1965).

41. Conway B. E., Gileadi E., Angerstein-Kozlowska H., J. Electrochem. Soc. 112, 341 (1965).

42. Conway B. E., Sattar M. A., Gilroy D., Electrochim. Acta 14, 677 (1969).

43. Conway B. E. and Wojtowicz J., Proc. 2nd Internat. Congress on Fuel Cells, S.E.R.A.I., Brussels, p64 (1967).

44. Cowan R. L. and Staehle R. W., J. Electrochem. Soc. 118, 557 (1971).

45. Criss C. M. and Cobble J. W., J. Am. Chem. Soc. 86, 5385, 5390 (1964).

46. Croft G. T., J. Electrochem. Soc. 106, 278 (1959).

47. Croft G. T. and Tuomi D., J. Electrochem. Soc. 108, 915 (1961).

48. Darken L. S. and Meier H. F., J. Am. Chem. Soc. 64, 621 (1942).

49. deBethune A. J., Licht T. S. and Swendeman, J. Electrochem. Soc. 106, 617 (1959).

50. Debye P., Polar Molecules, Dover Publications, New York (1929).

51. Delahay P., J. Am. Chem. Soc. 75, 1190 (1953).

52. Delahay P., Adv. Electrochem. and Electrochem. Eng. 1, 233 (1961).

53. Delahay P., New Instrumental Methods in Electrochemistry, Interscience Publishers, New York (1954).

54. Delépine M., and Bonnet P., Compt. Rend. 149, 39 (1909).

55. de Levie R., Electrochim. Acta 10, 113 (1965).

56. de Levie R., Electrochim. Acta 10, 395 (1965).

57. de Levie R., Adv. Electrochem. and Electrochem. Eng. 6, 329 (1967).

58. Devanathan M.A.V., Bockris J. O'M., and Reddy J.K.N., Proc. Roy. Soc., London A279, 327 (1964).

59. Dignam M. J., Barrett H. M., and Nagy G., Can. J. Chem. 47, 4253 (1969).
60. Dirkse T. P., J. Electrochem. Soc. 106, 453 (1959).
61. Dirkse T. P., J. Electrochem. Soc. 107, 859 (1960).
62. Dirkse T. P., J. Electrochem. Soc. 109, 173 (1962).
63. Dirkse T. P., J. Chem. Eng. Data 6, 538 (1961).
64. Dirkse T. P. and De Vries D. B., J. Phys. Chem. 63, 107 (1959).
65. Dirkse T. P., de Wit D., and Schoemaker R., J. Electrochem. Soc. 114, 1196 (1967).
66. Dirkse T. P., Van Der Lugt L. and Schnyders H., J. Inorg. Nucl. Chem. 25, 859 (1963).
67. Dirkse T. P. and Wiers B., J. Electrochem. Soc. 106, 284 (1959).
68. Dobson J. V., Chapman B. R., and Thirsk H. R., paper presented to the International Conference on High Temperature High Pressure Electrochemistry in Aqueous Solutions (N.A.C.E.), University of Surrey (1973).
69. Dobson J. V., Dickinson T., and Snodin P. R., J. Electroanal. Chem. 69, 215 (1976).
70. Ellis P. J. and Fyfe W. S., Rev. Pure and App. Chem. 7, 261 (1957).
71. Ershler B. V., Disc. Faraday Soc. 1, 269 (1947).
72. Ershler B. V., Zhur. Fiz. Khim. 22, 683 (1948).
73. Erdey-Gruz T., Kinetics of Electrode Processes, Hilger, London (1972).
74. Eversole W. G. and Boardman W. W., J. Phys. Chem. 46, 914 (1942).
75. Faivre R., Ann. Chim. 19, 58 (1944).
76. Falkenhagen H., Electrolytes, Clarendon Press, Oxford (1934).
77. Fisher J. R. and Barnes H. L., J. Phys. Chem. 76, 90 (1972).
78. Fleischer A., J. Electrochem. Soc. 115, 816 (1968).
79. Fleischmann M., Lax D. J. and Thirsk H. R., Trans. Faraday Soc. 64, 3128 (1968).
80. Fleischmann M., Lax D. J. and Thirsk H. R., Trans. Faraday Soc. 64, 3137 (1968).
81. Fleischmann M. and Thirsk H. R., Electrochim. Acta 1, 146 (1959).
82. Fleischmann M. and Thirsk H. R., Adv. Electrochem. and Electrochem. Eng. 3, 123 (1963).
83. Fried F., Z. Physik. Chem. 123, 406 (1926).
84. Gerischer H., Z. Physik. Chem. 198, 286 (1951).
85. Gerischer H., Z. Physik. Chem. 201, 55 (1952).
86. Gileadi E. and Conway B. E. in: Modern Aspects of Electrochemistry (ed. Conway B. E. and Bockris J. O'M.), Butterworths, London, 3, 443 (1964).

87. Giles R. D. and Harrison J. A., J. Electroanal. Chem. 27, 161 (1970).

88. Giles R. D., Harrison J. A. and Thirsk H. R., J. Electroanal. Chem. 22, 375 (1969).

89. Gilman S., J. Phys. Chem. 66, 2657 (1962).

90. Gilroy D. and Conway B. E. J. Phys. Chem. 69, 1259 (1965).

91. Gol'dshtein S. L. and Seleznev V. D., Elektrokhimiya 11, 694 (1975).

92. Goodrich J. C., Goyan F. H., Morse E. E., Preston R. G., and Young M. B., J. Am. Chem. Soc. 72, 4411 (1950).

93. Graff W. S. and Stadelmaier H. H., J. Electrochem. Soc. 105, 446 (1958).

94. Grahame D. C., J. Electrochem. Soc., 99, 370C (1952).

95. Hamer H. G. and Craig D. N., J. Electrochem. Soc. 104, 206 (1957).

96. Hampson N. A., Electrochemistry 2, 117 (1972).

97. Hampson N. A., Larkin D. and Morley J. R., J. Electrochem. Soc. 114, 817 (1967).

98. Hampson N. A., Lee J. B. and Morley J. R., Electrochim. Acta 16, 637 (1971).

99. Owen B. B. and Zeldes H., J. Chem. Phys. 13, 473 (1945).

100. Helgeson H. C., Am. J. Sci. 267, 729 (1969).

101. Henderson P., Z. Physik. Chem. 59, 118 (1907); 63, 325 (1908).

102. Hewlett-Packard Company, Operating and Service Manual for the Model 3465 A Multimeter (1975).

103. Hickling A. and Taylor D., Disc. Faraday Soc. 1, 277 (1947).

104. Hoare J. P., The Electrochemistry of Oxygen, Interscience, New York (1968).

105. Hopkinson B. E., Am. Soc. Mech. Engrs. Paper 62-WA-274 (1962).

106. Houston Instrument, Instruction Manual for the Series 2000 Omnigraphic X-Y recorder.

107. Ives D.J.G. and Janz G. J., Reference Electrodes, Academic Press, New York (1961).

108. Johnston H. L., Cuta F. and Garrett A. B., J. Am. Chem. Soc. 55, 2311 (1933).

109. Jones D. de G. and Masterton H. G., Adv. in Corrosion Sci. and Tech. 1, 1 (1970).

110. Jones P. and Thirsk H. R., Trans. Faraday Soc. 50, 732 (1954).

111. Kabanov B. N. and Leikis D. I., Z. Elektrochem., 62, 660 (1958).

112. Kelley K. K., Bulletin 584, U.S. Bureau of Mines (1960).

113. Keyes, International Critical Tables, New York, McGraw-Hill.

114. Kohlrausch F. W., Ann. Phys., 6, 1 (1879).

115. Kortuem G. and Haeussermann W. F., Ber. Bunsenges. Phys. Chem. 69, 594 (1965).

116. Damaskin B. B., The Principles of Current Methods for the Study of Electrochemical Reactions, McGraw-Hill, New York (1967).

117. Kubaschewski O., Evans E. El. and Alcock C. B. Metallurgical Thermochemistry (4th Ed.), Pergamon Press, Oxford (1967).

118. Laliberetē L. and Conway B. E., Ref. 37 in Electrochim. Acta 17, 1447 (1972).

119. Latimer W. M., J. Chem. Phys. 23, 90 (1955).

120. Le Blane M. and Sachse H., Z. Physik. 32 , 887 (1931).

121. Leikis D. I., Vidovitsh G. L., Kuoz L. L. and Kabanov B. N., Z. Physik. Chem. 214, 334 (1960).

122. Lietzke M. H., Greeley R. G., Smith W. T. and Stoughton R. W., J. Phys. Chem. 64, 652 (1960).

123. Lietzke M. H. and Vaughen J. V., J. Am. Chem. Soc. 77, 876 (1955).

124. Liu C. and Lindsay W. T., J. Solution Chem. 1, 45 (1972).

125. Llopis J., Fernandez-Biarge J. and Perez-Fernandez M., Electrochim. Acta 1, 130 (1959).

126. Luther R. and Pokorney F., Z. Anorg. U. Allgem. Chem. 57, 290 (1908).

127. Macdonald D. D., J. Electrochem. Soc. 121, 651 (1974).

128. Macdonald D. D. in: Modern Aspects of Electrochemistry (ed. Conway B. E. and Bockris J. O'M.) Butterworths, London 2, 141 (1975).

129. Macdonald D. D., Electrochim. Acta 21, 169 (1976).

130. Macdonald D. D., paper presented at the conference "Corrosion/77", (N.A.C.E.), San Francisco (1977).

131. Macdonald D. D., Transient Techniques in Electrochemistry, in press.

132. Macdonald D. D. and Butler P., Corrosion Sci. 13, 259 (1973).

133. Macdonald D. D. and Owen D., J. Electrochem. Soc., 120, 317 (1973).

134. Macdonald D. D. and Owen D., paper presented at the International Conference on High Temperature High Pressure Electrochemistry in Aqueous Solutions (N.A.C.E.), University of Surrey (1973).

135. Macdonald D. D., Shierman G. R., and Butler P., Atomic Energy of Canada Ltd, AECL-4136 (1972).

136. MacMillan J. A., Nature 195, 594 (1962).

137. MacMillan J. A., Chem. Rev. 62, 65 (1962).

138. McKie A. and Clark D., in Batteries, ed. D. H. Collins, p.285. Pergamon, Oxford (1963).

139. Mehl W. and Bockris J. O'M., Can. J. Chem. 37, 190 (1959).

140. Melik-Gaikazyan V. I., Zh. Fiz. Khim. 26, 560 (1952).

141. Miller B., J. Electrochem. Soc. 117, 491 (1970).

142. Miller D. G., Chem. Rev. 60, 15 (1960).

143. Moore, J. C. and Bindley D., Proc. 2nd Int. Conf. Met. Corr., 391 (1963).

144. Morley J. R., Thesis, Loughborough, University of Technology (1969).

145. Morley J. R., Unpublished data (see reference 34).

146. Muller W. J., Trans. Faraday Soc. 27, 737 (1931).

147. N.B.S. Technical Note 270-1 (1965).

148. N.B.S. Technical Note 270-4 (1969).

149. Nicholson R. S., Anal. Chem. 37, 1351 (1965).

150. Nicholson R. S. and Shain I. Anal. Chem. 36, 706 (1964).

151. Oshe A. I., Elektrokhimiya 4, 1214 (1968).

152. Osteryoung R. A., Lauer G. and Anson F. C., J. Electrochem. Soc. 110, 926 (1963).

153. Ostrovskii V. and Temkin M., Kinetics Catalysis 7, 466 (1966).

154. Perkins R. S., Tilak B. V., Conway B. E. and Kozlowska H. A., Electrochim. Acta 17, 1471 (1972).

155. Pleskov Y. V., Dokl. Akad. Nauk. S.S.S.R. 117, 645 (1957).

156. Pletcher D., Chem. Soc. Revs. 4, 471 (1975).

157. Postlethwaite J., Electrochim. Acta 12, 333 (1967).

158. Potter E. C. and Mann G.M.W., in Proc. First Int. Cong. Met. Corrosion, Butterworths, London, 1961, p.417.

159. Pourbaix M., Atlas of Electrochemical Equilibria, Pergamon, Oxford (1964).

160. Princeton Applied Research Corp., Instruction Manual for the Two Phase/ Vector Lock-in Amplifier Model 129 A (1973).

161. Quist A. S., J. Phys. Chem. 74, 3396 (1970).

162. Randles J.E.B., Trans. Faraday Soc. 44, 327 (1948).

163. Randles J.E.B., Disc. Faraday Soc. 1, 11 (1947).

164. Randles J.E.B. and Somerton K. W., Trans. Faraday Soc. 48, 937, 951 (1952).

165. Riddiford A. C., J. Phys. Chem. 56, 745 (1952); Taylor H. S., J. Chem. Phys. 6, 331 (1938).

166. Rius A., Polo S., and Llopis J., Anales. Real Soc. Espan. Fis. y Quim. 45, 1029 (1949).

167. Robinson R. A. and Stokes R. H., Electrolyte Solutions, Butterworths, London (1959).

168. Scatturin V. and Bellon P., J. Electrochem. Soc. 108, 819 (1961).

169. Scatturin V., Bellon P. L. and Salkind A. J., J. Electrochem. Soc. 108, 819 (1961).

170. Sevcik A., Coll. Czech. Chem. Communs. 13, 349 (1948).

171. Seys A. A. and Van Haute A. A., paper presented to the International Conference on High Temperature High Pressure Electrochemistry in Aqueous Solutions (N.A.C.E.), University of Surrey (1973).

172. Sluyters-Rehbach M. and Sluyters J. H. in: Electroanalytical Chemistry (Bard A. J., ed.) 4, 1, Marcel Dekker, New York (1970).

173. Smith D. E., in Electroanalytical Chemistry (Bard A. J., ed.) 1, 1, Marcel Dekker, New York (1966).

174. Owen B. B., Miller R. C., Milner C. E. and Cogan H. L., J. Phys. Chem. 65, 2065 (1961).

175. Srinivasan S. and Gileadi E., Electrochim. Acta 11, 321 (1966).

176. Stehlik B., Chem. Zveshi, 17, 6 (1963).

177. Stonehart P., Electrochim. Acta 13, 1789 (1968).

178. Stonehart P., Kozlowska H. A. and Conway B. E., Proc. Roy. Soc., London A310, 541 (1969).

179. Stonehart P. and Portante F. P., Electrochim. Acta 13, 1805 (1968).

180. Takehara Z., Namba Y. and Yoshizawa S., Electrochim. Acta 13, 1395 (1968).

181. Thirsk H. R. and Harrison J. A., A Guide to the Study of Electrode Kinetics, Academic Press, London (1972).

182. Tilak B. V., Perkins R. S., Kozlowska H. A. and Conway B. E., Electrochim. Acta 17, 1447 (1972).

183. Timmer B., Sluyters-Rehbach M. and Sluyters J. H., J. Electroanal. Chem. 18, 93 (1968).

184. Towns M. G., Greeley R. S., and Lietzke M. H., J. Phys. Chem. 64, 1861 (1960).

185. Vermilyea D. A., Adv. in Electrochem. and Electrochem. Eng. 3, 211 (1963).

186. Veselovskii V. I., Act. Physicochim. U.R.S.S. 14, 483 (1942).

187. Veselovskii V. I. and Borisova T., Electrochim. Acta 10, 325 (1965).

188. Vetter K. J., Electrochemical Kinetics, Academic Press, New York (1967).

189. Vidovitsh G. L., Leikis D. I. and Kabanov B. N., Dokl. Akad. Nauk. S.S.S.R., 124, 855 (1959), 142, 109 (1962).

190. Vol Y. T. and Shishakov N. A., Isv. Akad. Nauk. S.S.R., Ser. Khim., 1963 (11).

191. Von Fraunhofer J. H. and Banks C. H., Potentiostat and its Applications, London, Butterworths 1972.

192. Waggener W. C., Oak Ridge National Laboratory, private communication (see ref. 122).

193. Wales C. P. and Burbank J., J. Electrochem. Soc. 106, 885 (1959).

194. Warburg E., Ann. Physik. 67, 493 (1899); 6, 125 (1901).

195. Warwzanek S., Science 155, 39 (1967).

196. Wicks C. E. and Block F. E., Bulletin 605, U.S. Bureau of Mines (1963).

197. Will F. and Knorr C.A., Z. Elektrochem. 64, 258, 270 (1960).

198. Williams D. E. and Wright G. A., Electrochim. Acta 21, 1009 (1976).

199. Yoshi A., J. Chem. Ind., Tokyo 64, 600 (1961).

200. Young L., Anodic Oxide Films, Academic Press, New York (1961).

201. Weber W., Z. Angew. Phys. 7, 96 (1955).

202. Shewmon P. G., Diffusion in Solids, McGraw-Hill, New York (1963).

203. International Critical Tables, McGraw-Hill, New York.

204. Flynn C. P., Point Defects and Diffusion, Clarendon Press, Oxford (1972).

Acknowledgements

I am very grateful for the assistance given by Professor J. W. Tomlinson, particularly for his guidance and helpful discussions, and Dr D. D. Macdonald who initiated this research and maintained an interest throughout it. Their support and knowledge offered during this time were very much valued.

I would also like to express my appreciation of the interest and contributions, in particular of Mr C. Snell for his extensive technical work and willing advice, Mr C. Taylor, Mr I. Crighton and Mr C. Heath, their aid being invaluable in conducting the experimental work in this thesis. Also greatly appreciated were the many useful suggestions and practical help of my colleague, Dr M. McKubre, and the advice and assistance of Mr E. Stevens in the preparation of diagrams.